Formation of Young Massive Star Clusters: a High-Resolution Multi-Wavelength Study of Intensely Star-Forming Galaxies

Submitted in fulfilment of the requirements
for the degree of Doctor of Philosophy
in the Department of Astronomy
University of Cape Town

Rojovola Zara-Nomena RANDRIAMANAKOTO

Supervisors:
Dr. Petri Väisänen[a]
Dr. Kurt van der Heyden[b]

MAY 2015

[a] South African Astronomical Observatory
[b] Astronomy Department, University of Cape Town

Declaration

The work presented in this thesis is partly based on collaborations with my supervisor Petri Väisänen together with Erkki Kankare, Seppo Mattila, Stuart Ryder, and Andres Escala. The other collaborators include Sudhanshu Barway, Jari Kotilainen and Angela Adamo. Some of the work has already been published in the following peer-reviewed papers:

- **Randriamanakoto Z.**, Väisänen P., Ryder S., et al.
  The K-band luminosity functions of super star clusters in luminous infrared galaxies, their slopes and the effects of blending
  2013, MNRAS, 431, 554 [Chapter 3]

- **Randriamanakoto Z.**, Escala A., Väisänen P., et al.
  Near-infrared Adaptive Optics Imaging of Infrared Luminous Galaxies: The Brightest Cluster Magnitude-Star Formation Rate Relation
  2013, ApJ Letters, 775, 38 [Chapter 4]

- Väisänen P., Barway S. & **Randriamanakoto Z.**
  Star clusters in a nuclear star-forming ring: The disappearing string of pearls
  2014, ApJ Letters, 797, 16 [Chapter 5]

This thesis has been typeset from a TEX/LATEX file prepared by the author with the template designed by Florent Renaud.

I know the meaning of plagiarism and hereby declare that this thesis is my own. It has not been submitted before, either in the same or different form, for any degree or examination in any other University.

Zara Randriamanakoto

Abstract

Super star clusters (SSCs) represent the youngest and most massive form of known gravitationally bound star clusters in the Universe. They are born abundantly in environments that trigger strong and violent star formation (SF) such as in galaxy mergers and interacting systems. SSCs are thus used as fundamental tools to understand the context of massive SF and galaxy evolution in general.

This thesis investigates properties of these young, massive and dense star clusters in a sample of 42 nearby starbursts and luminous infrared galaxies (LIRGs) with IR luminosities between $10^{10.6} - 10^{11.9}\,L_{\odot}$ and distances $D_L \sim 25 - 150\,\mathrm{Mpc}$, with $D_L \approx 200\,\mathrm{Mpc}$ for a handful of the most distant galaxies. The targets form the sample of the SUperNovae and starBursts in the InfraReD (SUNBIRD) survey that were imaged using near-infrared K-band adaptive optics mounted on the Gemini/NIRI and the VLT/NaCo instruments.

We fitted power-laws to the SSC K-band luminosity functions and found index values ranging between 1.5 and 2.4 with a median value of $\alpha \sim 1.86 \pm 0.24$. This is shallower than the average of ≈ 2.4 associated with normal spiral galaxies indicating that SSCs hosted by star-forming galaxies are disrupted in a way depending on their mass or environment. Using simulations we found that blending effects are not significant for targets closer than $\approx 100\,\mathrm{Mpc}$. We also established the first ever near-infrared (NIR) brightest star cluster magnitude − star formation rate (SFR) relation. The correlation has a steeper slope compared to the one with optical data at lower SFRs which could indicate a simple statistical effect, though we argue that a physical truncation of the mass distribution at high masses would better explain the tight scatter of the observed relation.

Finally, we combined new NIR imaging of seven LIRG targets with their optical HST archival data to derive the age, mass, and extinction distributions of optically-selected SSC candidates using `Yggdrasil` SSP models. Apart from having a high mass range of $10^4 - 10^8 M_{\odot}$, more than a quarter of the cluster population is younger than 30 Myr. We also derived the cluster initial mass functions and found that at least in one of the LIRGs, a mass-dependent disruption mechanism is responsible for the deficiency in low-mass star clusters. The cluster formation efficiencies $\Gamma = 10 - 23\,\%$, on the other hand, support the arguments that highly-pressurized environments favor SF in bound star clusters.

This work has shown the importance of studying SSC host galaxies with high SFR levels to address the details of star cluster formation and evolution and the universality of the cluster initial mass function.

To my mother,
who gave me everything

"Avia, Neny tiako f'aza miahiahy
Ny ataoko anie sombin'ny vitanao hatrizay
Aoka izay fa ianao ilay niaro indray no mba mila fiarovana "

Acknowledgments

I don't believe my own strength would have been enough to finish this thesis all by myself. I gratefully acknowledge YOU Lord God Almighty for providing me the right supervisor and the necessary health, skills and knowledge throughout this long journey. The road has not been easy but Your faithfulness and grace were always new every morning. Thank you Lord! "You alone are my strength, my shield".

Next, I would like to express my gratitude to my supervisor, Dr Petri Väisänen, whose guidance has been extremely helpful in shaping my academic career. You have passed on so many invaluable skills that I will surely always need. Without your enthusiasm, patience, encouragement, but most especially your kindness, I would have easily given up when things became tough. I am also grateful to Dr Kurt van der Heyden, my co-supervisor. I hope that our collaboration has just started! My thanks also go to the examiners who provided very useful comments to improve the quality of this work. I take this opportunity to acknowledge Dr Angela Adamo who helped me a lot in writing my cluster age modelling code. Fellow students and the faculty members during the 13^{th} Vatican Observatory Summer School are also greatly appreciated. A special thanks goes to the SUNBIRD survey team especially Rajin Ramphul and Dr Abiy Tekola.

I would like to extend my gratitude to the Malagasy community in Cape Town (South Africa), Voary Ramanandraitsiory, Erica Le Roux, Doreen Agaba, the Väisänen family, the SAAO staff, in particular Jacky and Ellen, and most especially the students and young adults fellowships at Mowbray Baptist Church. You have been there when work was too much and I needed some break away from it. Your friendship is always appreciated.

A special thanks also goes to my caring family. Those two months before submission have been so intense and stressful but your love and encouragement were more than enough for me to carry on. I would like to single out my mother whose perseverance has led me to go way beyond my goals. Finally, words are not enough to thank you Dr Bishop Mongwane or Bish Kely (cough). You have helped me so much and gave all the support that I could have ever needed throughout this thesis. I am so blessed to have you in my life and sincerely wish that God will always be the foundation of our relationship.

Finally, I gratefully acknowledge funding from the South African Square Kilometre Array project for supporting my postgraduate studies since 2008.

Misaotra betsaka anareo rehetra tsy misy ankanavaka!

Contents

Chapter 1

Introduction

Overview

This Chapter covers a brief background on galaxy formation and evolution. It then focuses on the properties of the super star clusters hosted by nearby star-forming infrared luminous galaxies. Updates in the field of star cluster research are also outlined.

1.1 General overview

1.1.1 The expanding Universe

In the early 20th century, a pioneering discovery by Hubble (1929) opened a new window into the understanding of the possible origin and the evolution of our Universe. ¨Spiral nebulae˝ were found to move away from one another, with recessional velocities that were directly proportional to their distances from the Milky Way. This striking behavior, referred to as *the Hubble law*, was upheld by subsequent observations of extragalactic sources. Meanwhile, theoretical studies of relativistic cosmology favored the Big Bang Model to explain the beginning and the evolution of the Universe (Lemaître 1931). This well-known cosmological theory suggests that primordial explosion of a hot and dense initial condition occurred approximately 12 to 14 billion years ago, and is the starting-point of the present-day expanding Universe. The discovery of the cosmic microwave background (CMB) radiation which is the residual heat from the initial explosion has provided strong observational evidence of the Big Bang scenario. Based on the same framework, theory suggests that it took almost 500 million years after the Big Bang before the first stars and the very early bright quasars could have emerged through gravitational collapse of neutral hydrogen gas in the Universe (e.g. Barkana & Loeb 2001). Identified with the UKIRT Infrared Deep Sky Survey (UKIDSS) by Mortlock

et al. (2011), the highest-redshift quasar known to date, at $z \sim 7.1$, falls in the tail-end of the cosmic reionization (i.e. $7 \lesssim z \lesssim 12$). This epoch marks the formation of the fundamental seeds to the present-day large-scales structures. *How did the universe structure exactly form?* Doroshkevich et al. (1974) introduced two different scenarios to address the issue: the adiabatic versus the isothermal cosmological models. The former suggests that large-scale structures initially form and later will give rise to the fine-scale structures such as stars and galaxies through the process of fragmentation, assuming that perturbations in the pre-recombination era are adiabatic sound waves. In contrast, the latter considers isothermal perturbations: stars, galaxies and galaxy clusters emerge through hierarchical clustering to form together the components of the large scale structures. Also called top-down and bottom-up scenarios, respectively, they were largely superseded by the cosmological constant Cold Dark Matter (ΛCDM) model by the late 20th century.

Satellites such as the Cosmic Microwave Background Explorer (COBE), the Wilkinson Microwave Anisotropy Probe (WMAP), and Planck space observatory have detected small fluctuations in the temperature of the CMB (Bennett et al. 1996, 2003; Planck Collaboration 2014a). Such observations provided clues on how matter was formed and distributed during the epoch of reionization. Furthermore, the fluctuations in all directions put constraints on the CMB anisotropies and thus favored a spatially flat Universe with an accelerated expansion. Most commonly adopted to explain the growth of structure nowadays, the standard ΛCDM or concordance model has many similarities with the isothermal perturbation scenario, except that non-baryonic matter known as dark energy (represented by the cosmological constant Λ) together with non-relativistic cold dark matter should be the main components of the structure formation. Based on recent measurements from Planck observations, baryonic matter (e.g. protons, neutrons, and electrons) constitutes only $\sim 5\,\%$ of the large-scale structures (Planck Collaboration 2014b). The bright explosions of high-redshift Type Ia supernovae (SNe) have also long been used to demonstrate the accelerating expansion of a ΛCDM universe (Riess et al. 1998; Perlmutter et al. 1999). If there is no dark energy, and hence an non-accelerating Universe, these cosmological standard candles would appear fainter than expected. Despite being the best fit to the Universe to date, ΛCDM model has its own limitations. Predictions based on the model present discrepancies with some observational data such as "the missing satellites problem" in the Local Group, in spite of the recent discovery of more than a dozen dwarf galaxies that nearly doubled the actual observed number of these dark matter dominated galaxies within a decade (e.g. Willman 2010; Karachentsev et al. 2015). This is why powerful and more advanced telescopes such as the Large Synoptic Survey Telescope (LSST), the James Webb Space Telescope (JWST) and the Square Kilometre Array (SKA) are being built to hopefully provide more insight into the puzzling Universe.

1.1.2 The Hubble tuning fork

Observations from the 2 degree-Field Galaxy Redshift Survey (2dFGRS) revealed that there are approximately 250,000 galaxies in an area of about 2,000 square degrees at a median redshift of $z < 0.11$ (Colless et al. 2001). Over hundred billions of galaxies are therefore expected to be present in the visible cosmos. With such a gigantic population, distant galaxies are commonly used as cosmological tools for a deeper exploration of the expanding universe. Galaxies are gravitationally bound systems hosting a large number of stars (around 400 billion in the Milky Way, our own galaxy) mixed together with a large amount of gas and dust clouds. Originally referred to as ˜nebulae˝, these astronomical objects were assumed to reside inside the Milky Way until Hubble (1925a,b) successfully demonstrated using Cepheid variables that they are in fact part of the extragalactic field. By studying the various types of galaxies, Hubble (1926) identified two fundamental groups:

- the early-type galaxies, ellipticals (E); these are featureless massive galaxies with no disk. Sub-groups were created based on varying degrees of eccentricity. Note that elliptical galaxies have exhausted most of their cold gas and dust clouds and therefore, host an older stellar population.

- the late-type galaxies, spirals (S); they have very distinct spiral arms with a galactic bulge component at the center. They are also sub-divided into groups depending on the prominence of the arms and the dominance of the bulge. For these types of galaxies, young stars cohabit with a large amount of gas clouds and dust inside the galaxies.

Any galaxy with an unusual type that did not fit in the above classes was called irregular (Irr). These peculiar galaxies are actively evolving and have not yet become regular or they have undergone some chaotic interaction that may have disturbed their original morphologies. Irregular galaxies are often factories of ongoing star formation (SF) activity and thus potential hosts of very young blue stars.

In order to separate the normal spirals from the barred spirals in his classification scheme, Hubble (1936) established the pitch fork diagram (see Figure 1.1). This *Hubble tuning fork* includes an intermediate type of galaxy to smooth the classification between the ellipticals and the spirals: the so-called lenticular galaxies (S0). They are generally thin disk galaxies with a bulge component.

Besides the morphological classification, there are also other ways to group galaxies. They can be split into different categories depending on their current star formation rates (SFRs), masses, luminosities, nuclear activities, etc. Nevertheless, the simplified but concise Hubble scheme is still extensively in use. Note, however, that *Hubble tuning fork* is not a galaxy evolutionary sequence. Physical properties from one to another

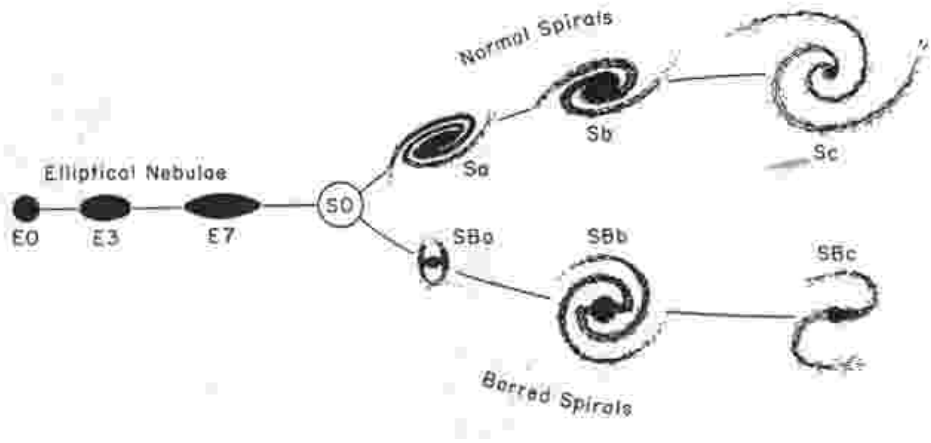

Figure 1.1: An illustration of the *Hubble tuning fork* diagram taken from *The Realm of the Nebulae* (Hubble 1936). The sketch shows a morphological classification of galaxies with various types.

Hubble type do not seem to correlate, though the evolution of late-type spiral galaxies to early-type ellipticals could be possible.

Some features of the galaxies (e.g. spiral arms, bulge, disks) are only visible/prominent within a certain range of frequencies. The same applies to the galaxy contents (e.g. gas, stars, star clusters): young objects with heavy extinction are often hidden by dust clouds in the optical wavelength. However, such limitations may be circumvented with state-of-the-art multi-wavelength observations that combine complementary information gathered throughout the electromagnetic spectrum.

1.1.3 Overview on galaxy formation and evolution

The first CfA Redshift Survey pioneered in mapping the large-scale structure in a slice of the nearby Universe (Huchra et al. 1983). The survey revealed that galaxies form an apparent bubble-like structure with large empty spaces, known as voids, in between. Such distributions conveyed useful information on how structure initially formed. A more complete map from the CfA showed that large-scale structure is organized as a cosmic web which is a vast network of galaxy clusters, galaxy filaments, sheets and voids (de Lapparent et al. 1986). The densest regions of the web, which host rich clusters of galaxies, are linked to one another by the filaments of galaxies. Subsequent large surveys such as the Sloan Digital Sky Survey (SDSS, York et al. 2000) and the 2dFGRS (Colless et al. 2001) have enhanced further understanding of the geometry and dynamics of the universe. Darvish et al. (2014) recently discovered while investigating the Cosmic Evolution Survey (COSMOS) field that star formation process is more ubiquitous in galaxies residing the filaments which is possibly caused by a recurrent gravitational interaction between the galaxies. High-resolution numerical simulations such as the *Millennium Sim-*

ulation (Springel et al. 2005b) and the *Illustris Project* (Vogelsberger et al. 2014; Genel et al. 2014) are also powerful tools to provide theoretical perspectives on galaxy evolution and formation. The former simulation confirmed that protogalaxies had emerged through the gravitational collapse of clumps of cold dark matter and neutral hydrogen gas when the Universe was only 1 Gyr old. With an unprecedented simulation of galaxy formation, *Illustris Project*, predicts, for instance, that the majority of gas resides in the intergalactic medium at $z = 0$, however, this gas contains only one third of the heavy metals being produced so far in the universe.

A color-mass diagram of hundreds of thousands galaxies from the SDSS and 2dFGRS catalogues indicated that galaxies exhibit a bimodal color distribution (e.g. Baldry et al. 2004; Faber et al. 2007). The existence of such distribution is somewhat related to the fact that there are two major types of galaxies, red ellipticals and blue spirals (Hubble 1922). Below is a brief overview of the two distinct groups forming the color-mass diagram in Figure 1.2:

- the "dead" red sequence; these are mainly quiescent E/S0 galaxies with almost no SF activity situated on top of the diagram, they have redder colors due to an overall old stellar population. Most of the gas-poor massive galaxies are believed to converge in this sequence.
- the blue cloud; these are S/Irr galaxies with blue colors hosting younger stellar populations and ongoing SF activity. They reside at the bottom of the diagram and are suggested to migrate toward the red sequence via a transition region due to the quenching of SF, though such evolution is still under debate.

The transition region which separates the two populations is called the green valley (the region in between the solid lines in Figure 1.2). Ultraviolet photometry from GALEX uncovered the existence of such a region for the first time (Martin et al. 2007). Intermediate galaxies, whether spirals or ellipticals, but in between the red and blue colors are suggested to form this sequence. And they are most likely to host active galactic nuclei (AGN) which could be responsible for quenching SF mechanisms in the galaxy nuclear regions when all the cold gas necessary to form stars is heated up by the central super massive black hole (SMBH) within a short timescale. The process is called *AGN feedback*. The quenching of SF is one possible scenario of how a galaxy from the blue cloud could evolve into the red sequence (Salim et al. 2007; Mendez et al. 2011). Note that starbursts also have a potential to stop SF prematurely since such mechanisms rapidly consume the gas reservoir instead of a slow and continuous SF activity (e.g. Springel et al. 2005a).

For a more accurate distribution of the color-mass diagram, observational bias due to dust-attenuation depending on the viewing angle must be corrected. For example, an edge-on blue star-forming galaxy could be classified into the green valley by making it appear redder than it otherwise would be in the diagram (Schiminovich et al. 2007).

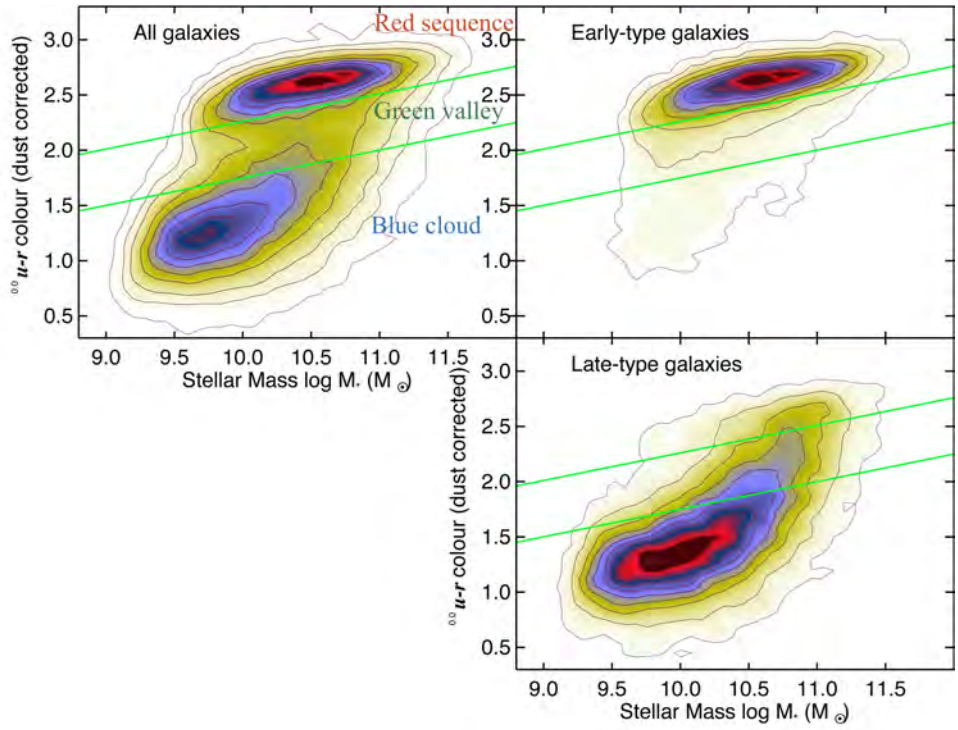

Figure 1.2: A figure taken from Schawinski et al. (2014) shows the bimodal galaxy color-mass distribution of galaxies: the red sequence (upper right panel) and the blue cloud (bottom right panel). The two populations are separated by a transition hetereogeneous class of objects called the green valley (demarcated with the two solid lines). There are a variety of evolutionary tracks a galaxy would follow throughout the diagram.

But in what types of environments do the red sequence and the blue cloud preferentially live? Star formation histories for galaxies with different masses revealed that most of the stars in more massive galaxies have formed earlier within a short timescale than those hosted by less massive galaxies. This is known as *downsizing* of the process of galaxy formation (Cowie et al. 1996; Juneau et al. 2005). The effects of downsizing can be seen, for example, in the distribution of galaxies in the local Universe where passively evolved red sequence galaxies are hosted by dense environments while active star-forming blue cloud galaxies lie within regions with low density. However, observations of this phenomenon in the context of galaxy formation and evolution have been a source of controversy. *Is downsizing an anti-hierarchical evolution or not, i.e. does it conflict with the predictions from the standard ΛCDM model?* Note that in the high-redshift universe, the SFR-density relation is reversed in the sense that the densest regions have the highest SFRs (e.g. Elbaz et al. 2007). The issue is, however, complicated due to observational biases. Nevertheless, to study galaxy evolution over the cosmic history, it is crucial to also understand the star formation processes in detail, to which we now turn.

1.1.4 Star formation in giant molecular clouds

Not all the gas in a galaxy can precipitate star formation; stars are primarily born through the gravitational collapse of overdense regions within a giant molecular cloud (GMC). These stellar nurseries are opaque in the visible light and they form because supersonic turbulence in the diffuse interstellar medium (ISM) pushes the cold gas to concentrate into high-density molecular gas. Such conglomerations in the form of clumps and filaments are also known as dark nebulae. With a typical mass of $10^4 M_\odot$, the star-forming clumps become unstable and too heavy to sustain their own gravity: the so-called Jean's mass criterion for a molecular gas to potentially form stars. As a result, the cores of the dense clumps start to collapse and split into smaller fragments of clouds with stellar sizes. These *protostars* will then increase in mass through free-fall accretion of infalling matter that are driven toward the pre-stellar inner cores. Unable to support their own gravity, they will also collapse until the inner cores are hot enough to ignite thermonuclear reactions a few Myr later. The feedback from the nuclear fusion will provide enough pressure to balance with gravity and to stop any further collapse. This is how a (T-Tauri) star is born. And until its fuel is completely used up, the star will keep burning hydrogen into helium (through a proton-proton chain or a CNO-cycle depending on its mass) as it evolves in the main sequence of the HR diagram. Deuterium burning is also a vital nuclear fusion that sustains low-mass objects such as brown dwarfs. These failed stars are massive enough ($\gtrsim 13$ times Jupiter mass) to ignite this thermonuclear fusion but they are not hot enough for hydrogen burning. A newly born star has an initial mass ranging between $0.1 - 150\,M_\odot$ and is still embedded in its dust cocoon while ejecting strong stellar winds that help regulate the star formation efficiency (SFE or ϵ) of the surrounding GMCs. Similar processes apply to the formation of multiple stars and star clusters, except that these ones obey a scaled-up version of the formation of a single star. Refer to McKee & Ostriker (2007) for a recent review on the theory of SF.

The three dominant locations for SF in the local Universe are the spiral arms of late-type galaxies, the nuclear and circumnuclear rings of early-type galaxies, and finally the tidal tails of mergers and interacting systems. Each region has its own level of SFR because of a different density of the gas reservoir. In fact, there is an empirical relation between the SF surface density and the local (atomic + molecular) gas surface density known as the first form of the Kennicutt-Schmidt relations (Schmidt 1959, Kennicutt 1998a). These densities are respectively referred to as $\Sigma_\star$ and Σ_{gas} where:

$$\Sigma_\star \sim \Sigma_{gas}^{\mathrm{N}} \tag{1.1}$$

and $0.9 < \mathrm{N} < 2.4$ with a typical index of 1.4. This empirical relation implies that all galaxies follow the same rule of global SF where those with higher gas densities ($\gtrsim 10 M_\odot\,\mathrm{pc}^{-3}$) are expected to convert most of their gas into stars. To illustrate the Kennicutt-Schmidt law, compare ϵ within a period of 100 Myr in two different types of environments: quiescent vs. disturbed environments. The parameter ϵ is only about 5 % inside spiral disk galaxies because quiescent environments cannot boost the creation of

GMCs. In contrast, ϵ can reach as high as 100 % inside merging and interacting galaxies because the violent dynamical mechanisms (e.g. tidal fields) occuring in these systems enhance the formation of GMCs, denser gas reservoirs will then be available to form more coeval stars that are often associated with newly formed star clusters.

Over the past decade, spatially-resolved surveys such as Spitzer Infrared Nearby Galaxies Survey (SINGs) have shown that a power-law relationship between $\Sigma_\star$ and Σ_{gas} is not compatible with a turnover seen at low surface gas densities $\Sigma \approx 10\,M_\odot\,\mathrm{pc}^{-2}$. This implies that not all the galaxies follow the global star formation Kennicutt-Schmidt law and that the SFR on galactic scales rather depends on the molecular surface density alone than the total (atomic + molecular) surface density. Refer to Krumholz (2014) for a recent review.

1.1.5 Stars in clusters

A dense aggregation of tens to several millions of stars with individual masses greater than $0.5\,M_\odot$ and that formed at the same time in an equilibrium state is a simplified definition of a star cluster (SC). Extensive studies over the past decades actually suggest that stars are preferentially born in clusters but they could escape easily the systems because of a violent early disruption. In particular, Lada & Lada (2003) claim that cluster formation efficiency (CFE or Γ, the fraction of SF in a bound stellar cluster) may range between $50-100\,\%$ in the Milky Way. They appended the following criteria to identify a cluster: the SC *evaporation time*[a] has to be higher than 100 Myr for a better chance of survival against the various disruption effects; if the timescale is below this threshold, then we are simply looking at a loose group of field stars that will soon disperse. In addition, a dynamical definition by Gieles & Portegies Zwart (2011) introduced the parameter Π to separate a SC from a stellar association:

$$\Pi = \frac{\tau}{t_{cross}} \quad \begin{cases} > 1 \text{ for a self} - \text{gravitated bound cluster} \\ \\ < 1 \text{ for an unbound association} \end{cases} \tag{1.2}$$

where τ is the cluster age and t_{cross} the *crossing time*[b].

- **OB associations:** Making use of the dynamical age Π is very practical; one could easily confuse (open) SCs with stellar OB associations (especially at younger ages) as both classes are made up of loose stellar agglomerates. Despite the fact that OB unbound associations are short-lived, they are among the best test beds of SF mechanisms and early-type stellar evolution (e.g. Blaauw 1964). Premature destruction of the association arises because they are extended moving groups of 10 to hundreds O- and/or B-type stars, and with a low stellar mass density, $\lesssim 0.1\,M_\odot\,\mathrm{pc}^{-3}$,

[a] Evaporation time is the timescale required for the complete dissolution of SC.
[b] Crossing time is the dynamical timescale necessary for a star member to cross the cluster.

they are vulnerable to Galactic tidal forces (de Zeeuw et al. 1997, and references therein). Numerical simulations of the collapse of GMCs by Weidner et al. (2010) reported that the presence of a shear in Milky Way-like galaxies favors their formation. There are quite a lot of OB associations in the solar neighborhood as recorded in the Hipparcos catalogue (with Scorpius Centauri the nearest candidate containing at least ~ 150 B stars). They are believed to play a major role in the total Galactic SF process (de Zeeuw et al. 1999). Note that a "T association" has almost the same characteristics as an OB association, except that low-mass T-Tauri stars dominate the stellar population.

- **Open versus globular clusters:** Figure 1.3 shows HST images of two distinct SCs: the loosely bound M45 well-known as the Pleiades (*left*) and the tightly-bound M80 or NGC 6093 (*right*). They are classified as open (galactic) clusters and globular clusters, respectively. A classical open cluster (OC) has a typical age less than 1 Gyr and a mass range of $10^2 M_\odot$ to $10^4 M_\odot$. On the other hand, the more massive $10^4 - 10^6 M_\odot$ globular clusters (GCs) with a spherical shape are believed to be $12-13$ Gyr old, an age range comparable to the ages of their host galaxies or even older, making them often the oldest parts of galaxies. In the case of M45 and M80, the former SC is less condensed and mostly composed of a few tens to thousands young blue stars, whereas $10^4 - 10^6$ populous old stars are all held together by their mutual gravitational force in a densely packed system to form the latter SC. In our own Galaxy, the two types of clusters are very prominent and they are distributed in a way that the GCs occupy the bulge (if they are metal-rich, [Fe/H] ≈ -0.5) and the halo (if they are metal-poor, [Fe/H] ≈ -1.5) of the Galaxy, whereas the

Figure 1.3: Two well-known star clusters in the Milky Way. *Left:* A classical open cluster with very young stars known as M45 or The Pleiades (Image credit: NASA, ESA, F. R. Ferraro, M. Shara, and the Hubble Heritage Team). *Right:* M80 or NGC 6093 is a tightly bound system of old stars with a spherical shape; it is one of the ~ 150 globular clusters orbiting either the bulge or the halo of the Galaxy (Image credit: NASA, ESA, and AURA).

young OCs are scattered all over the Galactic disk/plane. Such spatial distribution can be used as indicative of the star formation history (SFH) that had taken place in the Milky Way since its formation. Refer to e.g. Battinelli & Capuzzo-Dolcetta (1991), Ashman & Zepf (1998), Portegies Zwart et al. (2010) for a review on OCs and GCs.

- **Embedded clusters:** Embedded clusters are heavily obscured young protoclusters with a typical age not exceeding 5 Myr and because of the high extinction they are ideally detected in mid-infrared to sub-mm wavelengths. As time goes by, they may become (partially) unbound or tightly bound exposed clusters depending on the effects of gas removal surrounding the systems (Lada et al. 2010). The majority of coeval stars in the nearby universe are suggested to form within embedded clusters but due to the ongoing expulsion of gas and dust, 70 to 90 % of the vulnerable SCs get destroyed in less than 10 Myr. Embedded clusters with a large number of O-type stars are the ones to likely undergo such catastrophic evolutionary stages (Lada & Lada 2003). On the other hand, provided that they are not susceptible to external disruption effects, the few survivors may evolve to become super star clusters which are the most massive gravitationally bound systems with very compact stellar densities (e.g. Kruijssen et al. 2012). Refer to Section 1.2 for more details on super star clusters and their link with embedded clusters. First discovered by Trumpler (1931), The Trapezium is a well-studied embedded cluster in the Orion Nebula with an age less than 1 Myr old and a total number of approximately 700 stars (Muench et al. 2002). Like any other young galactic OC, embedded clusters are also good laboratories to probe early stellar evolution and ongoing SF activity.

- **Nuclear star clusters:** Another type of bound stellar clusters called compact stellar nuclei or nuclear star clusters (NSCs) were reported by Binggeli et al. (1987). With masses ranging between $10^5 - 10^7\,M_\odot$, star members of the NSCs are densely packed within a typical size of only a few parsec to a few tens of parsec (e.g. Walcher et al. 2005; Côté et al. 2006). By the late 20th century, high spatial resolution photometric images from modern telescopes revealed that most galaxies, regardless of their Hubble types, harbor these compact SCs: almost 80 % of early-type galaxies contain NSCs in their photometric centers and a slightly lower fraction, i.e. 50 - 70 %, for the late-type galaxies (e.g. Phillips et al. 1996; Carollo et al. 1998; Böker et al. 2002; Côté et al. 2006). In addition, it has been observed that a NSC often coexists with a SMBH inside the galaxy nucleus (e.g. Seth et al. 2008; Graham & Spitler 2009) which could indicate a mutual correlation in the formation and evolution of these two central massive objects (Neumayer & Walcher 2012), though this still remains an open question.

From their NSC census in late-spiral galaxies, Böker et al. (2002) have found that the compact stellar nuclei typical sizes and luminosities fall within the range of a super star cluster (SSC) size and brightness. This would mean that a NSC is simply one of the population of SSCs that happened to reside in the galaxy nuclear regions. Note, however,

that unlike the SSCs, NSCs have extended star formation histories at least in spiral galaxies. Because of the episodic gas accretion occuring onto the NSC, intermediate-age stars ($\sim 50-100$ Myr) coexist with an old ($\gtrsim 1$ Gyr) metal-poor star population (e.g. Seth et al. 2008). SSCs with their own peculiar characteristics have been used as fundamental tools to trace SFH of the host galaxy as well as to study the effects of various disruption mechanisms in the evolution of SCs. The present thesis focuses on the understanding of the initial mass function (IMF) of such extremely luminous and compact SSCs.

1.2 Super star clusters

Although previous generations of ground-based telescopes delivered poor resolution images, pioneers such as van den Bergh (1971), Arp & Sandage (1985) and Melnick et al. (1985) discovered SCs more luminous than seen before, widely known as super star clusters. Other terms were also adopted to define the new type of clusters: e.g. "young massive star clusters (YMCs)", "super-association", "blue-globular clusters", or "blue populous clusters" (Melnick et al. 1985, and references therein). However, information regarding the properties of the newly found objects were limited before HST became operational. Thanks to the high spatial resolution capabilities of the HST/WFPC2, the individual sizes of these exotic SCs while imaging NGC 1275 could be resolved for the first time (Holtzman et al. 1992). Such results subsequently affected our general knowledge of stellar cluster systems, e.g. by opening new perspectives in the formation and evolution of GCs; these old SCs were thought to only form in the early Universe but ever since the SSC discoveries an alternative scenario has emerged suggesting that GCs are still forming in the present day through secular evolution of their SSC progenitors (e.g. Ashman & Zepf 1992; Portegies Zwart et al. 2010; Longmore et al. 2014). Westerlund I (Clark et al. 2005) and R136 within 30 Doradus (e.g. Crowther et al. 2010) are among the closest and best-studied "blue-globular clusters" with resolved stellar populations of hundreds of massive stars (see Figure 1.4). They are hosted by the Milky Way and the LMC, respectively. A wide variety of extragalactic SSC hosts are highlighted in Section 1.2.5.

1.2.1 General properties

The "super" star cluster terminology was adopted because of the outstanding characteristics that the new class of young SC features right from its birth. While the age of an SSC coincides with the ages of the young OCs, its mass and size are, however, surprisingly similar to those of the old GCs (e.g. Whitmore 2003; Portegies Zwart et al. 2010). In fact, SSC have masses of $\sim 10^4$ - 10^8 $M_\odot$ and are gravitationally bound within an effective radius of $\sim 3-5$ pc (Portegies Zwart et al. 2010 and references therein). They are not only compact objects, they also have very young ages of $10-100$ Myr in general. Moreover, SSC optical luminosities can be as bright as $M_V = -14$ at ages of ~ 10 Myr,

Figure 1.4: Two prototypical resolved SSCs that are observed in the Local Group. The stellar populations of the clusters are mainly composed of hundreds massive and young blue stars. *Left:* Westerlund I is our nearest SSC located 16,000 light-years away from the Earth. It has a mass of $\sim 6 \times 10^4\, M_\odot$ (Image credit: 2MASS/UMass/IPAC-Caltech/NASA/NSF). *Right:* With a mass estimate of $4.5 \times 10^5\, M_\odot$, R136 in the center of 30 Doradus nebula is a well-studied case hosted by the LMC at a distance of 170,000 light-years away. The snapshot from HST/WFC3 has captured the effects of strong stellar winds and bright ultraviolet (UV) emission from the hot stars on the surrounding gas and dust clouds (Image credit: NASA, ESA, F. Paresce, R. O'Connell, and the HST WFC3 Science Oversight Committee).

depending on their masses. It is essential for the young massive SSCs to have high densities; such criteria will help them remain "bound systems" at least up to 1 Gyr of age after surviving the severe *infant mortality* and other external disruption effects occurring throughout the early stages of cluster evolution (see Section 1.2.2 & Section 1.2.4).

In spite of the use of high resolution instruments, distant extragalactic SSCs at $D_L \gtrsim 10$ Mpc can only be imaged as massive knots of unresolved "coeval" stars. Therefore, one should refer to the observations carried out in the Local Group and the very nearby galaxies to evaluate their stellar contents. Results from extensive studies have reported that SSCs are composed of a few hundred to about 10^5 young stars; many of which are highly massive O- and B-type stars as well as a substantial number of low-mass stars. The proportion between these two populations of stars plays an important role in determining the cluster IMF shape (see Section 1.4.3 for a broader discussion) which is crucial as it provides some clues on the ultimate fate of the SSC (e.g. McCrady & Graham 2007). Apart from highly-massive stars and low-mass stars, dozens of Wolf-Rayet stars and tens to hundreds of red supergiant giants (RSGs) may also inhabit the SSC stellar populations (e.g. Clark et al. 2005; Andersen et al. 2009).

Massive UV-photon emitters, O- and B-type stars, are the major source of ionization processes necessary to produce HII regions; these glowing gas clouds are only prominent in their first few Myr of age (i.e. $\lesssim 5$ Myr old), spreading all around the newly born

embedded SCs (e.g. Johnson 2004; Schombert et al. 2013). However, the peak emission of such a young HII region is unlikely to coincide with any spatial location of the "deeply" embedded SSC. On the other hand, an intermediate HII region with a dissipating gas, i.e. between $\sim 5-7$ Myr, may overlap with a more or less visible "emerging" SSC counterpart. But again, no coincidence is expected beyond 7 Myr as the gas covering the "exposed" cluster is no longer dense enough. Alonso-Herrero et al. (2002) and references therein suggested to first order that the lack/existence of coincidence is a simple reflection of an ongoing evolutionary sequence and therefore gives very crude estimates of the HII region and SSC ages. In addition, they found that HII regions associated with SSCs have Hα luminosities as high as the prototypical giant 30 Doradus (log$\mathrm{H}\alpha \sim 39.70\,\mathrm{erg\,s^{-1}}$) due to a high SFR of their host galaxies (more ionizing massive stars are expected to form in such conditions). Because young SSCs are also exceptionally bright objects in extragalactic broad band observations, it is not trivial to differentiate them from the giant HII regions. Nevertheless, the presence of both SSCs and HII regions indicate that the host galaxy has active star-forming regions, though each object represents an exclusive episode of the galaxy SFHs: short-lived HII regions ($\lesssim 10$ Myr) reflect the *current* still ongoing local SF activity whereas, exposed SSCs are relevant tools in tracing the *recent* SF activity, i.e. between a few Myr up to ~ 1 Gyr.

1.2.2 Formation and evolution

SSC birth, evolution and disruption mechanisms are not well understood despite their relevance in the context of clustered SF in general (e.g. Lada & Lada 2003) and in particular the possibility that they might be young proto-globular clusters (e.g. Ashman & Zepf 1992; Portegies Zwart et al. 2010; Longmore et al. 2014). Nevertheless, a compilation of extensive studies over the past decades shows that significant progress has been made; a detailed framework for the theory of SC evolution, excluding the obscured phase between the cluster formation and its early stages of evolution, were being proposed to provide further explanations of the overall matter. Because of the diverging opinions concerning the role of external disruption mechanisms throughout the SC evolution, the predicted scenarios were recently a subject of intense debate (see the Baltimore vs. Utrecht groups in Section 1.2.4).

SSC early stages of evolution remain the most puzzling phase in the cluster lifetime. This is not surprising since global SF itself has not yet been fully understood either. Nevertheless, both numerical and observational results agree that the following criteria have to be met before a GMC could potentially harbor massive clumps of proto-clusters within their ultra-dense regions:

- For a more frequent assembly and condensation of the parent GMC, violent and extreme episodes of SF are required to feed in gas accretion in their central regions through, for example, particle collisions, close encounters and especially momentum

from SNe and stellar winds. Such events are usually abundant in starburst galaxies and interacting systems (Bekki & Couch 2001).

- Ultra-dense and highly pressurized environments are also vital to allow a massive growth of the clumpy and compact proto-clusters emerging from the condensed GMC (Elmegreen 2002). Therefore, higher rates of SFE are expected from the ongoing SF mechanism instead of only 10 - 30 % of the molecular gas to turn into star members of the stellar cluster system (Lada & Lada 2003). Again, any active star-forming regions are potential SSC birthplaces because of the presence of compressive tidal shocks.

Under these extreme conditions, peculiar proto-clusters are now cradles of future massive and dense "super star clusters".

As already discussed in Section 1.1.5, massive proto-clusters are embedded SCs with a gravitationally bound equilibrium state at birth. They are heavily enshrouded in their natal gas while surrounded by ionized giant HII regions. It roughly takes $2-5$ Myr for the newly born SCs to emerge from their dusty birth cocoons with the help from strong SN explosions that had finally expelled any left over ionized gas away from these infant star clusters (Longmore et al. 2014). As they are seeking for a new potential well, the emerging stellar cluster systems gradually become optically visible. Any re-virialized SC that remained gravitationally bound at the end of this initial dynamical evolution has become a fully-emerged dense and massive SSC. "*Infant mortality*" refers to the destruction of embedded star clusters on a short timescale due to the removal of natal gas (Lada & Lada 2003). The fate of a loose aggregation of stars is therefore not certain as it strongly depends on the strength of this internal process (e.g. Whitmore et al. 1999). If the impact from such a phenomenon is too intense, the aggregate of stars will rapidly expand and will be left severely out of virial equilibrium. The cluster will be destroyed by losing most of its mass through the escape of star members with high velocity dispersion to become field stars. Numerical simulations by Goodwin & Bastian (2006) have shown that embedded clusters with a SFE below $\sim 30\%$ are at high risk of dissolving during infant mortality. In contrast, SCs with an initial number of $\sim 10^5$ stars will most likely survive this gas expulsion phase and possibly evolve as young proto-GCs. Whitmore et al. (1999) have claimed that infant mortality is responsible for the low survival rate of SSC candidates in the well-known NGC 4038/NGC 4039 Antennae systems.

All SSC survivors from the initial mass-independent disruption mechanism are certainly expected to have lost some of their mass during the early stages of evolution. They now enter a slow and steady process in which they will gradually evaporate. The timescale of such secular evolution (from hundreds of Myr to a dozen Gyr) is partially governed by the number of remaining low-mass star members within the re-virialized SCs. Longer disruption times are expected for the ones with a substantial amount of low-mass

stars assuming there is no *mass-segregation*[c]. The disruption mechanisms at play during this stellar mass-loss evaporation are the subject of a lively debate (see e.g. Lamers 2009). *Are internal processes such as stellar evolution and two-body relaxation strong enough to completely dissolve very massive and dense SSCs? Or do they need help from mass- or/and environment-dependent external effects (e.g. strong tidal fields, higher GMC densities) at some stage?* These will be discussed further in Section 1.2.4. Nevertheless, only the most massive SSCs at birth that managed to re-virialize at the age of $\sim 40 - 50$ Myr (Bastian & Goodwin 2006) are believed to have a long-term survival chance and subsequently become potential progenitors of the present day GCs (e.g. Ho & Filippenko 1996).

1.2.3 Globular clusters: possible end products of YMCs

Apart from the striking similarities between the SSC and GC masses and sizes, many studies have indeed argued that the mass functions (MFs) of young SSCs could have dynamically evolved over time to give the present-day MF of GCs (e.g. Larsen 2008). However, the proposed SSC end products are yet another hot topic that has sparked much discussion. This is because young GCs were thought to be ubiquitous only in the early universe until the pioneering HST discovery of SSCs which opened up another perspective into the formation and evolution of the present-day GCs. In fact, Kruijssen (2014) and references therein explored a totally different approach to address the possible links between GCs and YMCs. The reasoning is mainly based on the physical environments required for globular cluster formation: highly-pressurized environments with high-gas densities ($P/k \sim 10^7\,\mathrm{K\,cm^{-3}}$ and $\Sigma \sim 10^2 - 10^{3.5}\,M_\odot\,\mathrm{pc^{-2}}$). No wonder why GCs formed abundantly during the peak of the cosmic star formation rate around $z \sim 2$ (e.g. Hopkins & Beacom 2006) and could survive over a Hubble time. The prominence of galaxy mergers at high-redshift significantly reduced the cluster disruption rate through recurrent migration of the massive star clusters away from their violent birth sites.

Similar environmental conditions are also required for the formation of YMCs in $z > 2$ galaxies. High-pressure environments are ubiquitous beyond that epoch and hence favor the formation of compact star clusters with an initial mass $M_{cl} > 10^5\,M_\odot$ that are likely to survive the gas expulsion phase. Furthermore, GMCs easily form in such extreme environments, resulting in a higher rate of the star formation efficiency (e.g. Elmegreen & Efremov 1997; Wright et al. 2014). It is suggested that higher SFEs increase the chances for the star clusters to remain bound in a high-gas density setting (e.g. Boily & Kroupa 2003; Kruijssen et al. 2012a). Therefore, YMCs in $z > 2$ galaxies could be the progenitors of the present-day GCs if at least they meet the following criteria: *i)* their birth sites undergo recurrent merging processes that boost the SFE; *ii)* they have a minimum initial mass of $M_{cl} = 10^5\,M_\odot$ to help them survive from infant mortality;

[c] Mass-segregation occurs when low-mass stars scatter all over the cluster outer radius while the massive ones sink into the cluster core as they lose their kinetic energies, see Binney & Tremaine 1987.

iii) they get displaced toward the galactic haloes to escape the highly-disturbed regions of the parent galaxy, *iv)* and the migration happens within a very short timescale to avoid "impulsive tidal shocks" from high-gas densities. More details on the star cluster migration process are highlighted in Section 1.4.5. Unfortunately, our limited knowledge of SSC formation and evolution, especially in high-redshift galaxies, is one of the obstacles to confirm whether there is really a tight connection between the SSCs and the GCs still forming today.

1.2.4 More on disruption mechanisms

It is of great importance to understand the controversies surrounding the SC disruption mechanisms at work after the gas removal process. The disagreement focuses on the universality of the cluster initial mass function (CIMF). Two research groups were well-known in proposing their respective scenarios regarding the matter (the "Baltimore" vs. "Utrecht" group):

- The "Baltimore"group has argued that *only* a constant mass-independent disruption mode occurs up to an age of 1 Gyr. This happens via successive internal mechanisms such as stellar evolution followed by a standard two-body relaxation to trigger the star cluster evaporation. These are natural processes that do not depend on the cluster mass or the environmental properties of the host galaxy. In this scenario, any turnover in the cluster mass-function[d] (CMF) results from a constant disruption triggered by internal mechanisms. Refer to e.g. Fall et al. (2009); Whitmore et al. (2007, 2010); Chandar et al. (2010, 2011).

- In contrast, the "Utrecht" group has proposed that the mass of the cluster and/or the environment of its host galaxy play(s) an important role in defining the disruption time (e.g. cluster evaporation may take more than 1 Gyr for more massive clusters) as well as the CMF shape (a truncated Schecther MF instead of a power-law distribution for a population of SSCs residing in extreme environments). This means that external disruption mechanisms due to strong tidal fields and higher GMC densities, for example, are also involved during a particular phase of the secular evolution. In fact, a *combination* of both internal and external effects are suggested to take over the constant disruption mode after $10 - 100$ Myr of steady internal dynamical evolution. Disturbed environments are likely to induce a more violent relaxation resulting in a higher degree of *mass-segregation*. SSCs with a large fraction of low-mass stars are consequently more vulnerable to the disruption effects because of early *selective destruction*. On the other hand, environments with low GMC densities would endure less disruption and their newly born SSCs will consequently stand a chance of a long term-survival. Refer to e.g. Lamers et

[d] The cluster mass function represents the number of clusters per mass interval.

al. (2005); Gieles et al. (2006c); Larsen (2008); Bastian et al. (2011); Kruijssen et al. (2012).

Because of these disagreements on the universality of CMFs and cluster disruption mechanisms, it is extremely important to study SSC characteristics over a wide range of galaxy properties and SF environments. The next section is a compilation of host galaxies from various studies over the past few decades.

1.2.5 Host galaxies: from quiescent to active merging systems

Young massive SCs are related to triggers of SF in galaxies and contain clues to the physical conditions under which extremely strong SF happens. Although they are often confined to starburst galaxies (e.g. M82 and M83; recently studied by Westmoquette et al. 2014 and Silva-Villa et al. 2014, respectively), ongoing mergers (e.g. NGC 1275, the Antennae and the Bird; Holtzman et al. 1992, Whitmore et al. 1999, Väisänen et al. 2008) and merger remnants (e.g. NGC 7252 and NGC 3256; Whitmore et al. 1993, Zepf et al. 1999), SSCs can also form in more quiescent environments such as in the circumnuclear star-forming rings (e.g. the sample in Maoz et al. 1996), in nearby dwarf galaxies (e.g. ESO 338-IG04; Östlin et al. 1998) and even in normal spiral galaxies (e.g. the sample in Larsen 2002). In a handful of cases, there are claims that some starburst dwarf galaxies seem to be "in isolation", i.e. they do not exhibit signs of merging or tidal interaction in their past SF activities (e.g. NGC 1569 by Anders et al. 2004 or NGC 5253 by Harris et al. 2004). Anders et al. (2004), Verbeke et al. (2014) and references therein attributed infalling of external HI clouds with masses $\sim 10^7\,M_\odot$ into the "isolated" systems to be one of the possible mechanisms to fuel their starburst events. The populations of SSCs are much larger in host galaxies exhibiting extreme starburst environments with a violent SF activity. More details on the variation of the star cluster efficiency Γ as a function of the galactic environment are presented in Section 1.4.4. Finally, it has also been observed that active star-forming galaxies with ultra-dense GMCs favor the formation of the most massive SSCs ($\gtrsim 10^5\,M_\odot$) unlike the quiescent galaxies where the cluster masses average around $\sim 10^4\,M_\odot$. Refer to Figure 1.5 for an HST three-color image of the barred spiral M83 (*left*) and the Antennae galaxies (*right*).

Distance-wise, the census begins within the normal spiral Milky Way galaxy, though it was originally believed that only extragalactic systems could host these young massive SCs. In spite of the Galaxy's modest star formation rate, Clark et al. (2005) have confirmed that a $\sim 10^5 M_\odot$ newly born SSC, known as Westerlund I, resides approximately $3-5$ kpc away from the Galactic Center. The Arches and Quintuplet clusters, however, are hosted in the GC itself (these are most local analogs with SSCs of cluster mass $\sim 10^4 M_\odot$, see Figer 2004). The presence of these Galactic Clusters once again supports the idea that GCs are still being formed in the local universe. Other members of the Local Group such as the Magellanic Clouds (e.g. Baumgardt et al. 2013) and the spiral

Figure 1.5: Hundreds of young SSCs are captured in the pictures of two well-known SSC host galaxies imaged with the HST ACS and WFC3 instruments. *Left:* The curving arms of the nearby barred spiral galaxy M83 (Image credit: NASA, ESA, R. O'Connell, and the Hubble Heritage Team.) *Right:* The central regions of the Antennae systems where the nucleus of NGC 4038 collides with that of NGC 4039 (Image credit: NASA, ESA, B. Whitmore and the Hubble Legacy Archive). SSCs are seen as bright and compact regions of star birth that are distributed along the high-gas density environments of the galaxies.

Andromeda/M31 galaxy (e.g. Fouesneau et al. 2014) also host a reasonable number of populations of young massive SCs, with R136/30 Doradus cluster in the LMC one of the most studied cases (e.g. Crowther et al. 2010). Note, however, that significant obscuration from the interstellar clouds of gas and dust could affect the completeness of SC detection; the observations become difficult, if not impossible, for the highly extinguished SSC candidates.

Beyond the Local Group, nearby galaxies such as M51 (e.g. Bik et al. 2003), and the nuclear starbursts M82 (e.g. Westmoquette et al. 2014; Li et al. 2015) and M83 (e.g. Silva-Villa et al. 2014) are home to hundreds of exotic SSCs. A follow-up study by Whitmore et al. (2014) is one of the most recent published work on SSCs in a sample of nearby star-forming galaxies with $D_L \lesssim 30$ Mpc. The census does not end there; Holtzman et al. (1992) pioneered the first SSC discoveries with HST/WFPC2 while observing the recent merger NGC 1275 at a luminosity distance of ~ 71 Mpc. Massive star clusters in a sample of luminous blue compact galaxies (BCGs) with distances $37\,\mathrm{Mpc} < D_L < 82\,\mathrm{Mpc}$ were also studied by Adamo et al. (2011) and references therein. Furthermore, de Grijs et al. (2003c) investigated the star cluster formation histories of the Mice ($D_L \sim 96$ Mpc) and the Tadpole ($D_L \sim 132$ Mpc) interacting galaxies. Vavilkin (2011), on the other hand, investigated the nature of optically-selected SSCs in a large sample of luminous infrared galaxies (LIRGs) as part of the Great Observatories All-sky LIRG Survey (GOALS).

Cluster-rich host galaxies of the sample have distances in between 50 and 160 Mpc. To push the limit, some host galaxies like the Bird triple-merger galaxies (Väisänen et al. 2008) are located as far as $D_L \sim 200$ Mpc away, though we may start to record knots of unresolved clusters instead of individual cases (Miralles-Caballero et al. 2011). The thesis itself will probe SSCs hosted by strongly star-forming galaxies within the distance range of $\sim 25 - 200$ Mpc (refer to Chapter 2).

As we wrap up the demographics of SSCs, one might conclude that any type of galactic environment can harbor young massive clusters as long as the host galaxy is able to offer a high enough SF level required to trigger SSC formation. Since extragalactic starbursts and interacting galaxies produce more SSCs than normal spiral galaxies, we will narrow down our interest to these systems.

1.3 Infrared luminous galaxies

Infrared (IR) luminous galaxies are extragalactic sources that emit most of their light in the IR regime ($\sim$8-1000 μm) via dust thermal re-radiation. Soifer et al. (1987) and Sanders & Mirabel (1996) reported thousands of such galaxies for the first time detected in the Infrared Astronomical Satellite (IRAS) all-sky survey. Luminous infrared galaxies (LIRGs, $L_{IR}/L_{\odot} > 11$), ultra-luminous infrared galaxies (ULIRGs, $L_{IR}/L_{\odot} > 12$), and finally hyper-luminous infrared galaxies (HyLIRGS, $L_{IR}/L_{\odot} > 13$) are the three main categories Sanders & Mirabel (1996) adopted to classify the new catalogued galaxies with respect to their far-IR ($8 - 1000\,\mu m$) luminosity emission, referred to as L_{IR}. Out of the 629 galaxies of the IRAS Revised Bright Galaxy Sample, 181 (29 %) and 21 (3 %) targets are classified as LIRGs and ULIRGs, respectively (Sanders et al. 2003). There are no HyLIRGs in the RBGS catalogue, though a handful of these very rare objects have been identified individually from other IRAS catalogues and recent deeper IR space surveys (see e.g. Rowan-Robinson 2000; Ivison et al. 2013). ULIRGs and HyLIRGS are among the most energetic objects in the Universe with luminosities and space densities comparable to those of quasars (Soifer et al. 1986). Using L_{IR} as an indicator of a galaxy's total amount of energy was not a random choice; most of the bolometric luminosity ($\sim$90%) is in fact emitted in the far-IR. *But what exactly powers the strong IR emission?* This has become a vital question that needs to be addressed in order to explain the dynamical evolution of the IR galaxies.

1.3.1 Nature of the IR emission

Sanders et al. (1988), Duc et al. (1997) and Colina et al. (2001) among many others showed that IR galaxies are likely merging or interacting systems. No wonder they emit high IR luminosities; such extreme environments nurture AGN activity or/and recurring

bursts of SF in their nuclear regions. In fact, it is the ongoing dust reprocessing from both phenomena that generate intense IR emission (Sanders & Mirabel 1996). *How do AGN and SF regulate the IR emission?* The possible explanations are as follows:

- **For starburst-dominated galaxies:** Extreme episodes of SF within a short timescale, typically $5 - 10$ Myr in star cluster regions, are believed to be the most dominant source of energy of the co-moving IR luminosity density (e.g. Farrah et al. 2003). Such phenomena also dominate the IR emission in galaxies with low L_{IR} residing in more quiescent environments (Genzel et al. 1998). Also referred to as "starburst", the violent SF activity happens abundantly in mergers and interacting galaxies; these are systems with very dense and massive GMCs. As already discussed in Section 1.1.4, whenever there are clumps of GMCs, there will eventually be ongoing SF activity. The heating up of dust by UV-emission from the newly born massive stars will in turn re-radiate at longer wavelengths to fuel the IR luminous galaxies.

- **For AGN-dominated galaxies:** On the other hand, the energy of the most luminous IR galaxies (e.g. ULIRGs and HyLIRGs) are predominantly powered by AGN that are heavily enshrouded in the core of the galaxies (e.g. Veilleux et al. 1995; Yuan et al. 2010). In these cases, the UV-emission arises when the accretion disk of material surrounding the obscured massive central black hole within the AGN loses its angular momentum as infalling gas to produce the black hole's fuel. Dust will then absorb this loss of energy and will re-radiate it in the IR.

Regarding the AGN vs. starburst contribution, an optical spectroscopic classification of the IR galaxies (see Figure 1.6) was used by Kim, Veilleux & Sanders et al. (1998) to demonstrate that higher IR luminosities are associated with a relatively high AGN activity; however, the same phenomenon is unlikely to dominate over starburst activity in galaxies with lower IR luminosities. Furthermore, Imanishi et al. (2010) and Alonso-Herrero et al. (2012) used the mid-IR spectral data of local (U)LIRGs from AKARI and Spitzer, respectively, to confirm that the bolometric contribution from buried AGN gradually increases with the far-IR luminosity of the galaxies. There is however a challenge in disentangling their "absolute"contribution when both phenomena co-exist in the nuclear regions of a galaxy, which is often the case. Soifer et al. (1987) used the IRAS flux ratio f_{25}/f_{60} to determine whether the IRAS bright IR galaxy is starburst-dominated or AGN-dominated: a cool dust within the galaxy would indicate that AGN is less likely present and therefore a starburst should dominate the galaxy energy. Because we are interested in environments that could offer high SFR, the rest of this literature review will focus on starburst-dominated IR luminous galaxies.

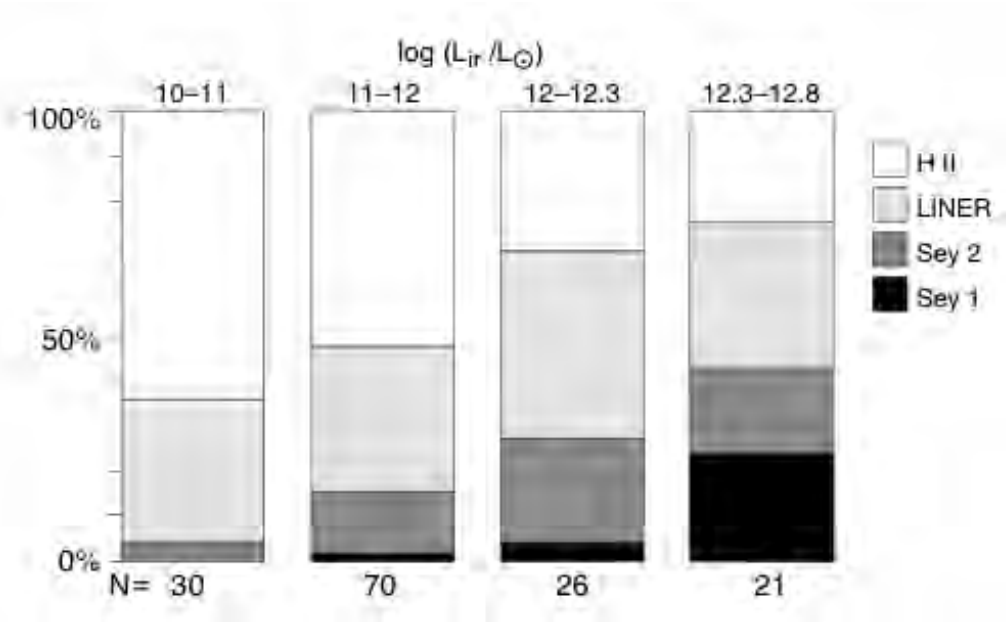

Figure 1.6: A diagram showing the variation of starburst and AGN contribution to the galaxy amount of energy in different bins of IR luminosities. Starburst events dominate the source of energy in low L_{IR} galaxies. They are no longer prominent in galaxies with high L_{IR} in which AGN activity is responsible for most of the IR emission. Kim, Veilleux & Sanders et al. (1998) used an optical spectral classification to draw the diagram.

1.3.2 Starburst galaxies

As already mentioned in Section 1.3.1, starburst events are not continuous processes; they are rather intense SF episodes of instantaneous bursts that dominate the luminosity of a galaxy in the local universe. The depletion of gas will not last longer than $\sim 100\,\mathrm{Myr}$ which is a very short timescale and insignificant compared to the age of the galaxy. Although there is no precise definition of starburst galaxies in the literature, one can easily identify a normal (spiral) galaxy from a starburst one by referring to the range of its SFR (assuming the AGN contribution to the far-IR emission is negligible). A normal spiral galaxy has a continuous SF mode that is usually spread throughout the disk with a relatively low SFR, i.e. less than a few $M_\odot\, yr^{-1}$. The SFR of a starburst galaxy can range between a few $M_\odot\, yr^{-1}$ up to $10^{2-3}\, M_\odot\, yr^{-1}$ in the most extreme cases like the ULIRGs (refer to Kennicutt 1998 for a review). This does not however take into account the size or mass of the galaxy. A dwarf galaxy may still be considered a starburst even if its total SFR is lower than e.g. $1\, M_\odot\, yr^{-1}$. In that case, it would be more appropriate to consider the SFR per mass, or per surface density as a measure. Using the density measure, a starburst can be defined for example by a high SFE (ϵ) as used in the Kennicutt-Schmidt relation discussed in Section 1.1.4.

The following empirical relation is usually adopted to estimate the SFR of the galaxy

knowing the value of its IR luminosity:

$$\frac{\mathrm{SFR}}{M_\odot\,\mathrm{yr}^{-1}} = 1.7 \times 10^{-10} L_{IR}\,[L_\odot]. \tag{1.3}$$

With their high SFRs, it is not surprising that four starburst galaxies alone (M82, NGC 253, M83, NGC 4945) host a quarter of all highly massive stars ($> 8M_\odot$) in the nearby universe, i.e. $D_L < 10$ Mpc (Heckman et al. 1998). Note that the four galaxies are all nuclear starbursts which means that the episodes of burst are only observed in the nuclear regions of the galaxies ($\sim 10^{2-3}$ pc). This is in contrast to a global burst which encompasses the whole galaxy where extensive birth of young SSCs occur everywhere to mark the large-scale events. While nuclear starbursts are often spiral galaxies with a more quiescent environment, the ones hosting a global burst are likely to be mergers and interacting systems with a violent and extreme SF environments, such as starburst-dominated IR galaxies with $L_{IR}/L_\odot > 11.7$ (i.e. LIRGs with high L_{IR} and ULIRGs).

One of the most interesting recent results from galaxy surveys emphasized the importance of starburst activity in the early universe. A tight correlation between the galaxy stellar mass and its SFR were derived at different redshifts from $z = 0$ to the epoch of $z = 7$ (e.g. Brinchmann et al. 2004; Elbaz et al. 2007; Daddi et al. 2007; González et al. 2010). This empirical relation indicates that more massive galaxies have higher SFRs and therefore potentially host a large amount of young stellar populations, the so-called *"main sequence of star-forming galaxies"* as illustrated in the left panel of Figure 1.7. As we look back in time, the normalization of the main sequence (MS) shifts toward higher SFR in the relation which suggests that more stars were being formed by the MS galaxies in the past than the present day (see right panel of Figure 1.7 taken from Whitaker et al. 2012). Quiescent normal star-forming galaxies occupy the MS, whereas off-sequence

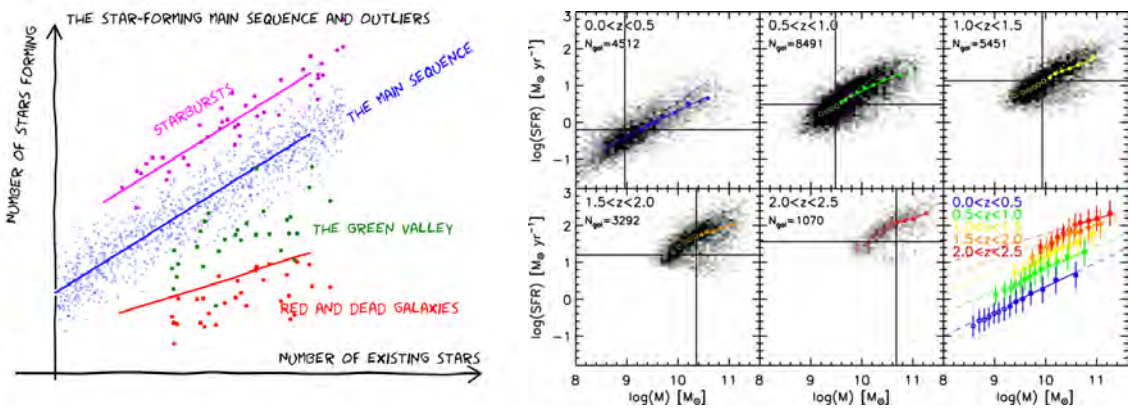

Figure 1.7: *Left:* A sketch by Ferguson (CANDELS team) to illustrate the main sequence of star-forming galaxies: starburst galaxies clearly show SFR excess whereas quiescent star-forming galaxies lie in the MS. Both red sequence and green valley galaxies are below the MS. *Right:* The evolution of the MS between $0.0 < z < 2.5$ taken from Whitaker et al. (2012).

starburst galaxies with a SFR excess populate the MS upper envelope (around the loci 4 to 10 times above the MS for $1.5 < z < 2.5$; Rodighiero et al. 2011). The existence of these two distinct populations supports the theory of a SF bi-modality occurring in the expanding universe, though it is still under debate: a steady SF mechanism versus an episodic strongly-star forming process. While the former dominate the SF at the low redshift universe, the latter is suggested to be responsible for the high cosmic star formation rate (CSFR) in the early universe because of the ubiquity of starburst episodes. Note that red sequence galaxies lie close to the lower limit of the SFR axis in the diagram which is not surprising because of the very scarce SF activity, if not quenched already, in the dead red giant ellipticals. Green valley galaxies are however slightly below the star-forming MS galaxies, i.e. they are still forming stars but at a lower SFR. Negative feedback from AGN activity could be the reason why SF process is slowing down in these galaxies, though this is still under debate.

The level of star formation gradually increases as we move further away to higher redshifts, which can be used to trace the history of bursts of SF in galaxies (e.g Bastian 2008; Escala & Larson 2008; Escala 2011). It is important to study what role do starburst activities exactly play during interaction and merging processes, particularly in the context of low-redshift galaxy formation since such a scenario could be similar to what is happening at $z > 1$.

1.3.3 Interacting galaxies and mergers

Irregular galaxies such as merging and interacting systems were originally referred to as ¨pathological cases˝ because they did not fit into the Hubble pitch fork diagram (see Figure 1.1). However, their unusual dynamical evolution associated with violent and disturbed environments has attracted a lot of interest from both observational and theoretical perspectives. They have been proven to play a fundamental role in the triggering of SF in IR luminous galaxies, the fueling of central SMBH in AGN, and the morphological metamorphosis of Hubble type galaxies.

A pair of colliding gas-rich spiral galaxies are also called prototypical LIRGs because they are believed to transform within a few hundred Myr to a very bright IR merging galaxy as a result of the strong dynamical interactions. The galaxy merger will then continue to evolve until it finally becomes a massive elliptical galaxy. A rough illustration of the evolutionary scenario is presented in Figure 1.8. Pioneering N-body simulations by Toomre & Toomre (1972) established a sequence which predicted the dynamical evolution of two colliding spiral galaxies. Later on, Toomre (1977) illustrated the numerical results by assembling photometric images of nearby galaxies into a sequence of various merging stages; the collection of the sample is widely known as the *¨Toomre sequence˝*. Sanders & Mirabel (1996) explain the evolutionary merger scenario as follows: the pre-merger sequence or the first pericenter passage begins to kick in when strong gravitational forces such as dynamical friction and tidal fields disturb the environments of two neighboring

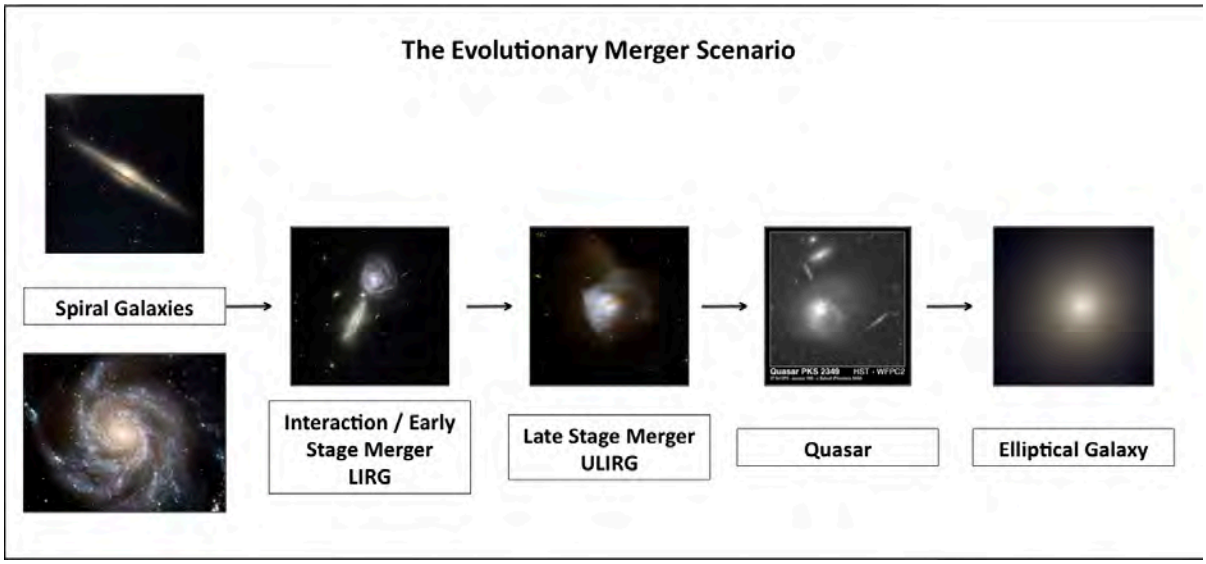

Figure 1.8: An illustration of the evolutionary merger scenario proposed by Sanders & Mirabel (1996). The merging of two spiral galaxies will end into an elliptical galaxy after evolving through the different merging stages in which the gas content gradually decrease with time (Image credit: NASA, ESA, J. Kartaltepe and the Hubble Legacy Archive).

galaxies in the same potential well and pull them to move toward each other to form an interacting system. During the close encounter, a large amount of gas and stars are moved from the outer regions and converge in the galaxy centers, which is often seen as a LIRG, or a starburst, due to increased SF in the centers. Plumes and extended tidal features emerging from the galaxy morphologies reflect this migration of the galactic material. The Antennae and the Mice are good examples of this dynamical stage. After the first pericenter passage, the two galaxies of the interacting system are so close that stronger gravitational torques completely distort the galaxy stellar densities and morphologies. This leads to the formation of a galaxy merger. Since the early-stage merger, the newly formed galaxy has gradually increased its IR luminosity due to the infalling gas in the coalesced nuclei; and by the time the system has regained a new virial equilibrium, the late-stage merger will qualify as a ULIRG. The post-merger phase takes place when the system begins to expel its gas slowly because of the triggering of SF bursts or/and a high demand of the accreting material to fuel the central massive black hole; and the emergence of an AGN after the gas dissipation marks the birth of a quasar. This merger remnant will then finally evolve into a quiescent and gas-free elliptical galaxy as the black hole completely shuts down its activity because of the lack of a powering source. Note, however, that the end product of the evolutionary stage can also be a bulge-dominated spiral galaxy depending on the amount of gas initially present and the intensity of the merging sequence. The collision between two large galaxies that are nearly of equal masses is called a *major merger* (mass ratio of 1:1 - 1:4, Lotz et al. 2011). Such a merger is more intense than a *minor merger* where the masses of the colliding galaxies are disproportionate (mass ratio of 1:4 or smaller), resulting in a weaker merging process

almost similar to galactic cannibalism[e] (Richstone 1976; Ostriker & Hausman 1977). Depending on the gas content initially involved, the timescale of the whole scenario, from the first pericenter passage until the end product, could range between hundreds of Myr to a few Gyr (refer to Bournaud 2011 for a review).

1.3.4 (U)LIRGs in the early universe

Gruppioni et al. (2013) used new data sets from Herschel PEP/HerMES surveys to derive a redshift evolution of the total IR energy density up to $z \sim 4$ (the black filled circles in the left panel of Figure 1.9). The results emphasized that the total CSFR follows a sequencial evolutionary scheme: before $z \sim 3$, the co-moving density steadily increases as large-scale structures start to build up; between $z \sim 3$ and $z \sim 1$, the evolution is almost constant; and at $z \lesssim 1$, the IR energy density falls rapidly. *What is the role of (U)LIRGs in such a picture?* Previous deep extragalactic IR redshift surveys (e.g. from ISO, Spitzer, and Herschel) revealed that (U)LIRGs are rare in the local universe where normal star-forming galaxies tend to make up the co-moving bolometric IR luminosity density. However, they become ubiquitous at higher-redshifts. They are the major contributors of the CSFR from $z \sim 1$ and further beyond (e.g Elbaz et al. 2002; Le Floc'h et al. 2005; Cowie et al. 2004; Caputi et al. 2007). If we break down the total CSFR with respect to the contributions from different IR populations, bolometric luminosities from LIRGs are found to be the most dominant component compared to any other source of IR emitters from $z \sim 1$ up to redshift $z \sim 2$ (right panel of Figure 1.9); and at $z \sim 2$, LIRGs and ULIRGs are suggested to share a similar proportion of global SFR, after which ULIRGs start to dominate. More multi-wavelength deep survey data are required to explore the contribution of (U)LIRGs or clumpy galaxies with similar characteristics toward the CSFR beyond these cosmic times. Note that the presence of peculiar and irregular galaxies such as mergers at low-z are not believed to influence in any way either the global CSFR or the number of the galaxies within that volume density; they only become a major ingredient of the IR energy density after $z \sim 1$ (e.g. Le Fèvre et al. 2000).

Regarding redshifts of $z \lesssim 1$, Sanders & Mirabel (1996) showed that there is a rapid decline in the (U)LIRG number density. This is reflected in the fall of CSFR with a sudden exponential drop by a factor of ~ 10 during that ~ 10 Gyr of age (e.g. Hopkins & Beacom 2006). The quenching of CSFR at $z \sim 0$ could be associated with the SFR-density anti-correlation of star-forming galaxies (see Section 1.1.3): the local universe is populated by blue cloud star-forming galaxies that lie in more quiescent environments. Their global SFR is barely significant in a large scale because of the moderate mode of SF. In contrast, a totally different scenario seems to be happening as we move away from the local universe. At $z \sim 1$, the epoch in which the CSFR seems to have reached

[e] A cannibalism occurs when a massive galaxy swallows its satellite galaxy because of dynamical friction.

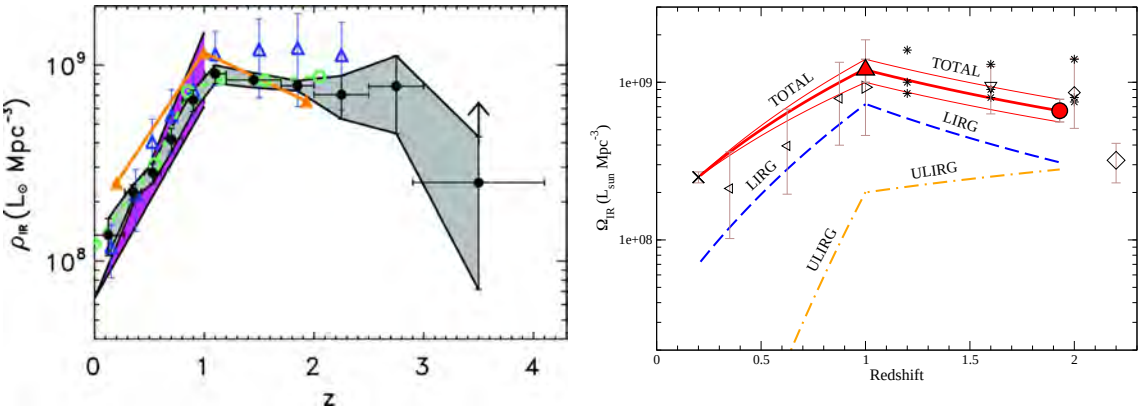

Figure 1.9: *Left:* A figure taken from Gruppioni et al. (2013) illustrates a recent determination of the co-moving IR energy density of the Universe as a function of redshift up to $z \sim 4$. *Right:* A zoomed in version of the evolution between $z \sim 0-2$ is retrieved from Caputi et al. (2007). Contributions from LIRGs and ULIRGs are represented by the blue dashed line and the orange dashed line, respectively.

its highest peak, high SFRs are seen possibly because of the violent SF mode inducing substantial formation of starburst-dominated (U)LIRGs. The existence of these two different SF modes consequently requires a smooth transition from an extreme starburst to a moderate SF activity as we evolve with time. More observations are required in order to provide a more concrete explanation of the role played by mergers. Finally, it is also important to understand the SF mechanisms and the dynamics of the local LIRGs which exhibit extreme SF and large populations of SSCs since they are believed to be good analogs for higher-z star formation in general (Alonso-Herrero et al. 2009; Elbaz et al. 2011; Tekola et al. 2012). Refer to Madau & Dickinson 2014 for a recent review.

1.4 SSCs in starburst-dominated galaxies

The first paragraph in Section 1.3.2 mentioned already that newly born stars clustered into a substantial population of massive SSCs are the signatures of ongoing short-episodes of SF bursts occurring all over the host galaxy. This is the reason why SSCs dominate the global SF activity of local starburst galaxies (e.g. Meurer et al. 1995; Zepf et al. 1999). Studying these extreme forms of SC is therefore necessary for a broader knowledge of SF mechanism and SC evolution in general. Note however, that research has focused more on SSCs within nearby ($D_L \lesssim 25$ Mpc) non-LIRG starburst systems over the past decades, simply because it is much easier (e.g. Whitmore et al. 1993, 1999; Bik et al. 2003; Haas et al. 2008). In particular, the closest major merger system, the Antennae (NGC 4038/4039, $\log L_{IR} = 11.0$), has been amongst the most studied SSC hosts, providing a sample of thousands of these clusters. Nevertheless, there have been some individual cases studied

further away, and at higher SF levels, such as Haro 11 with $\log L_{IR} = 11.22$ at 81.2 Mpc and the Bird galaxy (IRAS 19115-2124) with $\log L_{IR} = 11.87$ at 206 Mpc, by Adamo et al. (2010) and Väisänen et al. (2008), respectively. The only published work thus far characterizing SSCs from a significant sample of starburst galaxies is that of Miralles-Caballero et al. (2011), who analyzed optically-selected star forming knots, SSCs, or complexes of clusters in 32 LIRGs and ULIRGs. Their results indicate for example that SSCs in post-mergers are larger, more luminous and redder, than in less advanced systems. An even larger sample of SSCs in 87 LIRGs has been recently studied by Vavilkin (2011).

The last sections (Section 1.4.1 to Section 1.4.7) of the present literature review will be dedicated to highlight some of the most notable results and tools that have impacted our view on the stellar cluster dynamical evolution and the overall SF mechanisms.

1.4.1 The brightest cluster Vmag - SFR relation

Over the last decade, many studies have shown that there is an empirical relation between the V-band luminosity of the brightest cluster magnitude[f] and the global SFR of the galaxy (e.g. Larsen 2002; Weidner et al. 2004; Bastian 2008). Although various reasons have been suggested to explain the relation shown in Figure 1.10, they all highlight the important role SCs play in understanding their host galaxy properties.

Larsen (2002), Whitmore (2003) and Whitmore et al. (2014) emphasized the importance of the size-of-sample effect in a universal cluster formation, i.e. that large SSC populations preferentially sample the initial LFs to higher values, while Weidner et al. (2004) and Bastian (2008) showed through theoretical simulations that effects from physical processes could also generate the observed correlation. Weidner et al. (2004) derived an expression which directly relates the total SFR of the galaxy with the mass of the brightest star cluster, with the assumption that the most massive cluster is always the brightest. On the other hand, Bastian (2008) argued that the youngest clusters are the brightest implying the tight observed relation is an imprint of the current SFR of the galaxy. Adamo et al. (2011) found that clusters in BCGs preferentially lie above the relation fit to more "normal" galaxies suggesting that the environments of SSCs play a role in determining the relation.

1.4.2 The cluster luminosity function

The luminosity function (LF) of SSCs is a common tool used to help understand their formation and evolution (e.g. Whitmore et al. 1999; Gieles et al. 2006a). It is the number of clusters per luminosity interval. While theoretical and observational studies have

[f] Hereafter, we will refer to the "brightest cluster magnitude"as the "brightest cluster ".

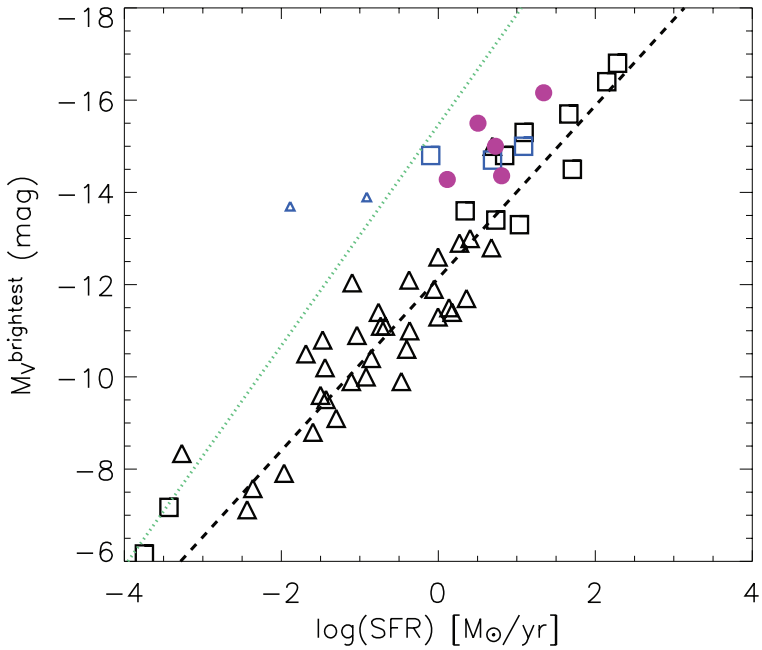

Figure 1.10: The V-band brightest cluster magnitude - SFR relation from Adamo et al. (2011) and references therein. Brightest clusters of BCGs (the purple dots) lie on top of the fit (the black dashed line) from Weidner et al. (2004) because of their high SFRs and extreme environments. The other points (the squares and triangles) are the data used in Bastian (2008). The green dotted line represents where the galaxies should be in the relation if their CMFs follow power-law distribution with index value of ~ 2 (refer to Section 1.4.2 for more details).

agreed that the LF of GCs is well-fitted with a Gaussian function, there are varying results regarding the LF of SSCs. Though power-laws (PLs) are usually found, and expected theoretically, log-normal distributions and bent PLs have also been advocated (e.g. Elmegreen & Efremov 1997, Fritze-v. Alvensleben 1999, Larsen 2002, de Grijs et al. 2003b, Lada & Lada 2003, Gieles et al. 2006a, Anders et al. 2007, Whitmore et al. 2010, Miralles-Caballero et al. 2011). To complicate matters, there are several observational issues to overcome as well to pin down the shapes, relating, for example, to stellar contamination, completeness, and blending (e.g. Robin et al. 2003; Anders et al. 2007; Fall et al. 2009; Adamo et al. 2010). The typical single PL approximation (e.g. Elmegreen & Efremov 1997) takes the form:

$$N(L)dL \sim L^{-\alpha}dL, \tag{1.4}$$

where $\alpha \sim 2$ with scatter in the range 1.5 to 2.5. And it is suggested that the cluster luminosity function (CLF) is a mere reflection of the CMF following the same distribution with the same value of the PL index (i.e. $\alpha \sim \beta$):

$$N(m)dm \sim m^{-\beta}dm \tag{1.5}$$

Gieles et al. (2006b), Bastian (2008), Haas et al. (2008) and Larsen (2009) among others, on the other hand, suggest a double PL or a Schechter function to better fit the CLF due to a turnover located at higher luminosities, which could be a sign of a truncated CMF. The interesting question is whether there are any systematic trends to those LF index values.

Normal spiral galaxies tend to have LFs biased to the steeper range of slopes at $\alpha \sim 2-2.4$ (e.g. Larsen 2002; de Grijs et al. 2003a; Gieles et al. 2006a; Mora et al. 2009). Based on recent SSC studies in 20 nearby star-forming galaxies, Whitmore et al. (2014) also consistently derived an average slope of $\alpha \approx 2.4$ from the I-band single PL CLFs. In addition, they found a weak correlation between the slope and the SFR in their sample: a shallower slope for galaxies with higher SFRs. Finally, they suspected that there might be a correlation between the morphological Hubble type of the galaxy and the value of α: a steeper slope for an early type spiral galaxy.

Other recent results from larger samples of LIRGs (Miralles-Caballero et al. 2011; Vavilkin 2011) show evidence that $\alpha \approx 1.8-2.0$, though at distances > 200 Mpc where resolution and blending effects may play a role, they find that the LF flattens to $\alpha \sim 1.7$. They also find evidence that the value of α varies with respect to the galaxy interaction phase: a system in its first approach will have a shallower LF (~ 1.50) but then, as it evolves, its PL index will be close or equal to 2 at a merger stage and will start to decrease again after the interaction (see Figure 1.11). Moreover, Östlin et al. (2003) and Adamo et al. (2010, 2011b,a) derived flatter slopes ranging between 1.5 to 1.8 for the I-band CLF in their very strongly star forming blue compact dwarf galaxies (54 to 82 Mpc), while Surace et al. (1998) and Inami et al. (2010) find similar slopes between 1.1 and 1.8 in the B-band for three (U)LIRGs.

1.4.3 The IMF of young star clusters

Although the CLF is a good proxy of the CMF, one should always keep in mind that the luminosity distribution is built from clusters with different ages. Deriving an accurate CIMF is not trivial because the youngest SSCs necessary to draw such a function are often very few in the photometric catalogue, especially for star-forming galaxies with low SFRs. This lack of information has sparked controversies around the universality of the CIMF: *is any detected variation because of simple statistical or selection effects or/and rather from ongoing physical process?* Indeed, the CIMF had long been assumed as uniform (independent of any physical process) and well-fitted by a PL function with $\beta = 2$ until recently when Larsen (2009) and Gieles (2009) introduced another form of CIMF that is suggested to be more consistent with the data in both low and high mass ends of the distribution. The newly proposed form of the CIMF is expressed as follows:

$$\phi(M) = \frac{dN}{dM} = AM^{-\beta}\exp(-M/M_{\star}) \tag{1.6}$$

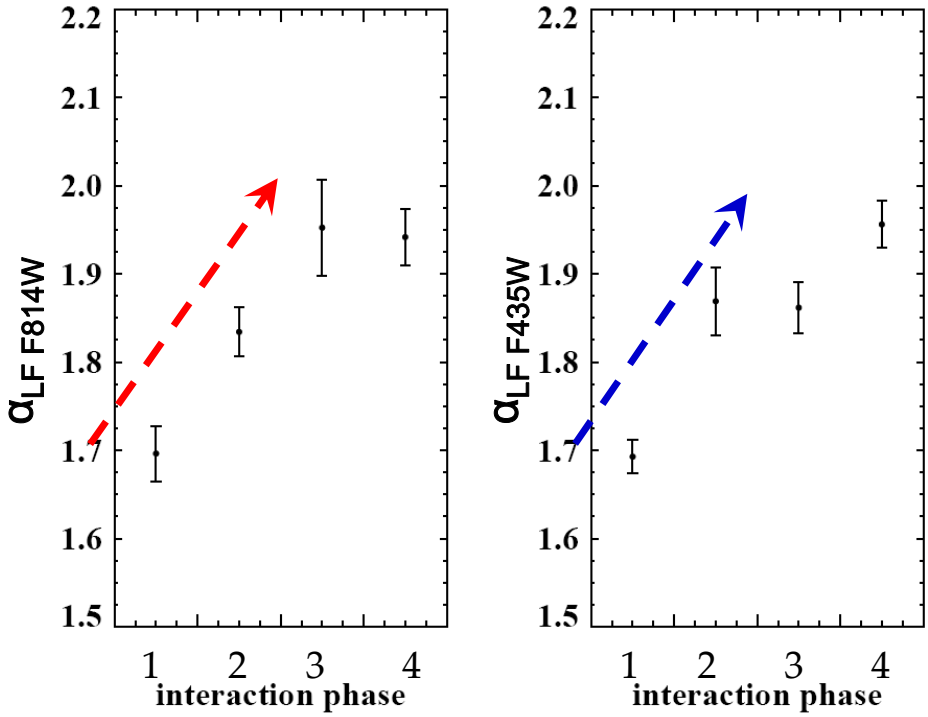

Figure 1.11: The variation of the power-law index α as a function of the host galaxy interaction stage in I- (left) and B-band (right). Figure taken from Miralles-Caballero talk during the workshop entitled: Extreme Starbursts in the Local Universe (Gonzalez Delgado et al. 2010).

the Schechter-like CIMF has the same slope $\beta = 2$ but with a truncated mass $M_\star$ varying with the cluster environments. A review by Portegies Zwart et al. (2010) compared the Schechter MFs of different galaxies including the LMC, a cluster-poor spiral galaxy, a cluster-rich one, and the disturbed Antennae galaxies, to explore the possibility of a mass or/and environment-dependent CIMF (see Figure 1.12). The results indicated that the location of the truncation is not the same for the different galaxies: quiescent normal galaxies have $M_\star \approx 2 \times 10^5 M_\odot$ while strongly interacting galaxies are associated with a higher value of $M_\star \approx 2 \times 10^6 M_\odot$.

Indeed, PL distributions still appear to be consistent with the low mass end of the CMFs, especially if the host galaxies do not have highly massive clusters. However, a truncated Schechter MF represents the data much better when the galaxy harbors very young and massive SC populations that could be associated with top-heavy IMFs (i.e. more massive stars form over the low-mass ones). *Why do we have two different forms of distributions?* There are two possible interpretations of such a behavior:

- The low SFR of normal spiral galaxies does not allow them to form very massive SCs. Truncated Schechter MFs preferentially fit the high SFR galaxies because of a simple size-of-sample effect, and thus could be the reason of a varying $M_\star$. In

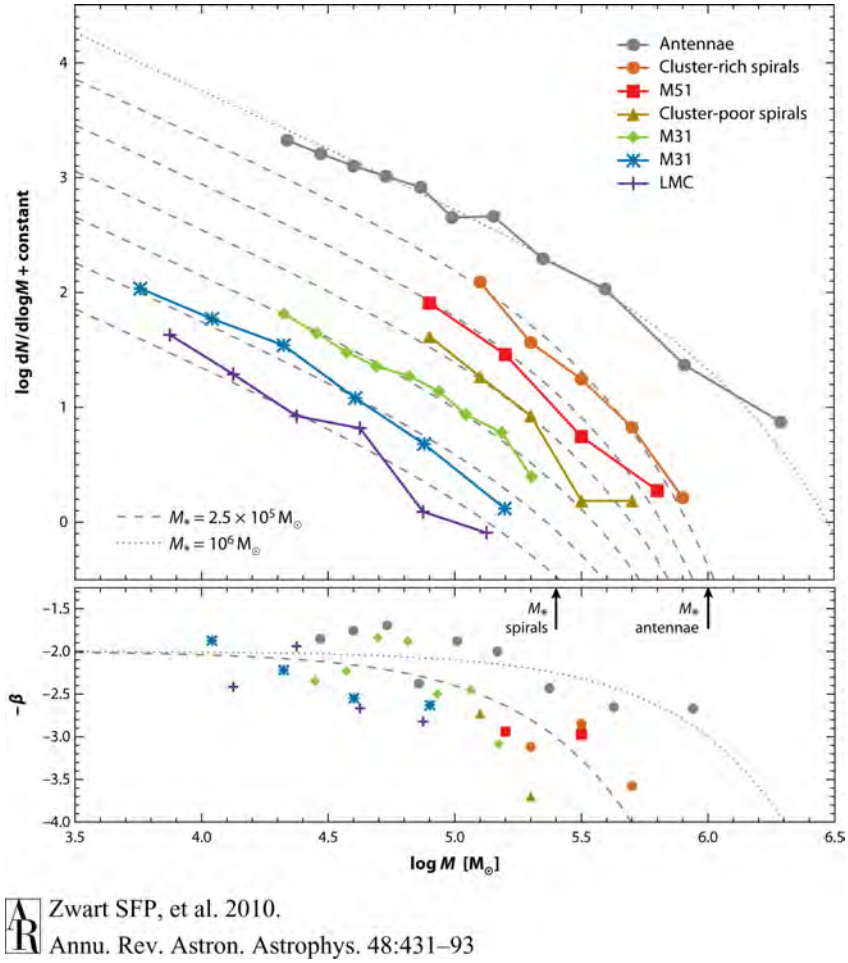

Figure 1.12: CMFs of some galaxies with different environments, from poor-spirals to violent and extreme systems such as the Antennae. Truncated Schechter functions seem to represent well the data. Figure taken from Portegies Zwart et al. (2010).

that case, one should not judge the universality of the CIMF based on its mass distribution. All galaxies follow the same SF and cluster disruption mechanisms regardless of their local environments (e.g. Zhang & Fall 1999; Bik et al. 2003).

- On the other hand, alternative explanations emphasize that a truncated CIMF is a signature of environmentally dependent dynamical process. In addition to a statistical effect, which should be expected, violent and dense environments offer higher probability for the galaxy to form newly born massive SCs. Such conditions are not met in the quiescent galaxies and this is why a PL MF is still consistent with the data (e.g Larsen 2009; Gieles 2009).

Finally, Fouesneau et al. (2014) recently published their work on stellar cluster systems in M31; the data are part of the ongoing Panchromatic Hubble Andromeda Treasury (PHAT) survey. They showed that the CMF varies with respect to the environment.

However, they suggested that the cluster mass distribution still follows a PL but with a varying index rather than a constant value of $\beta \sim 2$.

1.4.4 The cluster formation efficiency

Bastian (2008) refers to the fraction of star formation happening in bound stellar clusters as cluster formation efficiency (CFE or Γ). The author derives the value of such fraction by using the following expression:

$$\Gamma(\%) = \frac{\mathrm{CFR}}{\mathrm{SFR}} \times 100 \tag{1.7}$$

where SFR is the host galaxy star formation rate and CFR the cluster formation rate. The latter parameter is the total mass M_{tot} formed in clusters at a certain age interval Δt divided by the duration of time of such an interval, i.e.:

$$\mathrm{CFR} = \frac{M_{tot}}{\Delta t} \tag{1.8}$$

In the solar neighborhood, the value of Γ has been found to remain relatively constant: $\Gamma \simeq 5\,\%$ by Lada & Lada (2003), $\Gamma \simeq 7\,\%$ by Lamers & Gieles (2008), and $\Gamma \simeq 3\,\%$ for the SMC by Gieles & Bastian (2008). However, subsequent SSC extragalactic studies ruled out the concept of a constant parameter and rather suggested an environmentally-dependent CFE (Goddard et al. 2010; Adamo et al. 2011). Such arguments were supported with the predictions by e.g. Boily & Kroupa (2003), Pelupessy & Portegies Zwart (2012) and Kruijssen (2012). In fact, the fraction has been found to go beyond 40 % in high-SFR luminous blue compact galaxies (Adamo et al. 2011). Figure 1.13 shows the latest version of the CFE - SFR surface density (Σ_{SFR}) relation taken from Adamo & Bastian (2015). The correlation between the two parameters is thought to be a mere reflection of the CFE - gas density relation which means that high SFE environments produce more GMCs and are thus expected to have more stars forming in bound stellar clusters. However, the use of a diverse type of galaxies (normal spirals, starbursts, etc) to draw $\Gamma - \Sigma_{SFR}$ relation has raised some doubts. An inhomogeneous sample combined with low spatial resolution could affect the upper trend of the relation by showing a spurious increase of Γ at high SFR densities.

To circumvent such bias and to check the robustness of the relation, Silva-Villa et al. (2013) investigated the variation of the parameter Γ as a function of the galactocentric radius in the field of M83, a nearby gas-rich spiral. The fraction of stars remaining in bound clusters was found to decrease with increasing radius, and hence with decreasing gas density on sub-galactic scales. The central cluster formation efficiency of 30 % is relatively high compared to the fractions of 15 % (at $R \sim 1\,\mathrm{kpc}$) and 4 % (at $R > 2.7\,\mathrm{kpc}$) at other galactocentric radii (Goddard et al. 2010; Silva-Villa et al. 2013). The values of Γ based from the star cluster properties of NGC 2997 were also consistent with such

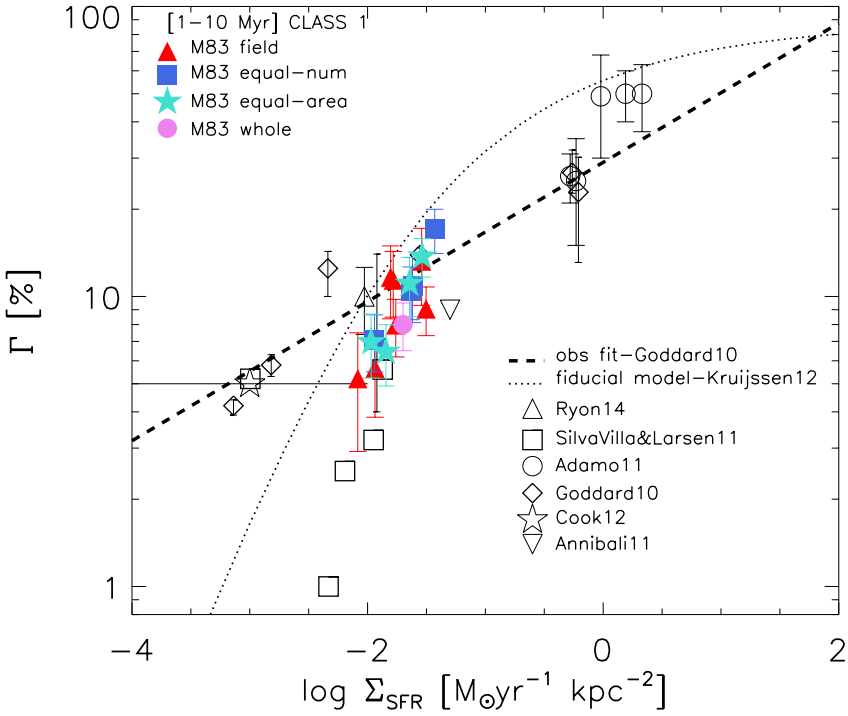

Figure 1.13: Cluster formation efficiency - SFR density relation based on measurements in different galaxies available in the literature. The dashed line and the dotted line represent the observational fit from Goddard et al. (2010) and the theoretical predictions of the relation by Kruijssen (2012), respectively. Figure taken from Adamo & Bastian (2015).

a trend (Ryon et al. 2014). High-pressure environments such as in the nuclear starburst regions enhance the formation of star clusters. Clumps of GMCs form easily in such environments. In contrast, there is not enough dense gas in the galactic halo to reproduce similar CFE as that of the central regions.

In conclusion, galactic environments play an important role in the star cluster formation mechanism whether on global or sub-galactic scale. Strongly star-forming galaxies such as starbursts and LIRGs are expected to have a high cluster formation efficiency. Refer to Kruijssen (2014) and Adamo & Bastian (2015) for a recent review.

1.4.5 Star cluster migration: the cruel cradle effect

While the high-pressure environments of starburst-dominated galaxies are ideal for SSC formation, their high-gas densities on the other hand also increase the probability of cluster destruction through strong tidal shocks (e.g. Gieles et al. 2006c; Kruijssen 2014).

As mentioned in Section 1.2.3, massive star clusters may need to migrate within a short timescale to a more quiescent environment for a higher survival chance away from their birth sites. Such a displacement is referred to as the "cruel cradle effect" (Elmegreen 2010; Kruijssen et al. 2011). Cluster migration processes occur efficiently in gas-rich mergers because galactic collisions favor rapid displacements of clusters through encounters with their neighboring GMCs. A short timescale is necessary for the immigrant clusters to escape ongoing disruptive effects (from strong tidal shock heating) and hence a high mass-loss rate in the gas-rich star-forming regions of the galaxy. Unlike infant mortality which only affects star clusters younger than 10 Myr, a much larger age range of the star cluster population (up to 200 Myr) is involved in the cruel cradle effect. Observational evidence of such an effect should be seen as a clear pattern in the spatial distribution of the SSC ages: concentration of new-born clusters in the high-gas densities, and a wider spatial distribution of older clusters in the low-disruptive environment (refer to Figure 1.14 for an illustration). Since the latter clusters have migrated into "safer" environments such as the galactic haloes, we therefore expect the cluster disruption rate to decrease and the ejected old clusters to possibly evolve as progenitors of present-day GCs (see Section 1.2.3).

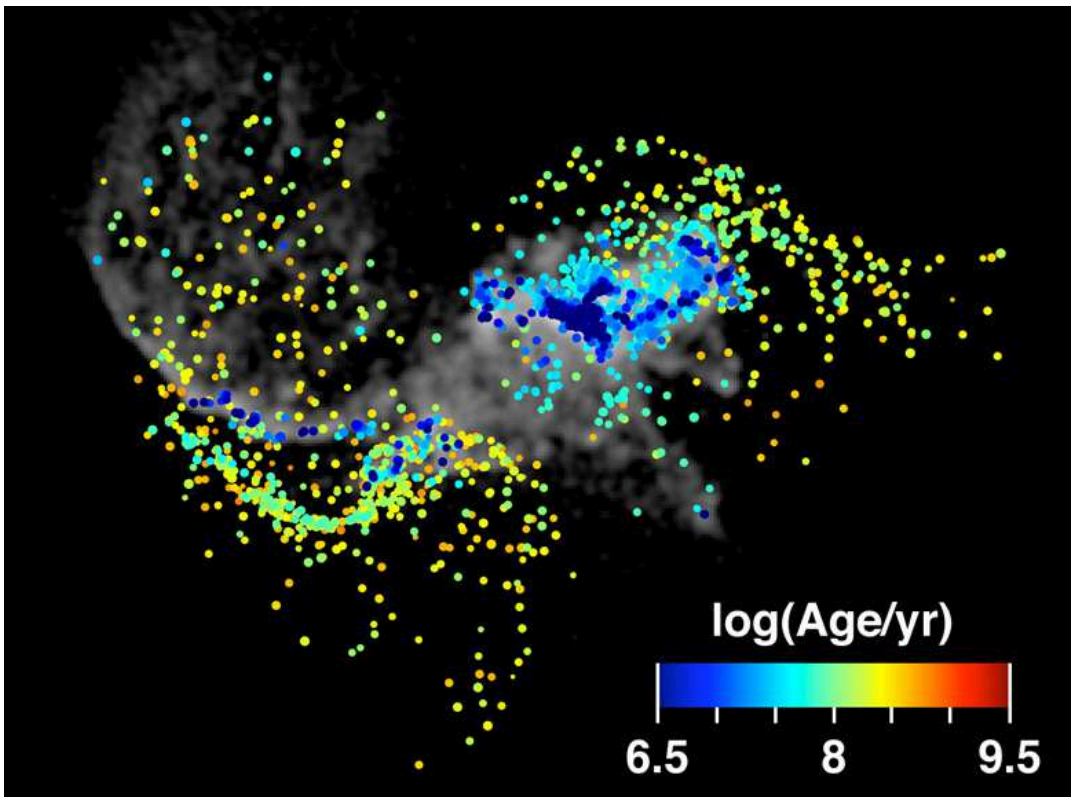

Figure 1.14: Snapshot from a merging galaxy simulation. Colored dots represent the spatial redistribution of the star clusters of different ages during the first pericenter passage of the two galaxies. The greyscale indicates the amount of gas. Figure taken from Kruijssen et al. (2012).

Another peculiarity of cluster evolution in gas-rich merging systems is that the disruption rate is likely to depend on the galaxy interaction stages (Kruijssen et al. 2011; Rieder et al. 2013; Renaud & Gieles 2013). Cluster disruption is believed to become more violent briefly after the first pericenter passage and during the nuclei coalescence. Such a variation in the destruction rate is regulated by the amount of gas being available throughout different merging stages. Therefore, immigrant clusters are likely those that formed before the gas inflow towards the SSC natal environments. The snapshot taken from Kruijssen et al. (2012) in Figure 1.14 represents simulated displacements of intermediate age clusters away from the galaxy discs during the first pericenter passage.

1.4.6 The IMF cluster stochastic sampling

Random effects, essentially small-number statistics, can have significant impact on star cluster studies in certain situations. Consider, for example, a star cluster where the existence, or not, of a single bright star can change the magnitude of the whole cluster significantly. When modelling such cases, an analytical IMF is thus not the best approach, but rather realistic stochastic sampling. In addition, it is essential to know how much uncertainty there is at a given mass and age in a model color due to these stochastic effects alone (e.g. Anders et al. 2013). Multi-band integrated photometry of star clusters (or the cluster spectral energy distribution, SED) is usually compared with a given SED model to derive the cluster physical properties such as the age, mass, metallicity and extinction (e.g. Anders et al. 2004; Adamo et al. 2010; de Grijs et al. 2013). Instead of adopting SED models based on the traditional fully sampled stellar IMF, stochastic models are nowadays being used to best reproduce the integrated photometry of the observed star clusters. In particular, such new models are proven to greatly improve the fit to the masses of low-mass clusters ($\lesssim 10^4\,M_{\odot}$) that are often highly contaminated by their massive stellar populations (e.g. Fouesneau et al. 2012; Anders et al. 2013). A single RSG in a star cluster is enough to contribute up to 80 % of the NIR flux depending of the cluster mass (see Figure 1.15) and since the effect is larger in the NIR than in the optical, the SEDs of the SSCs are affected (Riffel et al. 2008; Gazak et al. 2013).

Furthermore, RSG and/or asympotic giant branch (AGB) stars that appear approximately at 10 Myr and between $0.1 - 1$ Gyr, respectively, result in rapid changes in the magnitudes and colors of SSCs at these age ranges. This has the result that when one fits observed magnitudes to the models, a wider range of data points with inherent observational uncertainties ˜fall into ˝these narrow age ranges. The visible effect of this are the so-called chimneys, concentrations of points, evident in the age vs. mass plots of SSCs. While taking biased stochastic sampling into account may achieve more accurate photometric age dating of the luminous unresolved star clusters, these chimneys, at ages coinciding with the appearance of the massive RSG and AGB stars will still appear merely due to observational uncertainties and rapid age changes of models (e.g Bastian et al. 2005; de Grijs & Goodwin 2008; de Grijs et al. 2013).

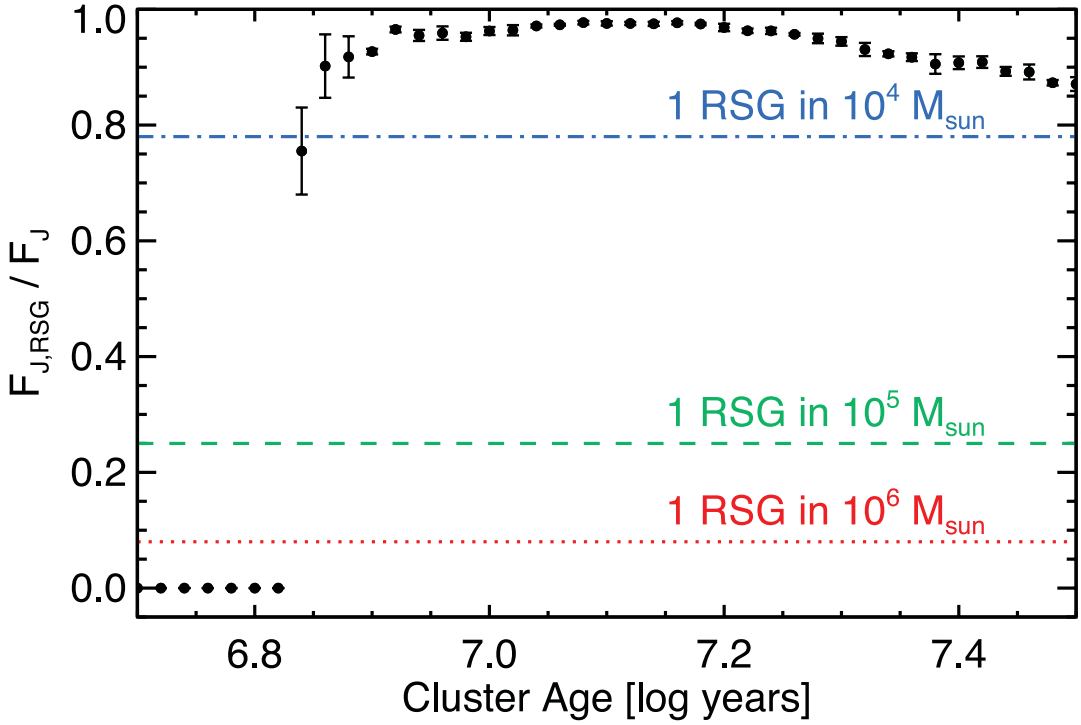

Figure 1.15: The variation of the J-band flux contribution of RSGs in a $10^5\,M_\odot$ SSC (the black points). The horizontal lines mark the flux contribution of a single RSG in a cluster with a certain mass ($10^4, 10^5$, and $10^6\,M_\odot$). Figure taken from Gazak et al. (2013).

1.4.7 The star cluster frequency

The number of clusters per time interval above a certain mass limit is defined as the cluster frequency. Such an age distribution is constructed to trace the cluster formation history of the host galaxy. A rapid decline of the star cluster population as a function of time is a general trend of the cluster frequency (see Figure 1.16 in the case of M83). This is mainly due to evolutionary fading effects, though other statistical and physical biases could also be responsible. Any strong peak in the age distribution indicates a period in which a starburst event took place in the galaxy, though one should be careful of possible spurious concentrations of ages in the mass-age modelling because of the appearance of RSGs and AGB stars (see Section 1.4.6).

The shape of the star cluster frequency is usually represented by a power-law function (e.g. Fall et al. 2005; Bastian et al. 2005) of the form:

$$dN/d\tau \sim \tau^{-\zeta} \tag{1.9}$$

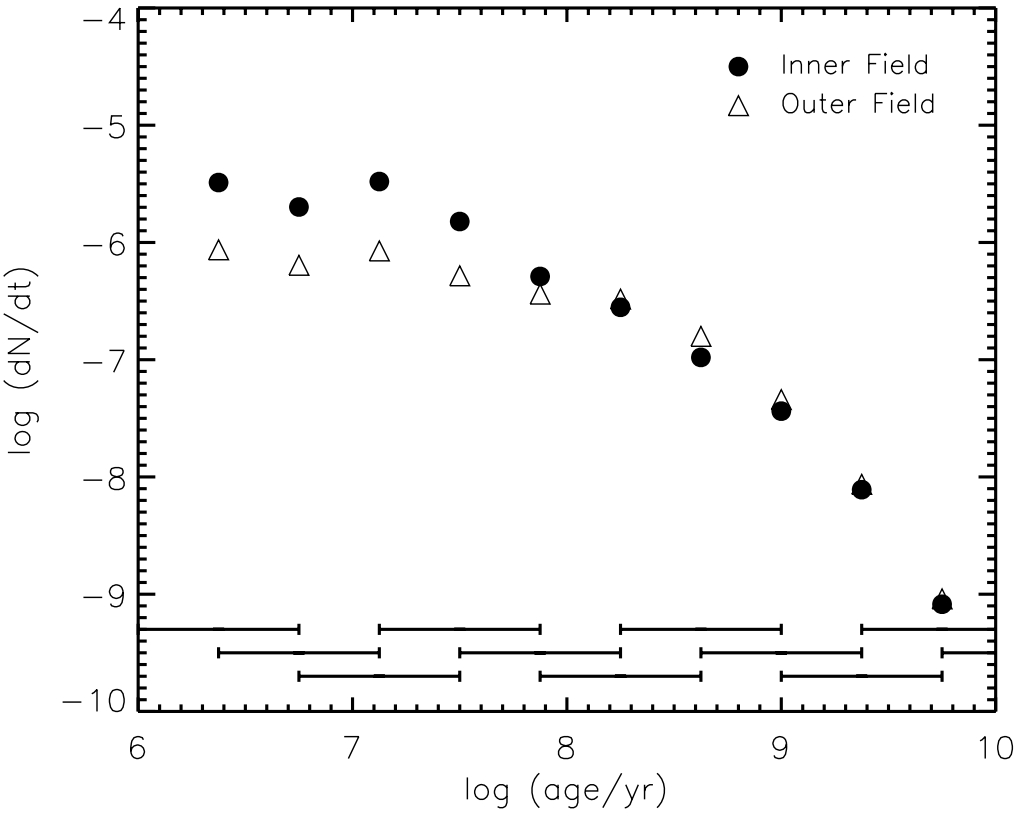

Figure 1.16: Star cluster frequency of M83. Only clusters with masses above $5 \times 10^3\,M_\odot$ are included in the plot. Filled circles and open triangles represent the distribution in the outer and inner field regions of the starburst galaxy, respectively. Figure taken from Bastian et al. (2012).

with the index ζ[g] suggested to reflect the intensity of the cluster disruption. Numerous works only fit the cluster frequency between 10 and 100 Myr because this time interval is deemed to be critical in the evolution of the cluster. A cluster population free of disruption and with a constant CFR has a flat distribution of $\zeta = 0$. Such a scenario corresponds to the cluster early stages of evolution where effects from infant mortality are still insignificant. On the other hand, if there is a constant disruption rate all over the age bins, the value of the slope approaches 1 (e.g. Fall et al. 2005; Chandar et al. 2010). This assumes a mass-independent disruption mechanism and that about 90 % of the star clusters are destroyed each age dex. Lamers et al. (2005), however, argued that the power-law index differs from $\zeta \sim 1$ in case of a mass-dependent disruption. Furthermore, a recent compilation of previous works by Adamo & Bastian (2015) showed that stronger cluster disruption mechanisms due to high-pressure environments result in a relatively steeper slope ($\zeta \sim 0.6$) compared to that of more quiescent environments ($\zeta \sim 0.3$). A

[g] The power-law index ζ is annotated as γ for some other works (e.g. Chandar et al. 2010).

much higher value of $\zeta = 1.4$ was suggested by Grosbøl & Dottori (2013) in the case of NGC 2997. The authors, however, did not apply any age or mass cuts to their sample.

The values of ζ across the galactocentric radius of M83 (inner vs outer field) are also consistent with an environmentally-dependent cluster frequency (Bastian et al. 2012; Silva-Villa et al. 2014). The influence of the environments on the disruption can also be observed through the variation of the shape of the cluster frequency as shown in Figure 1.16 (a flatter distribution for the outer field).

From this literature review, one can agree that the bottom line of the disagreements regarding SSC characteristics and evolution revolve around the universality of the CIMF as well as the cluster disruption mechanisms. *Are they environment and mass dependent or not?* The purpose of this thesis is to contribute toward understanding the puzzle by using NIR adaptive optics imaging combined with high-resolution archival optical data.

References

Adamo, A., Östlin, G., Zackrisson, E., et al. 2010, MNRAS, 407, 870

Adamo, A., Östlin, G., Zackrisson, E., & Hayes, M. 2011a, MNRAS, 414, 1793

Adamo, A., Östlin, G., Zackrisson, E., et al. 2011b, MNRAS, 415, 2388

Adamo, A., Östlin, G., & Zackrisson, E. 2011c, MNRAS, 417, 1904

Adamo, A., & Bastian, N. 2015, The lifecycle of clusters in galaxies, to appear in *T*he Birth of Star Clusters, editor S.W. Stahler, Springer edition, submitted

Allison, M. 2006, Star clusters and how to observe them, ISBN 1846281903, 2006

Alonso-Herrero, A., Pereira-Santaella, M., Rieke, G. H., & Rigopoulou, D. 2012, ApJ, 744, 2

Alonso-Herrero, A., Rieke, G. H., Colina, L., et al. 2009, ApJ, 697, 660

Alonso-Herrero, A., Rieke, G. H., Rieke, M. J., & Scoville, N. Z. 2002, AJ, 124, 166

Anders, P., Bissantz, N., Boysen, L., de Grijs, R., & Fritze-v. Alvensleben, U. 2007, MNRAS, 377, 91

Anders, P., Kotulla, R., de Grijs, R., & Wicker, J. 2013, ApJ, 778, 138

Anders, P., de Grijs, R., Fritze-v. Alvensleben, U., & Bissantz, N. 2004, MNRAS, 347, 17

Andersen, M., Zinnecker, H., Moneti, A., et al. 2009, ApJ, 707, 1347

Arp, H., & Sandage, A. 1985, AJ, 90, 1163

Ashman, K. M. & Zepf, S. E. 1992, ApJ, 384, 50

Ashman, K. M., & Zepf, S. E. 1998, Globular cluster systems / Keith M. Ashman, Stephen E. Zepf. Cambridge, U. K. ; New York : Cambridge University Press, 1998. (Cambridge astrophysics series ; 30) QB853.5 .A84 1998

Baldry, I. K., Glazebrook, K., Brinkmann, J., et al. 2004, ApJ, 600, 681

Barkana, R., & Loeb, A. 2001, Phys. Rep., 349, 125

Barnes, J. E., & Hernquist, L. 1996, ApJ, 471, 115

Bastian et al. 2005, A&A, 431, 905

Bastian, N. 2008, MNRAS, 390, 759

Bastian, N., Adamo, A., Gieles, M., et al. 2011, MNRAS, 417, L6

Bastian, N., Adamo, A., Gieles, M., et al. 2012, MNRAS, 419, 2606

Bastian, N., Cabrera-Ziri, I., Davies, B., & Larsen, S. S. 2013, MNRAS, 436, 2852

Bastian, N., & Goodwin, S. P. 2006, MNRAS, 369, L9

Battinelli, P., & Capuzzo-Dolcetta, R. 1991, MNRAS, 249, 76

Baumgardt, H., Parmentier, G., Anders, P., & Grebel, E. K. 2013, MNRAS, 430, 676

Bekki, K., & Couch, W. J. 2001, ApJL, 557, L19

Bennett, C. L., Banday, A. J., Gorski, K. M., et al. 1996, ApJL, 464, L1

Bennett, C. L., Halpern, M., Hinshaw, G., et al. 2003, ApJS, 148, 1

Bik, A., et al. 2003, A&A, 397, 473

Binggeli, B., Tammann, G. A., & Sandage, A. 1987, AJ, 94, 251

Binney, J., & Tremaine, S. 1987, Princeton, NJ, Princeton University Press, 1987, 747 p.,

Blaauw, A. 1964, ARA&A, 2, 213

Boily, C. M., & Kroupa, P. 2003, MNRAS, 338, 665

Böker, T., Laine, S., van der Marel, R. P., et al. 2002, AJ, 123, 1389

Bond, J. R., Kofman, L., & Pogosyan, D. 1996, Nature, 380, 603

Bournaud, F. 2011, EAS Publications Series, 51, 107

Boutloukos, S. G., & Lamers, H. J. G. L. M. 2003, MNRAS, 338, 717

Brinchmann, J., Charlot, S., White, S. D. M., et al. 2004, MNRAS, 351, 1151

Caputi, K. I., Lagache, G., Yan, L., et al. 2007, ApJ, 660, 97

Carollo, C. M., Stiavelli, M., & Mack, J. 1998, AJ, 116, 68

Chandar, R., Whitmore, B. C., Calzetti, D., et al. 2011, ApJ, 727, 88

Chandar, R., Whitmore, B. C., Kim, H., et al. 2010, ApJ, 719, 966

Clark, J. S., Negueruela, I., Crowther, P. A., & Goodwin, S. P. 2005, A&A, 434, 949

Colina, L., Borne, K., Bushouse, H., et al. 2001, ApJ, 563, 546

Colless, M., Dalton, G., Maddox, S., et al. 2001, MNRAS, 328, 1039

Côté, P., Piatek, S., Ferrarese, L., et al. 2006, ApJS, 165, 57

Cowie, L. L., Barger, A. J., Fomalont, E. B., & Capak, P. 2004, ApJL, 603, L69

Cowie, L. L., Songaila, A., Hu, E. M., & Cohen, J. G. 1996, AJ, 112, 839

Crowther, P. A., Schnurr, O., Hirschi, R., et al. 2010, MNRAS, 408, 731

Daddi, E., Dickinson, M., Morrison, G., et al. 2007, ApJ, 670, 156

Darvish, B., Sobral, D., Mobasher, B., et al. 2014, ApJ, 796, 51

de Grijs, R., Anders, P., Bastian, N., et al. 2003a, MNRAS, 343, 1285

de Grijs, R., Bastian, N., & Lamers, H. J. G. L. M. 2003b, ApJL, 583, L17

de Grijs, R., Lee, J. T., Clemencia Mora Herrera, M., Fritze-v. Alvensleben, U., & Anders, P. 2003c, New A, 8, 155

de Grijs, R., & Goodwin, S. P. 2008, MNRAS, 383, 1000

de Grijs, R., Anders, P., Zackrisson, E., & Östlin, G. 2013, MNRAS, 431, 2917

de Lapparent, V., Geller, M. J., & Huchra, J. P. 1986, ApJL, 302, L1

de Zeeuw, P. T., Brown, A. G. A., de Bruijne, J. H. J., et al. 1997, Hipparcos - Venice '97, 402, 495

de Zeeuw, P. T., Hoogerwerf, R., de Bruijne, J. H. J., Brown, A. G. A., & Blaauw, A. 1999, AJ, 117, 354

Duc, P.-A., Brinks, E., Wink, J. E., & Mirabel, I. F. 1997, A&A, 326, 537

Doroshkevich, A. G., Sunyaev, R. A., & Zeldovich, I. B. 1974, Confrontation of Cosmological Theories with Observational Data, 63, 213

Elbaz, D., Cesarsky, C. J., Chanial, P., et al. 2002, A&A, 384, 848

Elbaz, D., Daddi, E., Le Borgne, D., et al. 2007, A&A, 468, 33

Elbaz, D., Dickinson, M., Hwang, H. S., et al. 2011, A&A, 533, A119

Elmegreen, B. G. 2002, ApJ, 577, 206

Elmegreen, B. G. 2010, ApJL, 712, L184

Elmegreen, B. G., & Efremov, Y. N. 1997, ApJ, 480, 235

Elson, R. A. W., & Fall, S. M. 1985, PASP, 97, 692

Escala, A. 2011, ApJ, 735, 56

Escala, A., & Larson, R. B. 2008, ApJL, 685, L31

Faber, S. M., Willmer, C. N. A., Wolf, C., et al. 2007, ApJ, 665, 265

Farrah, D., Afonso, J., Efstathiou, A., et al. 2003, MNRAS, 343, 585

Fouesneau, M., Johnson, L. C., Weisz, D. R., et al. 2014, ApJ, 786, 117

Fouesneau, M., Lançon, A., Chandar, R., & Whitmore, B. C. 2012, ApJ, 750, 60

Fritze-v. Alvensleben, U. 1999, A&A, 342, L25

Gazak, J. Z., Bastian, N., Kudritzki, R.-P., et al. 2013, MNRAS, 430, L35

Genel, S., Vogelsberger, M., Springel, V., et al. 2014, MNRAS, 445, 175

Genzel, R., Lutz, D., & Tacconi, L. 1998, Nature, 395, 859

Gieles, M., & Bastian, N. 2008, A&A, 482, 165

Gieles, M. 2009, MNRAS, 394, 2113

Gieles, M., Larsen, S. S., Bastian, N., & Stein, I. T. 2006a, A&A, 450, 129

Gieles, M., Larsen, S. S., Scheepmaker, R. A., et al. 2006b, A&A, 446, L9

Gieles, M., & Portegies Zwart, S. F. 2011, MNRAS, 410, L6

Gieles, M., Portegies Zwart, S. F., Baumgardt, H., et al. 2006c, MNRAS, 371, 793

Goddard, Q. E., Bastian, N., & Kennicutt, R. C. 2010, MNRAS, 405, 857

Gonzalez Delgado, R. M., Rodriguez Zaurin, J., Perez, E., et al. 2010, arXiv:1008.2107

González, V., Labbé, I., Bouwens, R. J., et al. 2010, ApJ, 713, 115

Goodwin, S. P., & Bastian, N. 2006, MNRAS, 373, 752

Graham, A. W., & Spitler, L. R. 2009, MNRAS, 397, 2148

Grosbøl, P., & Dottori, H. 2013, A&A, 551, LL13

Gruppioni, C., Pozzi, F., Rodighiero, G., et al. 2013, MNRAS, 432, 23

Fall, S. M., Chandar, R., & Whitmore, B. C. 2005, ApJL, 631, L133

Fall, S. M., Chandar, R., & Whitmore, B. C. 2009, ApJ, 704, 453

Figer, D. F. 2004, The Formation and Evolution of Massive Young Star Clusters, 322, 49

Fouesneau, M., Johnson, L. C., Weisz, D. R., et al. 2014, ApJ, 786, 117

Haas, M. R., Gieles, M., Scheepmaker, R. A., Larsen, S. S., & Lamers, H. J. G. L. M. 2008, A&A, 487, 937

Harris, J., Calzetti, D., Gallagher, J. S., III, Smith, D. A., & Conselice, C. J. 2004, ApJ, 603, 503

Heckman, T. M., Robert, C., Leitherer, C., Garnett, D. R., & van der Rydt, F. 1998, ApJ, 503, 646

Ho, L. C. & Filippenko, A. V. 1996, ApJL, 466, L83

Holtzman, J. A., Faber, S. M., Shaya, E. J., et al. 1992, AJ, 103, 691

Hopkins, A. M., & Beacom, J. F. 2006, ApJ, 651, 142

Hubble, E. P. 1922, ApJ, 56, 400

Hubble, E. P. 1925a, Popular Astronomy, 33, 252

Hubble, E. P. 1925b, ApJ, 62, 409

Hubble, E. P. 1926, ApJ, 64, 321

Hubble, E. P. 1929, Proceedings of the National Academy of Science, 15, 168

Hubble, E. P. 1936, Realm of the Nebulae, Yale University Press, ISBN 9780300025002

Huchra, J., Davis, M., Latham, D., & Tonry, J. 1983, ApJS, 52, 89

Imanishi, M., Nakagawa, T., Shirahata, M., Ohyama, Y., & Onaka, T. 2010, ApJ, 721, 1233

Inami, H., Armus, L., Surace, J. A., et al. 2010, AJ, 140, 63

Ivison, R. J., Swinbank, A. M., Smail, I., et al. 2013, ApJ, 772, 137

Jeans, J. H. 1928, Cambridge [Eng.] The University Press, 1928

Johnson, K. E. 2004, The Formation and Evolution of Massive Young Star Clusters, 322, 339

Juneau, S., Glazebrook, K., Crampton, D., et al. 2005, ApJL, 619, L135

Karachentsev, I. D., Makarova, L. N., Makarov, D. I., Tully, R. B., & Rizzi, L. 2015, MNRAS, 447, L85

Kennicutt, R. C., Jr. 1998a, ApJ, 498, 541

Kennicutt, Jr., R. C. 1998b, ARA&A, 36, 189

Kim, D.-C., Veilleux, S., & Sanders, D. B. 1998, ApJ, 508, 627

Kruijssen, J. M. D., Pelupessy, F. I., Lamers, H. J. G. L. M., Portegies Zwart, S. F., & Icke, V. 2011, MNRAS, 414, 1339

Kruijssen, J. M. D., Pelupessy, F. I., Lamers, H. J. G. L. M., et al. 2012, MNRAS, 421, 1927

Kruijssen, J. M. D., Maschberger, T., Moeckel, N., et al. 2012a, MNRAS, 419, 841

Kruijssen, J. M. D. 2012b, MNRAS, 426, 3008

Kruijssen, J. M. D. 2014, Classical and Quantum Gravity, 31, 244006

Krumholz, M. R. 2014, arXiv:1402.0867

Lada, C. J. & Lada, E. A. 2003, ARA&A, 41, 57

Lada, C. J., Lombardi, M., & Alves, J. F. 2010, ApJ, 724, 687

Lamers, H. J. G. L. M. 2009, Ap&SS, 324, 183

Lamers, H. J. G. L. M., Gieles, M., Bastian, N., et al. 2005, A&A, 441, 117

Lamers, H. J. G. L. M., & Gieles, M. 2008, Mass Loss from Stars and the Evolution of Stellar Clusters, 388, 367

Lamers, H. J. G. L. M., Gieles, M., & Portegies Zwart, S. F. 2005, A&A, 429, 173

Larsen, S. S. 2002, AJ, 124, 1393

Larsen, S. S. 2008, Mass Loss from Stars and the Evolution of Stellar Clusters, 388, 279

Larsen, S. S. 2009, A&A, 494, 539

Le Fèvre, O., Abraham, R., Lilly, S. J., et al. 2000, MNRAS, 311, 565

Le Floc'h, E., Papovich, C., Dole, H., et al. 2005, ApJ, 632, 169

Lemaître, G. 1931, Nature, 127, 706

Li, S., de Grijs, R., Anders, P., & Li, C. 2015, ApJS, 216, 6

Longmore, S. N., Kruijssen, J. M. D., Bastian, N., et al. 2014, Protostars and Planets VI, 291

Lotz, J. M., Jonsson, P., Cox, T. J., et al. 2011, ApJ, 742, 103

Madau, P., & Dickinson, M. 2014, arXiv:1403.0007

Maoz, D., Barth, A. J., Sternberg, A., et al. 1996, AJ, 111, 2248

Martin, D. C., Wyder, T. K., Schiminovich, D., et al. 2007, ApJS, 173, 342

McCrady, N., & Graham, J. R. 2007, ApJ, 663, 844

McKee, C. F., & Ostriker, E. C. 2007, ARA&A, 45, 565

Melnick, J., Moles, M., & Terlevich, R. 1985, A&A, 149, L24

Mendez, A. J., Coil, A. L., Lotz, J., et al. 2011, ApJ, 736, 110

Meurer, G. R., Heckman, T. M., Leitherer, C., et al. 1995, AJ, 110, 2665

Miralles-Caballero, D., Colina, L., Arribas, S., & Duc, P.-A. 2011, AJ, 142, 79

Mora, M. D., Larsen, S. S., Kissler-Patig, M., Brodie, J. P., & Richtler, T. 2009, A&A, 501, 949

Mortlock, D. J., Warren, S. J., Venemans, B. P., et al. 2011, Nature, 474, 616

Muench, A. A., Lada, E. A., Lada, C. J., & Alves, J. 2002, ApJ, 573, 366

Neumayer, N., & Walcher, C. J. 2012, Advances in Astronomy, 2012

Östlin, G., Bergvall, N., & Roennback, J. 1998, A&A, 335, 8

Östlin, G., Zackrisson, E., Bergvall, N., Roennback, J. 2003, A&A, 408, 887

Ostriker, J. P., & Hausman, M. A. 1977, ApJL, 217, L125

Partridge, R. B. 1980, Phys. Scr, 21, 624

Pelupessy, F. I., & Portegies Zwart, S. 2012, MNRAS, 420, 1503

Perlmutter, S., Aldering, G., Goldhaber, G., et al. 1999, ApJ, 517, 565

Phillips, A. C., Illingworth, G. D., MacKenty, J. W., & Franx, M. 1996, AJ, 111, 1566

Planck Collaboration, Ade, P. A. R., Aghanim, N., et al. 2014a, A&A, 571, AA23

Planck Collaboration, Ade, P. A. R., Aghanim, N., et al. 2014b, A&A, 571, AA1

Portegies Zwart, S. F., et al. 2010, ARA&A, 48, 431

Richstone, D. O. 1976, ApJ, 204, 642

Rieder, S., Ishiyama, T., Langelaan, P., et al. 2013, MNRAS, 436, 3695

Riess, A. G., Filippenko, A. V., Challis, P., et al. 1998, AJ, 116, 1009

Riffel, R., Pastoriza, M. G., Rodríguez-Ardila, A., & Maraston, C. 2008, MNRAS, 388, 803

Renaud, F., & Gieles, M. 2013, MNRAS, 431, L83

Robin, A. C., Reylé, C., Derrière, S., & Picaud, S. 2003, A&A, 409, 523

Rodighiero, G., Daddi, E., Baronchelli, I., et al. 2011, ApJL, 739, L40

Rowan-Robinson, M. 2000, MNRAS, 316, 885

Ryon, J. E., Adamo, A., Bastian, N., et al. 2014, AJ, 148, 33

Salim, S., Rich, R. M., Charlot, S., et al. 2007, ApJS, 173, 267

Sanders, D. B., Soifer, B. T., Elias, J. H., et al. 1988, ApJ, 325, 74

Sanders, D. B., & Mirabel, I. F. 1996, ARA&A, 34, 749

Schiminovich, D., Wyder, T. K., Martin, D. C., et al. 2007, ApJS, 173, 315

Schmidt, M. 1959, ApJ, 129, 243

Schombert, J., McGaugh, S., & Maciel, T. 2013, AJ, 146, 41

Seth, A., Agüeros, M., Lee, D., & Basu-Zych, A. 2008, ApJ, 678, 116

Schawinski, K., Urry, C. M., Simmons, B. D., et al. 2014, MNRAS, 440, 889

Silva-Villa, E., Adamo, A., & Bastian, N. 2013, MNRAS, 436, L69

Silva-Villa, E., Adamo, A., Bastian, N., Fouesneau, M., & Zackrisson, E. 2014, MNRAS, 440, L116

Soifer, B. T., Sanders, D. B., Neugebauer, G., et al. 1986, ApJL, 303, L41

Soifer, B. T., Sanders, D. B., Madore, B. F., et al. 1987, ApJ, 320, 238

Springel, V., Di Matteo, T., & Hernquist, L. 2005a, MNRAS, 361, 776

Springel, V., White, S. D. M., Jenkins, A., et al. 2005b, Nature, 435, 629

Surace, J. A., Sanders, D. B., Vacca, W. D., Veilleux, S., & Mazzarella, J. M. 1998, ApJ, 492, 116

Tekola, A. G., Väisänen, P., & Berlind, A. 2012, MNRAS, 419, 1176

Toomre, A. 1977, Evolution of Galaxies and Stellar Populations, 401

Toomre, A., & Toomre, J. 1972, ApJ, 178, 623

Trumpler, R. J. 1931, PASP, 43, 255

Väisänen, P., Mattila, S., Kniazev, A., et al. 2008, MNRAS, 384, 886

van den Bergh, S. 1971, A&A, 12, 474

Vavilkin, T. 2011, Ph.D. Thesis,

Veilleux, S., Kim, D.-C., Sanders, D. B., Mazzarella, J. M., & Soifer, B. T. 1995, ApJS, 98, 171

Verbeke, R., De Rijcke, S., Koleva, M., et al. 2014, MNRAS, 442, 1830

Vogelsberger, M., Genel, S., Springel, V., et al. 2014, MNRAS, 444, 1518

Walcher, C. J., van der Marel, R. P., McLaughlin, D., et al. 2005, ApJ, 618, 237

Weidner, C., Bonnell, I. A., & Zinnecker, H. 2010, ApJ, 724, 1503

Weidner, C., Kroupa, P., & Larsen, S. S. 2004, MNRAS, 350, 1503

Westmoquette, M. S., Bastian, N., Smith, L. J., et al. 2014, arXiv:1405.7543

Whitaker, K. E., van Dokkum, P. G., Brammer, G., & Franx, M. 2012, ApJL, 754, L29

Whitmore, B. C. 2003, A Decade of Hubble Space Telescope Science, 153

Whitmore, B. C., Chandar, R., Bowers, A. S., et al. 2014, AJ, 147, 78

Whitmore, B. C., Chandar, R., & Fall, S. M. 2007, AJ, 133, 1067

Whitmore, B. C., Chandar, R., Schweizer, F., et al. 2010, AJ, 140, 75

Whitmore, B. C., Schweizer, F., Leitherer, C., Borne, K., & Robert, C. 1993, AJ, 106, 1354

Whitmore, B. C., Zhang, Q., Leitherer, C., et al. 1999, AJ, 118, 1551

Willman, B. 2010, Advances in Astronomy, 2010, 285454

Wright, N. J., Parker, R. J., Goodwin, S. P., & Drake, J. J. 2014, MNRAS, 438, 639

York, D. G., Adelman, J., Anderson, J. E., Jr., et al. 2000, AJ, 120, 1579

Yuan, T.-T., Kewley, L. J., & Sanders, D. B. 2010, ApJ, 709, 884

Zepf, S. E., Ashman, K. M., English, J., Freeman, K. C., & Sharples, R. M. 1999, AJ, 118, 752

Zhang, Q., & Fall, S. M. 1999, ApJL, 527, L81

Chapter 2

The thesis: objectives, data processing and SSC selection

Overview

This Chapter highlights the thesis goal and objectives. The sample, the observations and the NIR data reduction are presented as well as the SSC candidate selection criteria that were reported in Randriamanakoto et al. (2013a,b).

2.1 Overview & thesis outlines

The back-bone of this thesis is an ongoing multi-wavelength study of nearby strongly star-forming galaxies. It focuses on the understanding of formation and evolution of young massive SSC candidates in these targets with extreme starburst activities. In addition to facilitating SSC detections in obscured environments, because of the use of IR wavelengths, this work investigates properties of SSCs in host galaxies with higher SFRs than seen in most previous studies. The main specific objectives of the thesis are:

1. To derive the K_S-band[a] LFs of the massive star clusters and to evaluate the effect of blending on the LFs. Non-universal CIMFs have recently been suggested, hence questioning the universality of a PL CLF with canonical slope of $\alpha \approx 2$. *Will the range of the PL slopes in our starburst-dominated sample be similar with that from normal spiral galaxies? Is a PL function a good proxy of the SSC LFs?* This is the first ever study with a significant sample of starburst-dominated galaxies that were imaged using NIR adaptive optics (AO) systems. The results are presented in Chapter 3 and partly published in Randriamanakoto et al. (2013b).

[a] Hereafter, we will refer to both the Johnson K-band and 2MASS K_S-band observations as K-band.

2. To establish the NIR brightest star cluster magnitude vs. SFR relation. So far, the validity of the relation has only been tested in the optical regime, and mostly using fairly nearby star-forming galaxies. Extinction effects are difficult to correct for especially in the dustier galaxies and will necessarily introduce scatter in the relation; using redder wavelengths will significantly improve the situation. With AO it is now possible to probe more distant host galaxies and thus increase the SFR baseline. *Will the relation still hold in the NIR and at larger SFR levels? Can we see effects of random sampling, and/or are there clear physical processes behind the relation?* The results are presented in Chapter 4 and published in Randriamanakoto et al. (2013a).

3. To model the extinction, ages and masses of the SSC candidates in a subsample of LIRGs. SSC mass and age distribution are useful in tracing the SFH of the host galaxy. *Is the age spatial distribution of SSCs random or does it follow a clear pattern? Are the CMFs consistent with a PL function with index $\beta \approx 2$? What role do galactic environments play regarding the characteristics of the SSC populations?* High-resolution NIR AO imaging are combined with HST archival data to address these issues. The results are presented in Chapter 5.

The next sections of this Chapter (Chapter 2) describe the sample, the observations and data reduction, and finally provide details on the SSC selection. Conclusions and future work are presented in Chapter 6.

Throughout the thesis we assume the standard cosmology: $H_0 = 73$ km s^{-1} Mpc^{-1}, $\Omega_M = 0.27$, and $\Omega_\Lambda = 0.73$.

2.2 The sample: SUNBIRD survey

SSC properties of 42 nearby IR-bright galaxies, including LIRGs with extreme starburst activities are investigated in this thesis. The targets form a representative statistical sample of strongly star-forming galaxies. They are also part of an ongoing survey dubbed SUNBIRD (SUperNovae and starBursts in the InfraReD) to search for dust-obscured core-collapse SNe using NIR AO imaging (e.g. Mattila et al. 2007; Kankare et al. 2008, 2012; Väisänen et al. 2014). They are IRAS galaxies from the flux-limited Revised Bright Galaxy Sample (RBGS, Sanders et al. 2003), selected to have luminosity distances $D_L \lesssim 200$ Mpc with IR luminosities uniformly distributed from $\log(L_\odot/L_{\rm IR}) = 10.6$ to 11.9. Figure 2.1 shows the distribution of the parent sample in the IR luminosity - redshift plane where the SUNBIRD galaxies are labelled as blue points. The targets of this representative sample are all starburst-dominated based on their cool IRAS colors ($f_{25}/f_{60} < 0.2$), though AGN were not excluded a priori.

The sample covers a wide variety of morphologies and interaction stages. The different

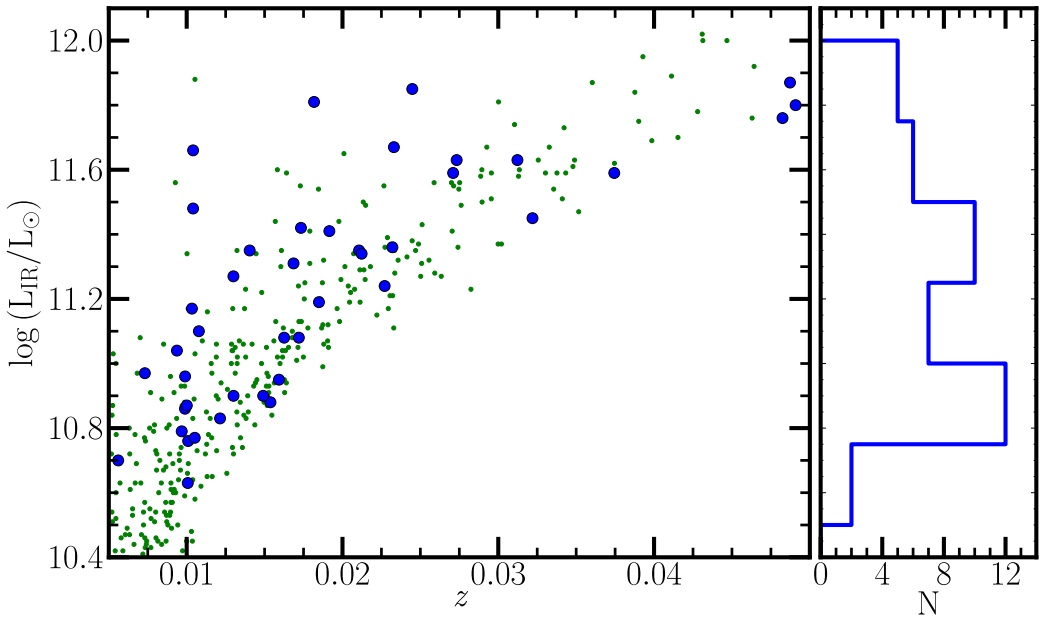

Figure 2.1: Distribitution of IRAS galaxies from RBGS (Sanders et al. 2003; green points) in the IR luminosity - redshift plane. Our targets from the SUNBIRD sample are shown as blue circles and are spread approximately homogeneously all over the 2D-plane up to $z \sim 0.04$. They form a random representative sample of all IR-cool RBGS galaxies since there are no other physical sample selection criteria. They are starburst galaxies and LIRGs. The right panel shows a histogram of IR luminosities of the SUNBIRD galaxy sample.

interaction phases, the first approach, pre-merger, merger, and post-merger stages, are respectively annotated as I, II, III and IV in Table 2.1. Note that the classification is based on studying the apparent morphologies of the targets observed in the high-spatial resolution NIR AO images (refer to Figure 2.2). The galaxy disks remain stable during the first approach, though the gas content becomes perturbed due to the violent dynamical evolution (Class I). Features such as tidal tails and bridges are indicative of pre-merger stages with the distances between the two disks and the two nuclei of the galaxies still far enough to be detected individually (Class II). However, merging stages are underway when the two coalesced nuclei are separated by a relatively small distance (not more than 2 kpc) and both disks are completely distorted to allow the formation of a common internal structure (Class III). When the coalesced nuclei have merged completely, the more relaxed post-merger system has a much brighter nucleus enveloped with some shell structures (Class IV). This customized classification scheme is a simplified version of that from Veilleux et al. (2002) and similar to the method adopted by Miralles-Caballero et al. (2011). Finally, targets that are apparently undisturbed with no obvious pair within 10 arcmin radius, corresponding to 100 to 300 kpc radius in the distance range of the bulk of the sample, are classified as isolated galaxies. They are identified as Class 0 in Table 2.1. In the following sample, around a quarter appear to be isolated and relaxed

Table 2.1: The SUNBIRD survey: a selected sample of starburst-dominated galaxies.

IRAS name	Common name	RA (J2000)	DEC (J2000)	l (deg)	b (deg)	$\log L_{\rm IR}$ ($L_\odot$)	D_L (Mpc)	$m-M$ (mag)	Interaction phase
(1)	(2)	(3)	(4)	(5)	(6)	(7)	(8)	(9)	(10)
F00163 − 1069	MCG −02-01-052	00h18m50.1s	−10d21m42s	96.77	−71.55	10.63†	110.0	35.20	II
01173 + 1405	CGCG 436−030	01h20m02.7s	+14d21m43s	133.30	−47.93	11.63	127.0	35.52	II
01364 − 1042		01h38m52.9s	−10d27m11s	159.01	−69.93	11.76	201.0	36.52	III
F02509 + 1248	NGC 1134	02h53m41.3s	+13d00m51s	163.29	−40.08	10.83	47.4	33.37	II
F03022 − 1232	NGC 1204	03h04m39.9s	−12d20m29s	194.18	−55.49	10.88	61.4	33.94	0
F04191 − 1855	ESO 550−IG025	04h21m20.0s	−18d48m48s	214.77	−41.31	11.45	135.0	35.65	II
F05091 + 0508	NGC 1819	05h11m46.1s	+05d12m02s	196.17	−19.39	10.90	61.9	33.96	0
05368 + 4940	MCG+08-11-002	05h40m43.7s	+49d41m41s	161.67	+9.96	11.41	79.9	34.51	IV
06076 − 2139		06h09m45.8s	−21d40m24s	228.35	−18.54	11.59	160.0	36.02	III
06164 + 0311		06h19m02.6s	+03d09m51s	206.39	−5.74	10.79	41.5	33.09	0
07077 − 2729	ESO 491−G020	07h09m48.1s	−27d34m15s	239.62	−8.50	10.86†	43.5	33.19	II
07202 − 2908	ESO 428−G023	07h22m09.4s	−29d14m08s	242.36	−6.83	10.76	44.5	33.24	0
F07329 + 1149	MCG+02-20-003	07h35m43.4s	+11d42m34s	207.29	+15.06	11.08	70.5	34.24	II
F09529 − 3253	IC 2522	09h55m08.9s	−33d08m14s	265.49	+16.63	10.63	46.1	33.32	I
F10015 − 0614	NGC 3110	10h04m02.1s	−06d28m29s	246.37	+37.39	11.31	75.2	34.38	II
10173 + 0828		10h20m00.2s	+08d13m34s	233.58	+49.52	11.80	215.0	36.66	I
F10409 − 4556	ESO 264−G036	10h43m07.7s	−46d12m45s	280.94	+11.11	11.35	92.0	34.82	I
F10567 − 4310	ESO 264−G057	10h59m01.8s	−43d26m26s	282.21	+14.86	11.08	75.8	34.39	II
F11005 − 1601	NGC 3508	11h02m59.7s	−16d17m22s	268.55	+39.23	10.90	59.1	33.86	0
F11143 − 7556	NGC 3620	11h16m04.7s	−76d12m59s	297.22	−14.41	10.70	24.9	31.98	0
F11255 − 4120	ESO 319−G022	11h27m54.1s	−41d36m52s	286.60	+18.59	11.04	72.3	33.18	0
F11257 + 5850	IC 694	11h28m27.3s	+58d34m43s	141.90	+55.39	11.66†	45.3	33.28	III
F11257 + 5850	NGC 3690	11h28m32.3s	+58d33m43	141.90	55.41	11.48†	45.3	33.28	III
F11506 − 3851	ESO 320−G030	11h53m11.7s	−39d07m49s	290.76	−21.71	11.10	49.0	33.45	0
F12043 − 3140	ESO 440−IG058	12h06m51.9s	−31d56m54s	292.02	−18.27	11.36	102.0	35.05	II
F12115 − 4656	ESO 267−G030	12h14m12.9s	−47d13m42s	296.39	+15.17	11.19	80.9	34.54	II
12116 − 5615		12h14m22.1s	−56d32m33s	297.81	+5.96	11.59	117.0	35.34	IV
F12250 − 0800	NGC 4433	12h27m38.6s	−08d16m42s	292.85	+54.13	10.87	46.3	33.33	II
F12351 − 4015	NGC 4575	12h37m51.1s	−40d32m14s	300.14	+22.26	10.96	45.0	33.26	I
F12596 − 1529	MCG−02-33-098	13h02m20.4s	−15d46m00s	306.78	+47.02	10.95†	70.8	34.25	III
13052 − 5711		13h08m18.7s	−57d27m30s	305.21	+5.34	11.34	91.6	34.81	IV
F13182 + 3424	IC 883	13h20m35.3s	+34d08m22s	82.93	+80.59	11.67	101.0	35.02	IV
F13473 − 4801	ESO 221−IG008	13h50m26.4s	−48d16m36s	312.96	+13.44	10.77	46.7	33.34	II
F13478 − 4848	ESO 221−IG010	13h50m56.9s	−49d03m20s	312.86	+12.66	11.17	45.9	33.31	II
F15107 + 0724	CGCG 049−057	15h13m13.1s	+07d13m32s	8.89	+50.95	11.27	56.4	33.76	0
F15467 − 2914	NGC 6000	15h49m49.5s	−29d23m13s	343.30	+19.17	10.97	32.1	32.53	IV
F16504 + 0228	NGC 6240	16h52m58.9s	+02d24m03s	20.73	+27.29	11.85	103.0	35.06	III
F16516 − 0948		16h54m24.0s	−09d53m21s	9.50	+20.50	11.24	94.8	34.88	IV
F17138 − 1017		17h16m35.8s	−10d20m39s	12.24	+15.67	11.42	72.2	34.29	III
F17578 − 0400		18h00m31.9s	−04d00m53s	23.45	+9.42	11.35	57.3	33.79	II
18293 − 3413		18h32m41.1s	−34d11m27s	0.15	−11.31	11.81	74.6	34.37	II
19115 − 2124	ESO 593−IG008	19h14m30.9s	−21d19m07s	16.07	−14.42	11.87	206.0	36.56	III

Notes. The targets are ordered with increasing RA. Column 1: IRAS survey name; Column 2: common name; Columns 3 & 4: equatorial coordinates; Columns 5 & 6: galactic coordinates; Column 7: galaxy IR luminosity from Sanders et al. (2003), any value marked by † is estimated by using the method described in Section 4.2; Columns 8 & 9: luminosity distance and distance modulus retrieved from NED database; Column 10: the galaxy interaction phase where I refers to the first approach, II to the pre-merger phase, III and IV for merger and post-merger stages, respectively. Class 0 regroups galaxies with undisturbed morphologies that are apparently isolated.

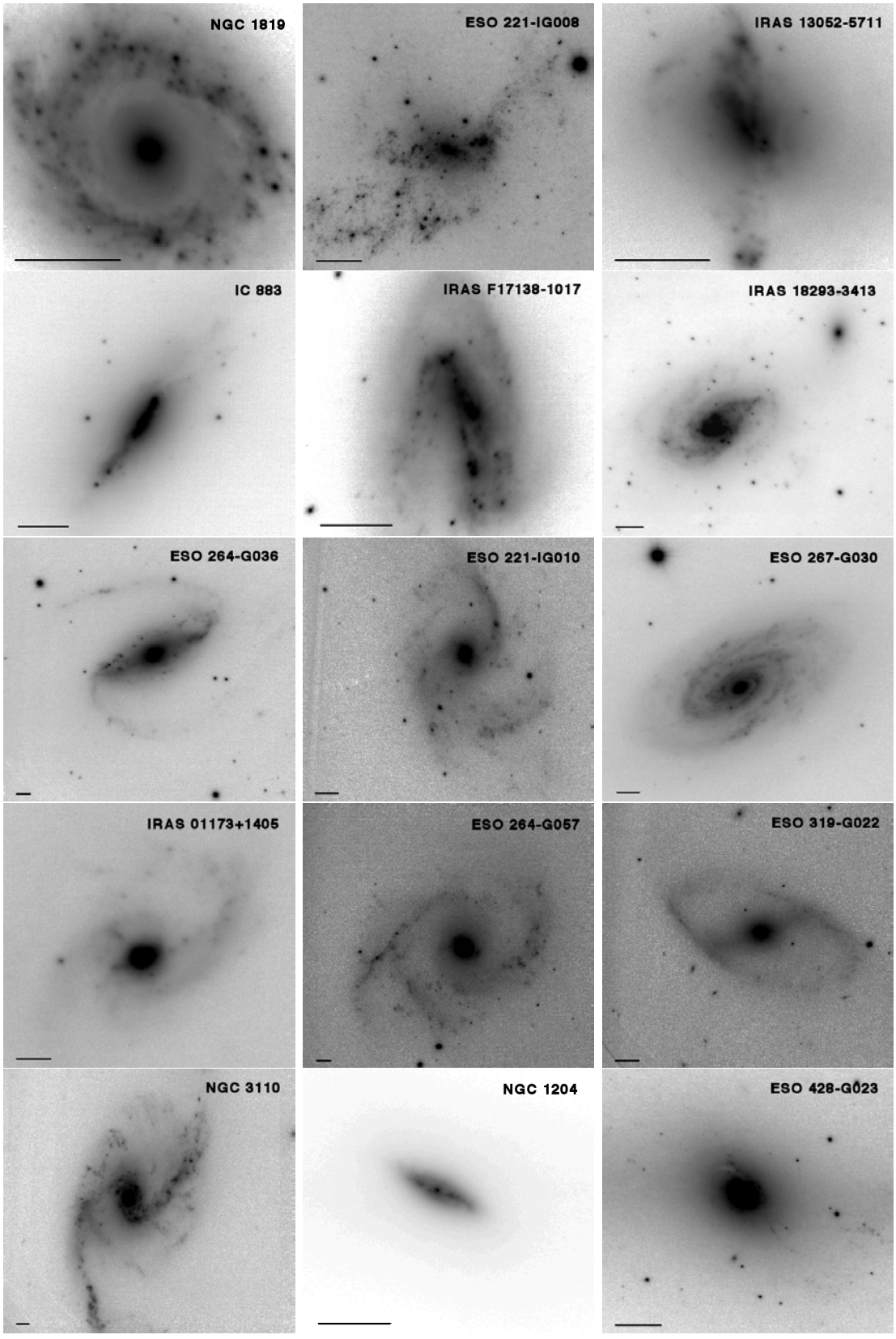

Figure 2.2: NIR AO images (zoomed-in version) of the SUNBIRD sample. Up is North and left is East. The horizontal line represents a scale of 1 kpc.

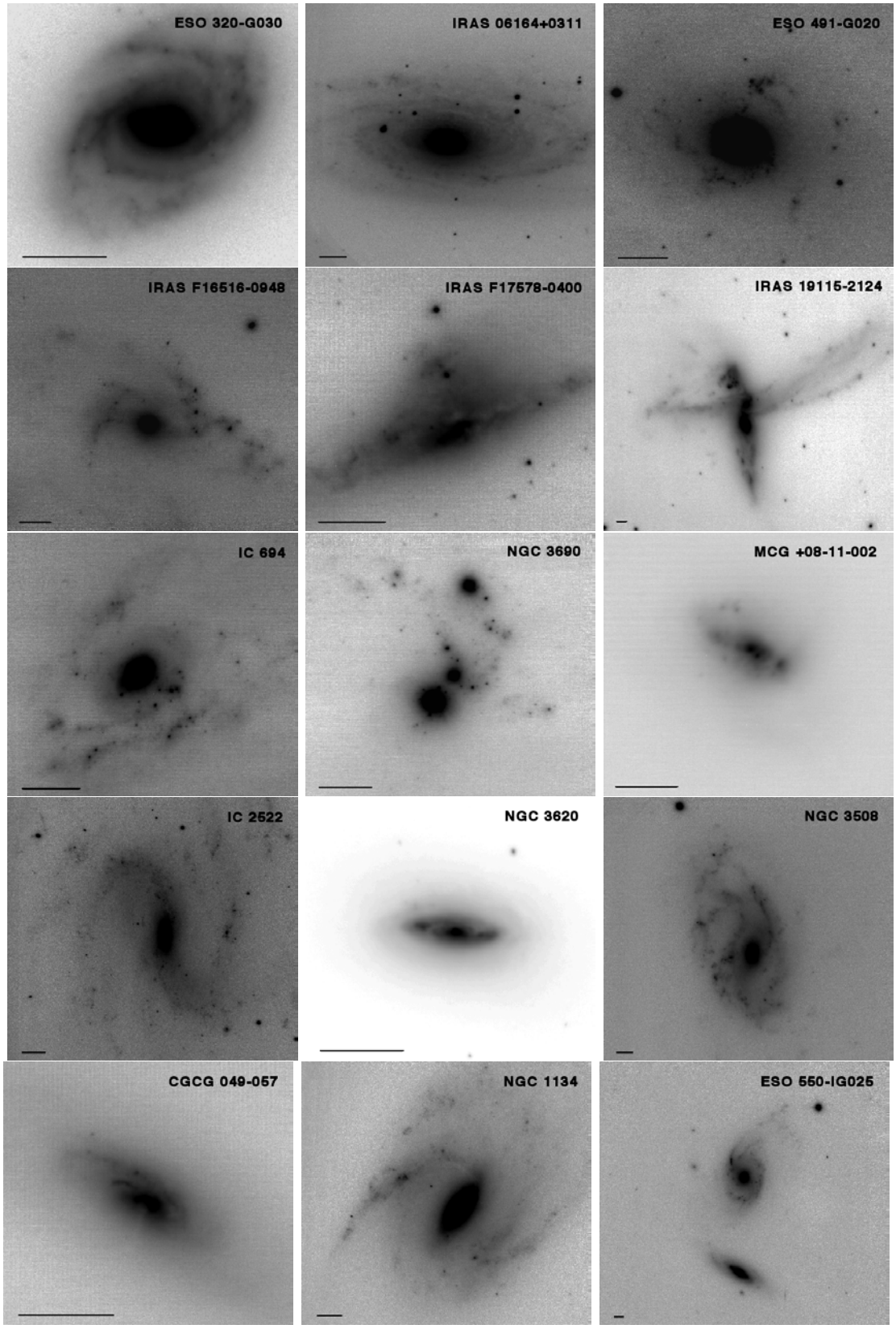

Figure 2.2: -Continued

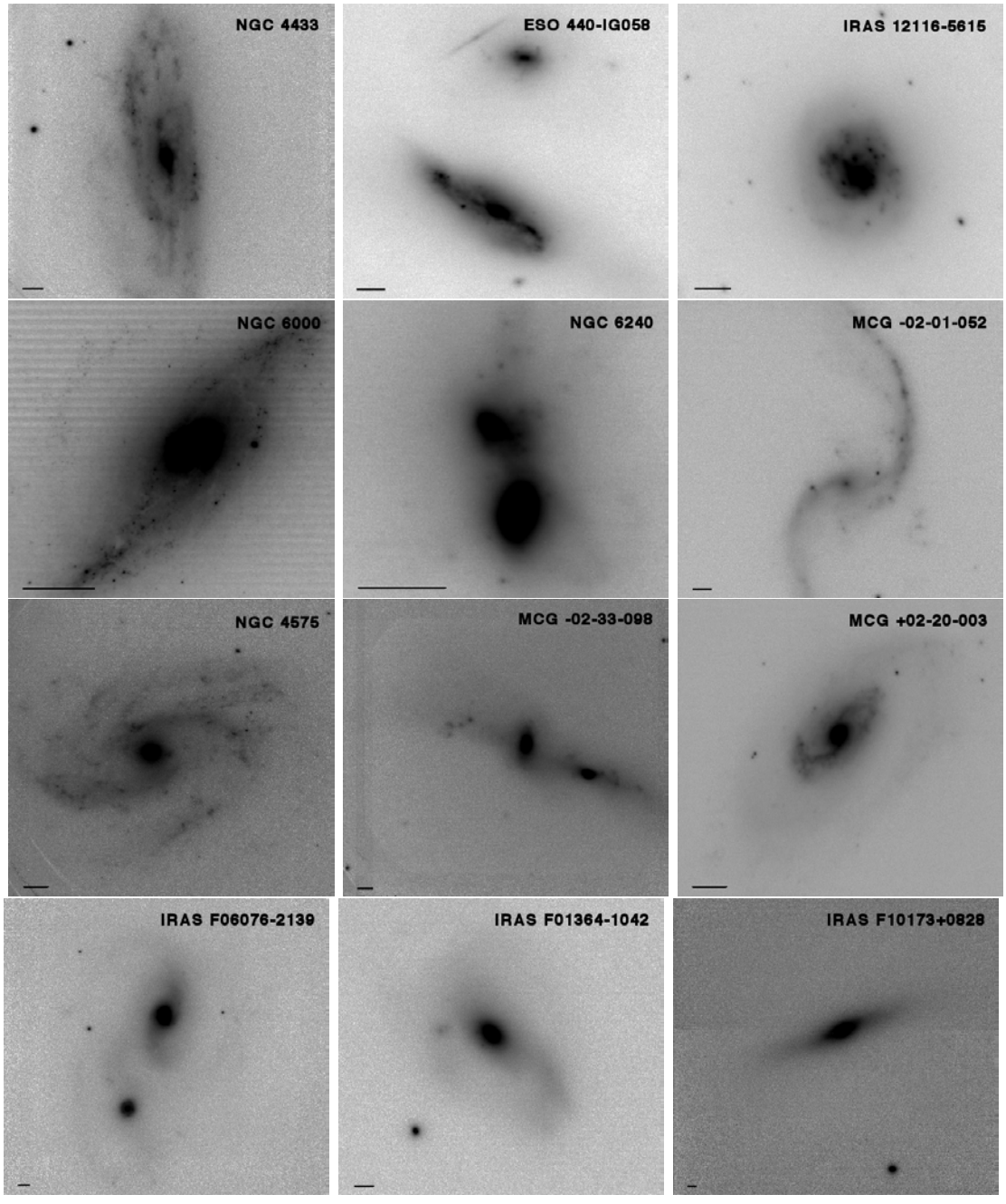

Figure 2.2: -Continued

spirals, though sometimes slightly perturbed, another quarter are in fairly wide pairs before the first pericenter passage, and the rest are strongly perturbed objects at various stages of interactions and/or merging.

Finally, the sample were also selected in such a way that there are complementary data set available in the archives, most importantly optical HST imaging; the NIR AO observations match the spatial resolution of HST/ACS data.

2.3 Observations and data reduction

Most of the thesis work deals with NIR AO K-band data which are relevant in studying the obscured nuclear regions of the selected targets. Combined with a redder filter such as K-band, AO systems could provide high angular resolution imaging similar to what instruments mounted on space-based telescopes are capable to deliver. The observations were taken using two different ground-based instruments: the NAOS-CONICA on the ESO Very Large Telescope (VLT/NaCo) and the ALTAIR/NIRI on the Gemini-North telescope (Gemini/NIRI). Figure 2.3 shows images of the telescopes where these AO systems are currently mounted on; the pictures were taken during observation using a *laser guide star* (LGS) wavefront sensing mode. One fifth of the sample were imaged with Gemini/NIRI as a pilot study of the project and the rest are galaxies observed with the 8 m-class VLT/UT4 telescope with a bright enough isolated star near the field-of-view (FoV) to serve as a *natural guide star* (NGS) of the AO system (refer to Section 2.3.1). This requirement of suitably bright reference stars is a further sample selection constraint, but does not correlate with the LIRG characteristics in any way. The AO correction worked well in both cases, resulting in a full width at half-maximum (FWHM) of ~ 0.1 arcsec for the point sources.

With the help of a reference star, AO systems mounted on ground-based telescopes correct for the turbulence of the lower atmosphere for a clearer view of target due to a smaller PSF. The AO module is composed of a wavefront sensor which records the scattered light from the NGS that will be used to compensate for the wavefront aberrations of the target source. A reference star has to be bright enough and located within the isoplanatic patch of the target; however, if there are no suitable point sources due to the limited sky coverage, alternative artificial LGS may be switched on. A new era of AO systems was marked by the development of more powerful instruments such as GEMS and ERIS[b]: with a multi-conjugate LGS wavefront sensing, even better resolution with wider fields and more uniform PSF shapes could be reached.

[b] Mounted on Gemini-South, the GEmini Multi-conjugate adaptive optics System or GEMS delivers a FoV of more than 1 arcmin. The Enhanced Resolution Imager and Spectrograph *aka* ERI is a proposed instrument for the VLT/UT4 telescope and assisted with AO systems as well.

Figure 2.3: Two telescopes with AO *laser guide stars* to correct for the diffraction of light due to the atmospheric perturbations. *Left:* Located in Mauna Kea Hawaii the Gemini-North telescope has its instruments mounted on a Cassegrain focus (altitude: 4213 m; image credit: GEMINI/AURA). *Right:* UT4 is one of the four Unit Telescopes to form the ESO VLT on Cerro Paranal Chile, it hosts a Nasmyth-focus AO setup (altitude: 2635 m; image credit: ESO/Yuri Beletsky).

2.3.1 NIR AO imaging data

Gemini/NIRI data: Eight targets of our sample come from a recent multi-epoch survey using the ALTAIR/NIRI mounted on a Cassegrain focus of the Gemini-North telescope during 2008-2012 (PI: Ryder, Programs: GN-2008A-Q- 38, GN-2008B-Q-32, GN-2009A-Q-12, GN-2009B-Q-23, GN-2010A-Q-40). The pixel scale is $0.022''\text{pix}^{-1}$, yielding a sky coverage of 22 by 22 arcsec. Each individual frame has an exposure time of $\sim 30\,sec$, and in this case separate sky-frames were taken for sky subtraction in addition to on-target dithering. Note that Gemini/NIRI data were imaged with LGS, with a tip/tilt reference star. They were reduced using `IRAF`[c]-based tasks including flat-fielding and sky subtraction. Individual frames with significantly lower quality PSFs were excluded, as well as some with abnormal electronic noise. A weaker, horizontal stripe pattern was still evident and was removed by a custom-made de-striping algorithm. Note that such a procedure does not introduce bias to the final image counts. This was tested by measuring the fluxes of isolated point-sources before and after the stripe removals. The final images were produced by average-combining the individual frames from different observing runs after shifting them to a common reference. Table 2.2 lists the effective integration times per target.

VLT/NaCo data: The other targets were taken with the Nasmyth-focus UT4/NACO of the ESO VLT telescope with NGS wavefront sensing. Depending on

[c] `IRAF` is distributed by the National Optical Astronomy Observatories, which are operated by the Association of Universities for Research in Astronomy, Inc., under cooperative agreement with the National Science Foundation.

Table 2.2: The K-band data observation log

Galaxy name	Date yy/mm/dd	Exp.time (sec)	Airmass	AO-star name	PSF/FWHM (arcsec)	a_c (mag)	m_0 (mag)
(1)	(2)	(3)	(4)	(5)	(6)	(7)	(8)
			VLT/NACO data				
MCG −02-01-052	10/10/15	1860	1.113	S000321339	1.19	1.69	22.85
	12/06/16		1.189				
IRAS 01173+1405	10/10/28	1320	1.332	N3233130168	0.18	1.84	23.09
IRAS F01364−1042*	10/10/15	1560	1.160	S0021103155	0.09	1.23	22.95
NGC 1134	10/10/15	1240	1.276	N3313110139	0.14	1.20	23.05
NGC 1204	10/10/15	1100	1.119	S031311013626	0.24	1.16	23.09
ESO 550−IG025	10/10/15	1950	1.005	S02303102572	0.13	1.20	23.19
	12/09/13		1.039				
NGC 1819	10/10/15	1950	1.180	N3002300434	0.15	0.91	23.05
IRAS F06076−2139*	10/10/15	1560	1.022	S10320037737	0.10	1.18	22.95
IRAS 06164+0311	10/12/02	1100	1.194	N220033112962	0.24	1.95	23.09
ESO 491−G020	12/12/02	1200	1.027	S101133143219	0.11	1.23	23.15
	12/12/12		1.100				
ESO 428−G023	10/10/30	1770	1.037	S1011310487	0.13	1.04	23.18
	12/12/12		1.003				
MCG +02-20-003	10/12/10	2340	1.253	N223210019344	0.22	1.07	22.95
IC 2522	10/12/10	1260	1.100	S13322106808	0.16	0.95	23.01
NGC 3110	10/12/28	2520	1.084	S121301023	0.28	1.21	23.05
	11/04/21		1.054				
IRAS F10173+0828	10/12/28	2400	1.191	N2021131203	0.22	1.49	22.79
ESO 264−G036	11/01/21	2340	1.119	S1303112277	0.18	1.77	23.15
	12/12/17		1.123				
ESO 264−G057	10/12/27	1120	1.083	S130030036038	0.12	1.08	23.19
NGC 3508	11/02/14	1860	1.124	S12333139511	0.25	1.21	23.09
	11/05/02		1.018				
NGC 3620	11/06/12	1780	1.663	S11012304170	0.21	1.79	23.05
	13/01/16		1.619				
ESO 319−G022	11/01/22	960	1.056	S1300010357	0.14	1.33	23.14
ESO 320−G030	11/02/18	1120	1.034	S122032013806	0.17	1.82	22.89
ESO 440−IG058	11/01/22	2280	1.148	S2012103171	0.13	1.21	23.14
ESO 267−G030	11/05/07	1920	1.092	S2120002890	0.16	1.28	23.08
IRAS 12116−5615*	11/06/12	1800	1.240	S212320351886	0.11	1.57	22.77
NGC 4433	11/02/18	1020	1.057	S2003332226	0.18	1.85	23.15
NGC 4575	11/05/07	720	1.070	S2320210695	0.22	1.93	23.19
MCG −02-33-098	11/02/18	960	1.081	J13022037-1545591	0.27	3.26	23.09
IRAS 13052−5711*	11/03/26	3480	1.195	S21233314306	0.11	1.47	23.14
	11/06/12		1.269				
ESO 221−IG008	11/03/26	4620	1.119	J13502641-4816306	0.15	0.98	23.14
	11/05/07		1.108				
ESO 221−IG010	11/02/14	240	1.099	S2321222258	0.18	1.82	22.99
NGC 6000	10/03/27	2880	1.011		0.14	1.03	23.09
NGC 6240*	11/05/31	720	1.145	N1002322503	0.08	1.09	23.09
IRAS 18293−3413*	05/08/03	1230	1.014	S30133006086	0.12	1.35	26.95
IRAS 19115−2124*	04/04/13	1410	1.082	S3030230270	0.13	1.453	26.30
			Gemini/NIRI data				
MCG+08-11-002	-	1140	1.162	-	0.07	1.23	26.66
IC 694	-	1260	1.286	-	0.13	1.23	26.81
NGC 3690	-	2192	1.281	-	0.14	1.23	27.23
IC 883	-	1440	1.067	-	0.13	1.23	26.80
CGCG 049−057	-	1680	1.041	-	0.08	1.23	26.46
IRAS F16516−0948	-	900	1.191	-	0.13	1.23	26.61
IRAS F17138−1017	-	990	1.245	-	0.12	1.23	26.53
IRAS F17578−0400	-	1470	1.177	-	0.14	1.23	26.54

Notes. The targets are ordered with increasing RA. Column 1: galaxy name, the K-band image of any target followed by an asterisk was observed using UT4/S27 camera; Column 2: date of observation. The Gemini data set consists of multiple epoch observations in between 2008 and 2012; Column 3: total exposure time; Column 4: airmass of the science image; Column 5: AO-star name, Gemini/NIRI data were observed with LGS; Column 6: FWHM of the PSF; Column 7: aperture correction; Column 8: magnitude zero-point for a frame of 1 sec exposure time, corrected for atmospheric extinction effect.

the size of the galaxy, either the S27 or S54 camera was used, resulting in a pixel scale of $0.027\,''\,\mathrm{pix}^{-1}$ or $0.054\,''\,\mathrm{pix}^{-1}$, respectively; most of the targets were observed with the S54 camera. With NGS brightnesses of $V_{NGS} < 15$ mag within 30 arcsec and $V_{NGS} < 13$ mag within 45 arcsec, AO correction is expected to deliver a good performance with Strehl ratios of $\sim 0.09 - 0.25$. This will push the detection limit to $M_K \simeq -14$ mag down to -12 mag within a distance range of $\sim 25 - 150$ Mpc to probe the SSCs adequately. We have three categories of data sets for the NACO targets:

1. SSC pilot study targets: IRAS 18293−3413 and IRAS 19115−2124, the latter being a relatively distant galaxy compared to most SSC hosts in this work. Frames were taken with exposure times of 30 *sec* in dithering mode with an integration time per pointing of 90 *sec*. The total exposure times are 1230 and 1410 *sec*, respectively (see Table 2.2). The data were ready to be analyzed; more details of the NACO observations as well as data reduction are given in Mattila et al. (2007) and Väisänen et al. (2008) for these two galaxies, respectively.

2. Unpublished CCSNe targets: NGC 6000 and NGC 6240. Individual frames were taken in dithering mode during 1 and 30 *sec*, respectively, with an integration time of 60 *sec* per pointing. The total exposure times are listed in Table 2.2. Combined science images were acquired from private communication with S. Mattila. Note, however, that we had to remove horizontal stripe pattern in the case of NGC 6000 to improve the signal-to-noise ratio (S/N) of the image.

3. SSC main data set of the thesis: these are the ones imaged under program ID: P.086.B-0901 during 2010−2011 (~ 30 galaxies, PI: Escala). However, some of the targets overlapped with a sample from program ID: P.089.D-0847 (PI: Mattila). Therefore, complementary data from the latter cycle were also included in this work, though only if the frames were taken under good conditions. This will give a better resolution of the faint sources in the field. Dithering mode with 120 *sec* per pointing was used, with total integration times per target ranging between 20 and 40 minutes. Our `IRAF`-based pipeline was used to perform sky-subtraction. The individual frames were then aligned before average-combining them to get the final science image. We checked for image quality in individual frames and those with non-optimal AO-corrections were excluded, resulting in shorter total integration times in the case of ESO 221−IG010, and NGC 4575 (Table 2.2). Some frames with obviously non-photometric conditions were also excluded. Less frames with good PSFs always produce better final results than more frames including worse PSFs.

NoTCAM data: Our collaborators (Kankare et al., private communication) obtained K-band images of all the Gemini targets using the Nordic Optical Telescope (NOT) NIR Camera (NOTCam). In the wide field imaging mode, NOTCam has a pixel scale of $0.234''\mathrm{pix}^{-1}$ and a FoV of 4 arcmin. The images were flat-field corrected,

sky subtracted and combined using `IRAF`-based tasks. The NOTCam images were used as intermediate images to determine photometric zero-points for the smaller FoV NIRI images.

The astrometric calibration of the NIR images was based on the Guide Star Catalog II (GSC-II) with an uncertainty of ~ 0.15 arcsec. `IRAF/CCMAP` was used to perform the task: we downloaded archival HST/ACS data (see Section 2.3.2) of the fields and accurately re-calibrated these using the GSC-II, and then added the World Coordinate System (WCS) into the FITS headers of our NIR images using the larger FoV HST frames as reference images. Besides astrometry calibration, HST data were also combined with NIR images to derive SSC age and mass modelling (see Chapter 5).

2.3.2 HST archival data

1. **ACS/WFC:** Blue and red optical images of 15 targets were retrieved from the Hubble Legacy Archive (HLA). These had been observed as part of the GOALS (Great Observatories All-sky LIRG survey) project entitled: An ACS survey of a Complete Sample of Luminous Infrared Galaxies in the Local Universe (Armus et al. 2009). The ACS broad-band images have a plate scale of 0.05 arcsec pix^{-1} with a large FoV of 210 × 210 arcsec, and a high-angular PSF resolution of ~ 0.1 arcsec. They were taken with the filters F435W and F814W during 2005-2006 (PI: Evans, ID: 10592). Table 2.3 lists the observing dates and total integration times in each filter. In this thesis, we refer to the F814W as the Johnson-Cousins I-band, since they are roughly equivalent, and to F435W as the B-band, though they differ in flux by 7 to 12 percent (Sirianni et al. 2005). The ACS data were resampled then rescaled using `GEOTRAN` and `GEOMAP IRAF` tasks to match spatially with the NIR AO-data pixel scale and orientation.

2. **WFC3/UVIS:** Finally, complementary data from F336W (U), F438W (B), and F814W (I) filters imaged with the WFC3/UVIS instrument were also available for Arp 299 (IC 694/NGC 3690) under the Program ID: 12995 (PI: Bond). The total integration times of the images are 790, 740 and 740 s, respectively. Compared to previous HST instruments such as WFPC2 and ACS, WFC3/UVIS provide sharper images with a more stable PSF. The pixel scale is 0.04 arcsec pixel^{-1}, yielding a FoV of 162 × 162 arcsec. The UVIS data were also resampled to match the spatial scale of the NIR AO data.

2.4 NIR detection and photometry

This section describes only the results from object detection and photometry in the NIR AO frames (the main data set of the thesis). HST data processing is reported in

Table 2.3: Observation log of the archival HST ACS/WFC imaging

Galaxy name	Obs.date	Dataset	Exp.time F435W, F814W
(1)	(2)	(3)	(4)
IRAS F17138−1017	2006-03-31	J9CV650*0	1260, 720
IC 883	2006-01-11	J9CV470*0	1290, 740
IC 694/NGC 3690†	2006-03-19	J9CV380*0	1425, 830
IRAS 12116−5615	2005-09-07	J9CV400*0	1425, 830
ESO 550−IG025	2006-08-31	J9CV130*0	1260, 720
IRAS 19115−2124	2006-03-20	J9CV720*0	1260, 720
IRAS 18293−3413	2006-04-01	J9CV690*0	1290, 740
MCG−02-01-052	2006-05-23	J9CV020*0	1260, 720
NGC 6240*	2006-02-11	J9CV630*0	1260, 720
IRAS 01173+1405	2005-08-26	J9CV060*0	840, 720
MCG+08-11-002*	2005-09-05	J9CV190*0	1350, 780
IRAS F06076−2139*	2005-11-14	J9CV200*0	1260, 720
IRAS F10173+0828*	2005-12-01	J9CV330*0	1260, 720
IRAS F01364−1042*	2005-12-05	J9CV070*0	1260, 720

Notes. Column 1: galaxy name; Column 2: date of observation; Column 3: name of the data set in HLA; Column 4: total exposure times of F435W and F814W filters, respectively. The dagger sign after IC694/NGC 3690 indicates that the merging system has WFC3/UVIS data available (see text). Any galaxy marked by * has a low detection of SSC candidates in the NIR AO images as listed in Table 2.4.

Chapter 5.

2.4.1 Source extraction

1. Unsharp-masking is a commonly adopted method to make point-source detection more uniform in varying background conditions: a blurred version of the original image is produced with a gaussian filter and it will then be subtracted from the parent image to achieve high-pass filtering. The function `UNSHARP_MASK` from `IDL` was used to output the unsharp-masked versions of the images. Figure 2.4 compares two sets of the NIR frames before (top panel) and after (lower panel) an unsharp-masking in the case of NGC 1819 and IRAS 13052−5711. We stress, however, that original science images remain the input files to perform photometry and further analyses.

2. We then ran `SExtractor v2.5.0` (Bertin & Arnouts 1996) on the unsharp-masked versions of the images with a configuration optimized to minimise the detection of spurious sources in the field and to include faint and also extended objects in the output catalogues. A threshold of 1.5σ above the background root-mean-square (RMS) noise combined with a minimum number of $\sim 8-10$ adjacent pixels above threshold were eventually chosen.

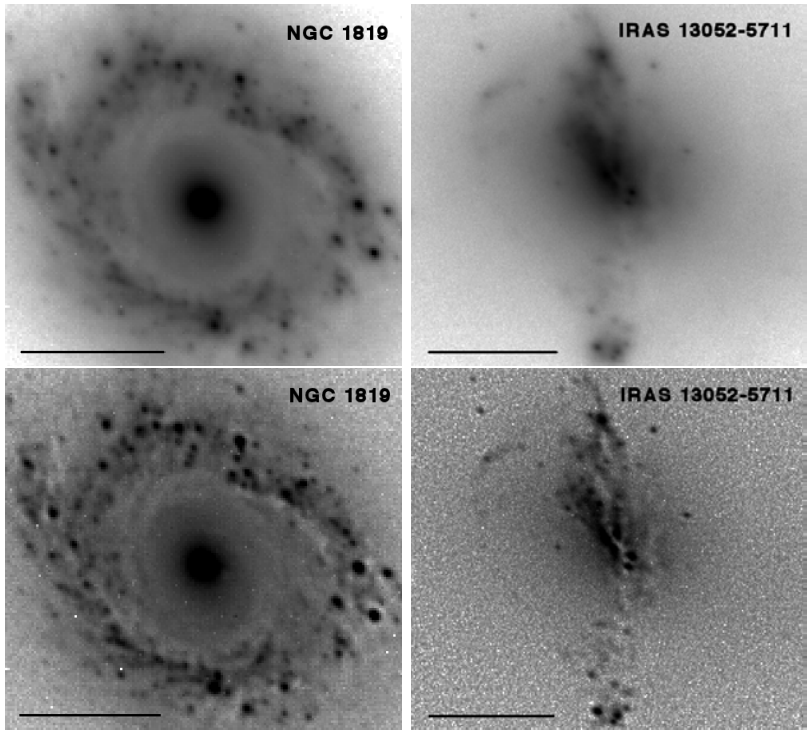

Figure 2.4: The NACO fields of NGC 1819 (left) and IRAS 13052−571 (right) before (upper panel) and after (lower panel) unsharp-masking. The horizontal line represents a scale of 1 kpc.

3. Any detections in the noisy edges of the frames were excluded from the output catalogues since they are most likely spurious objects recorded because of the low detection threshold in a high noise area.

2.4.2 Photometry

PSF-fitting photometry is usually adopted to estimate the integrated fluxes of extracted objects within a crowded field. However, in this case, it is wiser to perform aperture photometry on the combined images because the data were taken with AO systems resulting in a variable PSF accross the field. To output simultaneously the PFWHM[d] and the instrumental magnitude of the objects, we ran the task `IRAF/RADPROF` with 2, 3, and 5 pixel aperture radii (0.08, 0.09, and 0.1 arcsec) and with sky annuli from 3−4.5, 5−7, and 7−10 pixels for the NACO/S54, NACO/S27, and ALTAIR/NIRI data, respectively. A small sky annulus is necessary for a good sky sampling in the strongly varying background in between larger-scale features of the galaxy. On the other hand, small apertures are also needed to minimize blending effects, especially in the case of the crowded SSC populations detected in the NACO data (e.g. IRAS 18293-3413, NGC 3110, IC 2522).

[d] PFWHM is the fitted FWHM of the radial profile.

To derive the apparent magnitude m_{app} in a Vega-based system, we applied the following equation to the total *counts* of the sources:

$$m_{app} = m_0^{Vega} - 2.5 \times log\,(counts) + 2.5 \times log\,(\tau_{exp}) - a_c \tag{2.1}$$

where m_0^{Vega} is the Vega-based zero-point magnitude of a frame with 1 *sec* exposure time, τ_{exp} the exposure time per pointing in seconds, and a_c the aperture correction in magnitudes. Note that m_0^{Vega} is already corrected for atmospheric extinction and foreground galactic extinction effect was not considered since it is insignificant in the NIR regime. Values of a_c and m_0 of each target are listed in Table 2.2. More details on photometric calibrations are as follows:

- **Constant vs PSF AO-distance dependent aperture correction:** Because of the small aperture sizes, aperture corrections are essential. In addition, the PSF shape is expected to vary across the frames as a function of distance from the AO-reference star. To account for these data characteristics, sufficiently bright and isolated stars in the field were first used to derive curves-of-growth until 1 arcsec aperture radius. Aperture corrections a_c were then extracted for the small $\approx$ 0.1 arcsec aperture radii. Next, we calculated a *concentration index* C[e], defined as the difference between magnitudes measured in two different aperture radii for these stars; $C = m_{0.5px} - m_{1.5px}$, $C = m_{1px} - m_{3px}$ and $C = m_{3px} - m_{5px}$ for VLT/NaCo/S54, VLT/NaCo/S27 and Gemini/NIRI data, respectively. Any C value now corresponds to a certain a_c and if there were enough isolated point sources in the field, the following expression was derived:

  $$a_c = a_1 \times C + b_1 \tag{2.2}$$

  Such a correlation is shown in the left panel of Figure 2.5 in the case of IRAS 13052−5711. Moreover, C depends systematically on the location of the star in the field (i.e. distance from the AO-reference): we experimented using the concentration index of each detected object in the frame to determine its aperture correction but it turned out, however, that the background within the galaxies is too complex to derive accurate enough C-values for fainter objects. Therefore, we rather interpolated a new value of C of each detected object using the following equation (see right panel of Figure 2.5):

  $$C^{new} = a_2 \times Dist + b_2 \tag{2.3}$$

  where $Dist$ is the distance of the object to the AO-star. We then determined a_c by using the new value C^{new} in Equation 2.2. Note that this intermediate method implicitly assumes that we are detecting point-sources, which is supported by our simulations described in Section 3.3 and Section 3.5.1. It is more accurate than

[e] The concentration index C is a parameter used to get a rough estimate of the object PSF size.

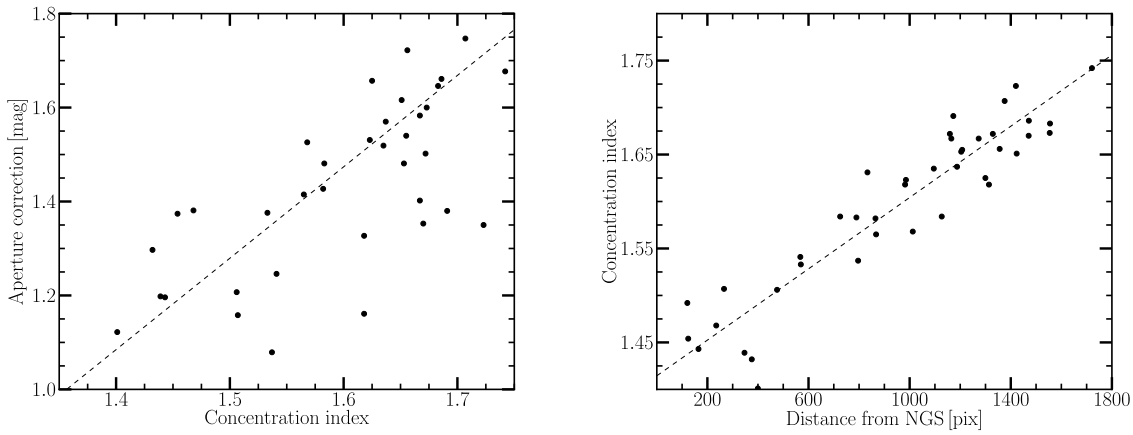

Figure 2.5: Two complementary relations adopted to get more accurate values of aperture corrections in the NIR AO field of IRAS 13052−5711. The dashed lines in both plots represent the linear fits between two parameters. *Left:* Aperture correction of bright and isolated star plotted against its concentration index. The relation exists because a_c is PSF-dependent: the closer a source is to the AO-star the better will be its PSF, hence a smaller value of C. *Right:* Concentration index of the bright star plotted against its distance with respect to the NGS of the AO system. Such correlation also indicates that aperture correction is AO-reference star distance-dependent.

using concentration index values determined from faint objects in crowded and complex fields to determine aperture corrections. The VLT/NaCo data a_c values applied to individual objects range from 0.92 to 1.93 mag. None of these methods worked for NGC 3110 and NGC 3508 because of the non-existence of isolated bright sources in the small field, hence we used an average value of 1.21 for them. For the Gemini/NIRI data, we found that no such position dependent correction was necessary – the artificial LGS is located in the centre of the field within the targeted galaxies and candidate SSCs. Therefore, an averaged constant $a_c \sim 1.23$ mag correction was applied to all Gemini frames. We estimate the uncertainty of the aperture correction in a single frame to be typically ~ 0.15.

- **Magnitude zero-point:** Gemini/NIRI photometric zero-points were referred to the 2MASS K_S-band point source catalogue using 2MASS common stars (bright but non-saturated) in the FoV. For the NACO data, photometric zero-points were either retrieved from the ESO/NACO official website, if recorded, or estimated by correlating with 2MASS K_S point-sources present in the field as previously adopted with the Gemini/NIRI data. Fields where both methods were available were used to check consistency of photometry: the values of the zero-points only differ by $\sigma \sim 0.15$. In cases where the 2MASS point-sources were outside the small FoV of the science images, NOTCam K-band images and complementary NACO data with larger FoV (P.089.D-0847) were used as intermediate images to estimate the zero-points for the Gemini/NIRI and VLT/NaCo data, respectively. For NGC 1819,

NGC 3110, NGC 4575, MCG+08-11-002, and CGCG 049−057, there were no stars available in the existing data, and thus comparing the total integrated flux of the galaxy with the corresponding 2MASS total magnitude was the only option to estimate their zero-points. For NGC 1204, NGC 3508, IRAS 06164+0311, and IRAS 01173+1405, the galaxy occupied the whole field and no stars were available, thus none of the above methods worked and an average value was used. The zero-point uncertainty of $\sigma \sim 0.1$ mag (for targets hosting 2MASS point-sources) is included in resulting SSC photometry. Note that our magnitude system is the same as that of the 2MASS Vega-based K_S filter.

We estimate the absolute calibration to be accurate to $\sim$0.3 mag including 2MASS catalogue photometric uncertainties and all systematic errors in our photometry and aperture corrections.

2.5 The NIR SSC candidates

Separating an SSC candidate from Galactic foreground stars and HII regions is challenging when working with a single filter and dealing with a sample of distant targets where both Galactic stars and extragalactic star clusters have similar PSF sizes. In our case, the following steps were carried out to generate the final K-band SSC catalogue for each target:

1. First, only objects falling on detectable optical or NIR emission from the galaxy within the frames were considered. The ones at the edges of frames, in case the host galaxy extended there, were already removed prior to aperture photometry (see Section 2.4.1). Since we had already tuned the detection parameters to avoid false detections in the inner regions of the frames, we assumed that the catalogue is mainly composed of real sources after this process.

2. Foreground contamination by Milky Way stars is a real possibility, especially for targets with low galactic latitude ($b < |20°|$, see Table 2.1). Therefore, we estimated the potential effect of contamination in our data by using the Besançon model (Robin et al. 2003). The model predicts galaxies such as IRAS 19115−2124 ($b = -14.4^o$), IRAS 18293−3413 ($b = -11.3^o$) and IRAS 17578−0400 ($b = 9.4^o$) to have the largest numbers of K-band foreground stars, but even in these fields the maximum number of contaminating stars at $K \sim 16$ mag, corresponding to the brightest magnitude bins of SSCs, is at most at $\sim 10\,\%$ of the total SSC candidate numbers within a typical $20'' \times 20''$area of the galaxies. At fainter magnitudes star counts are at negligible levels, as are counts at all magnitude bins for the rest of the fields, according to the models. However, as a consistency check, we also counted obvious point sources in the sky areas *outside* of the galaxies in our fields, derived

their surface densities in magnitude bins, and compared them with object numbers within the host galaxy area. As an example, we show the results for the low galactic latitude IRAS 18293-3413 case in the left panel of Figure 2.6.

The star counts are consistent with the Besançon model predictions at bright magnitudes, but tend to be somewhat larger at $K > 16$: it could, for example, be that there are some real SSCs well outside of the projected galaxy area of our targets, or, alternatively, that the models do not probe Milky Way stars at faint enough levels. Though there might be some contamination at the brightest $K \sim 15 - 16$ bins, these would be "obvious stars" that are removed in the final selection step (5) below, and at fainter levels the star numbers still are not large enough to make any significant difference to the ultimately derived LFs of SSCs. We hence conclude that foreground contamination is not significant for our results, and no further star vs. SSC separation was attempted for our data set.

3. Photometric uncertainties were taken into account fairly conservatively to have a robust list of SSC candidates: only detected objects having errors $\sigma_m \leq 0.35$ mag were considered for further selection process. The cutoff value was equal to 0.25 mag in the already published work Randriamanakoto et al. (2013b); the reason we pushed it a bit higher in uncertainties with the new NACO data was to include brighter SSC candidates with higher magnitude errors due to complex varying background they

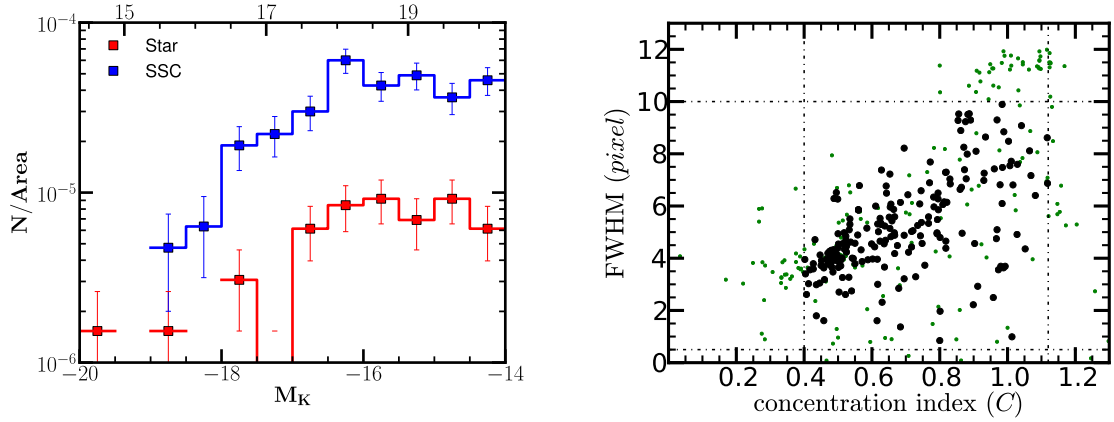

Figure 2.6: *Left:* raw surface densities of detected objects within the galaxy area of IRAS 18293−3413 are shown by the blue upper line, while those objects found outside the galaxy area in the same frame are shown by the red lower line. As the latter are likely foreground stars, it is seen that stellar foreground contamination is insignificant even in this low galactic latitude case. The apparent K-band magnitude scale is shown at the top. *Right:* an example of the SSC candidate selection for the same field of IRAS 18293−3413. A FHWM versus concentration index C plot of the detected objects from `SExtractor` with the cutoffs for candidate selection indicated. The limits are checked with simulations to be consistent with the parameter space of extracted *intrinsic* point sources (~ 4.5 pix in this case) in the fields. The filled black points represent the final SSC candidates, whereas all detected objects are shown in green.

reside in. We note that excluding less secure detections can in principle bias eventual LF values since fainter objects will not be included. However, we checked that if we had selected $\sigma_m < 1.0$ mag sources instead, we would have had only between 6 to 14 % more SSC candidates, and the final LF shapes and slope changes would have been negligible within the completeness levels considered in the analysis.

4. We then excluded objects that appeared to be extended in order to remove any background galaxies and resolved HII regions, while also taking into account the fact that fainter point sources will appear to have a broader FWHM when extracted on top of the varying diffuse background of the galaxy. For a candidate to be included in our photometric catalogue, we imposed cuts on the values of the concentration index C as well as cuts on the FWHM. A small value of the index ($C \sim 0.4$) typically results from a high S/N point source, such as a foreground star, whereas larger values ($C \sim 1.3$ and above) indicate potentially extended objects. Since the value of C is less accurate for fainter sources, we also used PFWHM of the detection, as measured by the task `RADPROF` in pixels to make the selections more robust. Plots such as that shown in the right panel of Figure 2.6, were generated for each target field to help us distinguish between truly fuzzy objects and unresolved SSC candidates at different S/N levels.

   The cutoff values were decided with the help of simulations and also by-eye checks interactively, for consistency. As part of Monte Carlo simulations to define completeness corrections (described in Section 3.3) simulated intrinsic point source PSFs were extracted from the real data frames, and the cutoffs in FWHM and C were adjusted to encompass the *output parameter space* of the detections of the *input point sources* in the simulations made on the real data frames. The differing AO corrections on different data sets introduce some variation, but in most of the cases SSC candidate selection included objects having values of $0.4 \lesssim C \lesssim 1.3$ and $1 \lesssim FWHM \lesssim 6$ pixels. In the case of IRAS F16516−0948 and IRAS 12116−5615, all objects are generally elongated, due to a degraded AO-correction; however, since all analysis was done using PSFs constructed from bright stars on the frame itself, this does not bias the selection in any way. Note that retaining only unresolved point sources at this step does not exclude the possibility of blending discrete SSCs smaller than our resolution PSF into one detected SSC candidate – this is discussed in more detail in Section 3.5.1.

5. Finally, we made a visual inspection of the images with the selected candidates in order to remove the nucleus/nuclei of the galaxy from the final catalogue and to remove several obvious very bright stars which happened to fall on top of the galaxies.

After applying the selection criteria detailed above, we obtained the final photometric catalogue for each target field. The total number of the SSC candidates per galaxy varies between $\sim 10 - 400$, and is listed in Table 2.4 along with the magnitude and other parameters of the most luminous SSC candidates.

Table 2.4: After imposing our selection criteria, the final number of SSC candidates for each target is given. We also tabulate some characteristics of the brightest star cluster in each galaxy.

Galaxy name	SFR ($M_\odot\,\mathrm{yr}^{-1}$)	$N(\sigma \leqslant \sigma_m)$	$N(M_K \leqslant$-14.5)	$M_K^{brightest}$ (mag)	Dist (kpc)
(1)	(2)	(3)	(4)	(5)	6
		VLT/NACO DATA			
ESO 440-IG058-N	7†	27	17	-15.89 ± 0.21	6.59
IC 2522	7	303	5	-15.52 ± 0.13	1.22
MCG -02-01-052	7†	41	20	-17.21 ± 0.13	1.47
NGC 3620	9	27	6	-15.65 ± 0.18	0.38
ESO 428-G023	10	98	2	-15.51 ± 0.15	0.32
ESO 221-IG008	10	421	19	-15.90 ± 0.13	1.37
IRAS 06164+0311	11	47	4	-16.06 ± 0.12	1.41
NGC 1134	12	130	26	-15.86 ± 0.12	0.87
ESO 491-G020	12†	55	14	-17.47 ± 0.19	0.15
NGC 4433	13	75	14	-16.39 ± 0.11	1.26
NGC 1204	13	2	2	-17.50 ± 0.21	0.28
NGC 3508	14	109	6	-16.42 ± 0.16	0.17
NGC 1819	14	139	67	-17.11 ± 0.11	1.19
MCG -02-33-098	15†	5	5	-15.69 ± 0.18	3.46
NGC 4575	16	48	2	-15.62 ± 0.12	3.52
NGC 6000	16	285	32	-16.36 ± 0.19	0.23
ESO 550-IG025-S	18†	5	4	-16.76 ± 0.18	1.10
ESO 319-G022	19	25	4	-15.98 ± 0.11	1.29
MCG +02-02-003	20	46	6	-16.19 ± 0.11	3.24
ESO 264-G057	20	147	29	-17.15 ± 0.21	0.32
ESO 320-G030	21	49	49	-15.70 ± 0.16	0.97
ESO 221-IG010	25	50	26	-17.19 ± 0.13	0.17
ESO 267-G030	26	94	54	-16.86 ± 0.14	0.79
ESO 550-IG025-N	30†	59	39	-17.07 ± 0.12	2.76
ESO 440-IG058-S	32†	2	2	-17.79 ± 0.11	1.42
NGC 3110	35	283	91	-17.74 ± 0.13	0.88
IRAS 13052-5711	37	31	18	-16.51 ± 0.15	0.24
ESO 264-G036	38	85	85	-17.98 ± 0.19	0.47
IRAS 12116-5615	66	45	39	-18.42 ± 0.14	0.42
IRAS F06076-2139	66	4	4	-19.61 ± 0.17	0.16
IRAS 01173+1405	73	26	26	-18.00 ± 0.20	0.53
IRAS F01364-1042	98	3	3	-20.01 ± 0.12	0.18
IRAS 18293-3413	110	204	157	-18.23 ± 0.15	0.61
NGC 6240	120	16	12	-18.79 ± 0.18	0.31
IRAS 19115-2124	126	56	56	-19.71 ± 0.15	2.38
		Gemini/NIRI DATA			
IRAS F16516-0948	30	41	38	-18.10 ± 0.15	2.78
CGCG 049-057	32	10	9	-17.14 ± 0.15	0.27
IRAS F17578-0400	38	45	19	-17.56 ± 0.15	1.69
MCG +08-11-002	44	12	7	-17.52 ± 0.15	0.61
IRAS F17138-1017	45	60	58	-18.48 ± 0.15	0.81
NGC 3690	52†	81	34	-17.88 ± 0.15	0.16
IC 694	77†	81	26	-16.95 ± 0.15	0.47
IC 883	80	29	28	-18.38 ± 0.15	1.09

Notes. The targets are ordered with increasing SFR. Column 1: galaxy name; Column 2: SFR based on the galaxy IR luminosity, any value marked by † is estimated by using the method described in Section 4.2; Columns 3 & 4: number of SSCs for $\sigma \leqslant \sigma_m$ and $M_K \leqslant -14.5$ mag, respectively; Column 5: K_S-band absolute magnitude of the brightest cluster; Column 6: physical distance of the cluster in kpc with respect to the galactic center.

References

Armus, L., et al. 2009, PASP, 121, 559

Bertin, E., & Arnouts, S. 1996, A&AS, 117, 393

Kankare, E., et al. 2008, ApJL, 689, L97

Kankare, E., et al. 2012, ApJL, 744, L19

Mattila, S., et al. 2007, ApJL, 659, L9

Miralles-Caballero, D., Colina, L., Arribas, S., & Duc, P.-A. 2011, AJ, 142, 79

Robin, A. C., et al. 2003, A&A, 409, 523

Sanders, D. B., et al. 2003, AJ, 126, 1607

Sirianni, et al. 2005 PASP, 117, 1049

Randriamanakoto, Z., Escala, A., Väisänen, P., et al. 2013a, ApJL, 775, L38

Randriamanakoto, Z., Väisänen, P., Ryder, S., et al. 2013b, MNRAS, 431, 554

Väisänen, P., et al. 2008, MNRAS, 384, 886

Väisänen, P., et al. 2009, arXiv:0908.3495

Väisänen, P., et al. 2014, arXiv:1402.2357

Veilleux, S., Kim, D.-C., & Sanders, D. B. 2002, ApJS, 143, 315

Chapter 3

The K-band SSC LFs

Overview

This Chapter reports the SSC luminosity functions of the sample. It also describes the analytical methods used to quantify the effects of blending in the slopes of the SSC power-law distributions. A pilot study of this work was published in Randriamanakoto et al. (2013b) and the results from the overall sample will be covered in Randriamanakoto et al., in prep.

3.1 Introduction

The luminosity function (LF) of SSCs, which is suggested to be a reflection of the cluster initial mass function, is a common tool used to help understand their formation and evolution (e.g. Whitmore et al. 1999; Gieles et al. 2006a). The main specific objectives of this work are to derive K-band LFs of the massive star clusters for the first time for a significant sample of host galaxies and to evaluate the effect of blending on the LFs, i.e. the effect of multiple star clusters detected as one complex cluster on the LFs.

In our study we are expanding the SFR range of SSC host galaxies to include starburst galaxies and LIRGs from their lowest limit to ULIRGs, and including galaxies in various stages of interactions, from isolated and paired galaxies, to interacting, merging and merger remnant stages with a sample of dozens of targets (Väisänen et al. 2012). Furthermore, most of the studies thus far have been done in the optical, making extinction effects potentially difficult in the notoriously complex dusty environments of gas-rich interactions. Crucially, the use of NIR AO has great potential in opening a new angle into the SSC populations in that they probe deeper into the dusty birth regions of the SSCs and the very obscured regions in the inner parts of the galaxies. There is also an interesting time-window at ages of ~ 10 Myr when SSCs are expected to be very

NIR-luminous due to their high-mass stars entering the RSG phase. There are very few NIR studies of SSCs compared with the optical ones; previous NIR studies include Lai et al. (1999), Mengel et al. (2005), Alonso-Herrero et al. (2006), Pollack et al. (2007), Väisänen et al. (2008), and Adamo et al. (2010). This work uses, to our knowledge, the largest NIR sample that would allow us to compare more accurately the power-law index α from normal spirals with those from active star-forming galaxies. In particular, results from a recent work by Whitmore et al. (2014) on SSC LFs in 20 normal spirals will be compared with the characteristics seen in the present NIR sample. The Chapter is organized as follows: Section 3.2 describes the data and the cluster analysis, while the completeness correction is presented in Section 3.3. The NIR CLFs of the sample are presented in Section 3.4 and interpreted in Section 3.5; finally, we summarize our findings in Section 3.6.

3.2 The NIR sample

As already highlighted in Chapter 2, AO-assisted Gemini/NIRI and VLT/NaCo instruments were used to image 42 starburst and luminous infrared galaxies in the $K(2.2\,\mu\mathrm{m})$-band. Apart from being laboratories for core-collapse SN searches (Ryder et al. 2014), another primary goal of the ongoing SUNBIRD survey is to detect tens to hundreds of young massive star clusters in these targets (see Table 2.4). Refer to Section 2.3 for a comprehensive description of the NIR observations and data reduction. More information on the source extraction, photometry, and the catalogue of the K-selected SSC candidates are presented in Section 2.4 and Section 2.5.

Due to the very small number of SSC candidates in NGC 1204, NGC 6240, MCG −02-33-098, IRAS F10173+0828, IRAS F01364−1042, IRAS F06076−2139, MCG +08-11-002, and CGCG 049−057, we did not attempt to construct their SSC LFs. The same treatment applies to the northern components of ESO 440-IG048 and ESO 550-IG025. The star cluster criteria brings the number of target galaxies down to 34 for further analyses.

3.3 Completeness correction

The raw SSC catalogues obtained in Section 2.5 are affected by incompleteness due to photometric detection limits of the observations, the varying and complicated background resulting from the different diffuse components of the host galaxies, and potential crowding of sources. To correct the data for incompleteness bias we ran Monte Carlo (MC) completeness simulations with each science image. A PSF model for each target field was first created. NGC 3110, NGC 1134, NGC 4575, NGC 6000, IRAS 01173+1405, and ESO 440−IG058 did not have isolated stars in their fields, and for them we used a representative PSF model from other fields having a similar distance from their tip-tilt

reference star, and hence similar AO-correction based from the reference star. Using the model, we created artificial stars with `IRAF/DAOPHOT` which were used in the simulation.

The main idea of the simulation is to record how many of the input objects, added randomly to the science images, are detected by `SExtractor` at a given magnitude range with exactly the same manner and configuration parameters as the ones chosen for optimal detection in Section 2.4.1, as well as with identical selection criteria to be included as an SSC candidate. These simulations were also used to define the latter selection criteria since the input source is by definition a point-source making the process iterative. We also checked the simulations for varying PSF sizes and verified that PSFs in a realistic range of point source sizes in the target fields do not result in corrections which would change any of the main results concerning the shapes of the eventual LFs. Details of this analysis are presented in Section 3.3.1.

The simulation ran from 13 to 23 K-mag in steps of 0.5 mag. We generated 1000 random positions of artificial star centroids. To minimize systematics, we used a new subset of random positions for each magnitude step. In addition we ran the simulation separately at different background levels of the field as illustrated in Figure 3.1. These levels were determined by defining three (four in cases of IC 2522, NGC 3110, IRAS 19115−2124 and IRAS 18293−3413, which had larger dynamical range between the background and point source brightness) approximately equal ranges in the pixel values of a smoothed background map in a logarithmic scale, ranging from an essentially empty sky to the galaxy core, but excluding the nucleus itself. Figure 3.2, left panel, shows as an example the resulting completeness curves for the case of IRAS 18293−3413. Completeness fractions of the new NIR dataset are also plotted in Figure 3.3. Those of the Gemini/NIRI and old VLT/NaCo data are ready to be used. In cases of ESO 319−G022, NGC 4575, and MCG−02-01-05, the completeness curves from the different regions are quite similar which indicates that the gradient in the background level does not change much throughout the galactic field.

The simulations were also used to test the accuracy of the photometry for systematic effects. The right panel of Figure 3.2 shows the difference of input and output magnitudes of the detected sources. In the fainter bins, magnitudes cannot be measured reliably anymore due to very variable background, crowding, and inaccurate aperture corrections. However, the Δmag values become larger than our typical overall photometric uncertainties only at or below the completeness limits relevant to each galaxy and background region used for subsequent LF analysis, and any corrections for these possible systematics are not attempted.

Each individual SSC photometric data point was then corrected for the incompleteness bias with respect to its observed magnitude as well as its location in the complex background field, as long as its magnitude value was above the 50 % completeness limit of the region in question. Representative completeness values are shown in Table 3.1. After this correction, we are ready to construct the luminosity functions of the SSCs in each target field.

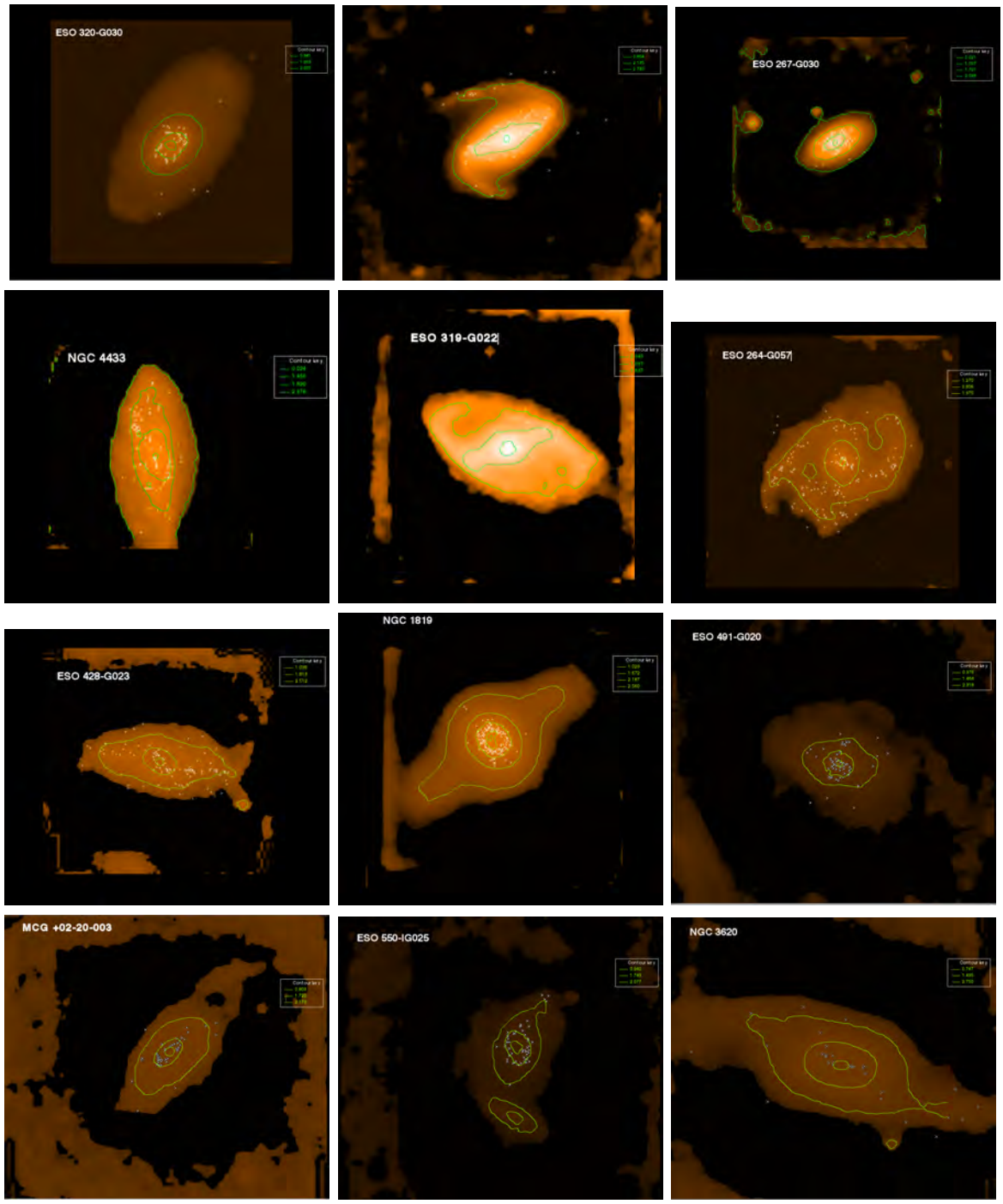

Figure 3.1: Background maps of the new VLT/NaCo targets in a logarithmic scale overlaid with the SSC spatial distribution (marked as white cross) and the contour levels (in green) defining the different simulated regions. Up is North and left is East. The field is normally divided into three equally-spaced regions while excluding the nucleus but if the variation of the galactic field is too complex, four regions are defined instead.

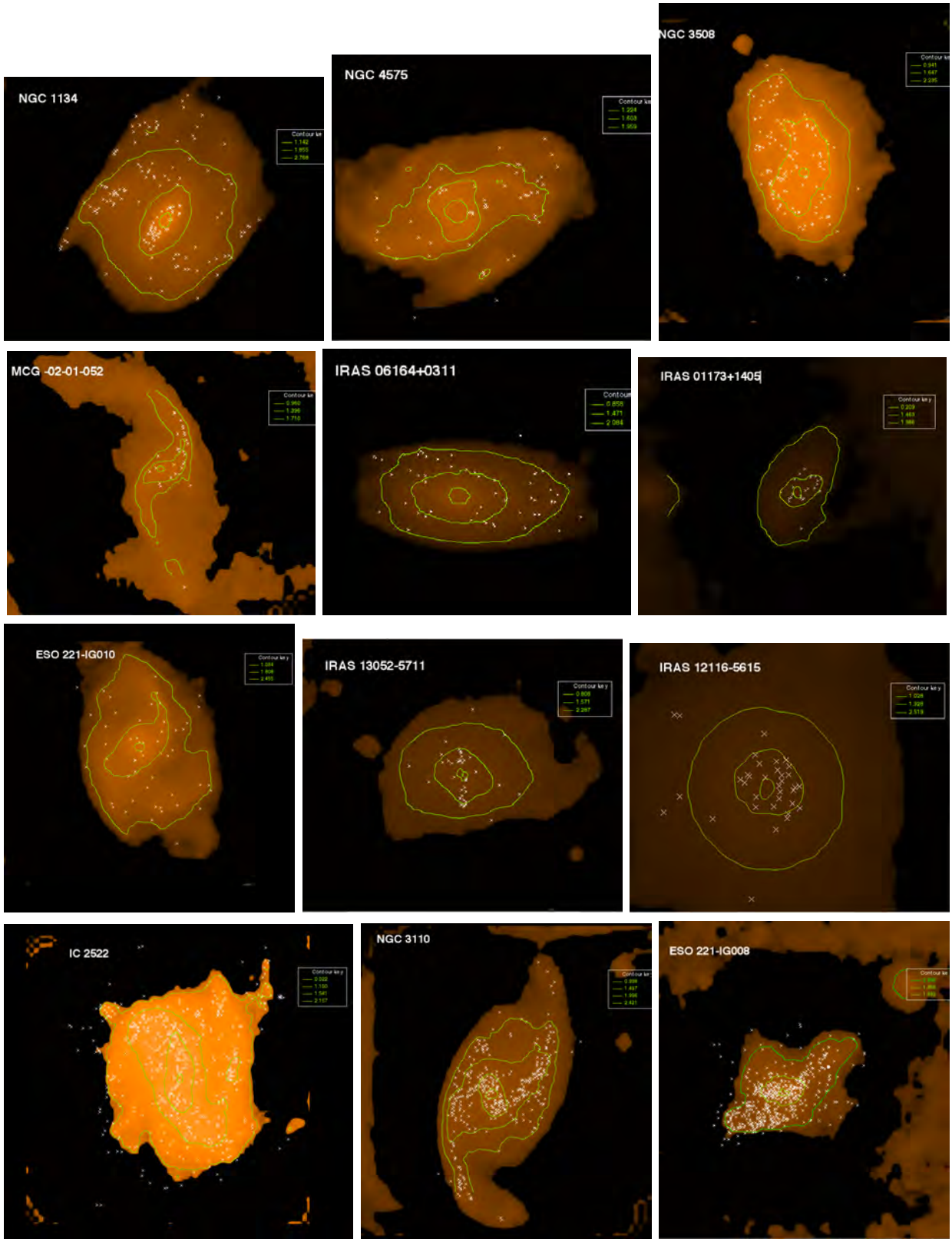

Figure 3.1: – Continued

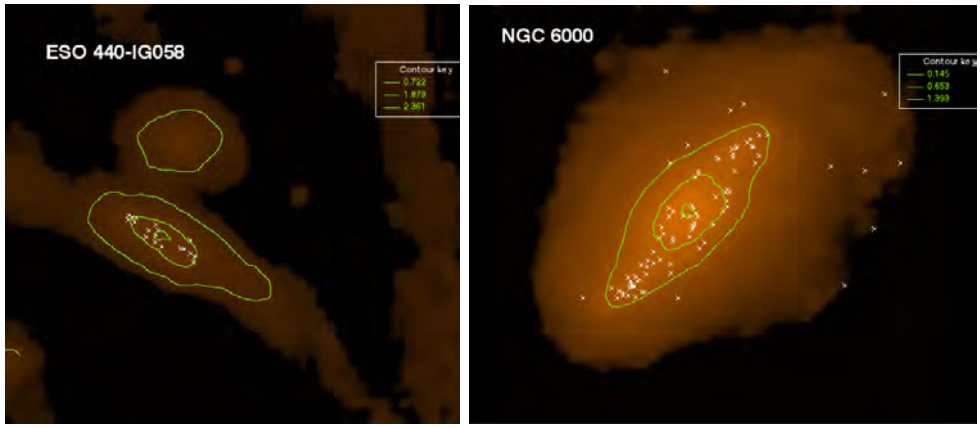

Figure 3.1: – Continued

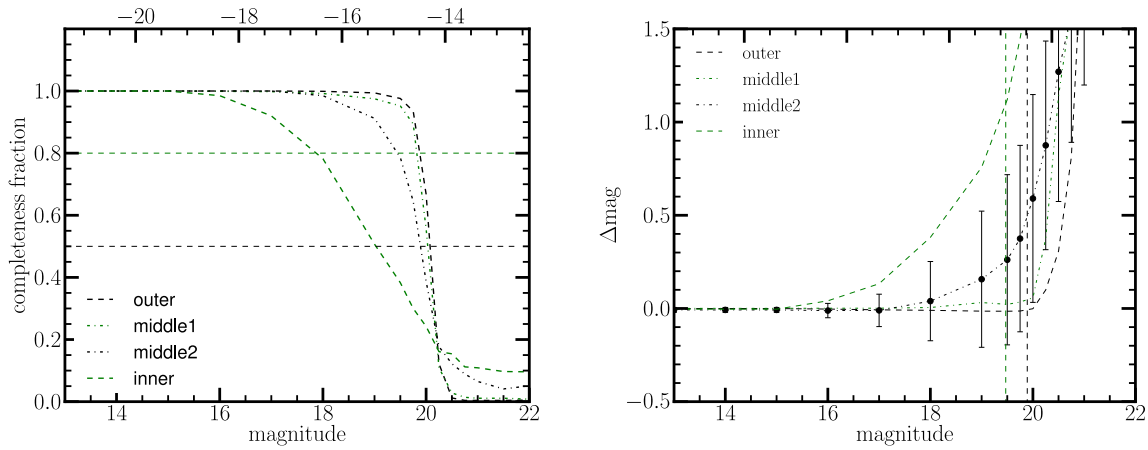

Figure 3.2: The results of Monte Carlo completeness simulations for IRAS 18293−3413 within regions of different background levels. The green dashed line corresponds to the innermost region with the highest background. *Left panel:* The fraction of simulated point sources recovered as SSC candidates in the simulation as a function of apparent and absolute K magnitude in the lower and upper axes, respectively. The 50 % and 80 % completeness limits corresponding to the "middle2" region are a reasonable approximation of overall completeness limits of point sources in IRAS 18293−3413; they are shown as the horizontal dashed lines. *Right panel:* The y-axis plots the input minus output magnitude as a function of the input magnitude in the same MC simulation. The error bars reflect the scatter of this difference in the simulation and is plotted for one curve only for clarity. The vertical dashed lines show the two completeness levels determined above from the "middle2" region.

3.3.1 Varying PSF size

The following analysis aims to investigate the effect of the PSF size on the simulated completeness fraction and, consequently, the shape of the corrected luminosity function and the value of power-law index α. The choice of the PSF model is essential because the

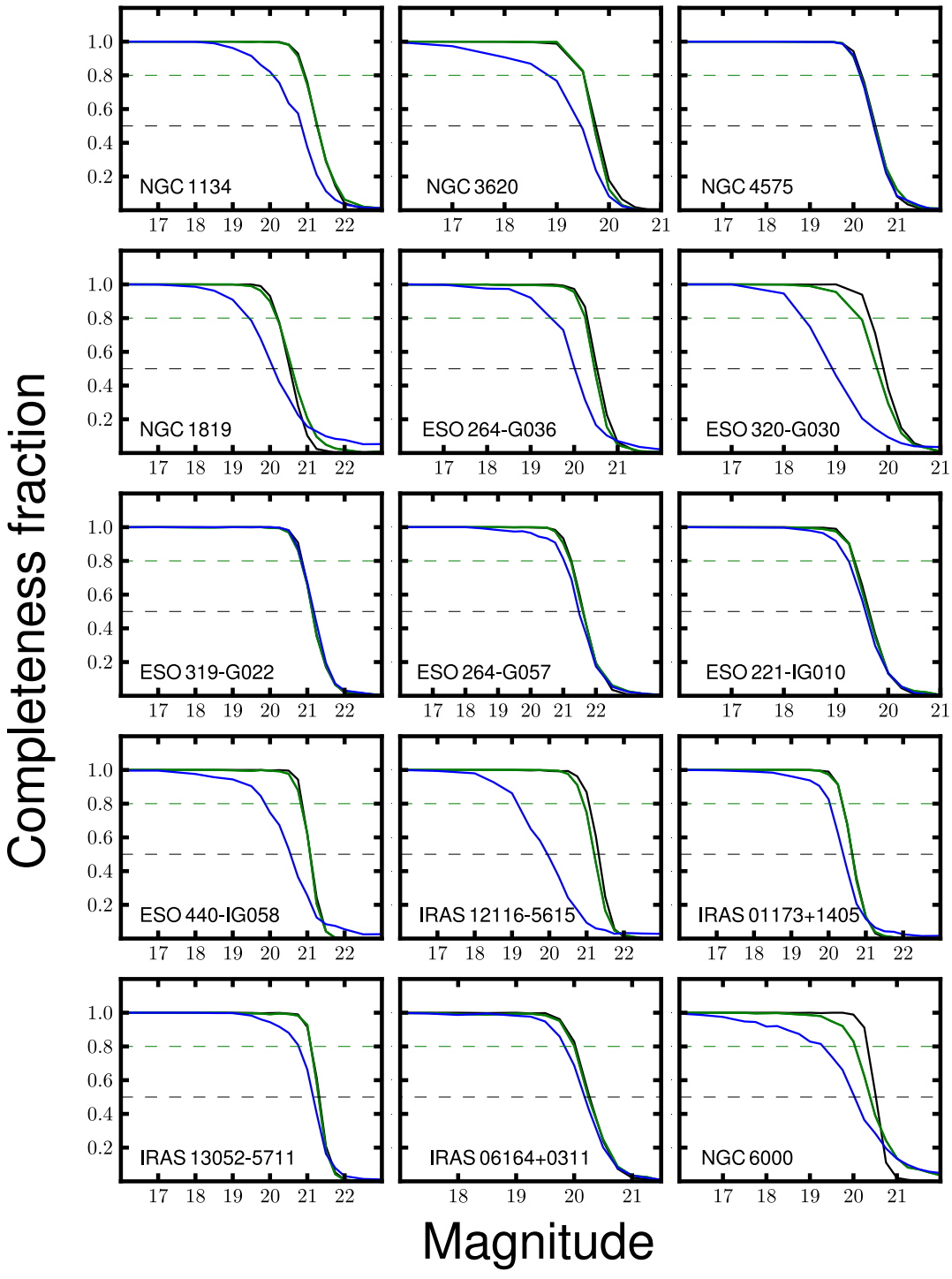

Figure 3.3: The results of Monte Carlo completeness simulations for the new VLT/NACO targets within regions of different background levels. Completeness fractions of the Gemini/NIRI and old VLT/NaCo data are ready to be used. The blue, green, and black solid lines correspond to the innermost, middle, and outer regions. The 50 % and 80 % completeness limits of the "middle" regions are shown as the horizontal dashed lines.

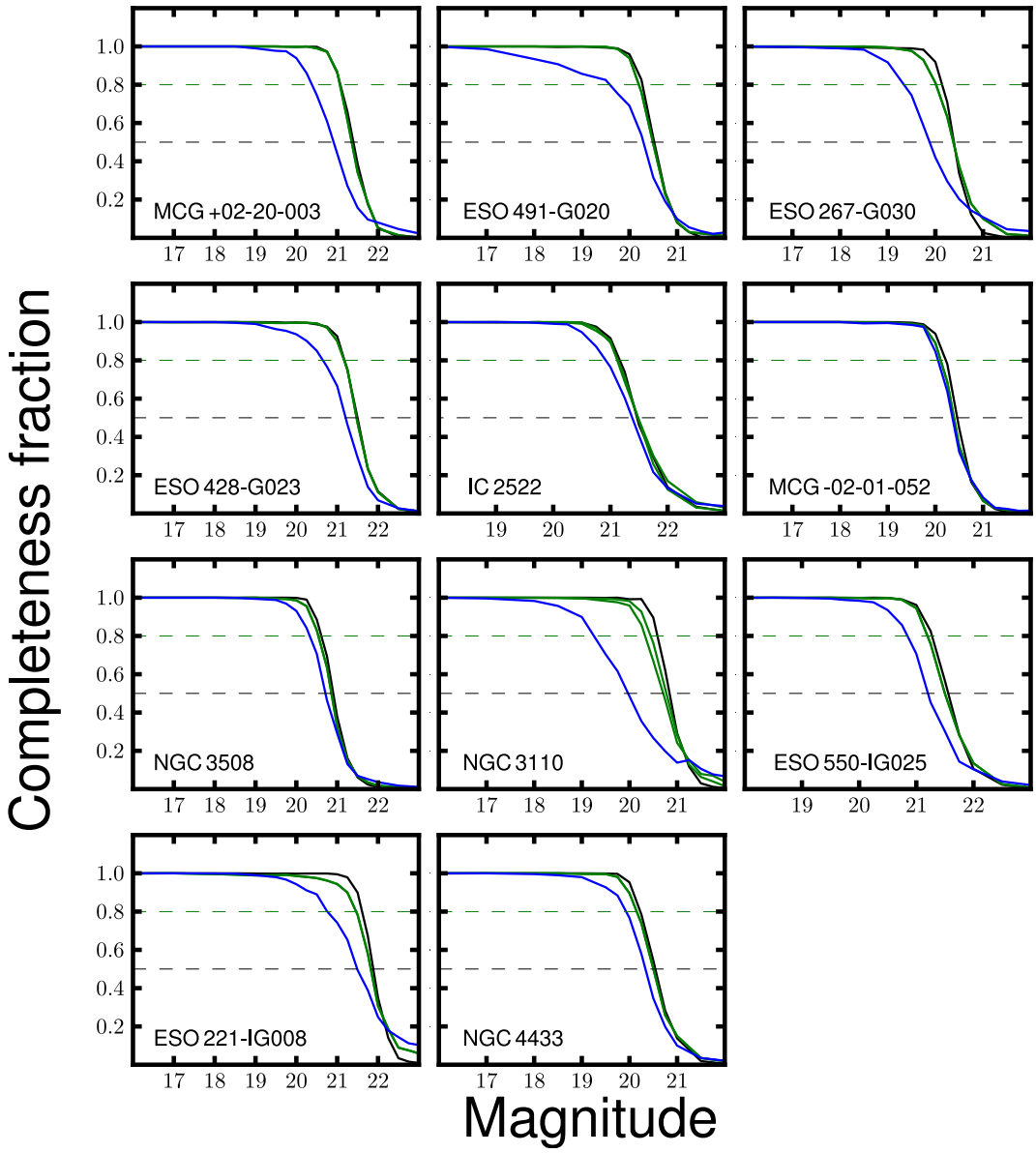

Figure 3.3: – Continued

Table 3.1: The 50 % and 80 % completeness levels

Name	50 % comp.limit		80 % comp.limit	
	App mag	Abs mag	App mag	Abs mag
(1)	(2)		(3)	
ESO 320−G030	19.8	−13.6	19.5	−13.9
ESO 264−G036	20.5	−14.3	20.2	−14.6
ESO 267−G030	20.4	−14.2	20.0	−14.5
NGC 4433	20.5	−12.8	20.2	−13.2
ESO 319−G022	21.1	−13.2	20.8	−13.5
ESO 264−G057	21.6	−12.8	21.2	−13.2
ESO 428−G023	21.5	−11.8	21.2	−12.0
NGC 1819	20.6	−13.4	20.2	−13.8
IC 2522	21.5	−11.8	21.1	−12.2
ESO 491−G020	20.5	−12.7	20.2	−13.0
MCG +02-20-003	21.4	−12.8	20.7	−13.5
ESO 550−IG025	21.3	−14.4	20.9	−14.8
NGC 3620	19.7	−12.3	19.5	−12.5
ESO 221−IG008	21.8	−11.5	21.5	−11.9
NGC 3110	20.9	−13.5	20.6	−13.8
NGC 1134	21.3	−12.1	20.9	−12.4
NGC 4575	20.5	−12.8	20.2	−13.1
NGC 3508	20.8	−13.1	20.4	−13.5
MCG −02-01-052	20.4	−14.8	20.1	−15.1
IRAS 06164+0311	20.3	−12.8	20.0	−13.1
IRAS 01173+1405	20.4	−15.1	20.0	−15.5
ESO 221−IG010	19.6	−13.7	19.4	−13.9
IRAS 13052−5711	21.3	−13.5	21.1	−13.7
IRAS 12116−5615	20.0	−15.4	19.2	−16.2
ESO 440−IG058	21.1	−14.0	20.8	−14.2
NGC 6000	20.4	−12.1	20.0	−12.5
IC 694	19.7	−13.6	19.4	−13.9
NGC 3690	19.4	−13.9	19.0	−14.3
IRAS F17578−0400	20.4	−13.4	19.9	−13.9
IRAS F17138−1017	20.0	−14.3	19.7	−14.6
IRAS 18293−3413	19.9	−14.5	19.5	−14.9
IRAS F16516−0948	19.9	−14.9	19.6	−15.3
IC 883	20.2	−14.8	20.0	−15.1
IRAS 19115−2124	20.1	−16.5	19.8	−16.8

Notes. Column 1: galaxy name; Columns 2 & 3: apparent and absolute magnitudes of the 50 % and 80 % completeness levels, respectively. These values correspond to the middle background region where more than ≈ 50 % of the data points are below the contour level limiting that region. The brighter absolute magnitude completeness limits for IRAS 19115−2124 are due to its much larger distance compared to the other targets.

data set was imaged using AO systems. As a result the detected objects are expected to have different PSF sizes across the field: the closer an object is to the natural guide star, the smaller its `FWHM` will be (refer to Table 3.2). Therefore, we performed a varying PSF test using the point sources in ESO 264−G036. Three bright and isolated stars scattered all over the field, which do not have the same distance with respect to the NGS, were selected to generate different PSFs. The left panel of Figure 3.4 depicts the radial profiles of the sharp (green and blue) and the extended (red) PSF models.

Table 3.2: Properties of the PSF stars and the resulting LF slopes

PSF/FWHM (pixels) (1)	$m_{\rm PSF}$ (mag) (2)	AO−dist (arcsec) (3)	comp.lims (abs mag) (4)	Δcomp-lim (80- 50)% (5)	α (6)
3.32	12.44	24.27	−14.75, −14.39	−0.36	1.87 ±0.09
4.04	13.66	36.37	−14.83, −14.50	−0.33	1.92 ±0.09
5.20	11.15	50.96	−15.23, −14.87	−0.36	1.89 ±0.10

Notes. Columns 1 & 2: `FWHM` and apparent magnitude of the star in the field of ESO 264−G036; Column 3: its distance to the AO-NGS; Column 4: absolute magnitudes of the 50 % and 80 % completeness levels, respectively; Column 5: difference between the two completeness limits; Column 6: value of the power-law index from the fitted LF.

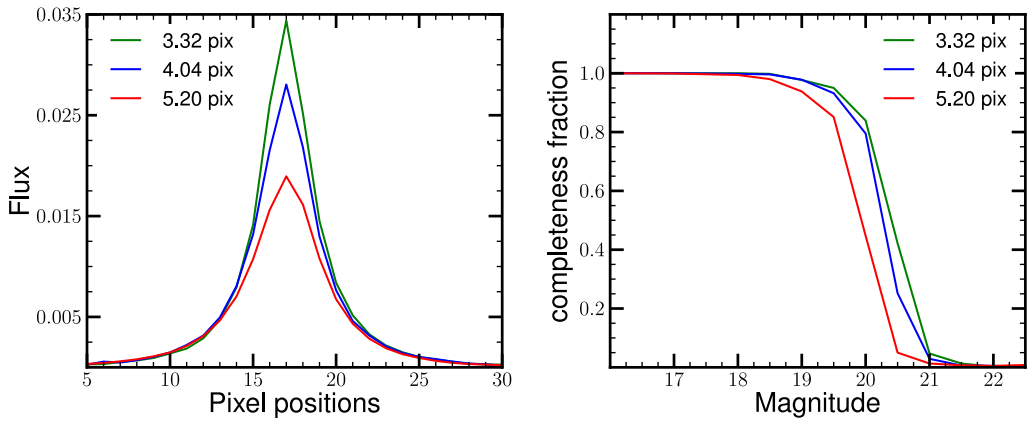

Figure 3.4: Comparison of the scaled PSF radial profiles (*left panel*) and the resulting Monte Carlo completeness simulations for ESO 264−G036 (*right panel*) by using three different PSF models. The values of the `PSF/FWHM` are 3.32, 4.04, and 5.20 pixels, which correspond to the PSFs labelled in green, blue, and red solid lines, respectively. Wider PSFs result in lower completeness fractions at fainter magnitudes.

Based on the representative models, we then generated three sets of completeness fractions at each magnitude level after running the MC simulation as described in Section 3.3. The right panel of Figure 3.4 indicates that the trends of the completeness curves are consistent with the varying size of the input models: simulations performed with a wider PSF size (red curve) record lower detection as we go towards fainter magnitudes compared to the ones that use smaller PSF sizes (the other curves). Choosing an optimal model is therefore important for a good representation of the star cluster PSFs and to derive accurate completeness fractions. *However, by how much would the different fractions change the shape of the corrected LF and the value of the power-law slope?*

If we fit the corrected LFs until their respective 80 % completeness levels (as listed in Table 3.2), we get power-law indices close to $\alpha \approx 1.88 \pm 0.09$. More details on how

to construct, correct and fit the LF are given in Section 3.4. As for the shapes of the LFs shown in Figure 3.5, there are no significant changes apart from the second-last magnitude bin of the LF in the last panel; it was corrected by using completeness fractions generated from a wider PSF. Note, however, that this particular bin is already below the 80 % completeness limit derived using the wide PSF, and would not enter our analysis. The change in the shape of the LF, and the value of α, as a function of *a realistic range* of PSF sizes are therefore negligible. The results from the test show that the location of the selected PSF stars, either close or distant from the NGS, does not bias further analysis. Essentially, choosing a wider PSF for the completeness simulation would make the depth reached by the measured LF smaller, but would not affect the slope at brighter magnitudes. Using a single PSF model is therefore a fair approximation to generate the simulated completeness fractions throughout the field.

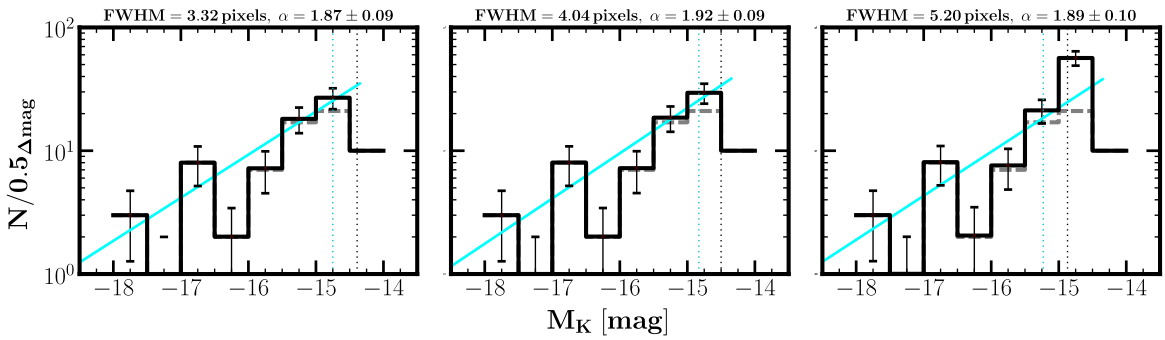

Figure 3.5: K-band SSC LFs of ESO 264−G036 corrected by different completeness fractions. The black solid line is the incompleteness-corrected LF while the dashed grey line is the original one. The single power-law fit of the data points is represented by the cyan solid line. The vertical lines mark the 50 % (grey) and the 80 % (cyan) completeness levels.

3.4 Constructing the K-band SSC LFs

Once the SSC candidates have been selected for each target, we can construct a binned LF and then fit a function to its shape. LFs are constructed as a function of absolute M_K magnitude; the distance modulus $m - M$ of the observed sample listed in Table 2.1 was used in the conversion. Completeness corrections were applied to the counts of SSC candidates as a function of observed magnitude and background region of the detections, as discussed earlier. Figure 3.6 shows all the observed LFs of our targets; both raw and completeness-corrected counts are shown.

After this, we fit a power-law of the form $N(L)dL \sim L^{-\alpha}dL$ in log-log space to the LF shape. The fitted data points are weighted using their respective Poisson-noise uncertainties $\sqrt{N}$. In a mag-logN plot, a linear fit is expressed as follows:

$$logN(M_K) = \beta\, M_K + const \tag{3.1}$$

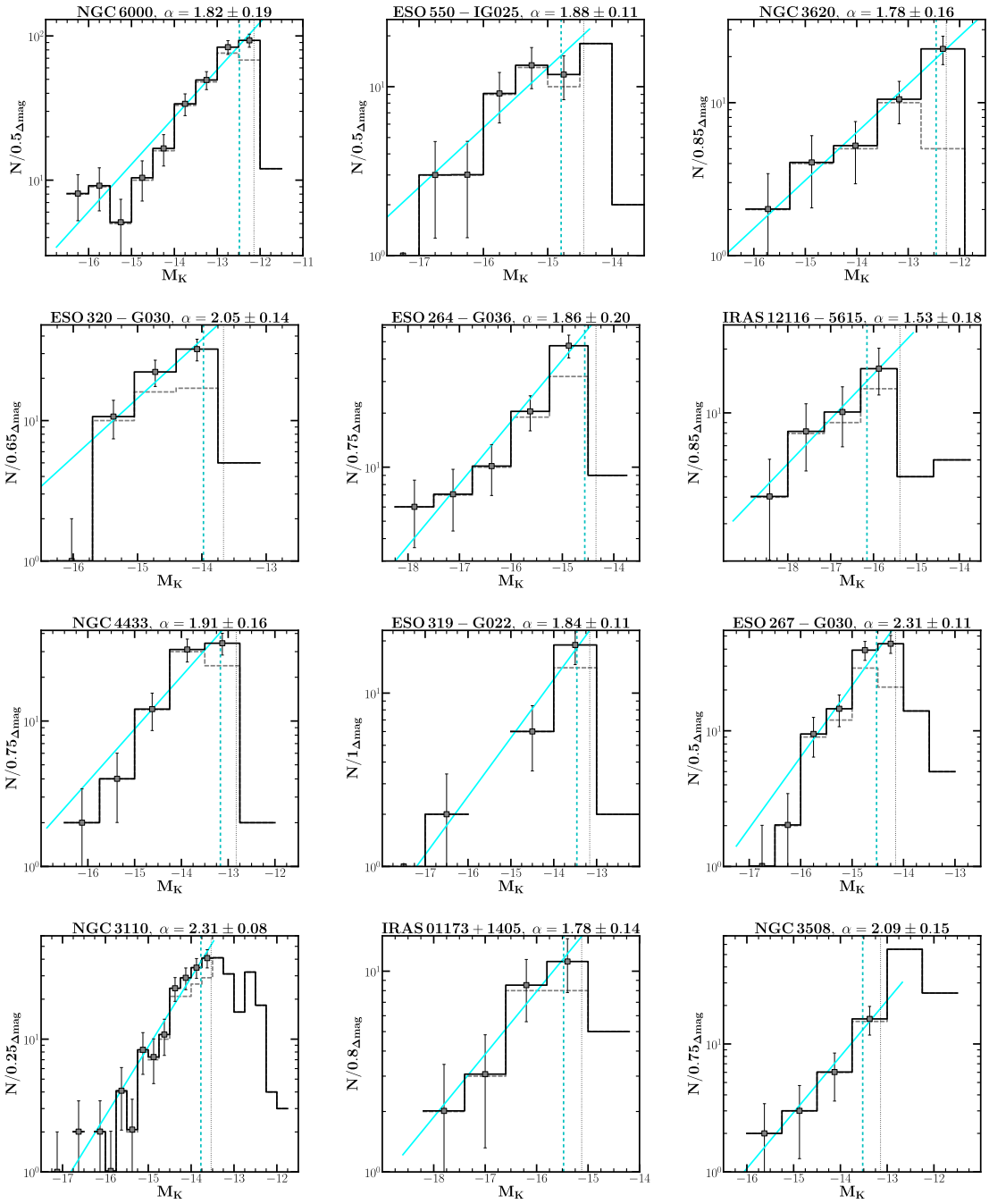

Figure 3.6: K-band LFs of the sample using a constant bin size. The black solid line is the incompleteness-corrected LF while the dashed grey line is the original one. The single power-law fit of the data points is represented by the cyan solid line. In the case of IRAS 18293−3413, the grey solid one and the dashed blue line result from broken power-law fits, and the curved green line is a Schechter function fit. The vertical lines mark the 50 % (grey) and the 80 % (cyan) completeness levels. The y-axes scales are not the same, because the number of SSC candidates differs from one target to another, making the optimal constant bin size different in each case.

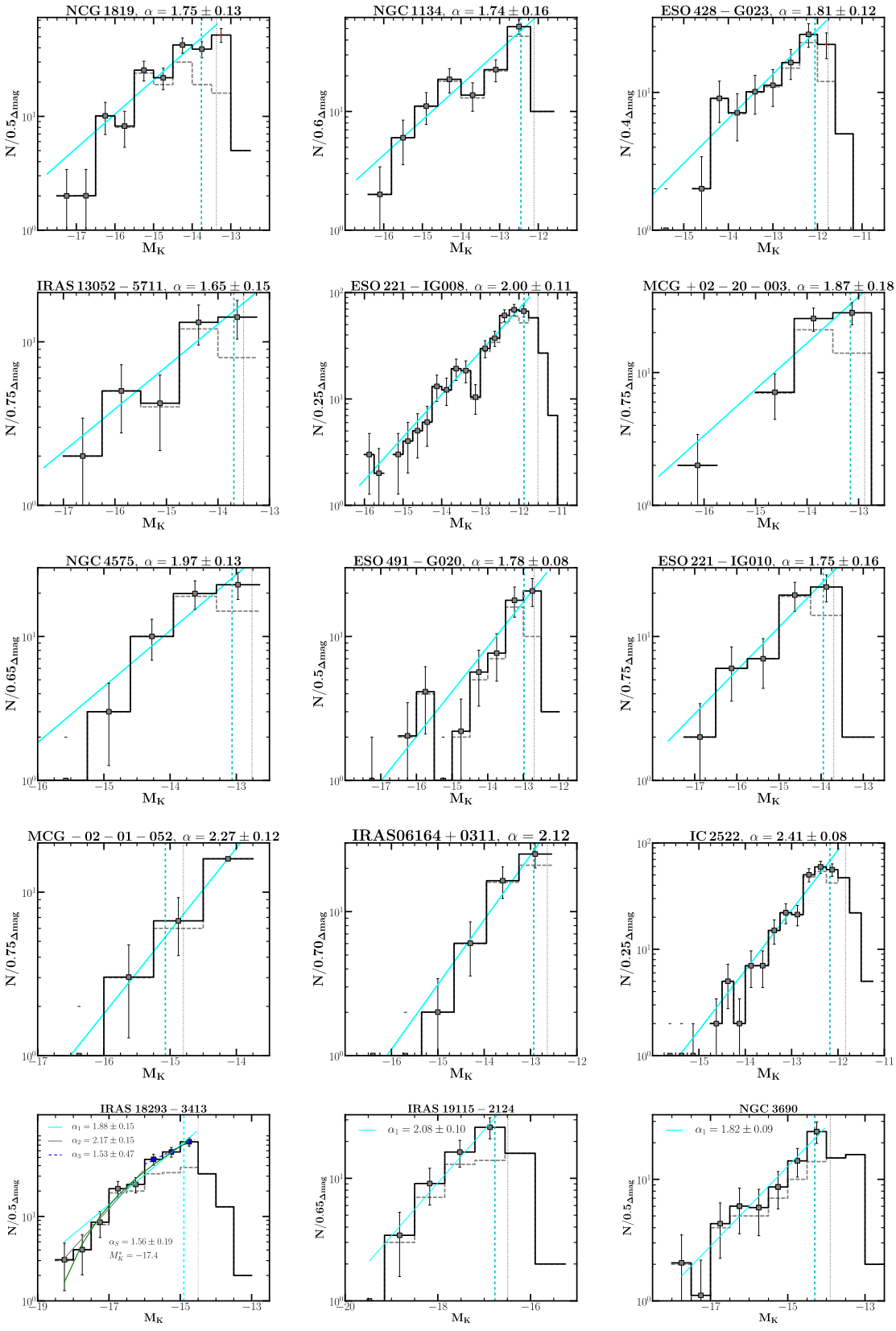

Figure 3.6: – Continued

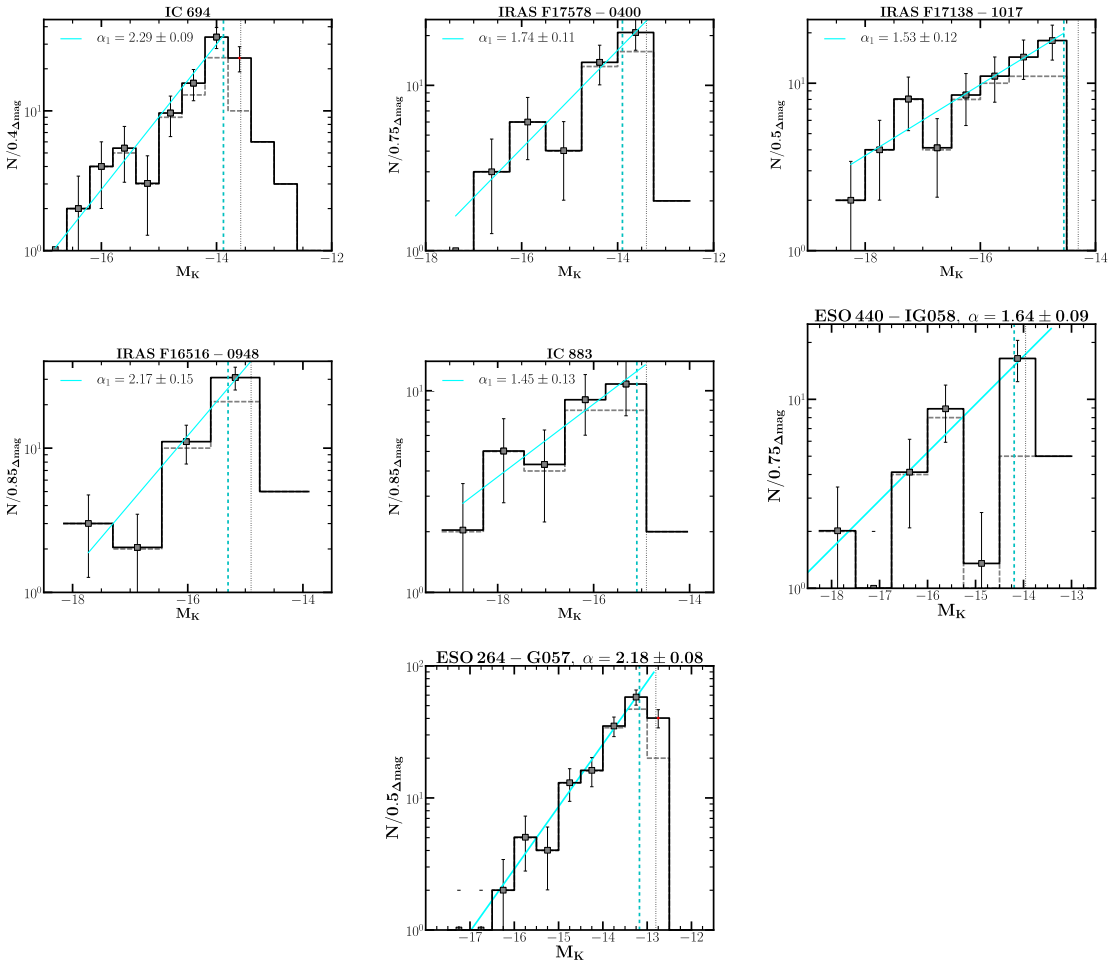

Figure 3.6: – Continued

where the relation between the power-law index α (see Equation 1.4) and the linear slope β is (Elmegreen & Efremov 1997):

$$\alpha = 2.5\beta + 1 \tag{3.2}$$

3.4.1 Single power-law fits

As a first step we fitted the SSC candidate LF distributions with a single power-law shape using a constant bin size. Since the targets do not have the same number of SSC candidates, each galaxy has its own constant bin size to balance having statistically enough sources per bin while trying to maximise the number of bins overall.

The LF bins were fitted from the brightest bin down to the last bin above the 80% completeness limit, the data points plotted as squares with error bars in Figure 3.6

indicating the bins which were fit. The resulting power-law indices estimated using Equation 3.2 are shown in Table 3.3 as α_1^{con}, and the fitted LFs are plotted in Figure 3.6 as the cyan line. The values of α_1^{con} range from 1.5 to 2.4. The median and the average over the sample are $\alpha_1^{con} = 1.86 \pm 0.24$ and $\alpha_1^{con} = 1.92 \pm 0.24$, respectively. If the most distant LIRG IRAS 19115−2124 is excluded the average is $\alpha_1^{con} = 1.91 \pm 0.25$. Fitting a single power-law function to the LF of the combined dataset down to a $M_K = -14.5$ mag (which includes the SSCs from all the targets in Figure 3.6 except for the most distant target IRAS 19115−2124 which has a significantly different magnitude), gives a slope $\alpha_1^{con} = 1.98$ with a formal uncertainty of 0.10 (Figure 3.7). This is consistent with the average slope.

To check whether a single power-law is a good approximation of the LF, we estimated the reduced chi-square statistic χ^2_{red} (the ratio of chi-square χ^2 and the degrees of freedom of the dataset) in each case. In most cases χ^2_{red} values (see Table 3.3) indicate that a single power-law appears to be a reasonable fit to the data. Note, however, that the value of χ^2_{red} may not reflect the goodness of the fit when dealing with a small number of data points.

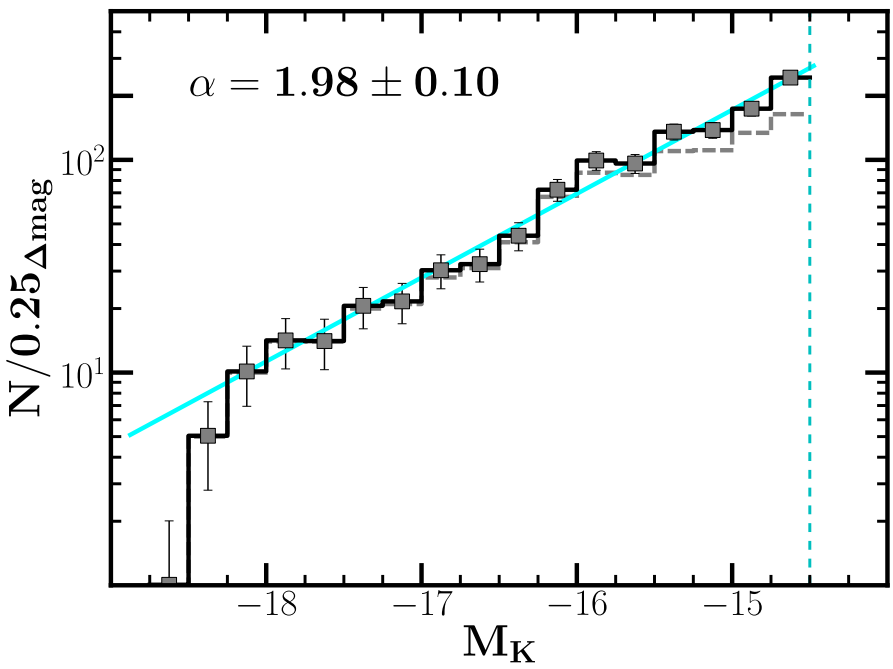

Figure 3.7: K-band SSC LF of the sample, except the data from IRAS 19115−2124. The single power-law fit of the data points is represented by the cyan solid line while the vertical line marks a completeness level of −14.5 mag.

Table 3.3: Power-law indices from weighted linear fitting of the LFs

Galaxy name (1)	α_1^{con} (2)	α_1^{var} (3)	χ^2_{red} (4)
ESO 320−G030	2.05 ± 0.14	2.11 ± 0.12	3.72, 3.32
ESO 264−G036	1.86 ± 0.20	1.90 ± 0.09	1.29, 3.38
ESO 267−G030	2.31 ± 0.11	2.28 ± 0.10	2.60, 3.73
NGC 4433	1.91 ± 0.16	2.24 ± 0.09	3.07, 0.51
ESO 319−G022	1.84 ± 0.11	1.85 ± 0.06	0.74, −
ESO 264−G057	2.18 ± 0.08	2.05 ± 0.09	0.40, 3.37
ESO 428−G023	1.81 ± 0.12	2.04 ± 0.10	0.92, 4.98
NGC 1819	1.75 ± 0.13	1.72 ± 0.10	2.62, 0.72
IC 2522	2.41 ± 0.08	2.25 ± 0.11	1.29, 12.71
ESO 491−G020	1.78 ± 0.08	1.74 ± 0.07	0.99, 0.93
MCG +02-20-003	1.87 ± 0.18	2.36 ± 0.10	4.81, −
ESO 550−IG025	1.88 ± 0.11	1.63 ± 0.09	1.17, 7.22
NGC 3620	1.78 ± 0.16	1.66 ± 0.09	0.24, 5.76
ESO 221−IG008	2.00 ± 0.11	2.02 ± 0.10	1.29, 10.42
NGC 3110	2.31 ± 0.08	2.19 ± 0.11	0.82, 4.42
NGC 1134	1.74 ± 0.16	1.78 ± 0.10	2.08, 5.70
NGC 4575	1.97 ± 0.13	2.10 ± 0.10	1.98, 2.66
NGC 3508	2.09 ± 0.15	1.88 ± 0.11	0.33, −
MCG −02-01-052	2.27 ± 0.12	2.39 ± 0.04	0.04, 0.90
IRAS 06164+0311	2.22 ± 0.10	1.88 ± 0.09	0.38, 2.84
IRAS 01173+1405	1.78 ± 0.14	1.90 ± 0.08	0.66, −
ESO 221−IG010	1.75 ± 0.16	1.75 ± 0.08	1.29, 0.54
IRAS 13052−5711	1.65 ± 0.15	1.63 ± 0.09	1.09, −
IRAS 12116−5615	1.53 ± 0.18	1.42 ± 0.09	0.30, −
ESO 440−IG058	1.64 ± 0.09	1.59 ± 0.05	2.47, 3.92
NGC 6000	1.82 ± 0.19	1.88 ± 0.09	1.96, 3.18
IC 694	2.29 ± 0.09	2.36 ± 0.10	0.85, 3.82
NGC 3690	1.82 ± 0.09	1.82 ± 0.10	0.43, 1.18
IRAS F17578−0400	1.74 ± 0.11	1.78 ± 0.07	0.82, 2.54
IRAS F17138−1017	1.53 ± 0.12	1.64 ± 0.08	0.58, 0.16
IRAS 18293−3413	1.88 ± 0.15	1.89 ± 0.09	1.49, 1.43
IRAS F16516−0948	2.17 ± 0.15	2.41 ± 0.07	2.17, 0.89
IC 883	1.45 ± 0.13	1.58 ± 0.07	0.47, 3.94
IRAS 19115−2124	2.08 ± 0.10	1.97 ± 0.08	0.61, 0.94
Average:	1.92 ± 0.24	1.93 ± 0.26	
Median:	1.86 ± 0.24	1.88 ± 0.26	

Notes. Column 1: galaxy name; Columns 2 & 3: the indices derived from binning with a constant and a variable bin width, respectively. The uncertainties in the slopes α are derived from the rules of propagation of errors in Equation 3.2, after calculating the uncertainty in β which is the weighted linear slope shown in Equation 3.1; Column 4: the reduced Chi Square values for the single power-law fits using the constant (left) and the variable (right) binning. Note that in the case of a small dataset, the value of χ^2_{red} may not be a good representation of the goodness of the fit, especially in the case of a variable binning.

3.4.2 Effect of binning on the LFs

The shape of the LF may be affected by sample binning: for example, Maíz Apellániz & Úbeda (2005) argued that the difference in the value of α can be as large as 0.3 for small datasets. To check for consistency of our results, we constructed the LFs using two different methods: first using a constant bin size as above, and secondly using a variable bin size and assigning an *equal number* of objects to each bin, as proposed by Maíz Apellániz & Úbeda (2005). Table 3.3 lists the values from both methods: α_1^{con} is the slope of the LF for a constant bin size, while α_1^{var} is the one that results from using a variable bin size. Though the values derived from the two binning methods are slightly different, they are consistent within the error estimates of each fit.

In addition, we ran systematic tests on the effect of using a particular size of the constant-size bin. The scatter of the fitted index values α with a wide range of bin sizes is of the same order, ~ 0.15, as the uncertainties of the slope fits presented in Table 3.3, and we conclude that bin size does not influence our final results. The characteristics of the resulting LF slopes will be discussed in Section 3.5.

3.4.3 Checking the accuracy of the completeness fractions

Data sets from the following targets were specifically chosen to test the robustness of the completeness corrections applied to LFs against the choice of the specific and separate "background regions" (Section 3.3) for this analysis. We selected four galaxies which each host at least ≈ 300 K-selected SSCs to have enough statistics: IC 2522, NGC 3110, NGC 6000, and ESO 221−IG008.

New sets of completeness fractions were then derived to construct the SSC LFs corrected from observational incompleteness. Therefore, we re-ran the MC simulations under the same conditions as in Section 3.3, except that two distinct regions were defined visually based on the galaxy morphology instead of the usual equally-spaced background levels (see Figure 3.8). The new completeness corrections were applied to the data before fitting the LFs to derive the values of the power-law indices α_1'. Figure 3.9 shows the eventual shapes of both raw and corrected LFs and Table 3.4 compares the values of the 50 % completeness limits and the slopes derived from the two different sets of fractions.

Although the completeness fractions differ in terms of the regions used during the MC simulation, the values of α_1 and α_1' and those of the completeness limits are quite similar within their uncertainties. The use of equally spaced background levels to define different regions of the galactic field in Section 3.3 is therefore a reasonable approach to derive the completeness fractions.

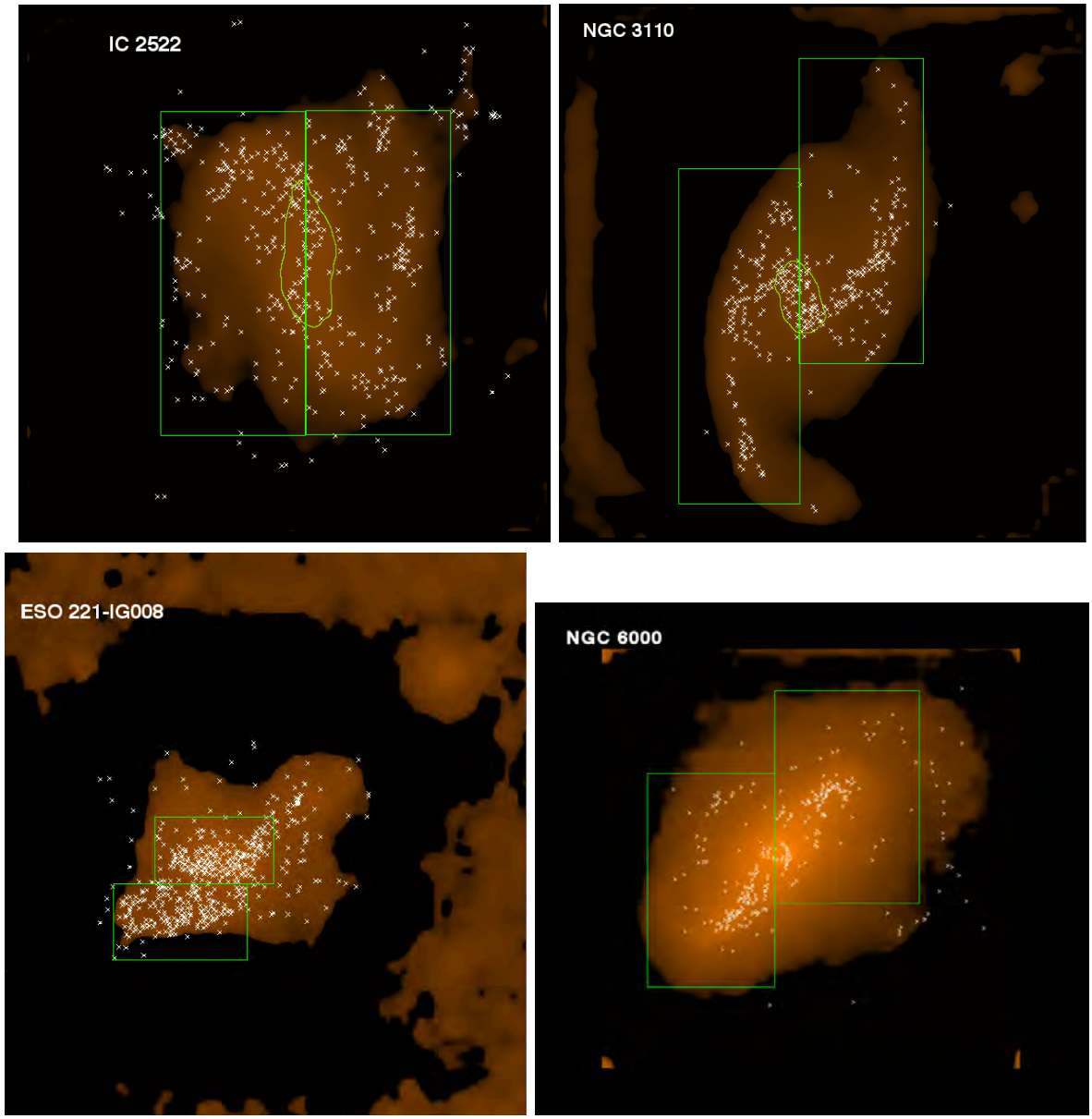

Figure 3.8: The NACO field of four targets with large SSC populations overlaid with their spatial distribution (marked as white crosses). The boxes define the distinct regions selected as a function of the galaxy morphology instead of the usual equally-spaced background levels as illustrated in Figure 3.1.

3.4.4 CLFs on sub-galactic scales

Ultimately, our goal is to study how SSCs in different physical regions are characterized. This is best studied when their masses and ages are known. However, it is interesting to see if distinct regions in galaxies have different LFs. At the same time, we check how any variation in the LFs over different physical regions of galaxies may affect the results

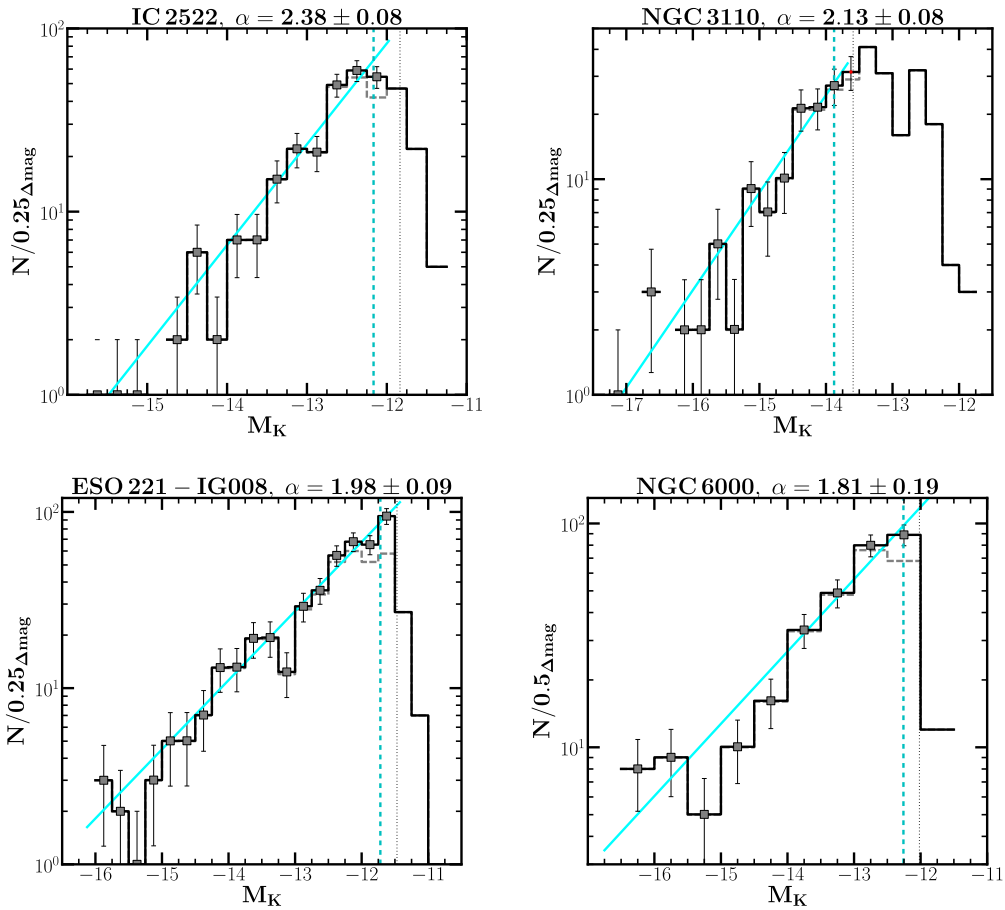

Figure 3.9: CLFs of four selected cluster-rich galaxies. There appear to be no differences in the derived power-law slopes compared to those of the same galaxies in Figure 3.6; labels the same as there. Different regions to estimate the completeness fractions were defined based from a visual inspection of the galaxy morphology.

of this Chapter where SSC LFs are summed over the whole host galaxies. We only check the cases of the most cluster-rich hosts, the same four galaxies as in the previous section. They also represent well the overall sample in term of morphological types: while IC 2522 and NGC 3110 present distinct spiral arms, NGC 6000 is a disk galaxy with a complex nuclear region. ESO 221−IG008, on the other hand, has a peculiar morphology with an irregular nuclear region (see Figure 3.10). *So, can a distinct sub-population of the SSCs be responsible for a power-law slope being steeper/shallower than the canonical value in this work?*

We divided the star cluster candidates into two distinct populations depending on their physical locations in the galaxy (nuclear regions vs. spiral arms or any other starburst regions of the galaxy). We then derived their corrected LFs and estimated the values of the slopes from the power-law fits (see Figure 3.11). While the bright end of the

Table 3.4: The power-law slope as a function of the completeness fractions

Galaxy name	Contour levels		Galaxy morphology	
	Comp.lim	α_1	Comp.lim	α_1'
(1)	(2)		(3)	
IC 2522	−11.8	2.41 ± 0.08	−12.2	2.38 ± 0.08
NGC 3110	−13.5	2.31 ± 0.08	−13.9	2.13 ± 0.08
ESO 221−IG008	−11.5	2.00 ± 0.11	−11.7	1.98 ± 0.09
NGC 6000	−12.1	1.82 ± 0.19	−12.3	1.81 ± 0.19

Notes. Column 1: galaxy name; Columns 2 & 3: the values of the 50 % completeness limit and the power-law slope using two different completeness fractions estimated based on regions defined with background contours levels and the galaxy morphology, respectively.

two LFs are slightly different in the case of IC 2522 and ESO 221−008, the values of the slopes remain consistent within the error estimates of the fit. However, for NGC 3110 and NGC 6000, CLFs of the nuclear regions have shallower slopes ($\alpha = 1.96 \pm 0.08$ and 1.44 ± 0.17, respectively) compared to those of the other regions ($\alpha = 2.35 \pm 0.09$ and 2.24 ± 0.10). Any differences of the LF slope in given physical locations of the host galaxy could be an imprint of an environment-dependent cluster formation, evolution or disruption mechanism. Such assumptions have to be confirmed in the future knowing the physical characteristics of the star cluster candidates, though the results seen here already hint at differences between strong SF regions (the nuclear regions) and those more quiescent.

3.4.5 IRAS 18293−3413: A good example of Schechter and broken power-law fits of the CLF

Figure 3.6 suggests that at least in the case of IRAS 18293−3413 a two-component power-law would be a better fit to the CLF. Hence we also fitted this LF of the target with a broken power-law with both slopes as free parameters, but the break, or bend point, M_{bend} fixed at a location chosen by eye. The form of the fit is expressed as follows in a mag-logN plot:

$$logN(M_K) \sim \begin{cases} \beta_3 M_K & \text{for} \quad M_K \geq M_{\rm bend} \\ \beta_2 M_K & \text{for} \quad M_K < M_{\rm bend} \end{cases} \tag{3.3}$$

where β_2 and β_3 are related, respectively, to the bright and faint slopes $\alpha_2 = 2.17 \pm 0.15$ and $\alpha_3 = 1.53 \pm 0.47$ of the CLF double power-law fits using Equation 3.2, also plotted and labelled in Figure 3.6 as α_2 and α_3.

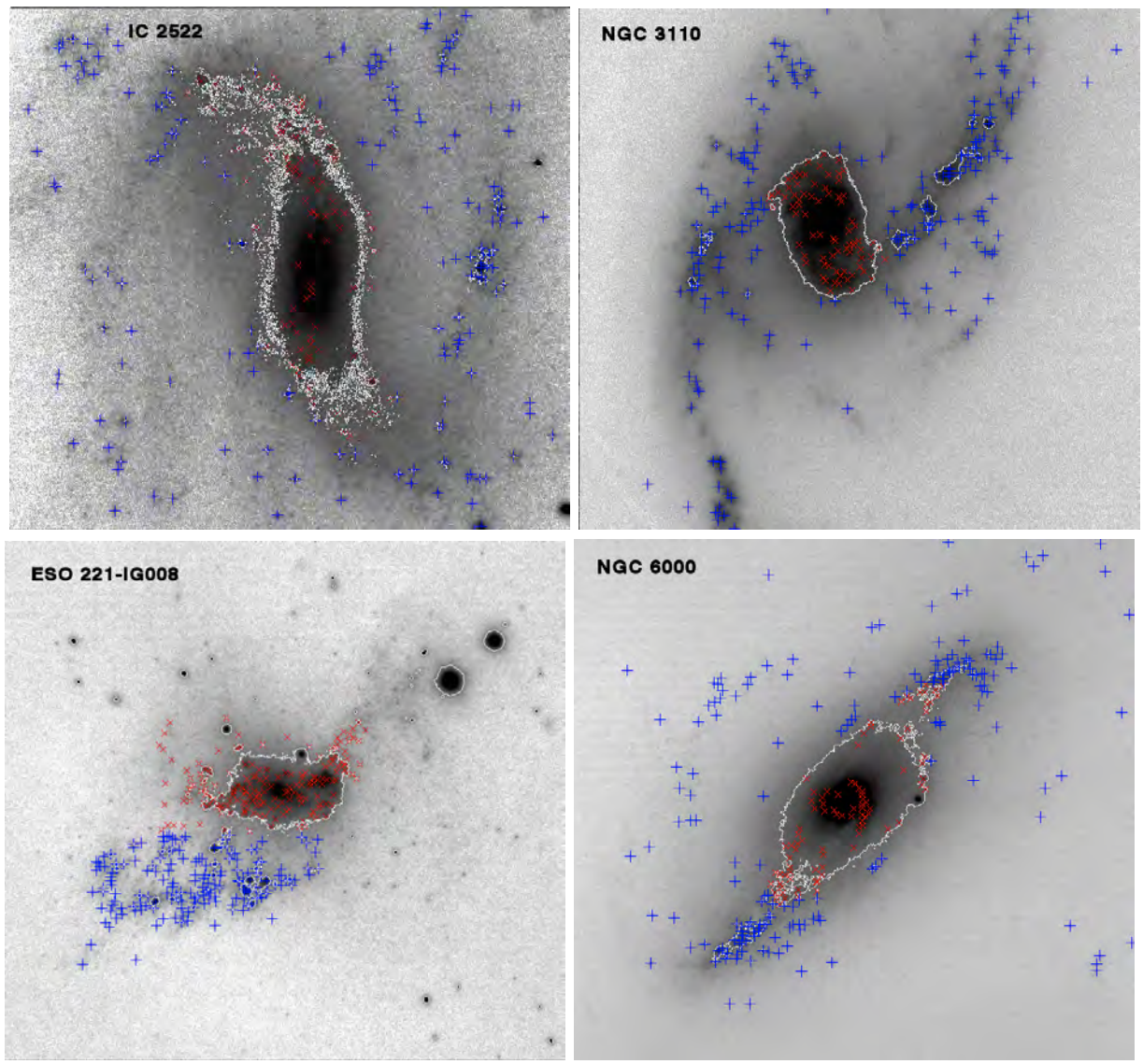

Figure 3.10: The NACO field of four targets with large SSC populations overlaid with their spatial distribution. The SSCs were split into two distinct groups based on their physical locations in the galactic field. Star clusters in the nuclear regions are labelled as red crosses, and the rest in blue.

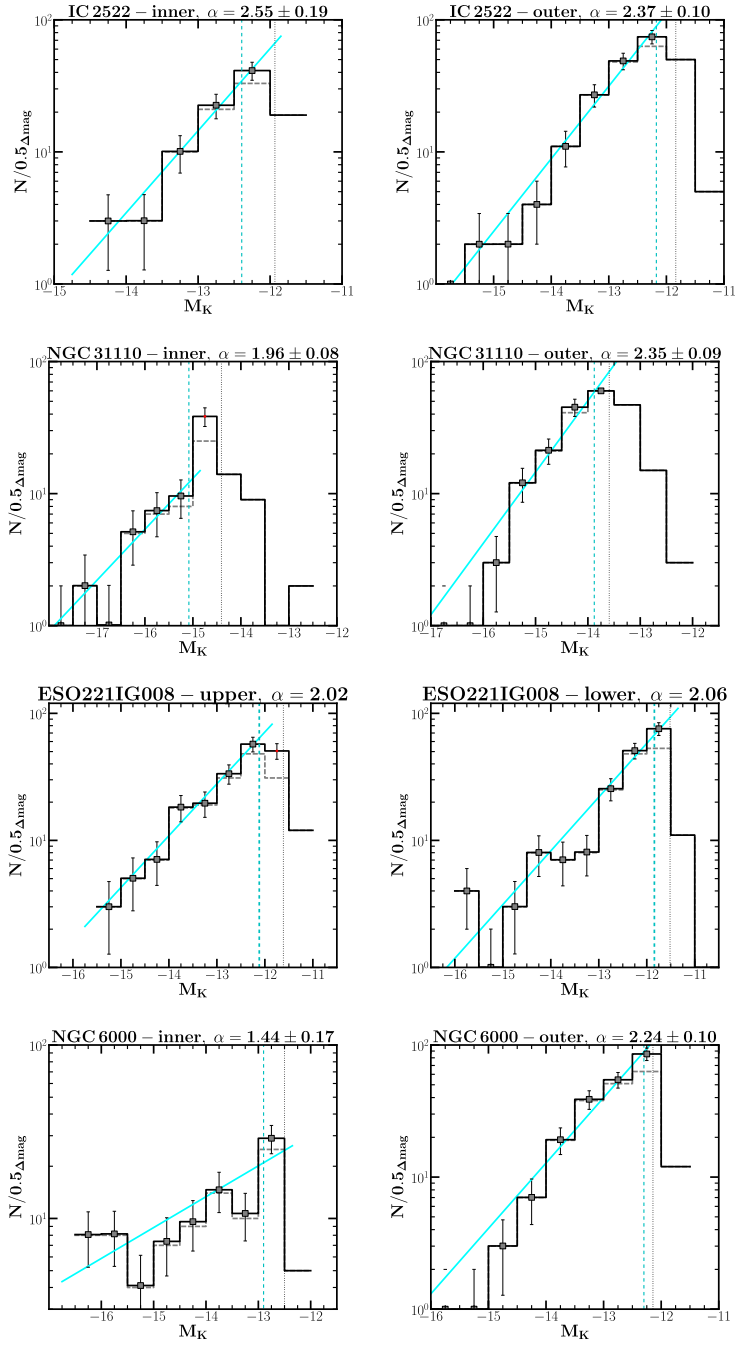

Figure 3.11: CLFs of two distinct SSC populations segregated by their physical locations in the galactic fields of IC 2522, NGC 3110, ESO 221−IG008 and NGC 6000, respectively. Labels are the same as in Figure 3.6 in all panels. K-band LFs of the SSCs in the nuclear regions are in the left panels whereas the right panels show the distributions for SSCs residing in the arms or other starburst regions of the galaxies. There are clearly differences in the CLF shapes and power-law slopes of NGC 3110 and NGC 6000.

We also performed a Schechter fit to the CLF of the target with the form of:

$$\phi(M)dM = con \times X^{\alpha_S+1}e^{-X}dM \tag{3.4}$$

where

$$X = 10^{0.4(M_K^\star - M)} \tag{3.5}$$

which resulted in a characteristic magnitude of $M_K^\star \approx -17.4$ mag and a faint end slope $\alpha_S = 1.56 \pm 0.19$. Note that the values of α_3 and α_S are similar for the two types of fit.

A bent LF for IRAS 18293−3413 fits better than a single power-law slope at the $\sim 1.5\sigma$ level. Though the difference is not very large, it is interesting, especially given that this galaxy has large statistics of SSCs in our present sample. We will discuss the case further in a subsection of Section 3.5.2.

3.5 Discussion

3.5.1 The effect of blending on the LFs

The distances of our sample galaxies, $25 \lesssim D_L(\mathrm{Mpc}) \lesssim 150$ and one at 200 Mpc, means that any individual SSC cannot be resolved. Our spatial resolution of $\sim 0.1''$ corresponds to a physical size of ~ 20 to 60 pc depending on the distance, and nearly 100 pc in the case of IRAS 19115−2124, and our photometric apertures are of comparable size. Given that the effective radii of SSCs from the literature are in the range of 3 to 5 pc (e.g. Whitmore et al. 1999), such aperture sizes may contain more than a single SSC candidate. Hence, blending of SSCs and complexes of SSCs will most probably contaminate our SSC counts despite the use of AO and HST imaging. *Is it then reasonable to even refer to these as SSCs, or should we rather talk, for example, about "knots of star-formation" (Miralles-Caballero et al. 2011)?* To address this we next attempt to estimate how much blending and crowding affect our analysis. We first perform a simulation estimating the effect of blending on the LF slopes, then examine what happens to photometry of SSCs of a nearby system when it is moved to a larger distance. We also investigate the relation between the SSC surface density and confusion limits. In the end we conclude that blending effects are not significant within the SSC luminosity range considered, especially if the target luminosity distance is less than 100 Mpc, and in our case the term "SSC candidate"is a perfectly reasonable one for sources in our photometric catalogues.

MC simulation of blending in LFs

We performed a MC blending simulation to quantify the effects of crowding on the values of the power-law index α. A random population of N artificial sources was created within

the same magnitude range as our observational data ($-20 \lesssim M_K \lesssim -12$) drawn from a LF with an initial index $\alpha_{init} = 2$. We randomly selected two artificial sources from this population then blended them together. This process was repeated x times until the original population had x blended sources in total, corresponding to a blending rate $y = 100 \times (x/N)$ percent. The blending was done step-by-step, so that a "new" blended source entered back into the catalogue as a new source and may be randomly blended with a third source, etc. A new power-law index, α_{new} was determined from a fit to the blended source luminosity distribution. The difference in the slopes, $\Delta\alpha = \alpha_{init} - \alpha_{new}$ was then determined. We ran the simulation with y ranging from 5 to 60 percent in steps of 5 %. A particular blending realisation was repeated 1000 times for each blending rate. We also ran the MC simulation for $\alpha_{init} = \{1.5, 1.8, 2.3\}$. We found that blends of 3 or more sources are rare below ~ 20 percent blending rates.

Figure 3.12, left panel, plots $\Delta\alpha$ against the blending rate with different values of α_{init}. The sense is always that of *flattening* of the slope. A blending rate of 10 % for example would lead to a deviation of $\Delta\alpha \sim 0.14$ from $\alpha_{init} = 2$. The figure indicates that to get significant flattening of α by 0.3 or more, one would need blending rates of ~ 25 % or higher for an initial slope of 2, or nearly 40 % for the slope to flatten from 2 to 1.5. The blending rates needed are higher for a steeper initial slope and lower for a flatter initial slope as expected. The blending rate is obviously related to the surface density of objects in the field, and we will return to the likely real blending rates of our targets at the end of this section.

Figure 3.12, middle panel, plots the change in magnitude of the brightest object; with more blending there is a greater chance that the brightest object is in fact a blend. Again

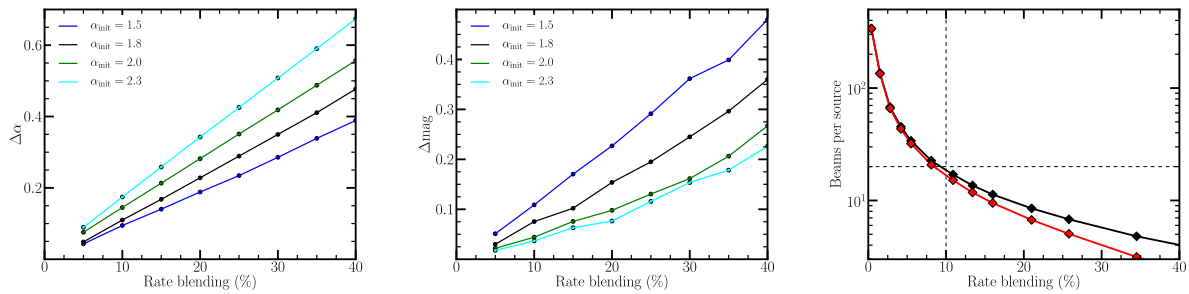

Figure 3.12: Results from our MC blending simulation. *Left*: the difference in the indices $\Delta\alpha = \alpha_{init} - \alpha_{new}$ plotted against the blending rate considering different values of α_{init}. The figure indicates for instance that a blending rate of 8 % would lead to a deviation of ~ 0.11 in the initial value of the index $\alpha_{init} = 2$. *Middle:* The same simulations, but plotting the magnitude difference of the *brightest* source. Note that intrinsic clustering characteristics are not taken into account in this simple simulation. *Right:* Surface density expressed as "beams per source" vs. blending rate. A figure of 20 "beams per source" is traditional confusion limit rule-of-thumb, and it is seen that at this surface density the blending rate is ~ 10 %, resulting in $\Delta\alpha \sim 0.1$ to 0.2 depending on the initial LF slope, according to the left panel.

we see that significant changes, Δmag > 0.5, in the magnitude require blending rates of 40 % or higher.

The simulation does not take into account varying degrees of blending, nor changes in completeness limit. Most significantly, however, the simulation implicitly assumes a random surface distribution of targets, whereas SSCs are clearly clustered in (most) galaxies. While the simulation gives a good feel for the expected levels of changes in LF slopes due to blending, a more realistic estimate should be based on real data.

SSCs in a redshifted Antennae

The Antennae system, at $D_L \sim 20$ Mpc, is a popular laboratory for young massive star cluster studies (e.g. Whitmore et al. 1999; Zhang et al. 2001; Whitmore et al. 2010; Cabrera-Ziri et al. 2015), and we use its well-studied star cluster population for a blending estimate. In particular, we retrieved *HST*/WFC3 images (PI: Whitmore) in the UVIS/F814W (I-band) and IR/F160W (H-band) filters from the Hubble Legacy Archives. Adopting a distance of 22 Mpc, the 0.04″ pixels in the I-band translate to a 4.3 pc physical size and the PSF of FWHM = 1.84 pixels to a FWHM $\sim$8 pc. In the H-band dataset the pixel size is 0.09″, and the adopted PSF of FWHM = 1.4 pixels translates to a physical PSF of FWHM $\sim$14 pc.

We first convolved and rebinned the I-band Antennae image to correspond to being 4 times further away. At 88 Mpc it is well within the distance range of our sample (Table 2.1), and the PSF resolution element of 32 pc is also similar to that in our NACO and ALTAIR/NIRI images. SSCs were detected both from the original and convolved images. We do not take into account the change in detection limits, so as to test only the effects of blending. The photometry and LF constructions were done similarly to our AO data described above, except that we do not attempt completeness corrections here as they are irrelevant to the main goal. Following other *HST* studies of the Antennae (e.g. Whitmore et al. 2010) an aperture radius of 0.1″ was used on the original (unbinned) image, corresponding to 10.8 pc. Nominal photometric zero-points and aperture corrections were taken from the WFC3 on-line manuals. The resulting LF is shown as the black points in Figure 3.13, left panel, and a single power-law slope of $\alpha = 2.22$ was found; the fit is performed down to $M_I \approx -8.5$ mag where incompleteness appears to be setting in. This value is in fact very consistent with other studies though no completeness or stellar contamination corrections were made in our test, for example Whitmore et al. (2010) found $\alpha = 2.26$ in the V-band.

The source extractions and photometry were done in the same way for the ¨redshifted″convolved image. An additional aperture correction is needed however since the PSF and pixel characteristics change, and the new correction was simply determined by matching the extracted magnitudes of a handful of foreground stars in the different images and apertures. The LF shown in blue in Figure 3.13 results from extractions from

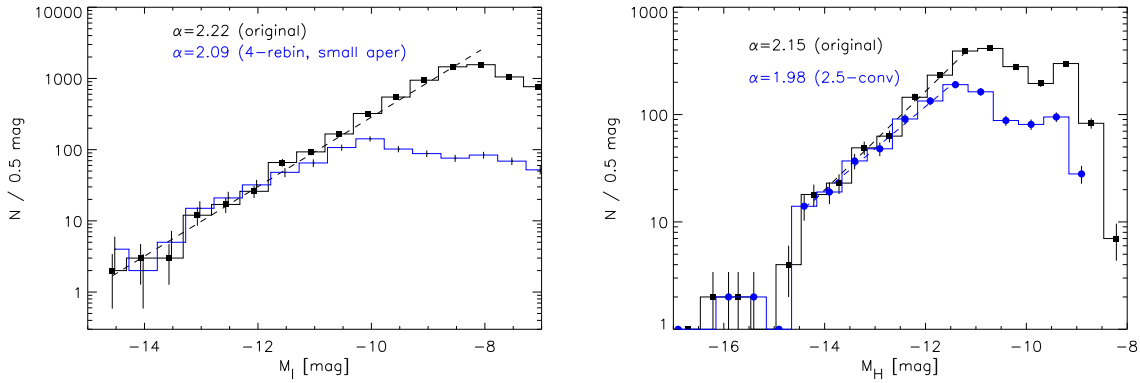

Figure 3.13: LFs of SSCs derived from *HST* images of the Antennae galaxies. *Left:* The black histogram shows the LF from the original I-band (F814W) image, and the blue after convolving and rebinning the image to correspond to a 4 times larger distance (≈ 84 Mpc). The best-fit power-law slopes are indicated. *Right:* The same test for the H-band (F160W) image, but now the comparison is made so that the convolved image matches both the PSF size and the pixel size of our IRAS 18293−3413 NACO image. In both tests only mild flattening of the LF slope is observed.

the convolved image when using a small 0.75 pixel aperture, corresponding to 13 pc radius. As expected, the completeness limit is some 2 magnitudes brighter due to blending only, while the LF slope becomes only slightly flatter at $\alpha = 2.09$. The aperture size used does not have an effect on the slope, but we will return to this aspect in more detail below.

We also examined what happens to the 50 and 200 brightest original SSCs in the convolved image. Of the 50 brightest ones 7 were not detected as individual objects after the "redshifting" (14 % blending rate) while 53 of the 200 brightest ones were not detected (27 % blending). In the previous MC blending simulation, these blending rates would have resulted in a flattening of the slope by $\Delta\alpha \approx 0.20$ and ≈ 0.37, respectively. These numbers are somewhat larger than the measured flattening in the range 0.1 to 0.15 of the convolved image LF slope in the test above (Figure 3.13). The recovered magnitudes of the brightest 50 SSCs are a mere ~ 0.1 mag brighter than in the original image.

In case clustering properties of SSCs would be different in the optical compared to NIR, we repeated a similar test using the H-band image of the Antennae. This time we modified the original *HST* image to match both the physical pixel scale and PSF size of the NACO IRAS 18293−3413 image at $D_L \approx 75$ Mpc. Rebinning was not necessary because of the smaller pixels of the NACO instrument, while a factor of 2.5 widening of the PSF was performed. Magnitudes were measured in 20 pc radii in the original image, matching the aperture used in the Whitmore et al. (e.g. 2010) NICMOS data, and 30 pc radii in the redshifted case, as done for the NACO IRAS 18293−3413 images. The resulting LFs are shown in Figure 3.13, right panel, indicating a flattening of the slope by 0.15, very similar to what was found for the I-band *HST* image. The magnitudes do

not change significantly this time either, the average difference being less than 0.1 mag for the 200 brightest SSCs.

To understand and differentiate between the effects of spatial resolution and photometric aperture used with a given resolution, we redid the tests above with different convolutions using PSFs ranging from 10 to 100 pc, as well as using numerous aperture sizes in the same range. Some results become clear. First of all, the photometric aperture used at a given resolution *does not change the slope significantly*. Variations of ~ 0.1 were typically found for the value of α. Secondly, the LF does however shift to brighter magnitudes as the apertures grow. To recover as closely as possible the intrinsic SSC counts *the smallest possible aperture should be used*, assuming a reliable aperture correction can still be determined. With the largest tested apertures the bright SSCs brighten by nearly a magnitude, while using apertures smaller than about $20 - 30$ pc radius, the brightening stays within typical photometric errors of ~ 0.2 mag. Thirdly, when analyzing the effects of different convolutions we found that the resulting LF slope remains relatively unchanged, staying within $\Delta\alpha = 0.2$ of the original slopes of 2.15 and 2.22 (H and I-band respectively) until PSF sizes of about 40 pc are reached, after which the slopes flatten rapidly reaching $\alpha \sim 1.5$ at the poorest spatial resolutions of a 100 pc physical size.

Figure 3.14 shows an example of a small region within the Antennae in both the original and convolved images of the *HST* I-band which illustrates these effects. While numerous faint SSCs disappear or are blended into bright SSCs, the latter are generally recovered in the convolved image with close to their proper magnitudes, unless located in very crowded regions. For example the more isolated bright SSCs on the edges of the image are recovered within ~ 0.1 mag of the original magnitudes, while the three bright SSCs in the middle of the central conglomeration have brightened by about 0.4 mag. The largest changes to the photometry are in cases where SSCs of similar brightness happen to lie near each other and blend into a single significantly brighter object, such as the bright SSC at bottom right which has blended into one source 1.1 mag brighter than either of the originals. How severe these effects are, naturally depends upon on the overall surface density of objects, which is discussed next.

The effects of confusion limits

Historically, blending and crowding as discussed above are referred to as ¨confusion˝ especially in the radio and far-IR studies, and in particular ¨bright source confusion˝. When a confusion limit is reached depends, in addition to the shape and size of the spatial resolution element, on the slope of the source counts. With very steep slopes *confusion noise* dominates, i.e. the many undetected sources at and below a detection limit give rise to an effective noise-level (see e.g. Väisänen et al. 2001 and references therein for full discussions) that deeper observations cannot penetrate. With much flatter slopes the bright sources lying too close together for satisfactory extraction

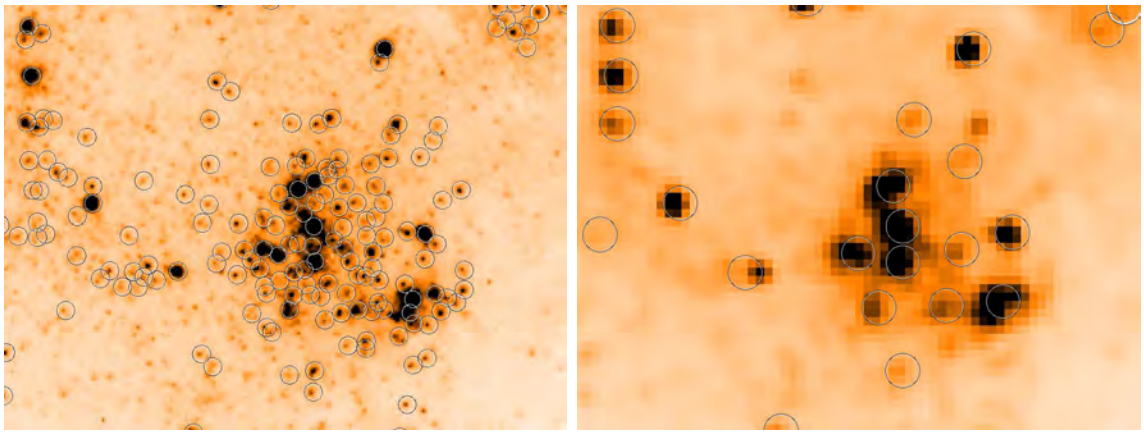

Figure 3.14: A 10″ by 8″(1.1 by 0.9 kpc) region in the *HST* I-band image within the Antennae (region E in Whitmore et al. 2010). *Left:* The original image with $\sim$ 160 SSC candidates detected. *Right:* The image after taking the galaxy four times further away. Only $\sim$ 20 SSCs are now detected due to blending, though the brighter population remains relatively unchanged.

at a given spatial resolution tend to dominate. The SSC source count slopes are closer to this latter regime, but it is prudent to search for this surface density-related confusion limit also in cases where the images are not truly confusion-limited yet.

A 20 to 40 "beams per source" confusion limit is often used as a rule-of-thumb (e.g. Väisänen et al. 2001). For example, for a resolution element FWHM = 0.1″, setting the beam size as

$$\Omega = \pi \frac{FWHM^2}{4\ \ln(2)},$$

then 20 beams per source corresponds to having one SSC per every 0.47″ × 0.47″ region. Hence, having over 500 sources within the area of IRAS 18293−3413, for instance, would mean reaching the limit, while we detected $\sim$200. However, in the core regions the surface density is definitely approaching the confusion limit.

It is worthwhile to define a general confusion limit in terms of physical sizes for SSCs. Taking SSCs to be of size 10 pc, the 20 beams-per-source criterion corresponds to a SSC density of 440 kpc^{-2}. If SSCs are seen more densely packed than this then better resolution is not likely to help extend SSC detection. Over the approximately 9×9 kpc^2 size of the Antennae, for example, this would mean some 40000 sources; extrapolating the counts we extracted from the *HST* image, this level would be reached around $M_I \sim -6.5$ mag. As seen above, in individual *regions* of the galaxy system, the confusion limit must be reached at much brighter magnitudes since the SSCs are clustered. This is reflected in the fact that significant incompleteness starts appearing already at $M_I \sim -8$ mag in our test (Figure 3.13, left panel). *If* the *HST* image was truly confusion-limited, and assuming a LF with $\alpha = 2$, the completeness limit would be expected to brighten by 3 magnitudes after the factor 4 convolution, whereas a change of 2 mag was observed.

We list in Table 3.5 *physical* surface densities per kpc^2 at which the confusion limit is likely to be reached at a given distance and spatial resolution, given the definitions above. With the typical PSF of $\sim 0.1''$, the distances of our sample, and the number of detected SSCs, only the core regions of IRAS 18293−3413, ESO 221−IG008, IC 2522, NGC 1819, and NGC 3110 come anywhere close to these confusion limits, as well as IRAS 19115−2124 due to its distance. This is not to say that individual SSCs will not blend of course, especially in clustered star-forming regions of the galaxies as shown in the tests based on the Antennae. For example, the surface density of detected objects in the left panel of Figure 3.14 is $\sim 160\,\mathrm{kpc}^{-2}$. At a distance of $\sim 20\,\mathrm{Mpc}$ and for a resolution element of $0.075''$this is not quite yet confusion-limited according to Table 3.5, though it is approaching it. This is also seen from the corresponding 78 beams-per-source surface density. However, within the clustered sub-region the equivalent values would be $\sim 500\,\mathrm{kpc}^{-2}$ and ~ 25 beams-per-source, respectively, i.e. that region is confusion-limited.

To see how the surface densities quantitatively relate to the LF slope changes, we ran another MC simulation adding increasing amounts of randomly distributed equally bright sources in an otherwise empty frame and extracting them with `SExtractor` using typical parameters. This was done hundreds of times at several surface densities, and the fraction of unrecovered sources is simply the *blending rate* at each surface density. The change in LF slope with a given intrinsic LF shape was already simulated earlier as a function of this blending rate and the results were shown in the left and middle panels of Figure 3.12. The right panel of Figure 3.12 connects the two by plotting the "beams per source" surface density against the blending rate. The black curve is the intrinsic surface density of the simulation, and the red curve is calculated from the extracted surface density. An *observed* surface density of objects can be used to get an expected

Table 3.5: Surface densities that would result in *confusion-limited* observations

PSF [arcsec]	Distance [Mpc]					
	10	20	40	80	120	200
0.050″	440 (1900)	440 (480)	220	130	58	22
0.075″	440 (850)	220	98	59	26	10
0.100″	440 (480)	120	55	33	15	5.6
0.200″	120	30	14	8.3	3.7	1.4
0.300″	53	13	6.1	3.7	1.6	0.62
0.500″	19	4.8	2.2	1.3	0.59	0.22
1.000″	4.8	1.2	0.55	0.33	0.15	0.06

Notes. In units of kpc^{-2}, the surface densities would result in *confusion-limited* observations of SSCs, when the limit is defined as 20 "beams per source". For small distances/PSFs the assumed 10 pc physical size of SSCs is *resolved* and the value corresponds to this confusion limit; the value corresponding to the actual resolution element is given in parentheses.

blending rate using the red curve (for completeness-corrected counts the black curve is more appropriate) and this can then be converted to a likely $\Delta\alpha$ value of the LF. While the vertical displacement of the surface density vs. blending rate curves will depend on the source detection algorithm and clustering of objects, our tests show that the relations do serve as a realistic approximation of the quantitative effects involved.

Effect of blending in our sample

The average surface density of detected SSC candidates in our target galaxies ranges from a low of 0.1 kpc^{-2}, or 168 beams per source, to a high of 0.8 kpc^{-2}, or 87 beams-per-source. According to Figure 3.12, the corresponding blending rates are well below 5 %, meaning that $\Delta\alpha < 0.1$ for any LF shape, most likely < 0.05 for most of the targets. Because of the uncertainties involved, such as the difficulties of properly accounting for clustering, we prefer not to attach $\Delta\alpha$ values for each individual target, but rather stress that these are likely to be less than 0.1. However, in our most extreme case of the *central* $\sim 2 \times 2$ kpc region of IRAS 18293−3413, the SSC surface density equates to 20–30 beams per source, and $\Delta\alpha \sim 0.15$ would be expected in that region.

As a further check, the top panels of Figure 3.15 show separately the LFs for SSCs out to distances $D_L \leq 60$ Mpc, and for $D_L > 60$ Mpc (excluding IRAS 19115−2124 since it is so much further away). The bottom panels of Figure 3.15, split the LFs for SSCs in between the distances $60 < D_L < 100$ Mpc, and for $D_L > 100$ Mpc. The single power-law indices of the LFs below 60 Mpc (top left) and in between 60 to 100 Mpc (bottom left) are 2.16 ± 0.07 and 2.02 ± 0.12, respectively, i.e. there is no significant difference in the LF slope, nor in the numbers of detected SSCs, with distance.

Figure 3.16 plots the values of the power-law slopes of Figure 3.6 against physical characteristics of the SSCs and the host galaxies. The shapes of the LFs as well as the resulting power-law indices in Figure 3.15 are in agreement with the failure to find a clear correlation between the value of α and the target luminosity distance or the number of SSCs brighter than a certain magnitude level as shown in the top panels of Figure 3.16. The LF for SSCs hosted by the more distant subsample in the bottom right panel of Figure 3.15, however, shows a flatter slope of 1.69 ± 0.08. Blending could thus be an issue and would lead to a $\Delta\alpha > 0.10$ in some of the cases at $D_L > 100$ Mpc.

In summary, we are confident that in the luminosity range of interest, $M_K <$ -14.5 mag, any flattening of LF slopes due to blending is below $\Delta\alpha \sim 0.1$. With the possible exception of any target at a distance $D_L > 100$ Mpc, especially IRAS 19115−2124 where the spatial resolution corresponds to a physical size of 90 pc, the luminosities of detected K-band point sources will be dominated by a single bright SSC rather than whole knots of star formation. In the case of Antennae-like SSC populations, blending and crowding do flatten the LF slope, but significantly so only at resolutions poorer than a 40 pc physical size. The photometric apertures used should be as small as possible to recover intrinsic

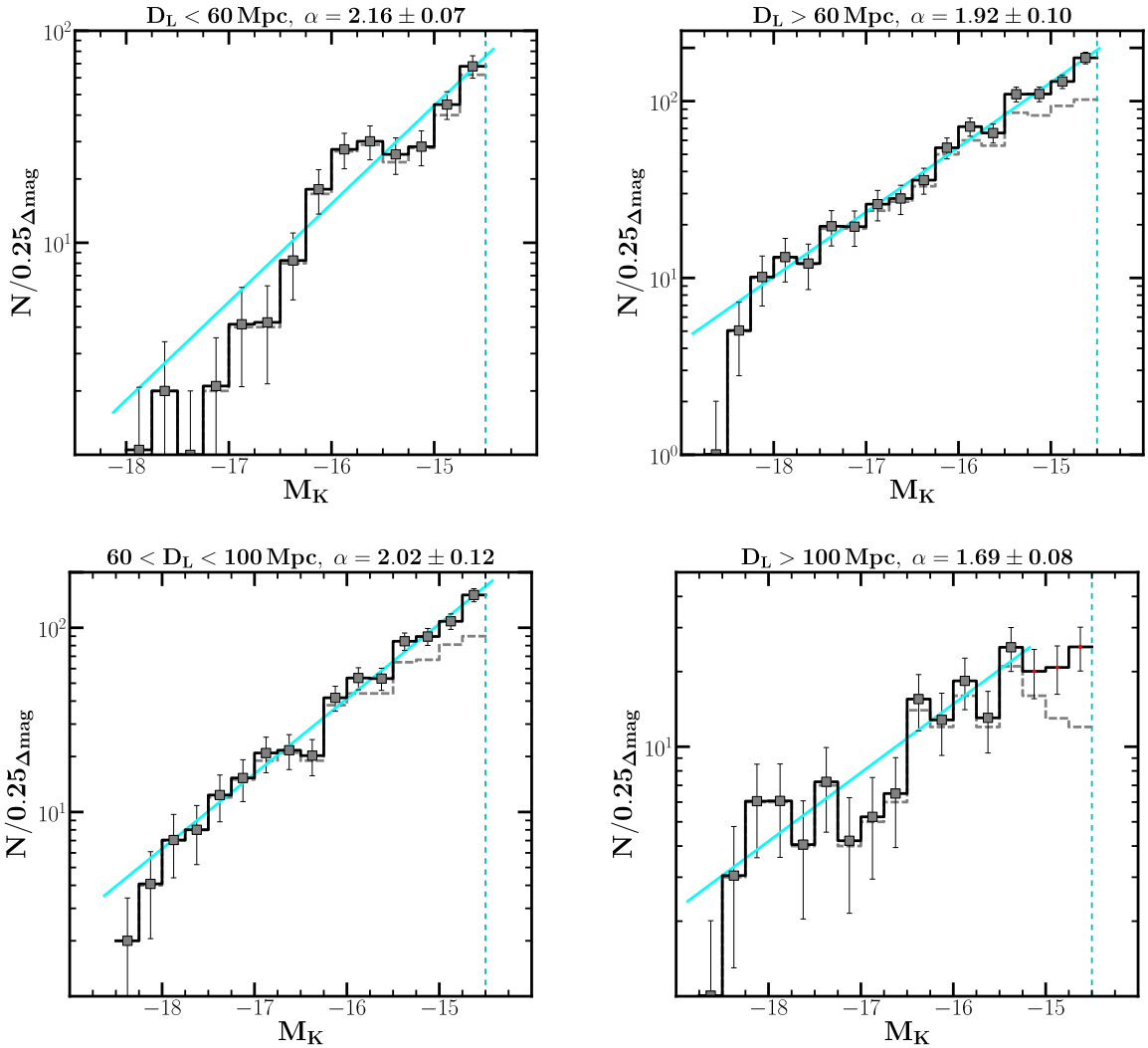

Figure 3.15: SSC LFs of four subsamples generated from our observational data but segregated by distance. The dataset from IRAS 19115−2124 is excluded to avoid bias in the analysis. *Top left:* SSC LF of the closest subsample where the targets have distances ≤ 60 Mpc. *Top right & Bottom left:* The SSC LFs for $D_L > 60$ Mpc and $60 < D_L \leq 100$ Mpc, respectively. *Bottom right:* SSC LF of the most distant targets, ie. $D_L > 100$ Mpc. The values of the slopes appear to be consistent within the uncertainties for $D_L \leq 100$ Mpc.

luminosities, though the aperture does not have a significant effect on the LF shape. Assuming a 10 pc scale for SSCs, the confusion limit is reached at a surface density of 440 SSCs per kpc^2, or less when clustering and larger resolution elements are a factor.

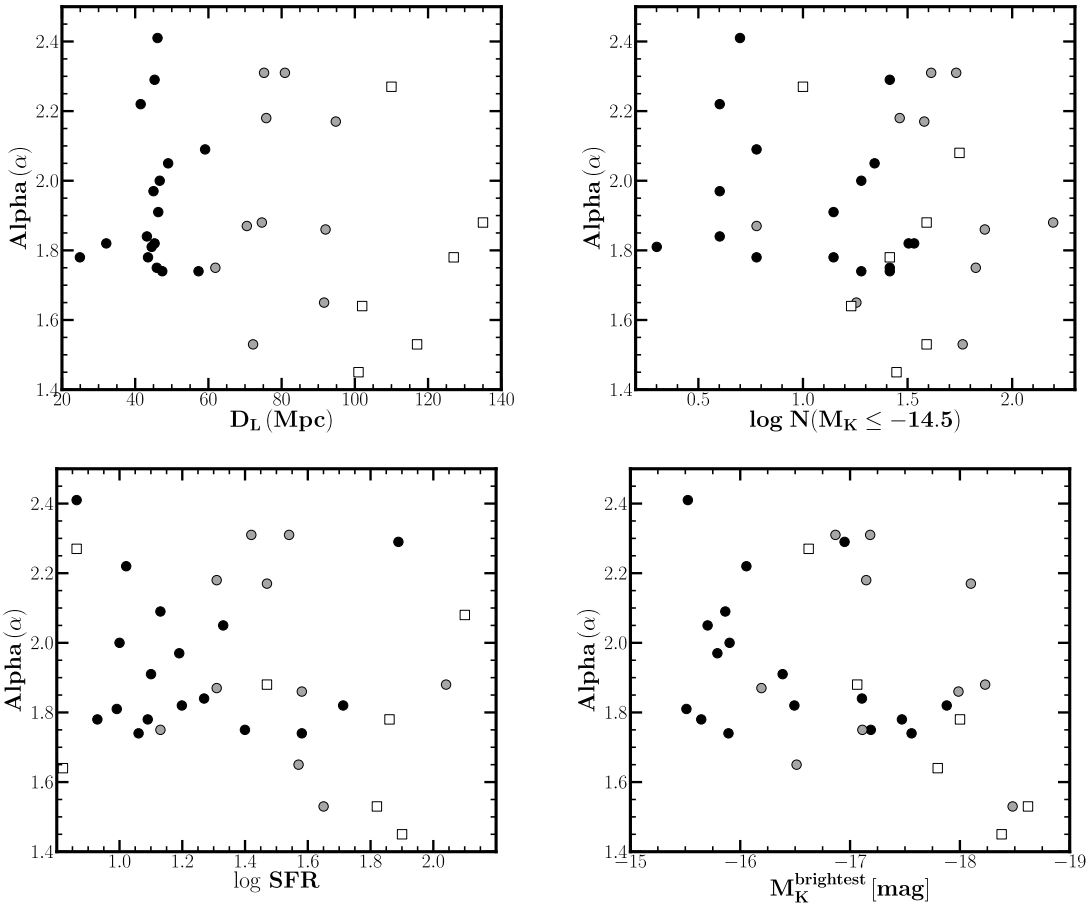

Figure 3.16: The power-law slope α plotted against the luminosity distance (top left panel), the number of the SSCs with $M_K \leq -14.5$ mag (top right), the star-formation rate (bottom left), and the magnitude of the brightest cluster (bottom right) to search for any correlation. The most distant targets at $D_L > 100$ Mpc are labelled as open squares, whereas the $D_L \leq 100$ Mpc targets are shown as circles: those at $D_L \leq 60$ Mpc are black and those at $60 < D_L \leq 100$ Mpc are grey.

3.5.2 Interpreting the values of α

The results from our fitting procedure in Section 3.4 show that a single power-law distribution is a reasonable approximation for the young stellar cluster LFs in our sample. A single power-law SSC LF has been reported by many theoretical and observational studies (Elmegreen & Efremov 1997; Lada & Lada 2003; Gieles et al. 2006a, e.g.), and such behaviour may be linked to the shape and characteristics of the physically more interesting underlying (initial) mass function and/or the evolution and disruption of the SSC population. As listed in Table 3.3, the fitted single power-law indices range from $\alpha \sim 1.5$ to 2.4, with average single slope values of $\alpha^{con} = 1.92 \pm 0.24$ for a constant bin size, and $\alpha^{var} = 1.93 \pm 0.26$ for a variable bin size. Values of α reported in the literature vary widely from 1.7 to 2.4 (e.g. Elmegreen & Efremov 1997, Whitmore et al. 1999,

Elmegreen et al. 2002; de Grijs et al. 2003a), with slopes in normal spirals often in the upper part of this range. Our α values tend to be in the less steep part of the range, and in at least one case (IRAS 18293−3413) either a broken power-law or a Schechter function would yield a better fit. These two issues are discussed next.

LF slopes: a difference between LIRGs and normal spirals?

Improper incompleteness corrections can produce artificially flattened slopes. We note however that the slopes are fitted to a range where at most 20 % of SSCs are missed, and where the corrections are still reliable. The most significant change is likely to be caused by blending of SSCs but as discussed in the previous section, this is expected to be $\Delta\alpha \approx 0.1$ at most for our targets, and likely less. Also, except for the ones where $D_L > 100$ Mpc, we did not see any significant change in the α values with distance to the galaxies, which would have been expected if significant blending was present (Figure 3.15). If the data sets from the more distant targets are excluded ($D_L > 100$ Mpc), the average in the slopes is 1.95 ± 0.23 with a median of 1.87. Therefore, we conclude that the intrinsic SSC LF slopes, the combined and averaged LFs having $\alpha \approx 1.98 \pm 0.10$ and 1.92 ± 0.24, respectively, should not be heavily affected by these observational effects, with any systematic effects being outweighed by the statistical uncertainties.

Normal spiral galaxies tend to have power-law indices in the range of $\alpha \sim 2$ to 2.4. Calculating the average from SSC LF studies which include several spirals each (Larsen 2002; Gieles et al. 2006a; Mora et al. 2009), we get $\alpha \approx 2.17 \pm 0.24$ from 10 spiral galaxies. If we include other individual galaxy studies (Schweizer et al. 1996; Buta et al. 1999; Elmegreen et al. 1999, 2002; Cantiello et al. 2009; Pellerin et al. 2010; Whitmore et al. 2010), where some targets are starbursts, though not yet LIRGs, we get an average of $\alpha \approx 2.18 \pm 0.19$ from a total of 19 galaxies. Note that the values come from different filters, mostly from V- and I-bands; if several bands were used, we chose the reddest band. As discussed earlier the well-studied interacting Antennae system also has $\alpha \sim 2.2$ (Whitmore et al. 2010). A recent work by Whitmore et al. (2014) considers more homogeneous HST archival data with the highest quality of 20 normal spiral galaxies. The I-band CLFs gave an average value of $\alpha \approx 2.37 \pm 0.18$. Note that this selected sample includes targets from previous works such as e.g. Larsen (2002) and Gieles et al. (2006a).

While most of the previous SSC LF determinations in the literature, including the Antennae, have been in actively star-forming galaxies, the vast majority of them have lower SFRs than LIRGs. Our average power-law slope for LIRGs, $\alpha \approx 1.9$, appears flatter than the slope in normal galaxies. The large sample of LIRGs studied in Vavilkin (2011) shows an average $\alpha \sim 1.8$, though blending effects there might still need to be explored. Similarly, Miralles-Caballero et al. (2011) find $\alpha \sim 1.9$ for their (U)LIRGs at < 100 Mpc, and even flatter values at certain interaction stages of LIRGs. Moreover, Adamo et al. (2010, 2011b) recently found flatter power-law slopes while probing the star cluster properties in Haro 11 and Mrk 930. Both of the targets are blue compact dwarfs

with intense star formation, and the former can also be classified as a LIRG. *Is it the case therefore that LFs are systematically flatter in extreme SF cases?*

To see if there is a trend with SFR *within* our sample, Figure 3.17 shows SSC LFs of four subsamples generated from our observational data but segregated by their star-formation rates. The top panels split the SSCs with host galaxy SFRs less than, or greater than the average $\overline{\mathrm{SFR}} \sim 30\,M_{\odot}\,yr^{-1}$, again with IRAS 19115−2124 excluded. The values of the slopes are $\alpha = 2.23 \pm 0.08$ for the subsample below the average and $\alpha = 1.81 \pm 0.10$ for those above. The bottom panels show the LFs for SSCs with

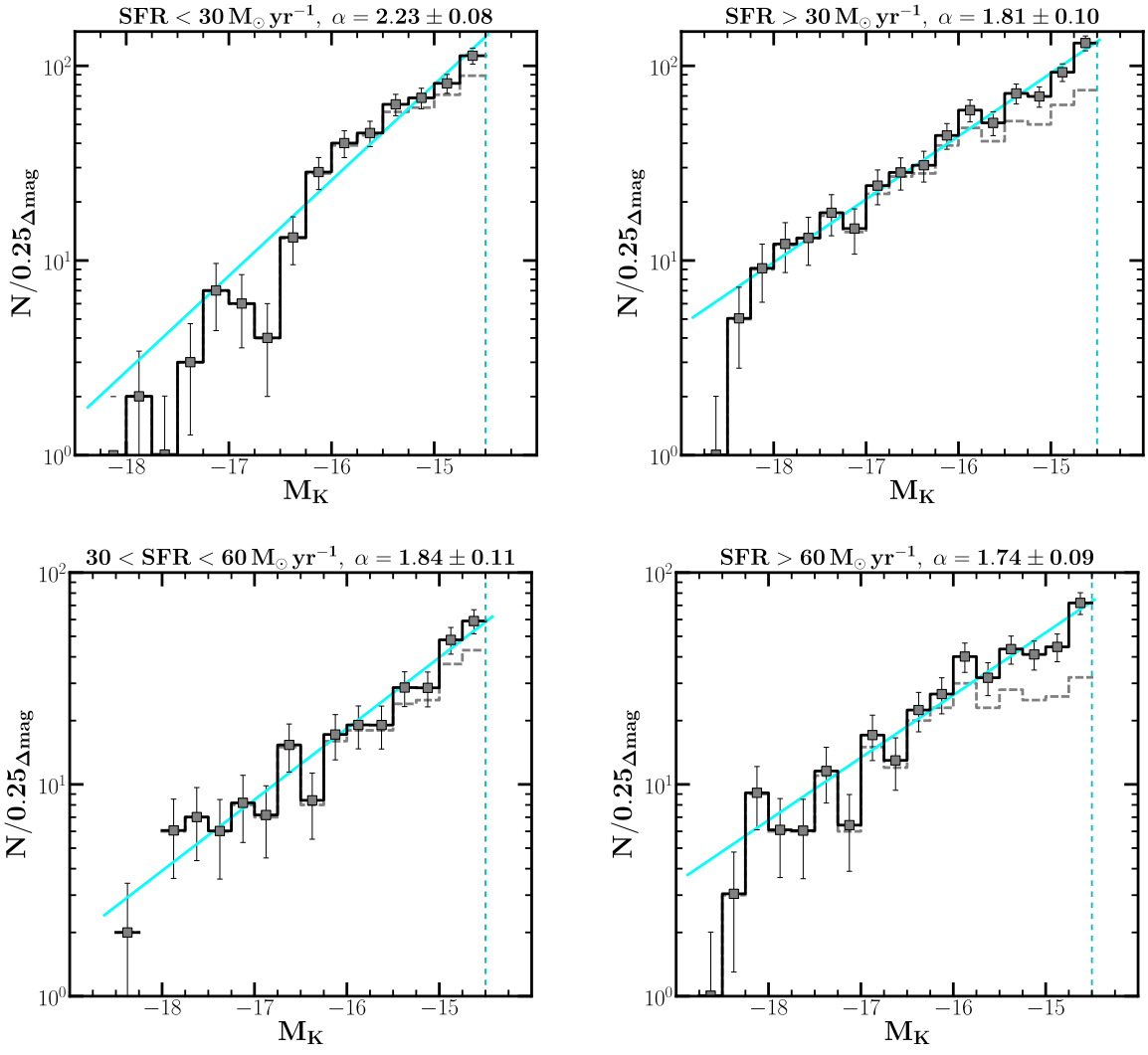

Figure 3.17: *Top panels:* SSC LFs of two subsamples generated from our observational data, excluding IRAS 19115−2124, but split by the average SFR. *Bottom panels:* SSC LFs of two other subsamples where the targets have $30 < \mathrm{SFR} \leq 60\,M_{\odot}\,yr^{-1}$ and $\mathrm{SFR} > 60\,M_{\odot}\,yr^{-1}$, respectively. The value of α appears to decrease with an increasing SFR.

$30 < \mathrm{SFR} \leq 60\,M_{\odot}\,yr^{-1}$ and $\mathrm{SFR} > 60\,M_{\odot}\,yr^{-1}$ with resulting power-law indices of $\alpha = 1.84 \pm 0.11$ and $\alpha = 1.74 \pm 0.09$, respectively. These figures clearly indicate that the values of α are steeper for the targets with less intense SF activity compared to those with high SFR. The bottom panels of Figure 3.16 plot the LF slope against the logarithm of the SFR (bottom left) and the magnitude of the brightest cluster (bottom right) where the data points are labelled with respect to their distances. Both plots suggest that there is at least a weak correlation between the parameters. They also have more or less the ¨same trends˝which are expected since targets with strong SFR are likely to form a rich cluster population sampling the brightest star cluster candidates. Further analyses on possible correlation that may exist between the galaxy SFR and K-band magnitude of the brightest cluster are explored in details in Chapter 4.

Finally, the plot in the bottom panel of Figure 3.16 is re-generated, but this time, with the targets labelled as a function of the SFR level (see Figure 3.18). With a correlation coefficient $r = -0.25 \pm 0.15$, there seems to be a weak relationship between the LF slope and the SFR within our star-forming galaxy sample. To check whether a correlation really exists or not, we binned the slopes α and hence generated the points labelled as red stars in Figure 3.18. With a correlation coefficient $r = -0.67 \pm 0.21$ from the binned data points, there is a statistical trend at a 2σ level of a flattening of the power-law index of the LF with an increasing SFR. This is in agreement with the findings claimed from previous works (e.g. Adamo et al. 2010, 2011b), though as is evident by eye, the actual trend cannot be described as strong. On the other hand, our results together with other recent studies also suggest that there is a real difference between the SSC LF slopes of LIRGs and those of more quiescent galaxies. This was also observed in the LF slopes of NGC 3110 and NGC 6000 on a sub-galactic scale: flatter slopes for the nuclear regions (Section 3.4.4).

Physical interpretations

Apart from effects related to the observations themselves, perhaps the most fundamental cause for flattened LFs, or breaks/bends in the LF for that matter, would come from mass- and/or age-dependent cluster disruption, as well as from differences in the cluster formation with different environments. Young star clusters are most vulnerable to disruption, leading to variation of the integrated LF as time passes. Since LFs are the integrated sum of the distributions of individual initial LFs of SSCs of different ages and masses, any selective (e.g. mass-dependent) disruption of them would be seen as changes in the (integral) total SSC LFs (e.g. Mengel et al. 2005; Gieles et al. 2006a; de Grijs & Parmentier 2007). Kruijssen et al. (2012) argue that cluster *formation* efficiencies decrease in galaxies with higher SFRs due to increased tidal disruption in the extreme environments (¨cruel cradle effect˝), which might lead to flatter LF slopes if lower mass SSC formation is more affected. Alternatively, high SFRs may favour the formation of more massive GMCs (e.g. Wei et al. 2012). However it is impossible to conclude whether disruption is the main cause of the flatter slopes until we have analysed data from other

filters to be able to derive LFs and MFs in different mass and age regimes.

IRAS 18293−3413: What could a broken power-law reflect?

In the case of IRAS 18293−3413, and possibly for five more other targets, fitting two independent slopes produces better Chi Square values ($\chi^2_{red} = 0.57$) than a single power-law. The break appears to be at $M_K \approx -16.5$ mag and persists regardless of how the data is binned. We note that the distribution can also be well fit with a Schechter function, giving a characteristic magnitude of $M^\star_K \approx -17.4$ mag ($\chi^2_{red} = 0.64$). In general, any bends or cutoffs found close to the detection or completeness limits should be viewed with caution, but in this case the break is more than a magnitude above the 80 % completeness limit. Note however that in case of significant clustering of the SSC population in the inner parts, it remains a possibility that some fraction of the SSCs actually do experience

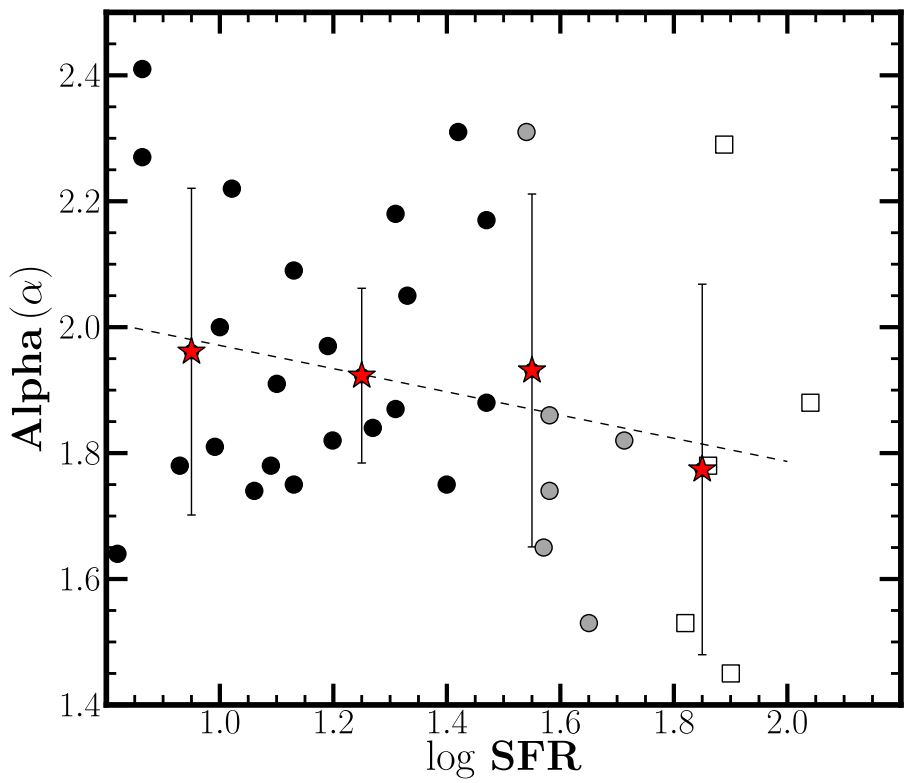

Figure 3.18: The same figure as in the bottom left panel of Figure 3.16 where α is plotted against log-SFR. However, the targets with SFR $> 60\,M_\odot\,yr^{-1}$ are labelled as open squares, whereas the SFR $\leq 60\,M_\odot\,yr^{-1}$ targets are marked as black circles: those with SFR $\leq 30\,M_\odot\,yr^{-1}$are black and those in between 30 and 60 $M_\odot\,yr^{-1}$ are grey. A constant binning of the slopes results in values shown as red stars, and the dashed line represents a linear fit to these new points.

more blending causing flattening of the LF and then showing up as bend.

Bends have been argued to result from physical truncations of the SSC high-mass end of the SSC mass functions or from disruptions of the less-massive SSC population (see e.g. Gieles et al. 2006a, Haas et al. 2008). The former results in a steepening of the bright end of the LFs if the truncation is a physical one and not merely a result of a size-of-sample effect; the latter affects the faint end of the LF by making it flatter. Thus both can result in bends in the shape of the LF, making for better fits with broken power-laws or Schechter functions. The absolute magnitude of the break point would increase with the maximum mass of the SSC population, though the exact relation is a complex function of the disruption models. The break is expected to occur at brighter magnitudes at redder wavelengths because of the expected red colour of the aged SSCs. Whether or not these bends and truncations are in fact seen in LFs or mass functions is still a matter of intense debate (see e.g. Gieles et al. 2006a, Larsen 2009, Whitmore et al. 2010, Fall & Chandar 2012 and references therein).

Bends in SSC LFs have typically been found in the range of $M \sim -9$ to -11 mag in VRI filters (e.g. Whitmore et al. 1999; Gieles et al. 2006a,b; Santiago-Cortés et al. 2010; Adamo et al. 2010, 2011a). Assuming typical *unextinguished* (and age dependent) optical-to-K-band colour indices of 2 to 3 mag, one would expect a corresponding bend to appear at $M_K \sim -12$ to -13 mag. Mengel et al. (2005) find a bend at a significantly brighter level $M_K \sim -15.5$ mag in the Antennae (but see Fall et al. 2009) not unlike our result for IRAS 18293−3413, suggesting significant extinction effects. The bend-point of a double power-law at $M_K \sim -16.5$ mag, or the Schechter characteristic magnitude at $M_K^\star \sim -17.4$ mag, would correspond to a *minimum* characteristic mass of $M^\star \approx 1 - 2 \times 10^6\,M_\odot$, or perhaps double this mass range if we adopt an average mass-to-light ratio over the first 30 Myr of age (see Section 3.5.3). These masses are higher by factors of 5 to 10 than the characteristic mass found for SSCs in normal spirals (Gieles et al. 2006a; Larsen 2009) while they are very similar to those suggested for galaxies with much higher SFRs, such as LIRGs (see e.g. Bastian 2008). However until there is clearer evidence for real bends in SSC LFs from a larger data set it, and proper analysis of clustering of star clusters inside galaxies, it is premature to read too much into these masses.

3.5.3 Mass range approximations of the K-band SSCs

An interesting characteristic of SSCs observed at NIR wavelenghts is a relatively narrow time-frame at ages of ∼10 Myr when the high mass stars in the SSCs enter the RSG phase making them very NIR-luminous and ¨suddenly˝ red in the optical-to-NIR colours compared to earlier blue stages. This is seen in Figure 3.19 which plots as an example the evolution of cluster brightness with time in the BIK filters, derived from a `Starburst99` (Leitherer et al. 1999) model assuming an instantaneous SF with a fixed mass of $2 \times 10^5\,M_\odot$, and a Kroupa IMF. Hence, a *lower limit on SSC masses* detected in

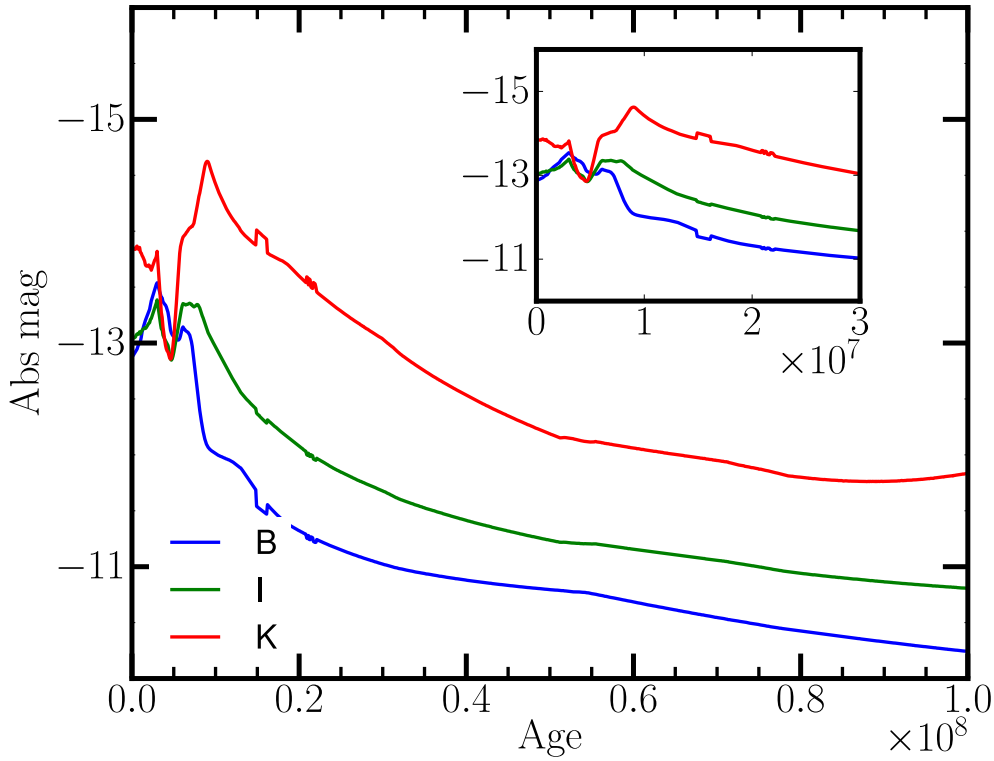

Figure 3.19: `Starburst99` model of $2 \times 10^5\,M_\odot$ SSP cluster with a Kroupa IMF. The three curves show the absolute magnitude of the star cluster in B-(blue), I-(green) and K-(red) bands. The inset highlights that the K-band luminosity of star clusters is likely to peak close to age 10 Myr while they peak somewhat earlier in the optical.

this work can be obtained by assuming the mass-to-light ratio at that ~ 10 Myr age. In many of our galaxies the most massive detected SSC has $M_K \sim -18$ mag corresponding to a mass of $4 \times 10^6\,M_\odot$ at 10 Myr of age or more than $2 \times 10^7\,M_\odot$ at 30 Myr; clearly we are sampling very massive clusters in LIRGs, assuming that there is no significant clustering of the SSC population.

SSCs with masses in excess of $10^7\,M_\odot$ have been found before (e.g. Bastian et al. 2006; Ma et al. 2006; Portegies Zwart et al. 2010). The faintest-detected SSCs in our sample have $M_K \sim -13$ corresponding to masses of $\approx 2 \times 10^4\,M_\odot$, while the photometric 80 % completeness limits in different targets correspond to lower limits of $1 - 2 \times 10^5\,M_\odot$. We note that with such massive clusters, the luminosities of individual bright RSG stars are negligible compared to the total integrated flux of the star cluster. Therefore, stochastic effects should not introduce significant scatter in the mass-to-light ratios and inferred ages of our clusters (e.g. Fouesneau et al. 2012; de Grijs et al. 2013). Careful mass and age modelling of the star cluster population are performed and discussed in Chapter 5.

3.6 Summary and conclusions

In this work we studied the characteristics of massive star clusters in the extreme environments of local starburst and interacting LIRGs. Observations were performed in the K-band filter using two different NIR AO instruments with pixel scales of ~ 0.022, 0.027 and 0.054 arcsec pix^{-1}, and a FWHM $\sim 0.1''$ for point sources. The galaxy sample consists of LIRGs in the redshift range $0.007 < z < 0.049$ or distances of $25 \lesssim D_L \lesssim 150$ Mpc and one at 200 Mpc. This study is opening new territory in SSC studies since both the distance range and the host galaxy SFR range are higher compared to most previous SSC studies. Specifically, we derived the K-band luminosity functions of SSC candidates in our targets, and because of the distances involved, we also carefully evaluated the effect of blending on the power-law index α of the LFs. Extensive photometric completeness simulations were done, as well as checking the effects of sample binning, cluster spatial distribution, and foreground contamination, which turned out to not be significant. The main results from this work can be summarised as:

1. The SSC luminosity function is probed at high completion down to $M_K \sim -14$ or -15 mag in our sample. In this range all the LFs are reasonably well fitted by a single power-law, though in the case of IRAS 18293−3413 a double power-law or a Schechter function is a better approximation. The values of the best-fit slopes vary with a wide range from $\alpha = 1.5$ to 2.4 with a median value of $\alpha = 1.86 \pm 0.24$, and the combined SSC LF, excluding the most distant target, at $\alpha \approx 1.98$. The slopes appear slightly flatter than those in normal spirals which typically have $\alpha \approx 2.4$. Targets with the most extreme SFR appear to exhibit a shallower LF slope. One or more of age, extinction, and mass-dependent cluster disruption effects can all lead to small α values at the faint end, but cannot be unambiguously separated from the present dataset alone.

2. We carefully examined the possibility of blending of SSCs in our target LIRGs. Though blending does happen with the typical resolutions of 30 to 40 pc physical sizes of our sample, we showed that it is not enough to change the LF slopes by more than $\Delta\alpha \approx 0.05 - 0.1$, nor change drastically the measured luminosities of SSCs as long as the target does not lie beyond ≈ 100 Mpc. Hence we conclude that out to that luminosity distance, it is quite possible to accurately measure SSC properties with 8-m class telescope adaptive optics and *HST* imaging. In addition to deriving some general blending/confusion properties, we found that the photometric apertures used do not affect the LF slope, but small apertures are necessary to recover the luminosities as correctly as possible. Worsening spatial resolution tends to flatten the measured LF slopes through increasing blending. However, the effect becomes pronounced only when close to the confusion limit. In the case of SSCs distributed as in the Antennae, we determined that LF slopes at $M_H < -12$ are not reliable if the spatial resolution corresponds to a physical size larger than ~ 50 pc.

All our findings in this Chapter are based on observations with a single filter and thus the estimation of ages of the star cluster candidates is beyond the scope of this Chapter. However, Chapter 5 reports the physical characteristics of the selected star cluster candidates with the help of archival HST data to be able to constrain the SSC evolution models. In addition, with a larger sample of southern LIRGs and starbursts with the VLT/NACO currently available, and the next generation of multi-conjugate AO systems promising to deliver much more stable PSFs across a larger field of view we expect to increase both the number and quality of SSC LFs to probe correlations with LIRG host galaxy characteristics and environments.

References

Adamo, A., Östlin, G., Zackrisson, E., et al. 2010, MNRAS, 407, 870

Adamo, A., Östlin, G., Zackrisson, E., & Hayes, M. 2011a, MNRAS, 414, 1793

Adamo, A., Östlin, G., Zackrisson, E., et al. 2011b, MNRAS, 415, 2388

Alonso-Herrero, A., Rieke, G. H., Colina, L., et al. 2009, ApJ, 697, 660

Alonso-Herrero, A., Rieke, G. H., Rieke, M. J., et al. 2006, ApJ, 650, 835

Anders, P., Bissantz, N., Boysen, L., et al. 2007, MNRAS, 377, 91

Ashman, K. M. & Zepf, S. E. 1992, ApJ, 384, 50

Bastian, N. 2008, MNRAS, 390, 759

Bastian, N., Adamo, A., Gieles, M., et al. 2011, MNRAS, 417, L6

Bastian, N., Saglia, R. P., Goudfrooij, P., et al. 2006, A&A, 448, 881

Benedict, G. F., Higdon, J. L., Jefferys, W. H., et al. 1993, AJ, 105, 1369

Bertin, E. & Arnouts, S. 1996, A&AS, 117, 393

Bik, A., et al. 2003, A&A, 397, 473

Buta, R., Crocker, D. A., & Byrd, G. G. 1999, AJ, 118, 2071

Cabrera-Ziri, I., Bastian, N., Longmore, S. N., et al. 2015, MNRAS, 448, 2224

Cantiello, M., Brocato, E., & Blakeslee, J. P. 2009, A&A, 503, 87

Chandar, R., Whitmore, B. C., Calzetti, D., et al. 2011, ApJ, 727, 88

Chandar, R., Whitmore, B. C., Kim, H., et al. 2010, ApJ, 719, 966

de Grijs, R., Anders, P., Bastian, N., et al. 2003a, MNRAS, 343, 1285

de Grijs, R., & Parmentier, G. 2007, Chinese J. Astron. Astrophys., 7, 155

de Grijs, R., Anders, P., Zackrisson, E., & Östlin, G. 2013, MNRAS, 431, 2917

Eddington, A. S. 1913, MNRAS, 73, 359

Elbaz, D., Dickinson, M., Hwang, et al. 2011, A&A, 533, A119

Elmegreen, B. G. & Efremov, Y. N. 1997, ApJ, 480, 235

Elmegreen, D. M., Chromey, F. R., McGrath, et al. 2002, AJ, 123, 1381

Elmegreen, D. M., Chromey, F. R., Sawyer, J. E., & Reinfeld, E. L. 1999, AJ, 118, 777

Escala, A. 2011, ApJ, 735, 56

Escala, A. & Larson, R. B. 2008, ApJL, 685, L31

Fall, S. M. & Chandar, R. 2012, ApJ, 752, 96

Fall, S. M., Chandar, R., & Whitmore, B. C. 2009, ApJ, 704, 453

Fouesneau, M., Lançon, A., Chandar, R., & Whitmore, B. C. 2012, ApJ, 750, 60

Fritze-v. Alvensleben, U. 1999, A&A, 342, L25
Gieles, M., Larsen, S. S., Bastian, N., & Stein, I. T. 2006a, A&A, 450, 129
Gieles, M., Larsen, S. S., Scheepmaker, R. A., et al. 2006b, A&A, 446, L9
Gieles, M., Portegies Zwart, S. F., Baumgardt, H., et al. 2006, MNRAS, 371, 793
Haas, M. R., Gieles, M., Scheepmaker, et al. 2008, A&A, 487, 937
Ho, L. C. & Filippenko, A. V. 1996, ApJL, 466, L83
Holtzman, J. A., Faber, S. M., Shaya, E. J., et al. 1992, AJ, 103, 691
Inami, H., Armus, L., Surace, J. A., et al. 2010, AJ, 140, 63
Kankare, E., Mattila, S., Ryder, S., et al. 2008, ApJL, 689, L97
Kankare, E., Mattila, S., Ryder, S., et al. 2012, ApJL, 744, LL19
Kennicutt, Jr., R. C. 1998, ARA&A, 36, 189
Kruijssen, J. M. D., et al. 2012, MNRAS, 421, 1927
Lada, C. J. & Lada, E. A. 2003, ARA&A, 41, 57
Lai, O., Rouan, D., Rigaut, F., Doyon, R., & Lacombe, F. 1999, A&A, 351, 834
Lamers, H. J. G. L. M. 2009, Ap&SS, 324, 183
Lamers, H. J. G. L. M., Gieles, M., & Portegies Zwart, S. F. 2005, A&A, 429, 173
Larsen, S. S. 2002, AJ, 124, 1393
Larsen, S. S. 2008, Mass Loss from Stars and the Evolution of Stellar Clusters, 388, 279
Larsen, S. S. 2009, A&A, 494, 539
Leitherer, C., Schaerer, D., Goldader, J. D., et al. 1999, ApJS, 123, 3
Ma, J., de Grijs, R., Yang, Y., et al. 2006, MNRAS, 368, 1443
Maíz Apellániz, J. & Úbeda, L. 2005, ApJ, 629, 873
Mattila, S., Dahlen, T., Efstathiou, A., et al. 2012, ApJ, 756, 111
Mattila, S., Väisänen, P., Farrah, D., et al. 2007, ApJL, 659, L9
Mengel, S., Lehnert, M. D., Thatte, N., & Genzel, R. 2005, A&A, 443,3 41
Miralles-Caballero, D., Colina, L., Arribas, S., & Duc, P.-A. 2011, AJ, 142, 79
Mora, M. D., Larsen, S. S., Kissler-Patig,et al. 2009, A&A, 501, 949
Östlin, G., Bergvall, N., & Roennback, J. 1998, A&A, 335, 8
Östlin, G., Zackrisson, E., Bergvall, N., & Rönnback, J. 2003, A&A, 408, 887
Pellerin, A., Meurer, G. R., Bekki, K., et al. 2010, AJ, 139, 1369
Pollack, L. K., Max, C. E., & Schneider, G. 2007, ApJ, 660, 288
Portegies Zwart, S. F., McMillan, S. L. W., & Gieles, M. 2010, ARA&A, 48, 431

Randriamanakoto, Z., Väisänen, P., Ryder, S., et al. 2013b, MNRAS, 431, 554
Robin, A. C., Reylé, C., Derrière, S., & Picaud, S. 2003, A&A, 409, 523
Ryder, S. D., Mattila, S., Kankare, E., Väisänen, P. 2014, Proc. SPIE, 9148, 91480D
Sanders, D. B., Mazzarella, J. M., Kim, et. al. 2003, AJ, 126, 1607
Santiago-Cortés, M., Mayya, Y. D., & Rosa-González, D. 2010, MNRAS, 405, 1293
Schweizer, F., Miller, B. W., Whitmore, B. C., & Fall, S. M. 1996, AJ, 112, 1839
Surace, J. A., Sanders, D. B., Vacca, W. D.,et al. 1998, ApJ, 492, 116
Tekola, A. G., Väisänen, P., & Berlind, A. 2012, MNRAS, 419, 1176
Väisänen, P., et al. 2012, Journal of Physics Conference Series, 372, 012045
Väisänen, P., Mattila, S., Kniazev, A., et al. 2008, MNRAS, 384, 886
Väisänen, P., Mattila, S., & Ryder, S. 2009, arXiv:0908.3495
Väisänen, P., Tollestrup, E. V., & Fazio, G. G. 2001, MNRAS, 325, 1241
Vavilkin, T. 2011, Ph.D. Thesis,
Wei, L. H., Keto, E., & Ho, L. C. 2012, ApJ, 750, 136
Whitmore, B. C., Chandar, R., & Fall, S. M. 2007, AJ, 133, 1067
Whitmore, B. C., Chandar, R., Schweizer, F., et al. 2010, AJ, 140, 75
Whitmore, B. C., Chandar, R., Bowers, A. S., et al. 2014, AJ, 147, 78
Whitmore, B. C., Schweizer, F., Leitherer, et al. 1993, AJ, 106, 1354
Whitmore, B. C., Zhang, Q., Leitherer, C., et al. 1999, AJ, 118, 1551
Zhang, Q., Fall, S. M., & Whitmore, B. C. 2001, ApJ, 561, 727

Chapter 4

The NIR brightest star cluster-galaxy SFR relation

Overview

This Chapter reports the first ever brightest cluster magnitude – SFR relation in the NIR regime. Statistical and physical interpretations are provided to explain the relation. This work is summarized in (Randriamanakoto et al. 2013a).

4.1 Introduction

The brightest star cluster magnitude versus the SFR of the host galaxy is a well-known empirical relation originally established by Larsen (2002) in the optical waveband (see Figure 1.10). Such a relation is used to investigate whether or not galactic environments influence the formation and evolution of massive star clusters. A compilation of all the optical data having been published so far was used by Adamo et al. (2011) to output the latest version of the empirical relation. Section 1.4.1 covers a brief overview of the various statistical and physical arguments being suggested to explain the correlation between the V-band cluster magnitude and the galaxy SFR.

So far the validity of the relation has only been tested in the optical regime, and mostly using fairly nearby star-forming galaxies. Extinction effects are difficult to correct for especially in the dustier galaxies and will necessarily introduce scatter in the relation; using redder wavelengths will significantly improve the situation. With adaptive optics, it is now possible to probe more distant host galaxies and thus increase the SFR baseline. *Will the relation still hold in the near infrared and at larger SFR levels? Can we see effects of random sampling, and/or are there clear physical processes behind the relation?* This work will use K-band AO imaging of strongly star-forming galaxies to address these

questions.

Along with Miralles-Caballero et al. (2011) and our pilot study Randriamanakoto et al. (2013b), it is now for the first time possible to use statistical samples of luminous infrared galaxies to study SSC properties. Such targets are interesting because they extend the SSC environments to high and extreme levels of SF activity. The Chapter is organized as follows: Section 4.2 describes the sample and observations. Section 4.3 discusses properties of the brightest star clusters. The results are presented in Section 4.4 and discussed in Section 4.5. Summary and conclusion of the work are given in Section 4.6.

4.2 The sample

Strongly star-forming galaxies of the SUNBIRD survey form the sample of this work. These are the targets listed in Table 2.1 but excluding IRAS 10173+0828 which, apparently, does not host any SSC candidates in its field down to our detection limits. The NIR FoV of ESO 440−IG058 and ESO 550−IG025 included both the northern and the eastern components of the interacting system. To increase statistics, we considered each galaxy pair as an individual target. We thus have a statistical representative sample of 43 IR-bright galaxies in total which were imaged in the K-band with the VLT/NaCo and the Gemini/NIRI instruments. More details on the observations and data reduction are described in Chapter 2.

Refer to Section 2.4.2 for a description of aperture photometry and photometric calibration which are crucial in order to output accurate estimates of the star cluster luminosities. SSC candidate selections were performed in a robust way to make sure that a foreground star on top of the galaxy is not to be confused with the brightest star cluster of the catalogue (see Section 2.5).

Star-formation rate of the targets

Since we had selected "cool" IRAS galaxies to form our sample and assuming, as usual, that the SFR of strongly star forming galaxies is well represented by their IR luminosity, the following empirical relation by Kennicutt (1998) was used to convert the L_{IR} to SFR for each galaxy:

$$\frac{\mathrm{SFR}}{\mathrm{M_{\odot}yr^{-1}}} = 1.7 \times 10^{-10} \mathrm{L_{IR}\,[L_{\odot}]}. \tag{4.1}$$

The resulting SFR of each target is listed in Table 2.4.

If the galaxy is a close pair or a multiple system, its IR luminosity has to be separated into individual components since the Sanders et al. (2003) values are for the whole system

due to the poor spatial resolution of IRAS. Therefore, we used WISE 12 and 22 μm, Spitzer/MIPS 24 and 60 μm, and Herschel/PACS 70 μm archival data[a] to measure the flux from each galaxy component and the IRAS-based L_{IR} was redistributed according to the average ratio from all those wavelengths that were available and resolved. This method was adopted for these targets: ESO 440−IG058, MCG −02-01-052, MCG −02-33-098, ESO 491−IG020, ESO 550−IG025, and IC 694/NGC 3690 (=Arp 299).

4.3 The brightest star cluster candidates

4.3.1 Luminosity

Once the SSC candidates were selected, the most luminous K-band star cluster was extracted from each catalogue to derive the brightest cluster magnitude − SFR relation. Note, however, that we might have missed the detection of the *real* brightest star cluster because of an unsuccessful AO correction and hence a poor resolution of the final science image. Another possibility is that the *real* brightest cluster lies within complex background regions of the galaxy. This results into a higher uncertainty of its magnitude and subsequently a potential exclusion from the final catalogue. Furthermore, it could simply be that the *real* brightest cluster is still enshrouded in its dust cocoon where heavy extinction makes it difficult to be detected even in the NIR. Nevertheless, we believe that there is no significant difference between the magnitude of the *real* brightest cluster and that of the selected one in a statistical sense over the sample.

With an uncertainty range of $\sim 0.1 - 0.2$ mag, K-band absolute magnitudes of the brightest star clusters vary between −18.8 mag and −15.5 mag in a Vega-based system for targets with a luminosity distance less than 150 Mpc. The luminosities of the clusters exceed −19 mag for the three most distant targets: IRAS 06076−2139 ($D_L = 160$ Mpc), IRAS 01364−1042 ($D_L = 201$ Mpc), and IRAS 19115−2124 ($D_L = 206$ Mpc). Blending effects may be a concern. The physical spatial resolution in our survey, corresponding to the $\sim 0.1''$ PSF size, is typically 20 to 60 pc. Thus, individual detections of SSC candidates could potentially be blends of more than one intrinsic SSC. The effect may not be too severe for the brightest clusters, since our MC simulation analyses in Section 3.5.1 showed that a single bright SSC will overwhelmingly dominate the luminosity of a SSC candidate detection when small apertures are used, except in the most distant targets approaching $D_L \sim 200$ Mpc, or in case of very strong clustering of SSC regions. Nevertheless, we perform further checks of blending effects in Section 4.4.1. The absolute magnitude of the brightest cluster as well as its distance from the nucleus are tabulated in Table 2.4.

[a] http://irsa.ipac.caltech.edu, http://herschel.esac.esa.int

4.3.2 Spatial distribution

Prior to exploring the brightest cluster magnitude − SFR relation, we first checked whether there is a correlation between the luminosity of the brightest cluster and its position in the galactic field. The resulting plot is displayed in Figure 4.1 which simply shows scattered data with no correlation. Most of the brightest clusters reside in the galaxy disks with a distance $\lesssim 1.5$ kpc from the nucleus. Assuming that the brightest star clusters are very young star clusters, their spatial distributions, which preferentially lie in the inner star-forming regions of the galaxy should not be surprising. It can be explained by the ongoing extreme SF activity that is able to produce very bright clusters at birth.

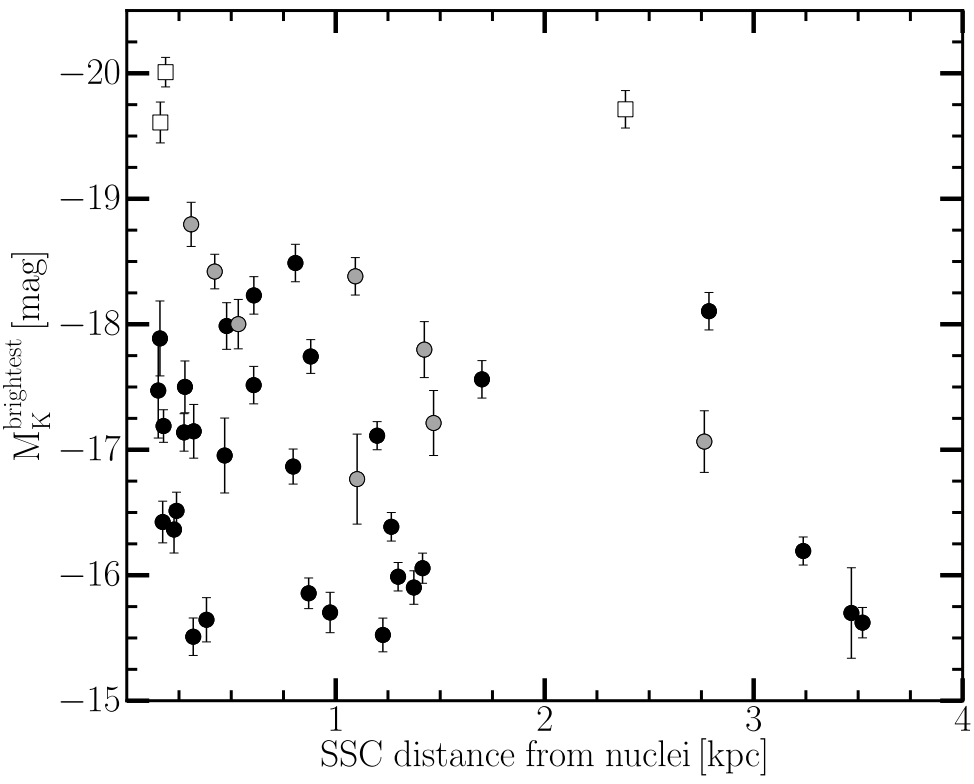

Figure 4.1: The K-band absolute magnitude of the brightest cluster plotted against its distance with respect to the galaxy nucleus. The three most distant targets at $D_L > 150$ Mpc are labelled as open squares, the $D_L \leq 150$ Mpc targets as filled circles where those at $D_L \leq 100$ Mpc are black and those at $100 < D_L \leq 150$ Mpc are grey.

4.4 The relation

The NIR brightest cluster − SFR relation is shown in Figure 4.2. A weighted linear fit to *all* the points results in the following relation, shown as the dashed line in Figure 4.2:

$$M_K^{brightest} = -3.10(\pm 0.06) \times \log \text{SFR} - 12.75. \tag{4.2}$$

Note that the photometric uncertainties of the redistributed L_{IR} points (see Section 4.2) were doubled as these cases may introduce bias to the fitting procedure.

As already mentioned in Section 4.3.1, blending effects cannot be neglected. Therefore, more analyses were done in Section 4.4.1 to generate a reliable relation. We also ran a MC simulation in Section 4.4.2 to investigate the origin of the scatter in the relation.

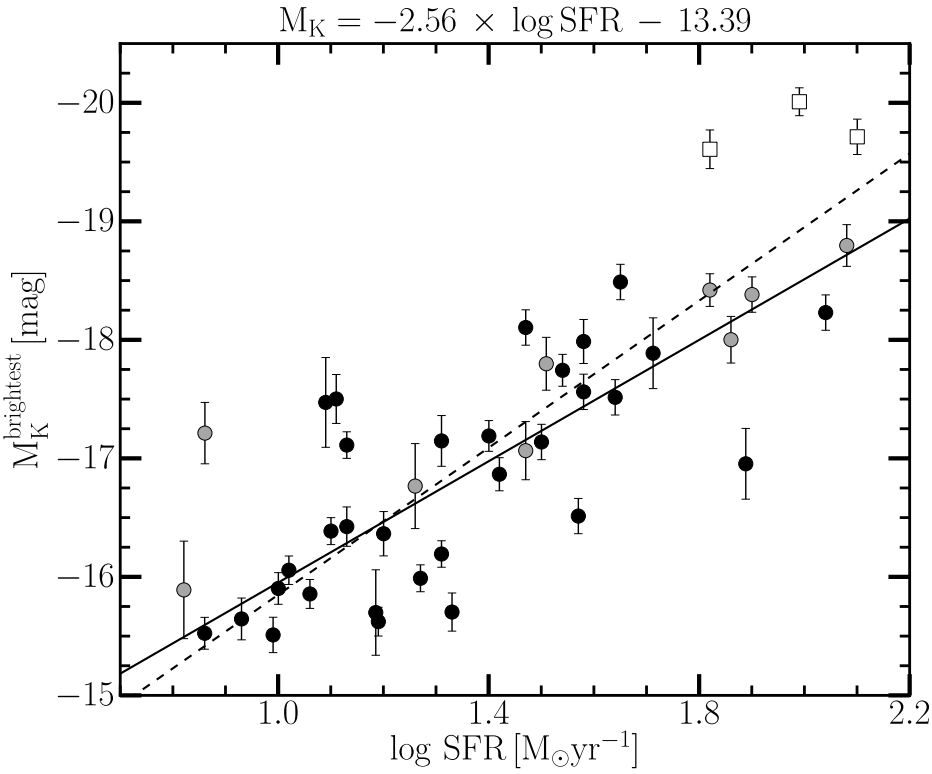

Figure 4.2: Empirical relation between the NIR magnitude of the brightest cluster and the SFR of the galaxy. The dashed line shows a weighted linear fit to all the data, including the three most distant targets at $D_L > 150$ Mpc shown as open squares. The solid line fits the $D_L \leq 150$ Mpc targets labeled as circles; those at $D_L \leq 100$ Mpc are black and those at $100 < D_L \leq 150$ Mpc are gray.

4.4.1 More analysis on blending effects

We also performed several linear fits to the relation by considering different distance cutoffs D_L^{cutoff} to the data points: i.e. $70 \leq D_L^{cutoff} \leq 210$ Mpc. Table 4.1 shows the values of the derived slopes and the corresponding reduced Chi-squares.

The slope does not vary significantly and spans in the range of -2.49 ± 0.08 to -2.56 ± 0.07 with distance limits set in between 80 and 150 Mpc. Therefore, we decided to check for blending effects in the following way: the M_K vs. SFR relation was fit for the "safe"galaxies at $D_L \leq 80$ Mpc (the slope is -2.50 ± 0.09 in this case), and Figure 4.3 then plots the *difference* of the brightest M_K from this best-fit relation versus the distance of the host. If distance plays no part, a scatter plot is expected. Indeed, no systematics are seen, apart from the 3 most distant targets falling significantly above the null-hypothesis line. We interpret this as the brightest SSC in those 3 targets potentially being contaminated by other clusters and exclude them from further analysis. In fact, the correlation coefficients, including and excluding the most distant targets, are equal to $r = 0.50 \pm 0.01$ and $r = 0.27 \pm 0.09$, respectively. We obtain a new best fit when using a $D_L \leq 150$ Mpc constraint:

$$M_K^{brightest} = -2.56 \times \log \mathrm{SFR} - 13.39 \tag{4.3}$$

where $\chi^2_{red} = 13.27$ with a formal uncertainty of ± 0.07 in the slope. The new fit is represented by the solid line in Figure 4.2.

Table 4.1: The different slopes and χ^2 values of the relation

D_L^{cutoff} (Mpc) (1)	# data (2)	slope (3)	χ^2_{red} (4)
210	43	-3.10 ± 0.06	17.53
200	41	-2.72 ± 0.07	15.16
150	**40**	$\mathbf{-2.56 \pm 0.07}$	**13.27**
130	38	-2.56 ± 0.07	14.03
110	36	-2.51 ± 0.07	14.63
100	31	-2.52 ± 0.08	15.49
90	28	-2.49 ± 0.08	13.83
80	27	-2.50 ± 0.09	14.38
70	19	-1.89 ± 0.11	17.24

Notes. Column 1: the distance cutoff; Column 2: the number of targets with distances $< D_L^{cutoff}$; Columns 3 & 4: the resulting slope and χ^2 from the linear fits to the relation. The row with bold texts corresponds to the best fit where $D_L^{cutoff} = 150$ Mpc.

Note that had we excluded the eight Gemini galaxies, we would still get a slope of -2.43 ± 0.08; the difference is within $\sim 1.5\sigma$ of the overall fit and does not affect any conclusions.

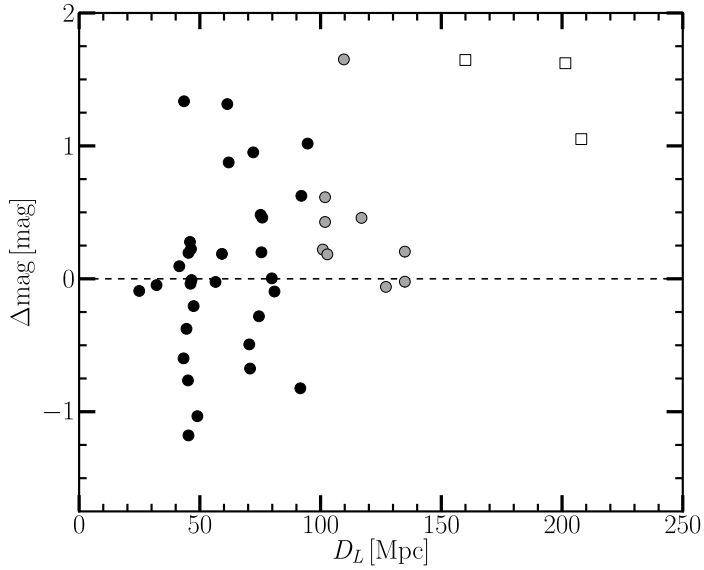

Figure 4.3: The difference in magnitudes, as a function of distance, of the brightest cluster M_K from a relation such as shown in Figure 4.2 but fit for targets closer than 80 Mpc. The dashed line represents the null-hypothesis line. Symbols as in Figure 4.2.

4.4.2 MC simulation: the scatter in the relation

The scatter of the observed M_K values in Figure 4.2 is ≈ 0.62 mag. Such a value is smaller than in relations derived in the optical showing $\sigma \sim 1$ mag (Larsen 2002), unsurprising since extinction effects are smaller. Given that the SFR determination uncertainties should be of the order of 0.4 dex the observed scatter is surprisingly small, however. We ran MC simulations where a given LF with no physical upper limit was sampled purely randomly and the magnitude of the brightest cluster was recorded. The $M^{brightest}$ distribution is narrower with steeper LFs parametrized with the power-law index α. In particular, we find $\sigma = 1.15$ for $\alpha = 2.0$, and $\sigma = 0.77$ and 0.58 for $\alpha = 2.5$ and 3.0, respectively, each with uncertainties of ≈ 0.02. In case of purely statistical sampling the scatter in our relation must hence be the result of steeper than observed LFs of $\alpha > 2.5$ – or there are other physical characteristics at play which determine the luminosity of the brightest cluster. More discussions on the results are presented in Section 4.5.

4.5 Discussion

Both statistical and physical interpretations are suggested to explain the brightest cluster magnitude − SFR relation in the NIR regime. We also compared our results with the optical V-band relation from the literature.

4.5.1 Statistical interpretation

Larsen (2002) suggested purely statistical terms to explain the brightest cluster − SFR relation in the V-band. To explore this possibility in the NIR, $M_K^{brightest}$ is plotted against the number of SSC candidates brighter than a certain absolute magnitude level. We select $M_K = -15$ mag since at that level we do not yet need completeness corrections. The result can be seen in Figure 4.4. This correlation is consistent with the idea that the more clusters are forming in a galaxy, the higher will be the probability to sample the brightest ones from a given LF of the overall population Larsen (2002). The empirical relation can also be tied to the slope of the LF. If the L^{max} of the most luminous object scales with the total number N of the clusters as given by Whitmore (2003):

$$L^{max} \sim \mathrm{N}^{\eta}, \tag{4.4}$$

then by using the equation from Hunter et al. (2003):

$$\eta = \frac{1}{\alpha - 1} \tag{4.5}$$

we can derive the power-law slope α of the cluster luminosity function at higher luminosities. The best-fit $\eta = 0.64$ corresponds to $\alpha = 2.56$ which is not unreasonable for bright parts of SSC LFs (Portegies Zwart et al. 2010). From the 10 LIRGs in Randriamanakoto et al. (2013b) we found a slope of $\alpha \sim 1.9$ (flatter than for normal spirals) which corresponds to $\eta = 1.1$ – this is overplotted in Figure 4.4 as the dashed line and is seen to represent the data at $\log \mathrm{N} > 0.5$ fairly well.

In summary, while the characteristics of the number of detected SSCs vs. SFR are consistent with a size-of-sample effect, the tightness of the brightest cluster vs. SFR relation in particular suggests that it would be premature to reject an underlying physical cause for this relation.

4.5.2 Physical interpretations

Clusters are born of collapsing giant molecular clouds which inevitably are affected by their galactic environments, especially in cases of interacting and merging galaxies – how this environment exactly defines SSC properties, and disruption, is a matter of intense debate (e.g. Lamers 2009). Specifically regarding the brightest cluster vs. SFR relation, Adamo et al. (2011) have shown how SSCs in luminous blue compact galaxies appear elevated from the general relation, and suggest this could be a result of a higher cluster formation efficiency in their extreme environments. Larsen (2009) and Gieles (2009) suggest that the characteristic cluster mass may change as a function of environment, and grow in the more intense SFR of interactions and mergers. One appealing possibility

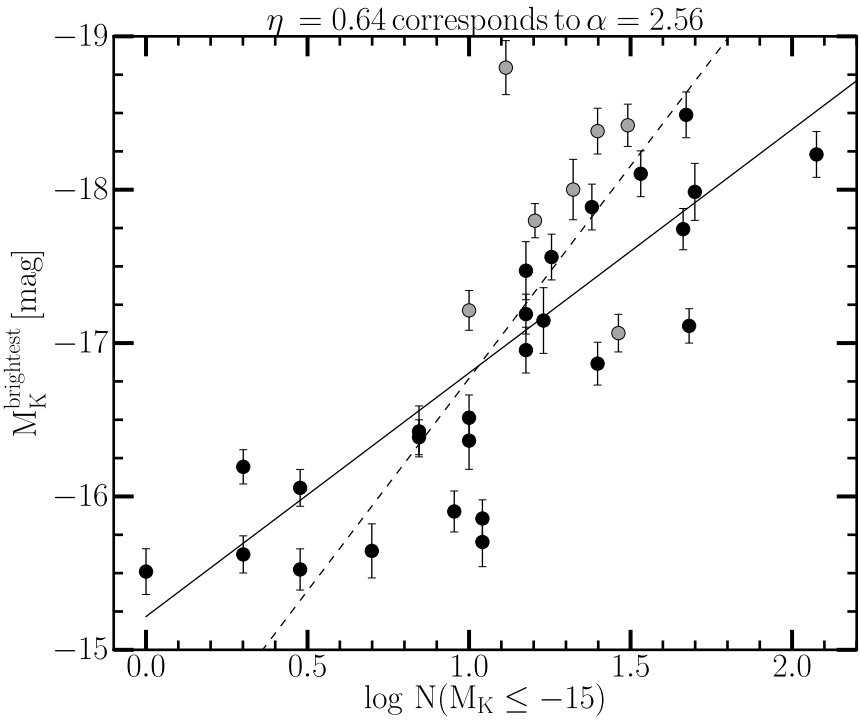

Figure 4.4: $M_K^{brightest}$ as a function of the number of the star clusters brighter than -15 mag for targets with $D_L \leq 150$ Mpc. The solid line is the best-fit relation with an uncertainty in the slope of ± 0.18, whereas the dashed line corresponds to a LF power-law slope of $\alpha = 1.9$. Within their respective uncertainty ranges, both dashed and solid lines still clearly represent two different sets of relation. Symbols as in Figure 4.2.

for such a change is the lack of large scale rotation in galaxy mergers (Escala & Larson 2008; Weidner et al. 2010; Escala et al. 2013).

In addition, there might well be internal constraints on SSC properties. In the following we outline a possible physical interpretation of the brightness vs. SFR relation based on the idea that the total luminosity, and mass, of a stellar cluster is weighted towards its highest-mass star, and these stellar masses may also be correlated with the environments of the clusters (e.g. Weidner et al. 2009).

The total luminosity of a cluster can be computed for a given IMF and mass-luminosity relation. Assuming a mass-luminosity relation of the form:

$$L \propto \mathrm{m}^{\alpha_1} \tag{4.6}$$

and a power law IMF:

$$dN/dm \propto m^{-\beta}\,, \tag{4.7}$$

the total luminosity of a cluster is given by:

$$L_{tot} \propto \mathrm{M}_{\mathrm{cl}}^{(\alpha_1-\beta+1)\gamma} \tag{4.8}$$

where $\mathrm{M_{cl}}$ is the total mass of the cluster. $\mathrm{M_{cl}}$ is assumed to satisfy a relation with the most massive star of such cluster:

$$M_{star}^{max} \sim M_{cl}^{\gamma} \tag{4.9}$$

where $\gamma \sim 0.45$ estimated from observations and $\gamma \sim 2/3$ predicted from simulations (see Weidner et al. 2009 for a review of different estimates).

Assuming that the most massive unstable gas cloud in a galaxy, $\mathrm{M_{cloud}^{max}} \sim \mathrm{f_{gas}^2 M_{gas}}$ (Escala & Larson 2008), leads to the formation of the most massive SSC ($\mathrm{M_{cl}} \propto \mathrm{M_{cloud}^{max}}$) and taking into account the correlation between such a cloud and the SFR in galaxies:

$$SFR \propto [M_{cloud}^{max}]^{\delta} \tag{4.10}$$

with $\delta \sim 1.5$ (Escala 2009, 2011), the total luminosity of the brightest cluster is given by:

$$L_{tot}^{brightest} \propto \mathrm{SFR}^{(\alpha_1-\beta+1)\gamma/\delta} \tag{4.11}$$

Finally, this can be expressed in terms of absolute magnitude by:

$$M_K^{brightest} \propto -2.5 \log L_K^{brightest} \tag{4.12}$$

resulting in the following expression:

$$M_K^{brightest} \propto -2.5 \, \frac{(\alpha_1 - \beta + 1)\gamma}{\delta} \, \log \mathrm{SFR} \tag{4.13}$$

For a Salpeter IMF ($\beta = 2.35$), $\delta = 1.5$ (Escala 2009, 2011), $\gamma \sim 0.45$ estimated from observations (Weidner et al. 2009) and a slope of the mass-luminosity relation of $\alpha_1 \sim 5$, Equation 4.13 gives a slope closer to -3 in the brightest cluster $-$ SFR relation, which is comparable to the slope observed if we use the whole sample (Equation 4.2). On the other hand, if the mass-luminosity relation has a slope of $\alpha_1 \sim 4$, Equation 4.13 gives a slope ~ -2, which is closer to that derived from our data excluding potentially blended cases (Equation 4.3).

Unfortunately, we do not have a good estimate for the slope α_1 of the mass-luminosity relation at high masses (Equation 4.6) – it may, for example, vary in between 1.76 and 8.87 depending on the highest mass of a star in a cluster for masses larger than $7\,\mathrm{M_\odot}$ (Parravano et al. 2003). Nevertheless, Equation 4.13 may be used as a simple physical interpretation of the effects characterizing SSC properties at scales ranging from internal to galactic.

4.5.3 Comparison to the V-band relation

Figure 4.5 shows the brightest cluster - SFR relation with an expanded scale. The triangles are V-band data as compiled by Adamo et al. (2011), assuming a constant $V - K = 2$ conversion, typical for a ~ 10 Myr age stellar population. The solid line is the best fit slope of -2.56 from our own NIR data extrapolated to lower SFRs. It appears that the optical points would require a slightly flatter slope, and indeed Weidner et al. (2004) find ~ -1.9 shown as the dashed line, though Larsen (2002) derives ~ -2.5 from a subset of the data. The simplest explanation could perhaps be extinction: the highest SFR galaxies, LIRGs and ULIRGs, are predominantly interactions and mergers with more dust on average than lower SFR galaxies (Piqueras López et al. 2013). The uncorrected optical points at higher SFR could lie too low artificially, thus flattening the slope. However, with this data-set alone it is not possible to confirm this – it could as well be that the brightest clusters detected in V-band are not necessarily (always) the most luminous clusters in K-band possibly implying age effects. That the slope appears slightly different necessarily points to some systematic effects along the SFR base-line, i.e. a constant $V - K$ shift is not appropriate.

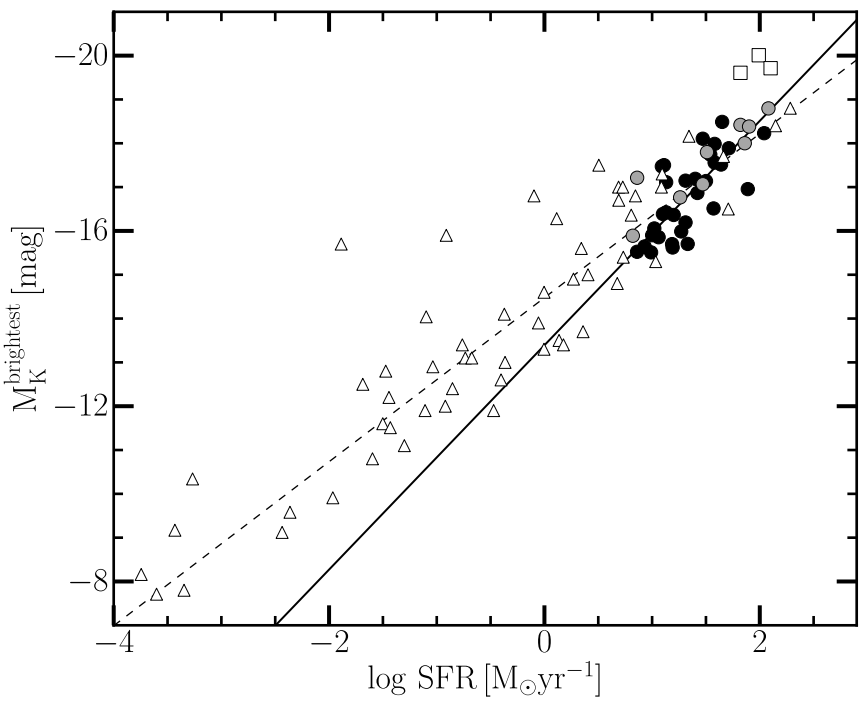

Figure 4.5: The $M^{brightest}$ – SFR relation with data from literature (the triangles, Adamo et al. 2011, and references therein) added to the present work (symbols as in Figure 4.2). The solid line is our best fit of Equation 4.3 and the dashed line is the fit from Weidner et al. (2004) to the optical V-band data after a constant $V - K = 2$ conversion.

The slope may become steeper if the points at higher SFR, preferentially, are bound results of mergers of individual SSCs in very dense star cluster complexes Fellhauer & Kroupa (2005). We also note that outliers below the relation can be understood as cases where the brightest SSC is not detected, or is severely extincted. And as discussed by Bastian (2008), outliers above the line may be cases where the detected cluster is significantly older than the general population of brightest SSCs. These are very interesting questions to tackle with combinations of optical and NIR data in the future.

4.6 Summary and conclusions

From a K-band AO sample of 43 strongly star-forming galaxies, mostly LIRGs, we establish the brightest cluster magnitude - SFR relation in the NIR regime. The relation is much less affected by extinction effects than similar comparisons in the V-band. We find a slope of -2.56 which is similar to those from optical derivations made at lower star formation rate levels, though the extension of our slope appears to not be consistent with the full range of optical SSC luminosities if a single $V-K$ conversion is adopted. We suggest that a systematic extinction effect, where SSCs in higher SFR hosts live in dustier environments, would be a simple explanation for the trend, but systematic age differences may also be involved.

A good correlation of the most luminous cluster and the number of SSCs with M_K magnitude brighter than -15 shows that a size-of-sample effect is broadly consistent with the observed $M_K^{brightest} - \mathrm{SFR}$ relation. On the other hand, the observed scatter in the relation is surprisingly small, and we show that it can be explained with random sampling effects *only* if the LF of SSCs is very steep at the bright end, steeper than usually observed. The steepening and the scatter would be naturally expected if the MF has a physical truncation at the bright end (Väisänen et al. 2014). Hence, physical reasons determining the luminosity of the brightest SSC from host properties, and/or internal cluster effects, likely play a role as well. We derived a relation tying the stellar IMF and mass-luminosity relations together with the global SF properties of the host in explaining the observed brightest cluster magnitude - SFR relation.

In the next steps of the work we will investigate the environments and extinctions of the host galaxies and masses and ages of the SSCs inside them in more detail with a combination of optical and NIR data. These will allow more secure disentanglement of the various effects governing the lives and characteristics of super star clusters in galaxies.

References

Adamo, A., et al. 2011, MNRAS, 417, 1904

Bastian, N. 2008, MNRAS, 390, 759

Escala, A. 2009, ArXiv e-prints

Escala, A., 2011, ApJ, 735, 56

Escala, A., Becerra, F., del Valle, L., & Castillo, E. 2013, ApJ, 763, 39

Escala, A. & Larson, R. B. 2008, ApJL, 685, L31

Fellhauer, M. & Kroupa, P. 2005, ApJ, 630, 879

Gieles, M. 2009, MNRAS, 394, 2113

Hunter, D. A., et. al. 2003, AJ, 126, 1836

Kennicutt, Jr., R. C. 1998, ARA&A, 36, 189

Lamers, H. J. G. L. M. 2009, Ap&SS, 324, 183

Larsen, S. S. 2002, AJ, 124, 1393

Larsen, S. S. 2009, A&A, 494, 539

Miralles-Caballero, D., Colina, L., Arribas, S., & Duc, P.-A. 2011, AJ, 142, 79

Parravano, A., et. al. 2003, ApJ, 584, 797

Piqueras López, J., et. al. 2013, A&A, 553A, 85

Randriamanakoto, Z., Escala, A., Väisänen, P., et al. 2013a, ApJL, 775, L38

Randriamanakoto, Z., Väisänen, P., Ryder, S., et al. 2013b, MNRAS, 431, 554

Sanders, D. B., et al. 2003, AJ, 126, 1607

Väisänen, P., et al. 2014, arXiv:1402.2357

Vavilkin, T. 2011, Ph.D. Thesis

Weidner, C., et. al. 2004, MNRAS, 350, 1503

Weidner, C., et. al. 2009, MNRAS, 393, 663

Weidner, C., et. al. 2010, ApJ, 724, 1503

Whitmore, B. C. 2003, in A Decade of Hubble Space Telescope Science, ed. M. Livio, K. Noll, & M. Stiavelli, 153–178

Chapter 5

SSC mass and age modelling

Overview

This Chapter focuses on modelling the star cluster age, mass, and extinction in a subsample of LIRGs. Mass functions and spatial distribution of age of the SSCs are interpreted to constrain the cluster formation history and to understand the cluster disruption mechanisms at play. The major findings from this work will be reported in Randriamanakoto et al., in prep.

5.1 Introduction

Interpreting the cluster age distribution and the shape of the cluster mass function are important as they can be used to test the universality of the CIMF and hence, to constrain the cluster formation history. Such analyses are also invaluable to determine whether galactic environments in any way influence the evolution and disruption mechanism of the massive proto-GCs (Chandar et al. 2010; Bastian et al. 2011; Johnson et al. 2012; Silva-Villa et al. 2014). Deriving reliable physical parameters of the SSC candidates is therefore necessary to address the issues above and to subsequently trace the star formation history of the host galaxy itself.

The main objective of this Chapter is to derive some of the SSC physical parameters (age, mass, and extinction) using multi-wavelength observations of a subsample of LIRGs. Carefully chosen single stellar population (SSP) models will be compared with the integrated broad-band SSC photometry from different filters to output the desired parameters. Such a photometric age-dating technique works quite well and it has been commonly adopted in the literature (e.g. Bik et al. 2003; Anders et al. 2004), though it may present some caveats in dealing with age-metallicity and age-extinction degeneracies. In this work, we will combine high-spatial resolution NIR AO images with archival HST

data for an optimal comparison with the model. The Chapter is split into two different but complementary main sections. Section 5.2 will report the SSC physical properties in the Arp 299 interacting system whereas Section 5.3 will discuss the star cluster properties hosted by a subsample of five other LIRGs. While each section has its own discussion and summary, general concluding remarks of the Chapter are given in Section 5.4.

5.2 The case of Arp 299

Arp 299 is a nearby luminous IR galaxy system ($\log L_{\rm IR} = 11.88\,L_{\odot}$, Sanders et al. 2003) in an early merging stage and at a distance of 45.3 Mpc (see Table 2.1). The interacting system consists of a pair of two irregular galaxies: IC 694[a] in the eastern part, and NGC 3690[b] the western component. While the former is possibly the remnant of a spiral galaxy, the latter on the other hand has a more disturbed morphology with multiple nuclei. Extensive works by Alonso-Herrero et al. (2000, 2002, 2009, 2013) based on multi-wavelength observations concluded that Arp 299 hosts extreme star formation activity with a recent episode of massive star formation mainly enshrouded in the dusty nuclear starburst regions. They also suggested along with Ballo et al. (2004) and Pérez-Torres et al. (2010) that the galaxy nuclei of the merging system harbor two buried AGN. While the AGN in NGC 3690 is a well-studied case due to its extreme activity, the presence of a low-luminosity AGN in the nucleus of IC 694 is still under debate, although it could be the one responsible for a large fraction of IR luminosity emitted by this component. Nevertheless, the co-existence of both AGN and starburst activity makes Arp 299 an excellent candidate to probe the starburst-AGN connection in nearby interacting LIRGs.

The nuclei of these merging galaxies are also known to host a relatively high number of supernova factories (e.g. Neff et al. 2004; Newton et al. 2010; Mattila & Kankare 2010; Bondi et al. 2012; Mattila et al. 2012). Kankare et al. (2014) adopted a novel technique to follow-up the activity of optically hidden core collapse SNe (CCSNe) in the circumnuclear regions of Arp 299. By using laser guide star AO in the NIR, mounted on large 10-m class telescopes, they were able to confirm the detection of SN2010O and SN2010P with a better estimate of the extinction. New SN candidates were also discovered for the first time in the core regions of other LIRGs while applying the same method (Ryder et al. 2014). It is important to study SNe/CCSNe as they can be a direct estimate of the galaxy SFR. In addition, they could be spatially associated with super star clusters (Kankare et al. 2014) which are known to be good tracers of recent massive star formation.

Lai et al. (1999) and Alonso-Herrero et al. (2000, 2002, 2009) have already found in the (near)-infrared regimes a large population of SSCs in the nuclear starbursts and the star-forming regions of Arp 299. Vavilkin (2011), on the other hand, made use of the detailed

[a] IC 694 is commonly known as source A in the literature.
[b] NGC 3690 is commonly known as sources B+C in the literature.

HST/ACS imaging as part of the GOALS survey to trace the photometric properties of the SSCs in this galaxy. For instance, their results argued that the interacting system has very young and extinguished star clusters with a mass range between $\approx 10^4 - 10^6 M_\odot$. However, these previous works did not cover the effects of the environment on the cluster evolution and disruption mechanisms. By combining the wealth of data from HST/WFC3 UVIS camera and the Gemini/NIRI AO systems, this work aims to address such issues with an unprecedented magnitude limit detecting even the low-mass clusters. Arp 299 is the only target that has U-band data available in our sample. Hence, this case definitely helps constrain the age-extinction degeneracy and to develop a more accurate approach on how to deal with the SSC analyses of the galaxies that have only been observed in BIK_s-filters (see Section 5.3). The main results and discussion will be reported in Randriamanakoto et al. (in prep).

5.2.1 Data, source extraction, and HST photometry

We retrieved already-processed science images of Arp 299 from the HST Legacy Archive. For this work we use the images taken in the following broad-band filters: F336W (U), F438W (B), and F814W (I) of WFC3/UVIS camera. More details of the HST observations are provided in Section 2.3.2. Next, we ran the `IRAF` tasks `GEOMAP` and `GEOTRAN` to resample the UBI-images so that their pixel scales match with that of the K-band NIR images. Figure 5.1 shows the galaxy false-color images using UBI- (left panel) and BIK-filters (right panel). A quick glimpse of these RGB images already indicates that Arp 299 hosts a significant number of blue young star clusters.

For object detection, `SExtractor` was ran twice on the unsharped-masked version of the combined BI-images. Such input files were chosen to gain deeper images and to facilitate the extraction of extended objects. The method (i.e. running the software twice with different parameters and combining the results) works quite well with the number of spurious sources in the galactic field being minimized. Two sets of input parameters were chosen to detect the objects from the outer and inner regions which are separated by a certain background contour level. While the minimum object area is always fixed to 10 pixels, the other critical parameters vary as a function of the given region. A minimum detection limit of 4σ combined with a background mesh width equal to 80 is recommended to optimally extract the sources in the outer field. In contrast, a higher threshold of 7σ with a smaller background mesh is necessary to reduce the number of spurious objects in the output catalogues from the inner field.

Since the optical images were resampled already to the K-band image scale, matched-aperture photometry was applied in all $UBIK$-images with a fixed aperture radius of 5 pixels ($\sim 0.1''$) and sky annuli from 7 to 10 pixels ($0.08''$ wide). Figure 5.2 shows the instrumental magnitudes plotted against the respective photometric uncertainties in all four filters for both IC 694 (top) and NGC 3690 (bottom). Such plots can help to estimate a crude error cutoff σ_m (Section 5.2.2). Growth curves of bright and isolated

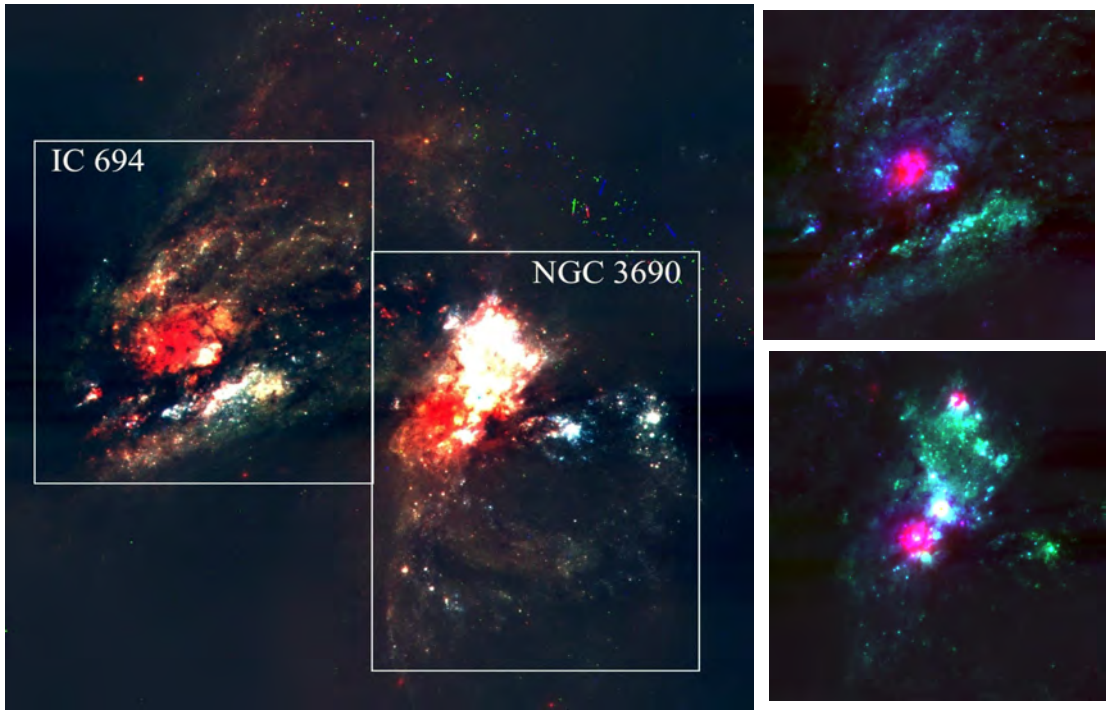

Figure 5.1: *Left:* WFC3/UVIS three-color image of Arp 299 in a 1.4 by 1.2 arcmin field: F336W (U-band, blue), F438W (B-band, green), F814W (I-band, red). The boxes indicate the FoV of the NIR data. Up is North and left is East. *Right:* BIK-color images of the individual components in a $22'' \times 22''$ field: IC 694 (top) and NGC 3690 (bottom). In these cases, B-band (blue) and I-band (green) images were resampled to match with K-band data (red) taken with Gemini/NIRI AO systems.

sources were used to measure the aperture correction, and the VEGAMAG photometric zeropoints were obtained from the HST/WFC3 data manuals. These values along with the foreground Galactic extinction of each filter are listed in Table 5.1. We then corrected the photometry using these parameters and applied a distance modulus of $m - M = 33.28$ mag to derive the Vega-based absolute magnitudes.

Finally, the resulting magnitudes were checked to see whether there is a need to correct for systematic effects because of resampling. Photometry of bright non-saturated sources in the field of both original and resampled HST images were derived using the exact same parameters. The comparison between the two measurements indicates that the values of the visual magnitudes are similar within their photometric errors. Such results confirm that resampling has worked well and that the offsets in the peak of fainter point sources should not be significant either, i.e below 0.5 pixels. Hence, we did not apply any correction. In some cases, the offset might be slightly higher than the above pixel range

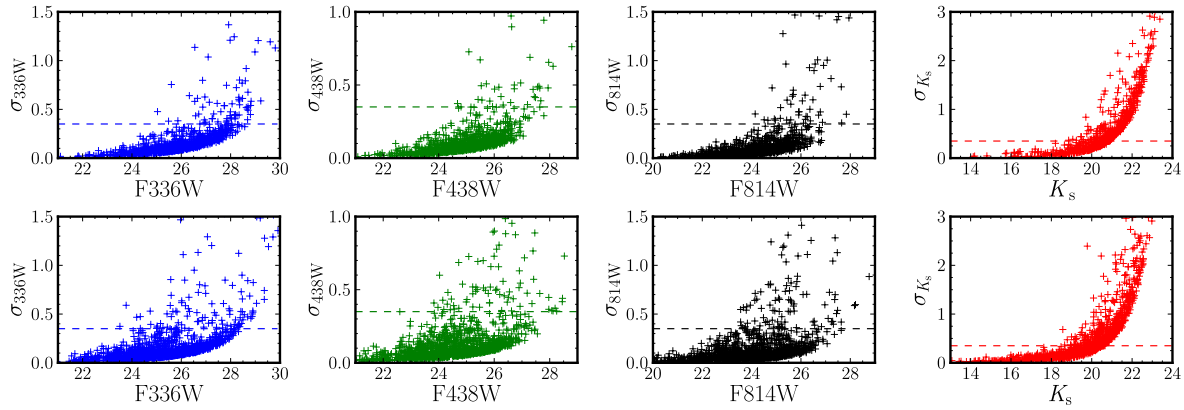

Figure 5.2: $UBIK$-photometric errors of the detected sources plotted against the instrumental magnitudes. Both the uncertainty range and scatter of the data points vary from filter to filter. Figures in the top panels show the data sets from IC 694, whereas the ones in the bottom panels show the plots associated with NGC 3690.

Table 5.1: Photometric measurements of Arp 299.

Filter	A_λ (mag)	PSF/FWHM (arcsec)	$m_0; a_c$ (mag)	N($\sigma < \sigma_m$) (A, B+C)	Mag.limit (Vega-mag)
(1)	(2)	(3)	(4)	(5)	(6)
F336W	0.07	0.09	23.46; −0.41	981, 1253	26.5
F438W	0.06	0.08	24.98; −0.40	1047, 1326	27.3
F814W	0.03	0.07	24.67; −0.52	1026, 1299	26.8
K_S-band	0.01	0.11	27.23; 26.81, −1.23	366, 519	21.6

Notes. Column 1: broad-band filter used; Column 2: foreground Galactic reddening from NED Database; Column 3: FWHM of bright isolated stars in the original image; Column 4: zeropoint magnitude and aperture correction (two different values in the case of K-band images); Column 5: number of SSCs with $\sigma_m \leq 0.35$ mag in both components A and B+C; Column 6: the corresponding Vega-based magnitude limits

simply because of relative extinction effects. We did not adjust the coordinates of such objects; the SSC positions are fixed in all four filters to deliver a measurement in exactly the same physical location.

Note that the above steps (starting from data extraction until photometry calibration) are repeated twice since the galaxy components of Arp 299 were imaged separately in the small FoV of Gemini/NIRI.

5.2.2 Optically-selected clusters and photometric diagrams

The philosophy adopted to draw the optically-selected cluster catalogues remains similar to the one implemented in Section 2.5, except that a cross-identification of the UBI

catalogues to identify common sources in all filters was applied instead of a criterion based on the concentration index vs. FWHM plot. But prior to that step, the catalogues were cleaned from spurious detections, foreground sources, and the galaxy nuclei, by visual inspection of the science images. In addition, only objects with S/N > 3 were to be considered further in each filter. The corresponding Vega-magnitude limits are listed in Table 5.1. In the case of IC 694, 981 (U), 1047 (B), 1026 (I), and 366 (K) objects satisfy such conditions. The numbers are, respectively, 1253, 1326, 1299, and 519 in the case of NGC 3690. Had we applied a much higher signal-to-noise ratio, we would have rejected a significant number of obvious SSCs. For instance, by setting a cutoff error of $\sigma_m = 0.20$ (i.e. S/N > 5), the recorded numbers in the I-band would have changed to 957 and 1181 for IC 694 and NGC 3690, respectively. Age and extinction ranges of the objects with photometric uncertainties close to the chosen upper limit are checked and evaluated separately anyway (refer to Section 5.2.6).

An object passing through the first selection will be included in the final $UBIK$-mag catalogue if it is detected simultaneously across UBI-filters. Hence, 921 and 1138 star cluster candidates were recovered for IC 694 and NGC 3690, respectively. These numbers become 995 and 1229 if the cross-identification only happens between the B- and I-band catalogues. Such numbers are relatively high compared to the ones recorded in Table 2.4 simply because of the different selection method and especially the capability of the new HST WFC3/UVIS camera to deliver sharper images than WFC/ACS data. In cases where `SExtractor` failed to detect an optically-selected SSC in the NIRI field, an actual magnitude, with an uncertainty of 0.5 mag, related to the corresponding K-band magnitude limit was set to represent the Vega-magnitude of the star cluster.

Besides having a much larger SSC population (Table 5.1), NGC 3690 also hosts candidates with brighter magnitudes; for instance, the SSCs have an absolute magnitude range of $-15.1 \lesssim M_B \lesssim -6.5$ in the B-band, whereas this becomes $-13.1 \lesssim M_B \lesssim -6.0$ in the case of IC 694. Section 5.2.6 and Section 5.2.7 give detailed comparison and physical interpretations of the SSC population in the galactic fields of the eastern vs. western components (e.g. spatial distributions, luminosity, age, extinction and mass ranges). Note that the results from our UVIS BI-band photometry are consistent with the measurements done by Vavilkin (2011) using ACS data. The high quality data from UVIS camera however include more SSC detections at fainter magnitude levels.

Figure 5.3 shows the color-magnitude and color-color diagrams (CMD and CCD) for the $UBIK$ SSC candidates (filled circles) with $\sigma_m \leq 0.35$ in IC 694 (left) and NGC 3690 (right). The blue solid line represents an `Yggdrasil` simple stellar population (SSP) model. Refer to Section 5.2.3 for a comprehensive description of this model along with `Starburst99`. For reference, different ages of the synthetic cluster in the evolutionary track are marked with multicolor squares. Constructing the CMD/CCDs are necessary because they provide rough preliminary estimates of the SSC age, mass, and extinction. In addition, they also help to separate star cluster candidates from bright stars, especially if the selection process did not work successfully. In the case of Arp 299, the CMDs

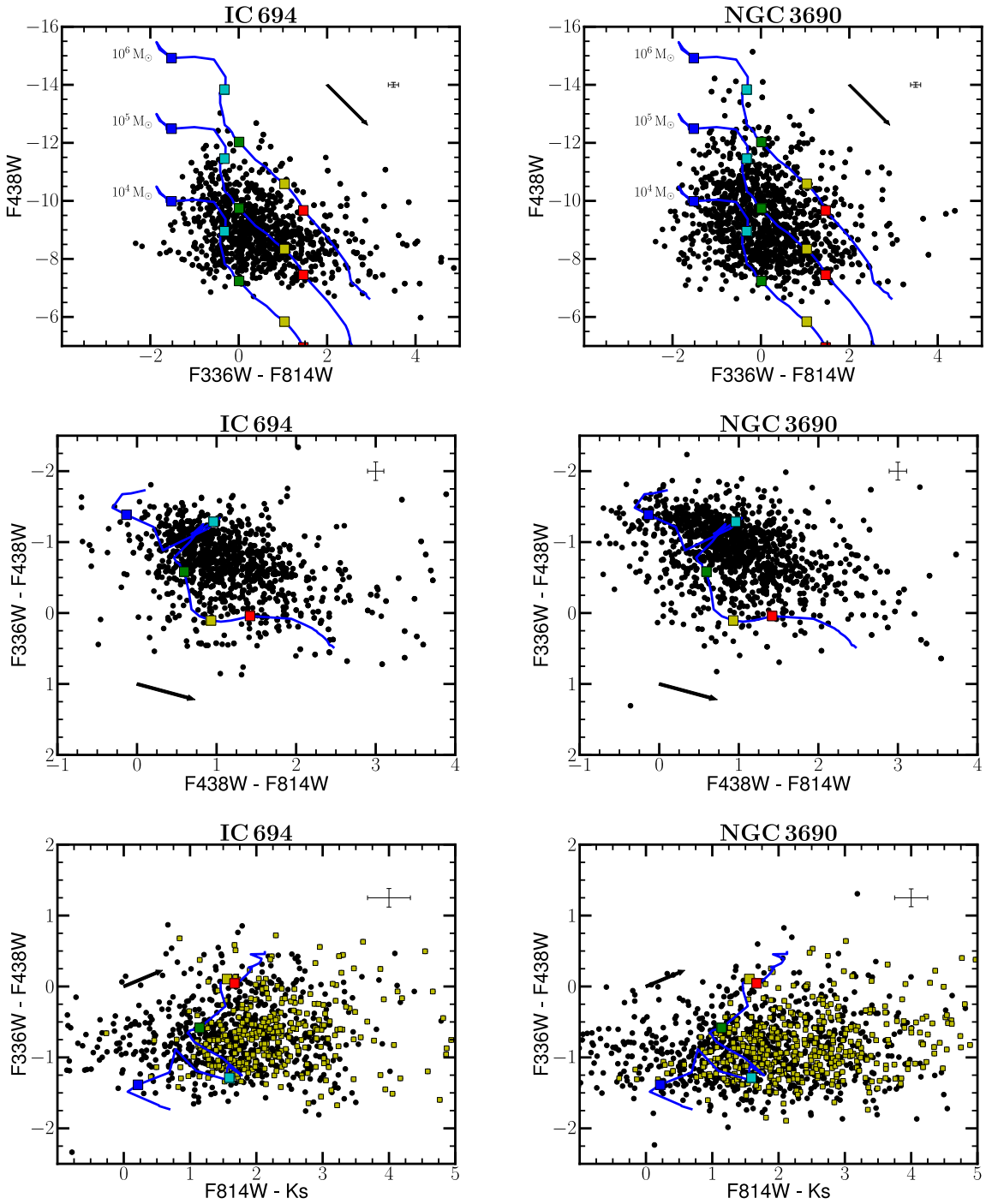

Figure 5.3: SSC CMDs and CCDs of Arp 299 overplotted with `Yggdrasil` SSP models (solid lines). Star clusters with $\sigma_m \leq 0.35$ in $UBIK$- and UBI-images are respectively labelled as filled circles and filled squares. Blue, cyan, green, yellow and red squares, respectively, mark 5, 10, 100, 500 and 1000 Myr in the evolutionary track. The arrows indicate a reddening of $E(B-V) = 0.25$. *Top:* B-band magnitude plotted against $U-I$ color. The model is plotted with 10^4, 10^5, and $10^6 M_\odot$. *Middle:* $U-B$ versus $B-I$ colors. *Bottom:* $U-B$ versus $I-K$ colors.

(top panels) indicate that a vast majority of the SSCs would have a mass range of $\approx 10^4 - 10^6 M_\odot$. The colors of the datapoints (middle & bottom panels), on the other hand, suggest that the merging system hosts a very young population of SSCs with a non-negligible extinction range. Most of the star clusters would probably have an age well below 100 Myr. These simple deductions are confronted with the final results in Section 5.2.6.

Finally, the privilege of having U-band data set should be exploited to its fullest as such a filter helps to break the age-extinction degeneracy. Color-color plots such as $U-B$ vs. $B-I$ are therefore very useful to single out potentially old star clusters amongst the rest of the population.

5.2.3 The models

Appropriate SSP models should be used to determine the age, mass and extinction of the unresolved star clusters. Since IC 694 and NGC 3690 are starburst-dominated galaxies, the SED fitting requires the use of theoretical evolutionary models that will take into account short episodes of extreme star-formation activity. This is the reason we chose `Starburst99 (SB99)` and `Yggdrasil` models to derive the star cluster properties in this work. A brief description of the models is given below:

- **Starburst99** is a well-known evolutionary synthesis code by Leitherer et al. (1999) and has been used extensively in the field of star cluster research (e.g. Zhang & Fall 1999; Bik et al. 2003; Gieles et al. 2007; Andrews et al. 2014). The synthetic cluster magnitudes are specifically designed to reproduce the physical parameters of active star-forming galaxies. Here, they were retrieved under the following assumptions: an instantaneous burst, a solar metallicity $Z = Z_\odot$, a Kroupa IMF with lower and upper mass boundaries of $0.1, 0.5, 100\,M_\odot$ and a Padova-AGB stellar evolutionary model. The age range of the evolutionary track is between 1 Myr and 10 Gyr. We should note that `SB99` models do not consider nebular emission.

- **Yggdrasil** is one of the most up-to-date SSP models, developed by Zackrisson et al. (2011). The computed photometric colors are primarily aimed at modelling the SED of first galaxies and population III stars but they also output reliable fits of star cluster ages (e.g Bastian et al. 2012; de Grijs et al. 2013; Bastian et al. 2014; Ryon et al. 2014). Note that `Yggdrasil` SSP models are based on the `SB99` code with Padova-AGB tracks. However, its interface enables the user to define the gas covering factor, $0 \leq f_{cov} \leq 1$, and the redshift coverage. A factor of $f_{cov} = 1$ and a low redshift coverage were selected. Setting the former parameter to its maximum value means that the model also considers the photoionized gas from nebular emission and continuum. This choice was made to have model colours representing also the very earliest stages at $1 - 3$ Myr when the SSCs have not

emerged from their cocoons yet. For older ages, where the majority of the SSCs are in any case, the covering factor choice makes no appreciably difference in the models. Finally, similar constraints as in `SB99` were set to the other parameters: an instantaneous burst, a solar metallicity with a Kroupa IMF, and an age range between 1 Myr to 10 Gyr.

SSP models with solar metallicity (Z = 0.02) were chosen for both `SB99` and `Yggdrasil` evolutionary tracks to align with the SALT/RSS spectroscopic analyses of the whole SUNBIRD sample where the targets are believed to exhibit a similar range of metallicity (Ramphul & Väisänen, private communication). Applying a constraint in the metallicity range of the model decreases the number of free parameters and hence will strengthen the accuracy of the fit.

As for the empirical reddening function, the extinction law for starburst galaxies, the Calzetti law, was adopted to estimate the extinction coefficient k_λ of each filter ($R_V = 4.05$, Calzetti et al. 2000). After assigning a certain value to the visual extinction A_V, the following formula can be used to estimate the extinctions A_λ of the other filters:

$$A_\lambda = k_\lambda \times \frac{A_V}{R_V} \tag{5.1}$$

The synthetic colors, either in Johnson-Cousins (`SB99`) or AB system (`Yggdrasil`), were first transformed to the Vega-mag system prior to the SED fitting. The resulting ages and extinctions from the two different SSP models are presented in Section 5.2.6.

5.2.4 Extinction map

Using the right SSP model is not enough if we want to derive accurate results from the age and mass modelling. A more quantitative way should also be applied to estimate the extinction to each cluster. Therefore, we produced an extinction map based on the broad-band color map, which is $U - I$ in the case of Arp 299 (Figure 5.4). Each cluster will have its own range of extinction as an input to the χ^2 fitting that way (see the third paragraph of Section 5.2.5 for more details). We adopted the following steps to produce the extinction maps of IC 694 and NGC 3690:

1. The keywords PHOTFLAM[c] and EXPTIME were retrieved from the headers of U and I-band images to convert each pixel value from count rates into flux units. Simultaneously, the Vega-flux zeropoints, $f^0_{\lambda,Vega}$, from Bessell et al. (1998) were also included to make sure that the measurements remain in the Vega-mag systems.

[c] PHOTFLAM represents the absolute calibration flux of the camera.

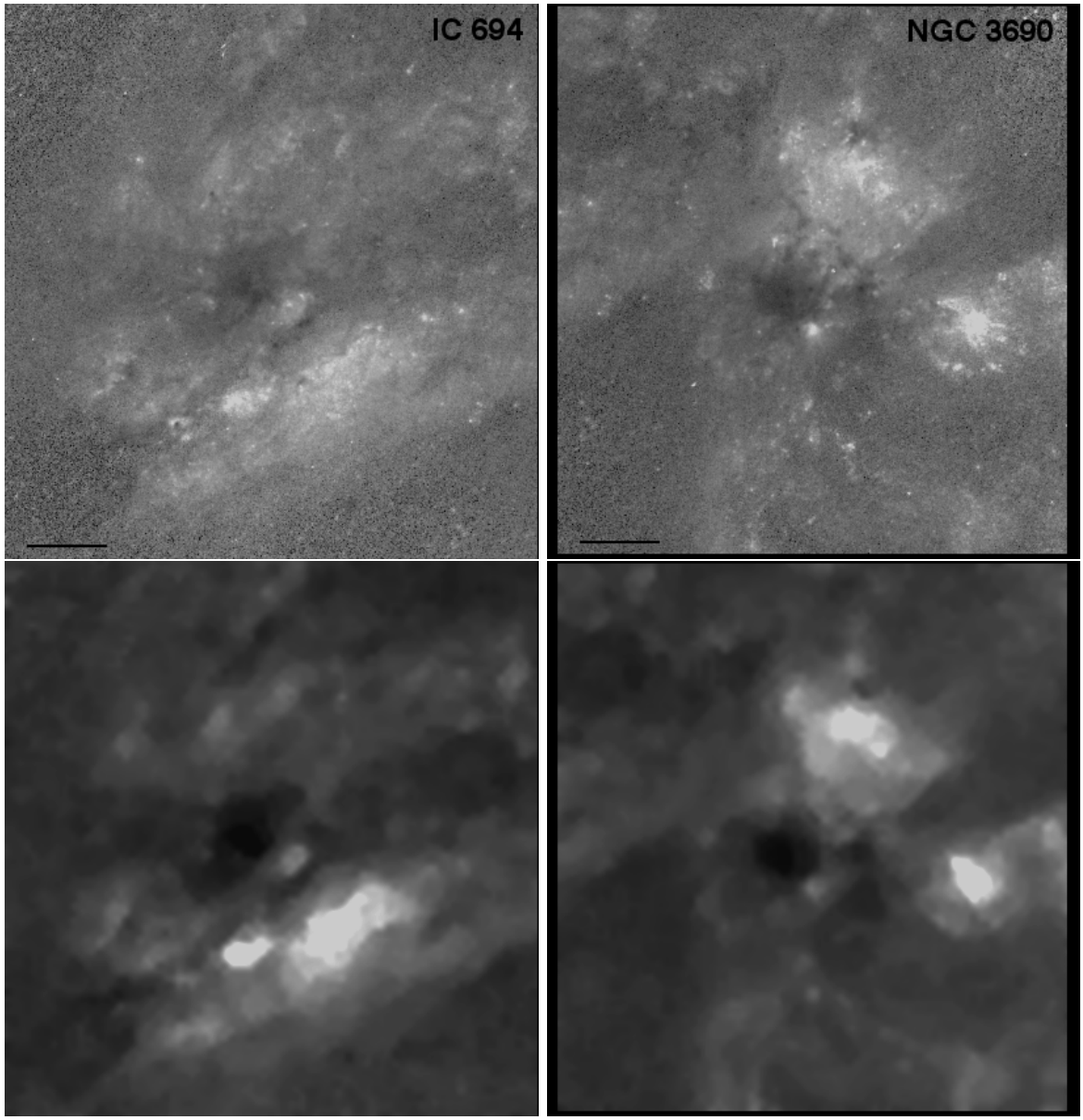

Figure 5.4: *Top:* $U-I$ color-map of Arp 299. *Bottom:* Extinction map produced from a smoothed version of the color map and assuming a uniform intrinsic color of $U-I \sim 0.35$ mag to the galaxy. Darker shades are associated with higher colors/extinctions in the maps.

The conversion can be summarized as below:

$$f_{\lambda,\,Vega} = \frac{counts}{f^0_{\lambda,\,Vega}} \times \frac{\mathrm{PHOTFLAM}}{\mathrm{EXPTIME}} \tag{5.2}$$

2. We then used the following expression to get a broad-band $U-I$ color map:

$$U - I = -2.5\ log\ \frac{f_{U,\,\mathrm{Vega}}}{f_{I,\,\mathrm{Vega}}} \tag{5.3}$$

The results are shown in the top panels of Figure 5.4. We are not concerned about the noisy distribution seen in the edges since they occur outside the galactic field and are beyond the cluster detections. Although $U - I$ color maps only probe the dust screen of the galaxy, they could already give the essence of the spatial distributions of the cluster ages and extinctions, assuming the SED fitting would be able to break the age-extinction degeneracy.

3. Note, however, that regions with blue $U - I$ colors might be biased if they host bright foreground or background sources. We, therefore, ran `SExtractor` to get a smoothed background version of the color map. The input parameters, especially the width of the background mesh, were set so that the main features from the original map still remain evident but the false distribution from any individual bright sources are being removed.

4. The next step was to get $(U - I)$ intrinsic color of a starburst galaxy from the literature. As a zeroth-order approximation, we will assume that the galaxy has a uniform color throughout its field, although this would of course not necessarily be the case with significant age variations. The synthetic spectrum fitting to a starburst galaxy template by Kinney et al. (1996) suggested that such a color should be around ≈ 0.35 mag in the Vega-mag system with $E(B - V) = 0$. The effects of this decision are tested below.

5. Under the Calzetti dust reddening law, we finally constructed the extinction map based on the smoothed broad-band color map combined with the above instrinsic galaxy color. The resulting maps for IC 694 (left) and NGC 3690 (right) are shown in the bottom panels of Figure 5.4. High extinction values ($A_V \gtrsim 3$ mag) are indeed associated to the nuclear starburst regions of the galaxies (the dark shades of the map). However, further checks will follow to assess the authenticity of the map extinction range (see text below).

Testing the accuracy of the map

Based on the derived extinction maps, the nuclear starburst regions of IC 694 and NGC 3690 have $A_V \sim 3.8$ mag and $A_V \sim 3.6$ mag, respectively. Alonso-Herrero et al. (2000) have reported similar extinction ranges using optical spectroscopy (Table 3). They have also estimated the extinction to the gas in the nuclei with NIR HST/NICMOS observations and by using an aperture of $2'' \times 2''$. They have found the following ranges: $A_V = 5 - 6$ mag for IC 694 and $A_V = 3 - 4$ mag for NGC 3690 (Table 6). The higher extinction range in the case of IC 694 is expected because estimates from optical data usually reflect the dust screen only, while measurements based on NIR observations probe deeper into the intrastellar medium. Nevertheless, these comparisons demonstrate that an intrinsic galaxy color of $U - I = 0.35$ mag is still a reasonable assumption in our case and, consequently, the extinction maps in Figure 5.4 should provide at least a crude approximation A_V^0 to the extinction of the cluster.

An area of 5 by 5 pixels centered at the given SSC spatial coordinates was used to calculate an average value for the initial extinction of that SSC. Subsequently, each cluster has its own extinction range $[A_V^0 - A_V^{low}, A_V^0 + A_V^{up}]$, where $A_V^0 - A_V^{low}$ and $A_V^0 + A_V^{up}$ are, respectively, suitably chosen lower and upper limit values for the allowed range of A_V. Note that if A_V^0 approaches 0, $A_V^{low} = A_V^0$.

5.2.5 χ^2 minimization

To get the cluster age and extinction, we adopted the two dimensional maximum likelihood photometric fitting by Bik et al. (2003). Although spectroscopic fitting is known to derive more consistent results, previous works on star cluster age modelling have demonstrated that the following technique can also deliver accurate estimates of the cluster physical parameters in the absence of spectroscopic data of clusters (e.g. de Grijs et al. 2003b; Anders et al. 2004; Bastian et al. 2005; Adamo et al. 2010). The main philosophy behind χ^2 minimization is to compare the observed SED of the star cluster to the synthetic colors of a grid of SSP models within a given age range. Such a fitting algorithm can be expressed as:

$$\chi^2(\tau, A_V) = \sum_{\lambda} W_\lambda \left(m_\lambda^{obs} - m_\lambda^{mod}\right)^2 \tag{5.4}$$

where m^{obs} and m^{mod} are respectively the observed and the synthetic magnitudes while W_λ is a normalization factor. Anders et al. (2004) argued that at least four filters, covering a large broad-band that includes the Balmer lines, are to be considered to secure results with a high precision. Nevertheless, χ^2 minimization can still be applied to a SED drawn using three filters only, though one should be more careful while interpreting the results (see Section 5.3). The evolutionary tracks of the SSP models are looped over a chosen extinction range (see text below) in steps of 0.01 mag to find the most probable age τ and reddening value A_V which are associated with the best reduced χ^2 values.

Once the values of τ and A_V are derived, the corresponding difference in magnitudes between m^{obs} and m^{mod} of a given filter can be used to determine the cluster mass $M_{\lambda,\,cluster}$:

$$M_{\lambda,\,cluster} = 10^6 \times 10^{-0.4\times(m^{obs} - m^{mod} + A_\lambda)} \tag{5.5}$$

assuming that the SSP evolutionary tracks have an initial mass of $10^6 M_\odot$. The final cluster mass is the median value of $M_{\lambda,\,cluster}$ where $\lambda = \{U, B, I\}$ or $\{B, I\}$, depending on the number of the filters. Luminosity from K-band data should not be used as it tends to overestimate the cluster mass (Section 5.2.10).

Setting suitable A_V ranges

The patchy distribution of the extinction maps in Figure 5.4 suggests that using only a single extinction range to compute the parameters of the overall SSC population would result in poor fitting of the cluster ages. Therefore, we have constrained different ranges as a function of the initial estimate A_V^0. The lower and upper limits of these extinction ranges are:

$$[A_V^0 - A_V^{low}, A_V^0 + A_V^{up}] = \begin{cases} [0, 0.25] & \text{if} \quad A_V^0 < 0.25 \\ A_V^0 - 0.25, A_V^0 + 0.25 & \text{if} \quad 0.25 \leq A_V^0 \leq 0.75 \\ A_V^0 - 0.75, A_V^0 + 0.75 & \text{if} \quad A_V^0 > 0.75 \end{cases} \tag{5.6}$$

These limits were chosen based on results from various tests and the comparison of the cluster mass functions. The tests suggest that SED fitting with the limits, derived using Equation 5.6, give reasonable results.

Testing the robustness of the fits

Before deriving the age and mass of all the cluster candidates, we first tested the χ^2 minimization on some specific datasets with low photometric uncertainties, i.e $\sigma_m < 0.25$ mag, and less patchy dust distributions. The cluster initial extinction A_V^0 were used to define these objects and the following checks were performed to find out whether the different extinction ranges in Equation 5.6 would determine accurate estimates of the cluster physical parameters:

- For the first test, we only considered objects with $A_V^0 < 0.25$ mag. We then performed the SED fitting within an extinction range of $0 - 0.15$ mag. The same procedure was repeated by considering another extinction range of $0 - 0.25$ mag. A crude approximation from the CCD indicated that the $A_V^0 < 0.25$ mag objects are expected to have low extinction values and are mainly very young objects with ages less than ~ 100 Myr. Both extinction ranges output the predicted results (Figure B.1); we will use a range of $A_V = [0, 0.25]$ mag to derive the final results.
- The second test considered objects with high extinction, specifically $1.2 < A_V^0(\text{mag}) < 2$. We ran the SED fitting with the following ranges: $A_V^0 \pm 0.25$ $A_V^0 \pm 0.5$, $A_V^0 \pm 0.75$, and $A_V^0 \pm 1$ mag. Again, the results are consistent with the distribution of the data points in the CCD regardless of the extinction ranges (Figure B.2 and Figure B.3). To output the final parameters, a range of $A_V^0 \pm 0.75$ mag was chosen and if $0.25 \leq A_V^0 \leq 0.75$, we used the smaller range $A_V^0 \pm 0.25$ mag.

The distribution of the tested datapoints in the CMD/CCD along with their ages, masses and extinction are shown in Appendix B. The results from the tests proved once again

that the extinction maps provide valuable information to constrain the extinction ranges necessary for the χ^2 minimization.

5.2.6 Mass, age and extinction of the clusters

We performed three sets of SED fitting to estimate the physical properties of the star clusters: the first set includes all four $UBIK$-filters, the second set excludes the K-band NIR filter and the third one considers BIK-filters. Figure 5.5 shows the resulting cluster distributions in the age-mass plane from the three different fits. The dashed lines represent the evolutionary fading of the SSP models with magnitude limits $M_U = -8.8$ mag (blue), $M_B = -8.12$ mag (green), and $M_I = -9.12$ mag (black). In all three cases, we find that the cluster masses generally lie in the range of $10^3 - 10^8 M_\odot$. Any datapoint with a derived mass above $10^8 M_\odot$ should be treated separately, in principle, as we could already be dealing with complexes of star clusters, unless they have NIR excess (see Section 5.2.10). Their ages are mostly below 1 Gyr and in the case of the UBI-fit, 56 (IC 694) and 68 percent (NGC 3690) of the clusters have ages $\tau \lesssim 15$ Myr with a mass range between $10^3 - 10^6 M_\odot$. In fact, the cluster parameters from this second set of fitting process are associated with the minimum values of the reduced χ^2 compared to the results from $UBIK$- and BIK-fits. Therefore, in the remainder of this work, we will consider results from the UBI-fit. The resulting dataset in this case allows the breaking of the age-extinction degeneracy and therefore constitutes a better fit to the data.

A closer look at the cluster age-mass distributions (middle panels of Figure 5.5) indicates that IC 694 hosts more star clusters with intermediate-ages ($7.5 < \log\tau(\mathrm{yrs}) < 9$) than NGC 3690. This is more evident in the upper panels of Figure 5.6 which plot the cluster age distributions only. However, both distributions present concentrations, referred to as "chimneys", at ages around $\log\tau \approx 6$, 7, and 8.3. Poor fitting of the youngest star clusters explains the chimney at $\log\tau = 6$ which corresponds to the lower age limit of the SSP models. The other chimneys at $\log\tau \approx 7$ and $\log\tau \approx 8.3$ exist because red super giants and asymptotic-giant branch stars of the star clusters become apparent at these ages, respectively (e.g Bastian et al. 2005; de Grijs & Goodwin 2008; de Grijs et al. 2013). Such stellar evolution affects the accuracy of the derived cluster ages; the real age-mass distribution is thus believed to spread into a wider range at these ages. Nevertheless, even though chimneys exist in age modelling, the mass of the clusters is much less affected by those uncertainties. Furthermore, the trends of Figure 5.5 clearly demonstrate that the population of star clusters decrease with time, which is due to various cluster disruption mechanisms (e.g. Bik et al. 2003; Gieles 2009; Lamers 2009).

Finally, the visual extinction A_V of the star clusters varies between 0 to 4.5 mag, i.e. $\mathrm{E(B-V)} = 0 - 1.1$. The middle panels of Figure 5.6 plot the initial estimate A_V^0 from the extinction maps in Figure 5.4 against the derived value A_V, whereas the lower panels show the resulting extinction distributions. NGC 3690 has a significant number of star clusters with a low extinction value $\mathrm{E(B-V)} < 0.1$ compared to the population

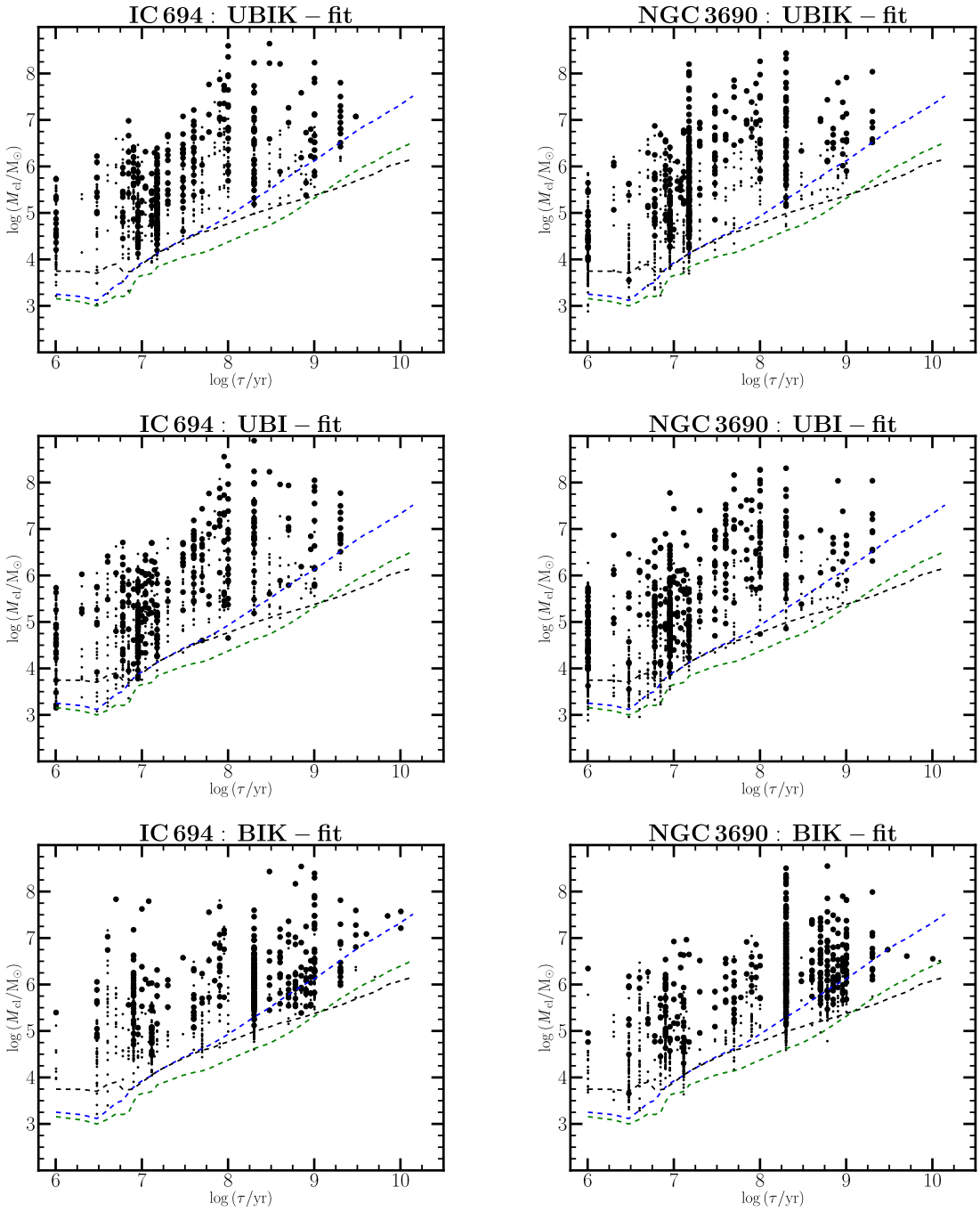

Figure 5.5: The cluster age-mass planes from the χ^2-fit considering $UBIK$- (top), UBI- (middle) and BIK-filters (bottom). Black points are the objects with $\sigma \leq 0.35$ in all four $UBIK$-images, whereas the dots are those below the error cutoff but in UBI-filters only. The dashed lines denote the photometric detection limits ($\sim 80\,\%$) of considering U- (blue), B- (green), and I-band (black) evolutionary tracks where $M_U = -8.8$, $M_B = -8.12$, $M_I = -9.12$ mag, respectively. Chimneys are observed at around 1 Myr, ≈ 10 Myr, and ≈ 200 Myr. Outputs from BIK-fit converge to an older age range compared with the resulting cluster ages of the other fits. For ease of visualization, we omit error bars, which are of order $0.2 - 0.3$ dex for both physical parameters, on the above plots.

of SSCs in IC 694. Apart from any possible physical interpretations, such a difference could arise because of a simple statistical effect (there are more SSCs detected in the western component of the interacting system). More analyses of the extinction spatial distribution are reported in Section 5.2.7.

SED fitting of the observed data with `Starburst99` model were also performed for comparison. The cluster age-mass distributions are shown in Figure C.2 of Appendix C. The resulting ages tend to converge and form more pronounced chimneys at $\log \tau \approx 6$ and $\log \tau \approx 7$ than those seen in Figure 5.5. The ages from `Yggdrasil` model spread in a wider distribution. Therefore, we chose not to use the results from `Starburst99` but rather focused our analyses based on the physical parameters derived with `Yggdrasil`.

5.2.7 Cluster spatial distributions

Top panels of Figure 5.7 display the spatial distribution of the SSC candidates split in three different age bins: younger than 30 Myr (stars), between 30 and 200 Myr (crosses), and older than 200 Myr (filled circles). In the case of IC 694, different age bins overlap spatially. Such a random distribution in terms of age may be an imprint of ongoing cluster migration due to the strong tidal shocks generated through the merging process of IC 694 with NGC 3690. In contrast, the star clusters hosted by NGC 3690 are segregated in a way that younger clusters are mostly located in the inner regions of the galaxy, while the older ones get dispersed in the outer field. This could be an imprint of the *"cruel cradle effect"* suggested by Elmegreen (2010) and Kruijssen et al. (2011) (see Section 1.4.5 for a brief overview). We also noticed that the regions which host most of the very young clusters in both components are close to the merging point (the center of the collision between the two galaxies) of the system. This is not surprising since massive star clusters are likely to be born under the extreme conditions of interaction. As a result, rough approximations of the star (cluster) formation history can be derived through the position of the star clusters in the galactic field (refer to Section 5.2.11 for an in-depth analysis).

Bottom panels of Figure 5.7 show the extinction spatial distributions in the galactic field of Arp 299. Stars, crosses, and filled circles respectively represent the values of the visual extinction A_V less than 1.5 mag, between 1.5 and 2 mag, and higher than 2 mag. The distribution of A_V output by the χ^2 fitting is indeed in agreement with the properties of the extinction maps (Figure 5.4): the majority of the most extinguished star clusters are within the obscured nuclear starburst regions. In the case of NGC 3690, these are very young clusters with ages $\lesssim$ 5 Myr that are probably still deeply embedded within their dust cocoons. Therefore, the chimney at around 1 Myr in the cluster age-mass plane of NGC 3690 (right panels of Figure 5.5) could partially be a true distribution. For that same component, most of the clusters with low extinction values also form the young population with ages between 10 to 30 Myr. These clusters have survived the gas expulsion phase where the surrounding dust and ionized gas has been blown away, thus

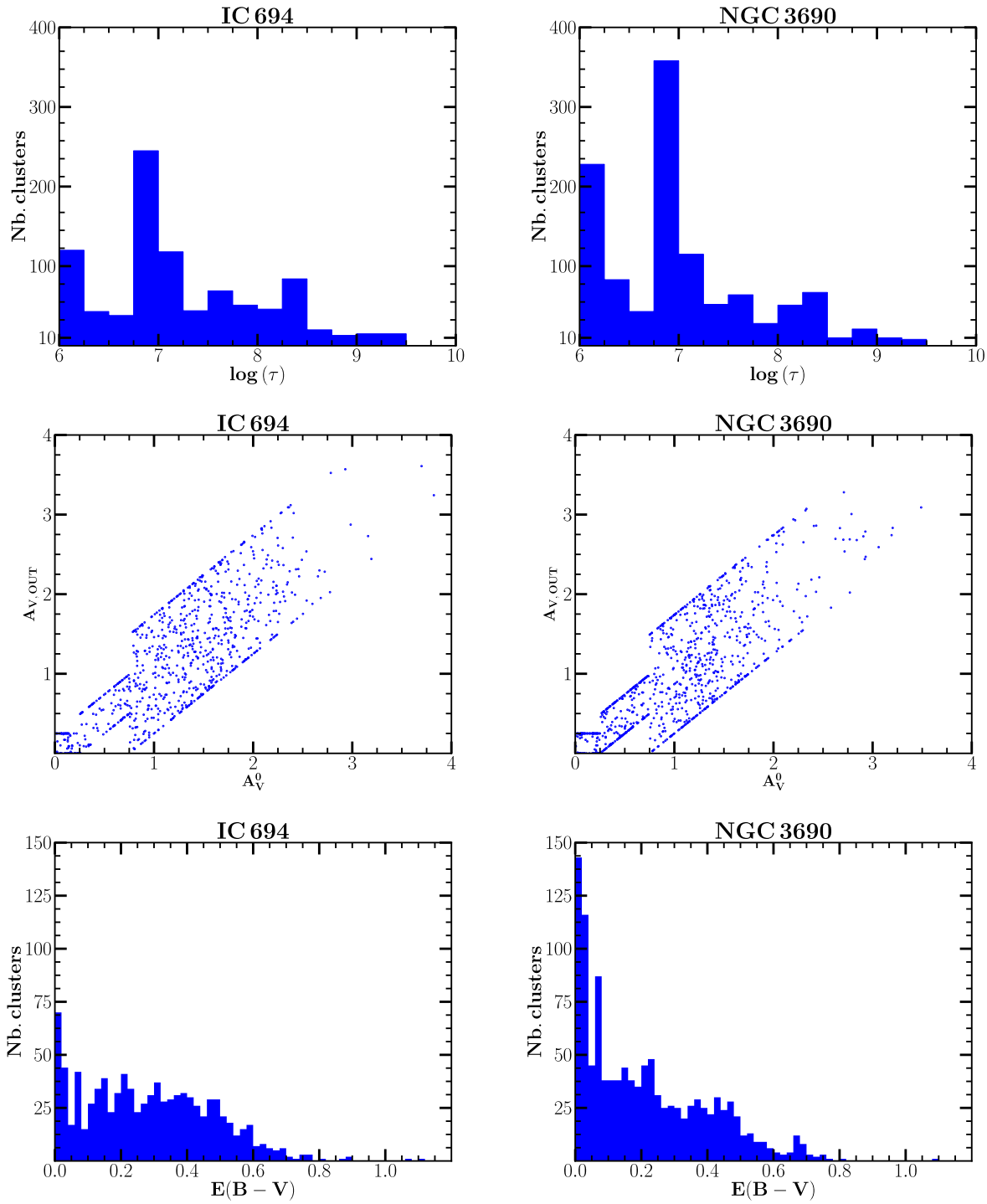

Figure 5.6: *Top*: The age distribution of the SSC candidates. The chimneys due to the evolution of the bright and massive star members are clearly visible here. *Middle*: Initial estimate of the cluster reddening plotted against the resulting value output by the χ^2 fitting technique. *Bottom*: The cluster extinction distribution. There are relatively a lot of SSC candidates with low extinction values in the case of NGC 3690.

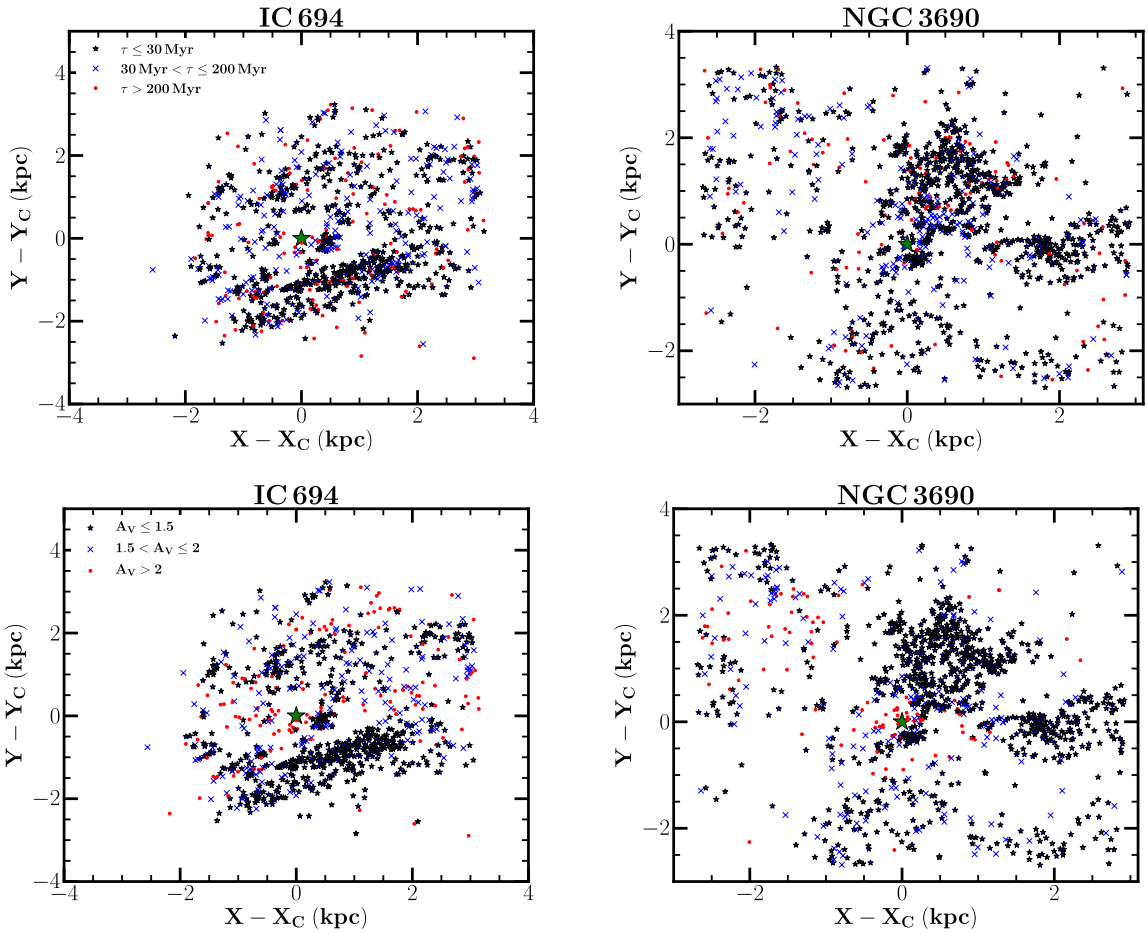

Figure 5.7: *Top:* The age spatial distributions of the SSC candidates in the field of Arp 299. The green star represents the postion of the galaxy center. The blue stars, the crosses and the filled circles respectively represent clusters younger than 30 Myr, those between 30 and 200 Myr and the ones older than 200 Myr. *Bottom:* The star cluster visual extinction spatial distributions. The different labels correspond to different extinction ranges.

allowing the SSCs to become optically visible. Finally, in the case of IC 694, there seems to be a correlation between the distribution of the least extinguished clusters and that of the younger ones ($\tau \leq 10$ Myr). Nevertheless, clusters from other age bins are also located in the low extinguished regions of the galaxy.

5.2.8 *UBI*-band luminosity functions

Before analysing the cluster mass functions (CMFs) in Section 5.2.9 , we first derived the luminosity functions (LFs) using *UBI*-data of each component. The same procedures

as in Section 3.4 were followed to construct and fit a power-law to the CLFs shown in Figure 5.8 using a constant bin size. Note, however, that we did not correct the optical data from observational incompleteness. Instead, we only fit the clusters with bright luminosities up to a certain characteristic magnitude referred to as $M^{\star}_{\lambda}$. For $\lambda = \{\mathrm{U}, \mathrm{B}, \mathrm{I}\}$, $M^{\star}_{\lambda}$ are, respectively, equal to -9.2, -8.5 and -10 mag in the case of IC 694 (upper panels). These values become -10.5, -9.5 and -10.8 mag in the case of NGC 3690 (lower panels). The effects of incompleteness on the data with magnitudes brighter than $M^{\star}_{\lambda}$ are expected to be negligible, or at most with an incompleteness factor of 20%, since these optically-bright star clusters were observed well beyond the detection threshold. U- and I-band CLFs of IC 694 generally follow a single power-law distribution. The

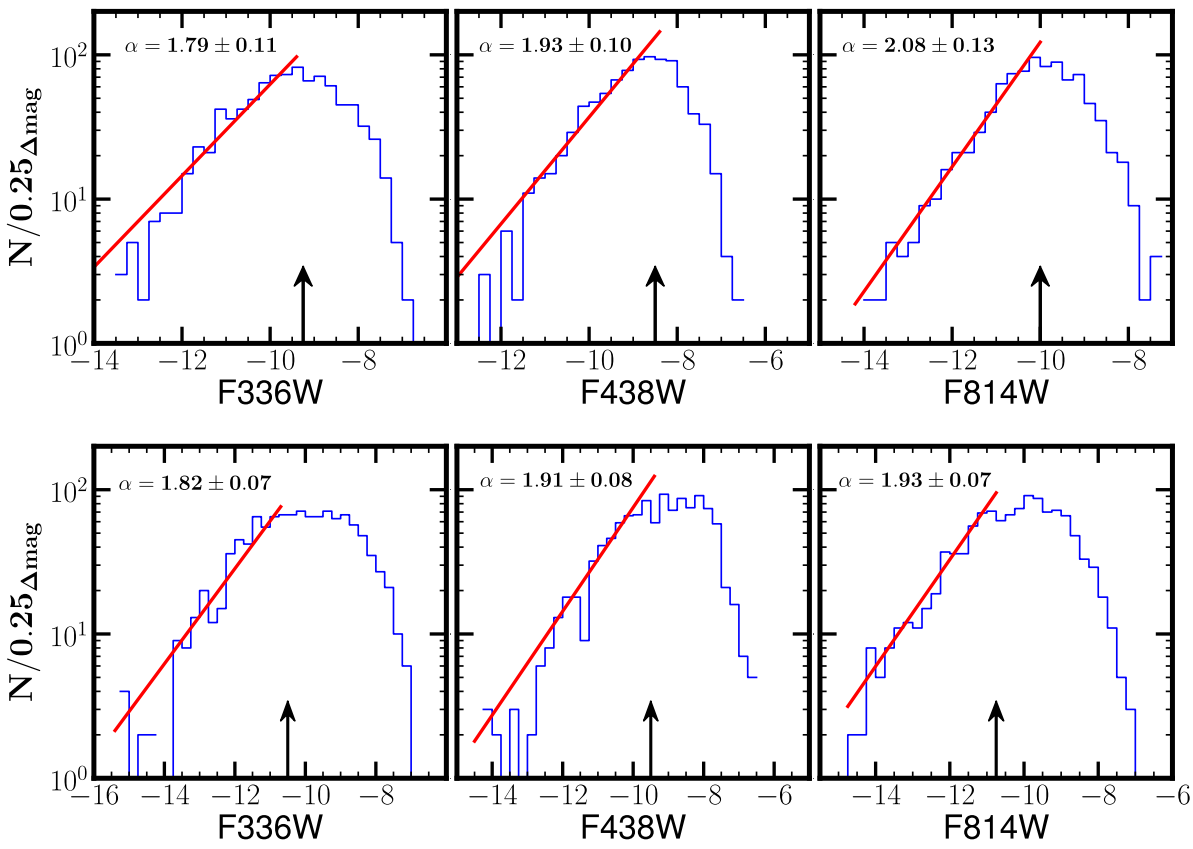

Figure 5.8: U- (*left*), B- (*middle*), I- (*right*) band LFs of the Arp 299 optically-selected star clusters using a constant binning. The solid lines represent the fit to a power-law distribution of the LF bright end and the vertical arrows indicate the characteristic magnitudes $M^{\star}$. The power-law slopes α get steeper at redder filters for both components. The datasets of NGC 3690 (*lower panels*) present an underlying truncation at the faint end of the CLF. In the case of IC 694 (*upper panels*), such a trend is weakly observed in B-band LF.

B-band LF, on the other hand, is suggestive of an underlying truncation at the faint end of the distribution. In principle, this could be attributed to the lack of incompleteness correction, though physical explanations are not precluded. In the case of NGC 3690, a Schechter distribution could also fit the optical CLFs especially the U-band dataset where the truncation is the most prominent. Since the CLF is believed to be a reflection of the CMF, we therefore expect the mass distribution to adopt the same shape. Otherwise, the observed truncation/bend is a simple statistical effect. The reasons behind the truncation observed in the CLFs are to be evaluated while dealing with the CMFs. Nevertheless, further investigations were done, using the U-band datasets, to check whether such a behaviour could simply be introduced by a non-constant detection limit while constructing the CLFs. Figure 5.9 shows the U-band LFs of three SSC sub-populations, separated as a function of their ages: less than 10 Myr (left panel), between $10-100$ Myr (middle), and finally between $0.1-1$ Gyr (right). Power-law fitting of the CLFs result in the following values of the slopes: $\alpha = 1.85 \pm 0.09, 1.53 \pm 0.07,$ and 1.43 ± 0.09. A decreasing slope as a function of age as well as an underlying truncation in the LF of the intermediate-age clusters definitely require more in-depth analyses (see Section 5.2.9).

A closer look at the CLFs of IC 694 and NGC 3690 shows that the power-law slopes of the western component ($\alpha = 1.82 \pm 0.07, 1.91 \pm 0.08,$ and 1.93 ± 0.07) are all shallower than the canonical slope of 2. For those of the eastern part ($\alpha = 1.79 \pm 0.11, 1.93 \pm 0.10,$ and 2.08 ± 0.13), the index associated with the I-band LF is slightly steeper than 2. Nevertheless, both components of the interacting LIRG have flatter indices than the average slope associated with normal spiral galaxies ($\alpha \approx 2.4$, see

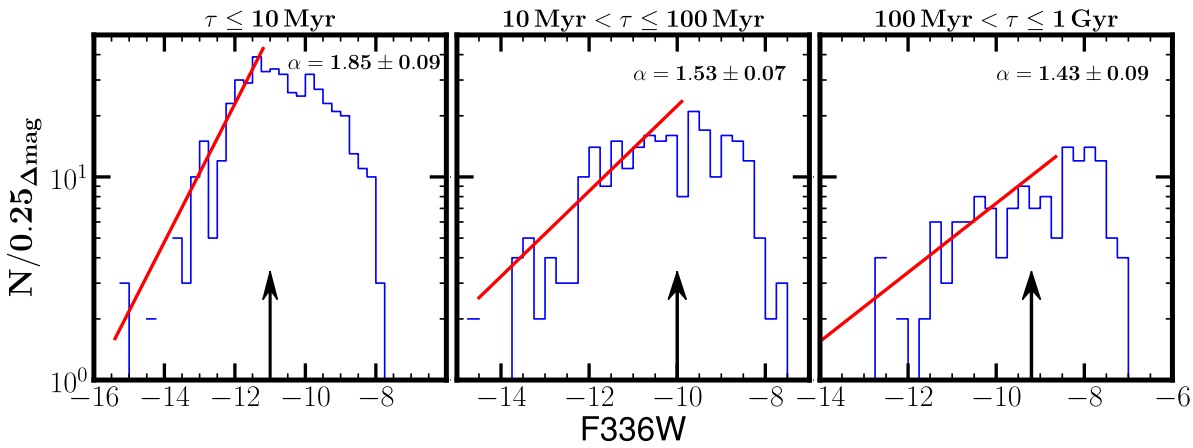

Figure 5.9: U-band LFs of the optically-selected star clusters of NGC 3690 within different age bins. The solid lines represent the fit to a power-law distribution of the LF bright end and the vertical arrows indicate the characteristic magnitudes $M^\star$. The power-law slopes α flattens as we move in to older age bins. The LF of the intermediate-age clusters (the middle panel) present an underlying truncation at the faint end of the CLF. Such a trend is weakly observed in the LFs of the old SSC populations.

e.g. Whitmore et al. 2014). In addition, the value of the slope increases as we move to a redder fllter. Haas et al. (2008), Johnson et al. (2012) and Ryon et al. (2014) among many others have also found the same pattern in their work. Gieles (2010) suggests that such a variation is due to the evolutionary fading of the star clusters with time.

5.2.9 Cluster mass functions

The resulting CMFs of Arp 299 are shown in Figure 5.10. The cluster populations were split in three different age bins for an optimal assessment of any turnover in the distribution and hence a better understanding of the cluster disruption mechanisms. The age ranges are: $\tau \leq 10\,\mathrm{Myr}$, $10\,\mathrm{Myr} < \tau \leq 100\,\mathrm{Myr}$ and $\tau > 1\,\mathrm{Gyr}$ (the same as in Section 5.2.8). In the following analysis, we did not apply any completeness correction to the data. Therefore, we only fit the high mass end of the CMFs to a power-law distribution of the form $N(m)dm \sim m^{-\beta}dm$. The values of the slopes β along with a critical mass M_{cl}^{critic} until which we performed the fit are listed in Table 5.2. Such a value is always higher than that of the photometric detecion limit ($\sim 80\,\%$, see Figure 5.5) which is represented by a vertical line in Figure 5.10 and was derived using the cluster age-mass plane in Figure 5.5. For both components, the values of M_{cl}^{critic} increase as we move to older age ranges, which is not surprising because of the evolutionary fading of the star clusters with time. As for the power-law slopes, they become flatter. If such a behaviour is not because of observational incompleteness, then a deficit in low mass star clusters could be another reason. The high-mass end of all the CMFs have slopes steeper than 2 within their uncertainties which is in agreement with the literature (e.g. Gieles 2009; Larsen 2009). Finally, we also noticed that the CMFs of NGC 3690 have shallower slopes than those of IC 694. The intensity of the cluster disruption in the western component could have been stronger.

Table 5.2: Characteristics of the cluster mass functions of Arp 299

Age range	M_{cl}^{critic} (A, B+C)	β (A, B+C)
(1)	(2)	(3)
$\tau \leq 10\,\mathrm{Myr}$	$10^4\,M_\odot$, $10^4\,M_\odot$	2.45 ± 0.35, 2.36 ± 0.45
$10\,\mathrm{Myr} < \tau \leq 100\,\mathrm{Myr}$	$10^5\,M_\odot$, $10^5\,M_\odot$	2.39 ± 0.26, 2.17 ± 0.23
$100\,\mathrm{Myr} < \tau \leq 1\,\mathrm{Gyr}$	$10^{5.3}\,M_\odot$, $10^{5.8}\,M_\odot$	2.06 ± 0.22, 1.98 ± 0.23

Notes. In the literature, the letter A commonly refers to IC 694 while B + C to NGC 3690. Column 1: the ages of the star clusters used to construct the MF; Column 2: the values of the critical cluster mass until which we performed the fit; Column 3: the values of the power-law slope β.

In fact, the MFs of NGC 3690 are the ones that mainly present a truncation at the low mass end, especially for the distribution of ages between 10 and 100 Myr. Such an age range is very critical in the evolution of star clusters. The cluster's chance for a long-term

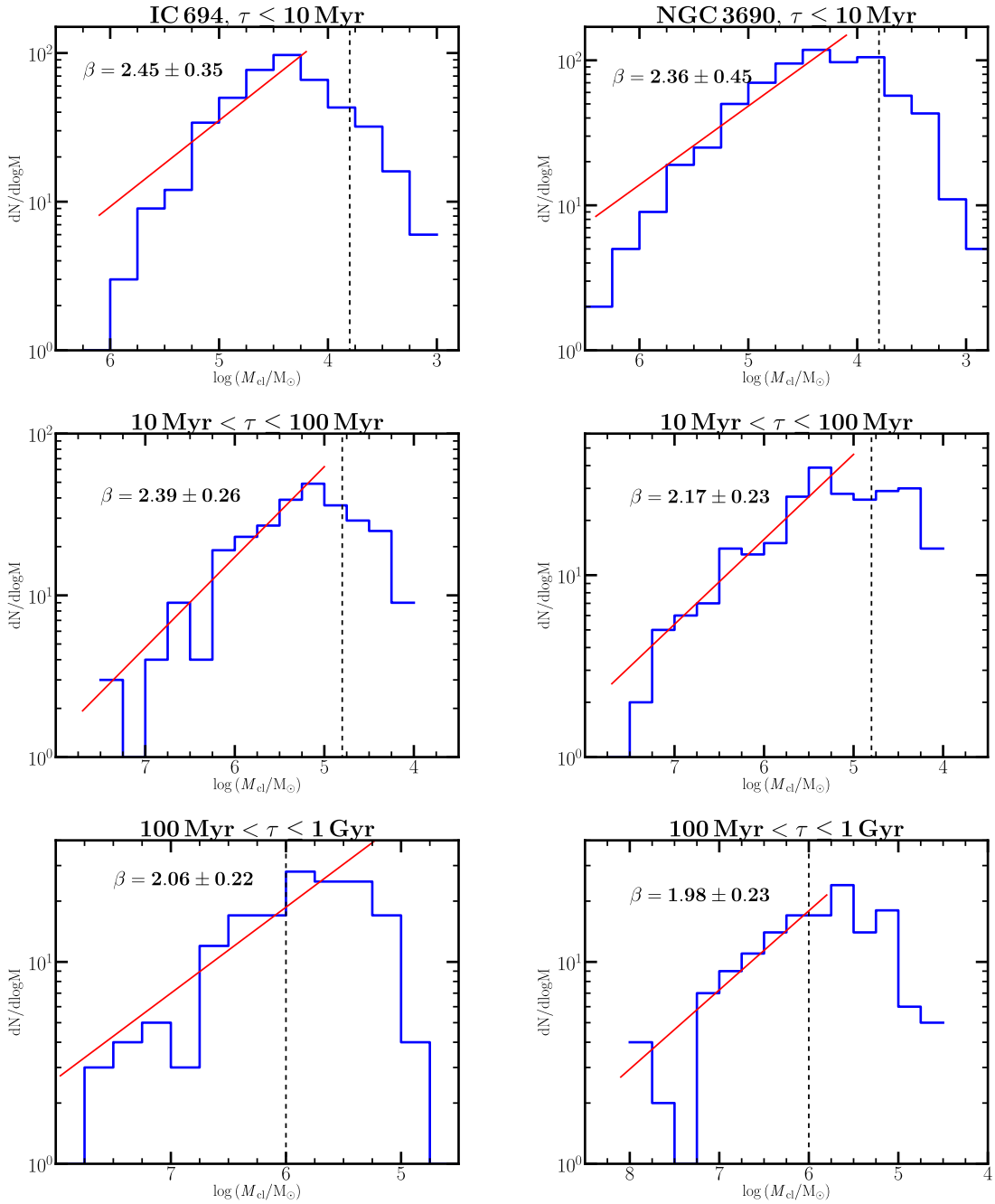

Figure 5.10: The cluster mass functions of IC 694 (*left*) and NGC 3690 (*right*) plotted with different age bins and using a constant bin size. The solid lines represent the resulting power-law fit to the high-mass end of the distribution. The dashed lines show approximate cluster mass completeness limits estimated using the age-mass plane. The top panels correspond to the distribution of young clusters with ages less than 10 Myr, the middle ones for cluster ages between 10 and 100 Myr and the bottom panels for the older clusters with ages between 100 Myr and 1 Gyr. The MFs of NGC 3690 have an underlying turnover especially for 10 Myr $< \tau \leq$ 100 Myr.

survival after escaping infant mortality will be at play during this period. Moreover, MFs of the younger ages could be contaminated by unresolved unbound stellar associations while the ones with ages above 100 Myr may be affected by the effect of evolutionary fading (Ryon et al. 2014). Therefore, to draw our conclusions, we will focus only on the MFs with ages between 10 and 100 Myr to assess whether the truncation is the result of a size-of-sample effect or that infant mortality destroyed most of the low-mass clusters at early ages. We remind the reader that the same trend has also been observed in the LFs of NGC 3690 (see the bottom panels Figure 5.8). A Schechter distribution could also fit the cluster LFs and MFs of that component. While the bend of such fit occurs around $2.1 \times 10^5\,M_\odot$ for normal spiral galaxies (Larsen 2009), a more massive value close to $10^6\,M_\odot$ is required for starbursts and merger galaxies such as LIRGs (Bastian 2008).

The cluster age-mass planes in Figure 5.5 indicate that the sample should be complete for sources more massive than $\approx 10^{4.3}\,M_\odot$ with ages younger than 100 Myr. Therefore, statistical effects are to be excluded while explaining the origin of the truncation in the MFs and subsequently in the LFs. The western component is possibly undergoing a cluster mass-dependent disruption mechanism.

5.2.10 NIR excess and the K-selected SSC candidates

The top panels of Figure 5.11 display $I-K$ vs. $B-I$ colors of the optically-selected clusters (filled circles) in Arp 299. Not all positions in the color-color diagram agree with the predicted distribution from `Yggdrasil` SSP model: there is a large spread at the upper level of the SSP $I-K$ color. In other words, some of the points in the diagram unexpectedly strech to redder colors. Such a dispersion cannot be linked to high photometric uncertainties as we have already excluded sources with $\sigma > 0.35$ mag. Therefore, these sources present "NIR excess" in their fluxes. Apart from stochastic sampling effects, the inclusion of the surrounding nebular emission (HII regions) in the photometric measurements could be the main reason behind such an excess (e.g. Adamo et al. 2010; de Grijs et al. 2013; Bastian et al. 2014).

We therefore focused on the mass distribution of young clusters ($\tau \lesssim 30$ Myr) with low extinction to investigate whether stochasticity is responsible for the NIR excess. If there is stochasticity, massive SSCs are expected to follow the distribution of the SSP model in the CCD, whereas low mass clusters ($M_{cl} < 10^5\,M_\odot$) would rather occupy the widespread in $I-K$ axis. The latter distribution would indicate an apparent NIR excess in the sources due to the RSGs in their stellar population (refer to Section 1.4.6). However, this is not always the case in the following data set: Figure B.4 in Appendix B does not show a larger scatter in the distribution of the low mass clusters compared to the massive star clusters. Therefore, stochasticity seems to only partly affect the data and other causes of the excess such as nebular emission or blending effects should also be considered. In fact, Bastian et al. (2014) recently reported that the intensity of the NIR excess strongly depends on the spatial resolution of the NIR data. Using a bigger

aperture size would include not only the flux from the surrounding nebular emission but also the fraction of light from any neighbouring source of similar mass. Since we have applied a smaller aperture radius to derive the cluster magnitudes and have already shown that blending effects are insignificant at distances below 100 Myr, NIR excess of the young clusters are thus likely due to the emission included in the measurements.

It is important to have a separate analysis of the NIR sources since the data sets of the SUNBIRD survey are mainly based on K-band observations only. Figure 5.11 also displays the photometric properties of the NIR cluster candidates (red diamonds) which were selected using the method in Section 2.5. Not all the K-selected sources were detected in the optical images of the system. Those located in the dust-obscured regions of the galaxy were apparently being missed while running `SExtractor` in Section 5.2.1 (these are ~ 25 percent of the total number). On the other hand, most optically-selected star clusters were not detected in the K-band images due to a low spatial resolution.

The distributions of the NIR clusters in a BIK CCD (top panels) generally follow the predicted colors of the SSP models. In other words, most of the K-selected cluster candidates of Arp 299 do not show any NIR excess. In addition, the middle panels of Figure 5.11 overplot UBI CCDs of the NIR sources with the model. Information based on UBI and BIK CCDs suggests that the NIR star clusters are massive and occupy a wide range of extinction and age. These correlate with the resulting age-mass planes presented in the bottom panels of Figure 5.11. In fact, the lower mass limits of the NIR clusters, in the order of $10^{4.5}\,M_{\odot}$, are higher than the ones of the optically-selected clusters. We remind the reader that UBI-filters were used to derive the cluster parameters. As we argued in Section 5.2.6, the resulting fits are robust enough to output reasonable values instead of using $UBIK$-filters.

5.2.11 The cluster formation history

Figure 5.12 shows the star cluster frequency[d] as a function of time for IC 694 (top) and NGC 3690 (bottom). Such a distribution is useful for reproducing the cluster formation history of the galaxy (e.g. Goddard et al. 2010; Baumgardt et al. 2013). Lower mass limits of $10^4\,M_{\odot}$ (blue), $10^5\,M_{\odot}$ (cyan), and $10^{5.5}\,M_{\odot}$ (green) were adopted to establish various formation rates which decrease with increasing ages because of observational incompleteness, evolutionary fading (especially at older ages), and disruption mechanisms such as stellar mass-loss (e.g. Bik et al. 2003; Goddard et al. 2010). We also notice that higher mass limits result in a flatter distribution at younger ages below ≈ 10 Myr. Such variations could indicate that massive star clusters preferentially have a slower formation rate compared to that of abundant low mass clusters. Denser giant molecular clouds are required to potentially give birth to the former category. In addition, the bumps seen around $\log \tau \sim 6.8 - 7.2$ are less likely to be real. They exist because of the

[d] The cluster frequency is the number of clusters per time interval.

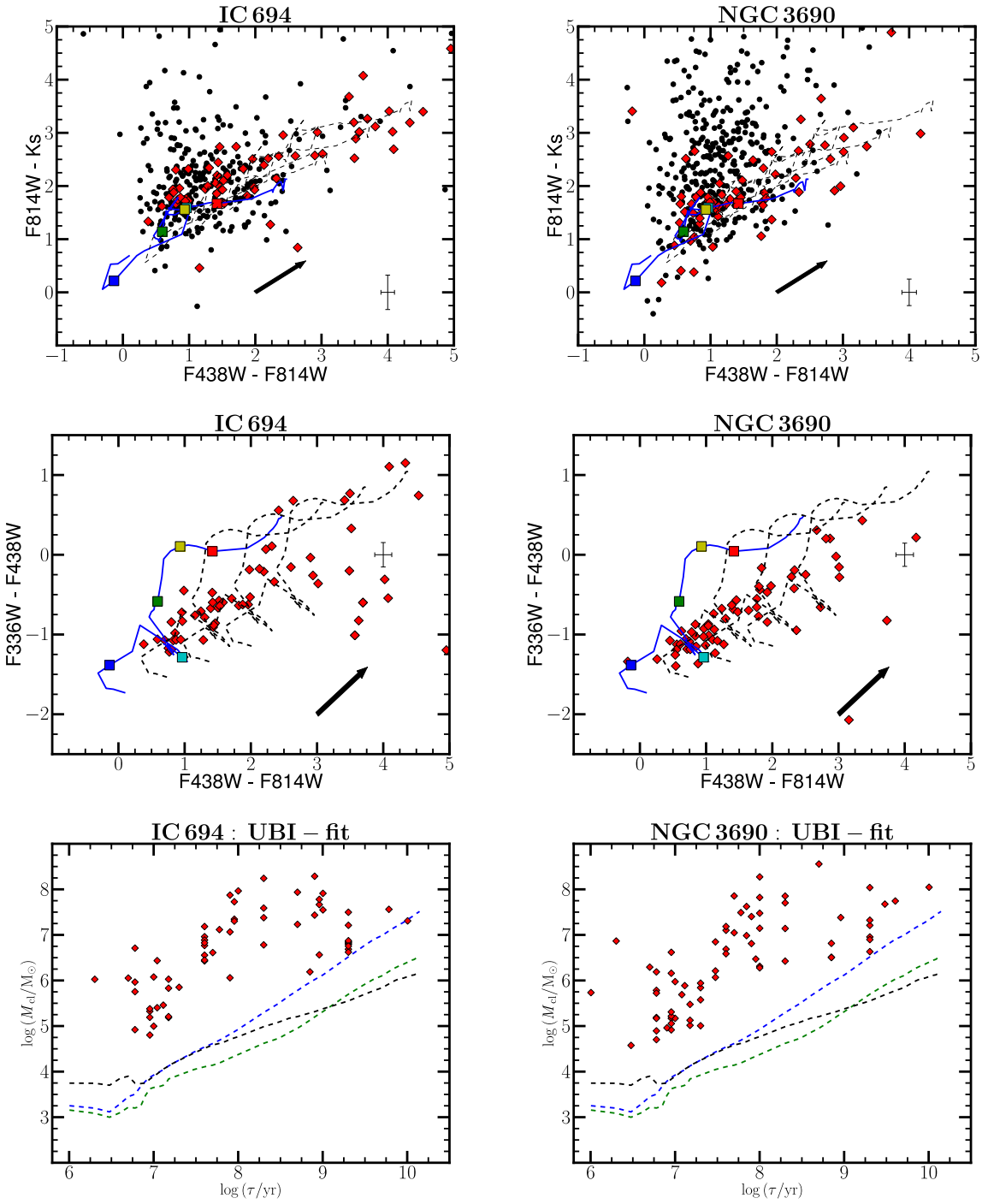

Figure 5.11: *Top: BIK* CCDs of the star clusters which are labelled as filled circles. The solid lines represent the SSP model and the arrows indicate a redenning of $E(B-V) = 0.25$. Red diamonds represent the positions of the K-selected objects. *Middle & Bottom:* The distribution of the K-selected objects in UBI CCDs and the resulting age-mass planes, respectively.

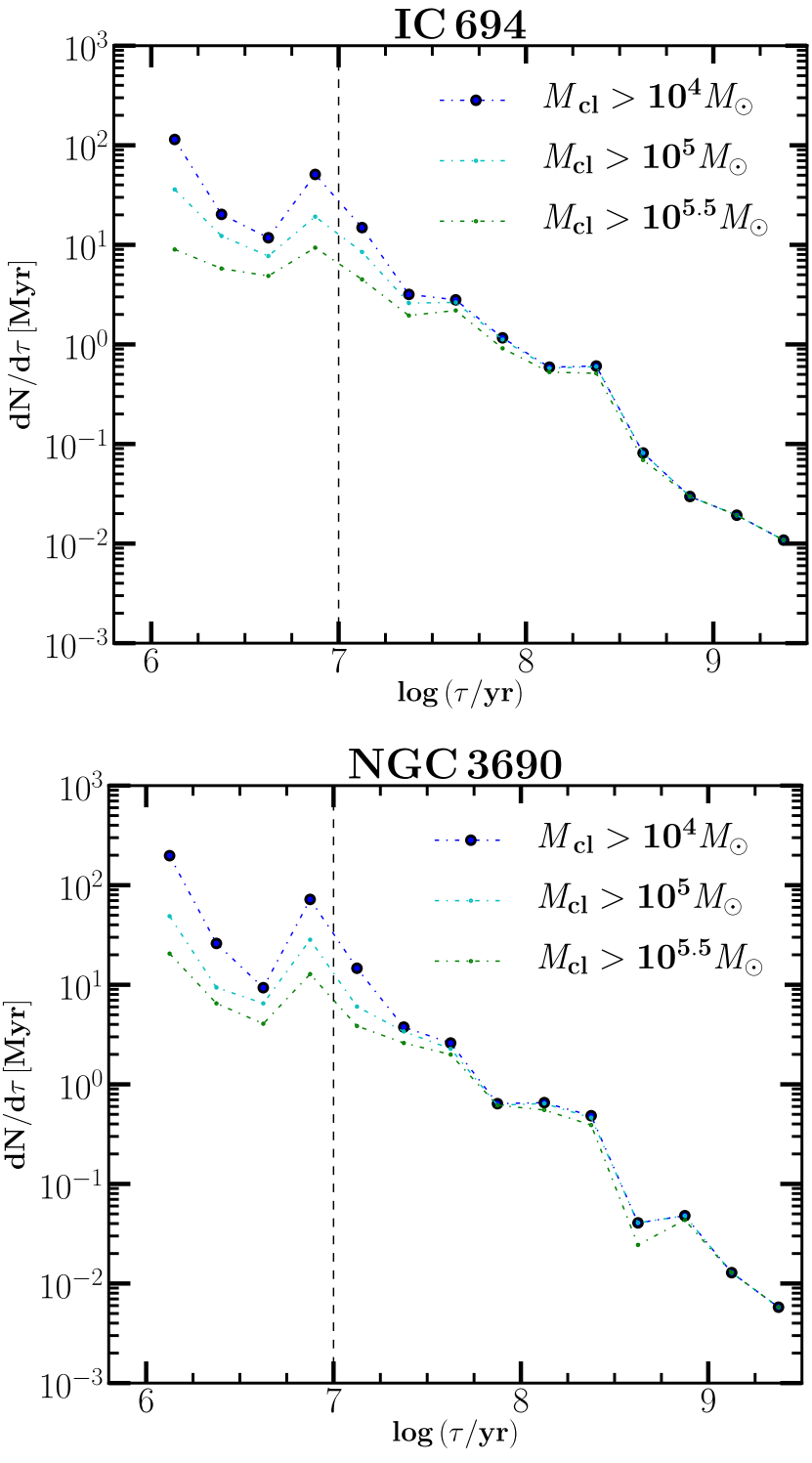

Figure 5.12: Star cluster frequency dN/dτ as a function of age for Arp 299. Three different lower mass limits were considered to derive various formation rates of the observed clusters. Blue, cyan, and green dashed lines correspond respectively to the frequency of clusters more massive than $10^4\,M_\odot$, $10^5\,M_\odot$, and $10^{5.5}\,M_\odot$. A limit of $10^4\,M_\odot$ is complete for clusters younger than 10 Myr which is represented by the vertical line.

chimneys which reflect the appearance of RSGs around that timescale (see Figure 5.5). However, the weak peak near 1 Gyr old, in the case of NGC 3690, could possibly trace an intense starburst activity that may have occured in the past. A first approach between the galaxy pairs of the merging system could have displaced/disturbed a large amount of gas and dust in the western component, and thus had favored the formation of SSCs. We should therefore consider studying the kinematics of gas and dust of Arp 299 over its lifetime in the future. Finally, Figure 5.12 also shows that over the last 10 Myr, the cluster formation rate (blue line) has not stopped increasing. This is likely due to the fact that Arp 299 is an actual ongoing merger. If the system keeps inducing violent and extreme starburst episodes, it is highly probable that the cluster and star formation rates will be increasing in the future (Bastian et al. 2009).

A power-law fit of the form $dN/d\tau \sim \tau^{-\zeta}$ was applied to the cluster frequency distribution older than 10 Myr which should be complete above the lower mass limit of $10^4\,M_\odot$. The values of ζ are respectively equal to 1.50 and 1.54 in the case of IC 694 and NGC 3690. Such high values indicate strong disruption, and in case of NGC 3690 it is also consistent with the high-mass truncation of CMF at younger ages (see right panels of Figure 5.10). Note, however, that one should assume a constant star formation history of the host galaxy over the chosen timescale to validate the hypothesis that links the value of ζ with the intensity of the cluster disruption mechanisms. The slopes approach unity if the fit is performed within the critical age range of 10 - 100 Myr.

The same age range of $10\,\mathrm{Myr} < \tau \leq 100\,\mathrm{Myr}$ was chosen to estimate the CFR using Equation 1.8. Once the value of the CFR is known, one can easily derive Γ or the cluster formation efficiency (CFE) using Equation 1.7.

In the case of Arp 299, the cluster formation efficiency Γ is equal to 10 and 16 percent for IC 694 and NGC 3690, respectively. These consider a SFR of 77 ± 27 and $52 \pm 18\,M_\odot\,\mathrm{yr}^{-1}$. The percentages may slightly increase after considering effects such as observational incompleteness. Our results are in agreement with the literature. For instance, Goddard et al. (2010) have found that the CFE on global scales of NGC 3256, which is an ongoing starburst merger, is equal to $\Gamma = 23 \pm 8\,\%$ (this value decreases to $12 \pm 2\,\%$ if one does not consider the bias from different effects). Since the extreme conditions necessary to form dense GMCs are easily met in the star-forming regions of Arp 299, more stars are therefore expected to form in bound stellar clusters. The results support the arguments that CFE is a parameter dependent on the galactic environments (Goddard et al. 2010; Adamo & Bastian 2015). CFE of starburst galaxies are relatively high compared to that associated with quiescent dwarf and gas-poor spiral galaxies where $\Gamma = 1\,\%$ (e.g. Larsen 2000; Bastian 2008; Ryon et al. 2014). Nevertheless, a lot of star clusters could be easily destroyed due to the effect of gas expulsion phase (infant mortality) before reaching $30 - 40$ Myr of age, unless there is an ongoing cluster migration during the merging process.

5.2.12 Summary

Over the course of Section 5.2, we have analysed the properties of super star clusters of Arp 299, an ongoing merger composed of IC 694 and NGC 3690. This work uses NIR AO imaging together with datasets from the new HST WFC3/UVIS camera. Optically-selected candidates were selected based on a cross identification in UBI-images and only objects with photometric errors below $\sigma_m = 0.35$ mag were included in the final catalogues. The major findings of this work are summarized as follows:

1. We have recovered 921 and 1138 star cluster candidates in the galactic fields of IC 694 (east) and NGC 3690 (west), respectively. Such a high number reflects the ongoing violent and extreme SF activity hosted by the interacting LIRG.

2. Prior to χ^2 minimization in order to fit the cluster parameters, we first constructed an extinction map of each component based on $U - I$ color. We measured a value of $A_V \sim 3.7$ mag in the nuclear starburst regions of Arp 299. Subsequently, we constrained the extinction range that should be used to perform the fit for each individual cluster as a function of its position in the field.

3. `Yggdrasil` SSP models with a solar metallicity were compared with the observed spectral energy distribution of each cluster to derive its age, mass and extinction. By including U-band data in our analysis, we have broken the degeneracy between the age and extinction. The majority of the clusters have ages below 1 Gyr with 56 % and 68 % of them having an age less than 15 Myr. In addition, the clusters are massive with a lower mass limit of $10^4\,M_\odot$ for a subsample that is complete around 10 Myr. Finally, the values of the resulting extinction A_V range between 0 and 4.5 mag. Apart from hosting more luminous star clusters, a significant number of the SSC population of NGC 3690 have a low extinction value and ages $\tau < 100$ Myr compared to the candidates hosted by IC 694.

4. The age and extinction spatial distributions indicated that star cluster population of the eastern component is randomly spread. In other words, the positions of the clusters in the galactic field do not follow a clear pattern. This is possibly because of violent physical processes such as starbursts. However, the candidates are clustered as a function of their ages in the field of the western component where the older clusters disperse in outer regions and most of the younger ones converged in the nuclear regions. Such a distribution could reflect the relics from of a cruel cradle effect meaning that SSCs have small survival chance in the starburst high-gas density area and hence need to displace toward the galactic halo via external process. Such a behavior was also noticed by Väisänen et al. (2014) in the cluster age distribution of NGC 2328.

5. We constructed the UBI-band luminosity functions of the optically-selected clusters. The CLFs present a clear break at a certain luminosity in the case of

NGC 3690. The same trend is also seen in the CLF of the galaxy intermediate-age clusters ($10\,\mathrm{Myr} < \tau < 100\,\mathrm{Myr}$) with a slope of $\alpha = 1.53 \pm 0.07$. Though we did not correct for observational completeness, the prominence of a flat distribution in the faint end magnitude requires physical explanations. A power-law fit of the UBI-band CLFs resulted in indices of $\alpha = 1.79 \pm 0.11, 1.93 \pm 0.10,$ and 2.08 ± 0.13 in the case of IC 694. These values are steeper, except for U-band, compared to the slopes of $\alpha = 1.82 \pm 0.07, 1.91 \pm 0.08,$ and 1.93 ± 0.07 that correspond to the CLFs of NGC 3690. Our results are in agreement with the literature which report that starburst galaxies such as LIRGs have shallower power-law slopes compared to those of normal spiral galaxies. In addition, the increasing slopes at redder wavelengths support the cluster evolutionary fading process.

6. We also derived the cluster mass functions using three different age bins. While a power-law fit generally represents the datasets of IC 694, this is not the case for NGC 3690. Only the high-mass end of the truncated distribution could be fit with a power-law, especially for the CMFs of young clusters ($\tau < 100\,\mathrm{Myr}$). The effect of infant mortality could have played an important role in shaping the CMF that way. Therefore, a Schechter fit would be more appropriate for the data with a characteristic mass around $10^6\,M_\odot$. Such a value is higher than the $2 \times 10^5\,M_\odot$ which is the characteristic mass associated with normal spirals. For the values of the slope β, they are all steeper than 2 and decrease with increasing age bin. The destruction of the clusters could have been mass-dependent.

7. The distribution of the data points in $I - K$ vs. $B - I$ diagram showed that some clusters suffer from NIR excess. Stochastic sampling effects were only one of the possible causes. More analysis on the contamination from the surrounding nebular emission should also be considered. Blending effects, however, were excluded since it has previously been shown that such bias only start to become an issue if the host galaxy is at a distance beyond $\sim 100\,\mathrm{Mpc}$ when working with the spatial resolution of our survey. We also examined the properties of the K-selected objects and have found that they are less likely to have redder colors. They do not have a specific age range, i.e they are uniformly distributed in the cluster age-mass plane. They are massive clusters ranging from $10^{4.5}\,M_\odot$ to $10^8\,M_\odot$ without any particular bias to a certain sub-population of SSCs. This was important to establish when we move to analyzing SSCs without U-band data.

8. The cluster frequency as a function of time for Arp 299 suggested that the cluster formation rates have increased over the past 10 Myr and will still increase in the future. This is because Arp 299 is currently undergoing a violent interaction thus inducing extreme starburst activities. The peaks around $\log \tau \sim 6.8 - 7.2$ are likely not real. They exist because of the artificial concentrations of the clusters at this age. The fitting method does not accurately take into account short-lived phases such as red supergiant stars. However, NGC 3690 may have hosted an episode of burst 1 Gyr ago, though this should be confirmed using stellar population studies

in the future. In addition, we fitted a power-law function to the cluster frequency of a $10^4\,M_\odot$ lower mass limit. With a slope $\zeta \sim 1.5$, we can suggest that the star clusters of Arp 299 endure strong disruption mechanisms. Finally, the values of the cluster formation efficiency Γ are respectively equal to 10 and 16 percent for IC 694 and NGC 3690. They are high compared to that of gas-poor spirals. This is in agreement with the results from previous works which suggest that more stars are likely to form in bound clusters in galaxies with extreme environments.

5.3 The case of a subsample of LIRGs

Having used Arp 299 in Section 5.2 as a blueprint in our star cluster analyses, we now extend our study to a larger subsample consisting of five more luminous infrared galaxies. The subsample is composed of IRAS F17138−1017, IRAS 18293−3413, IC 883, ESO 550−IG025, and IRAS 19115−2124, all taken from the SUNBIRD survey which we have already discussed in Chapter 2. These targets were chosen because they host a large population of optically-selected SSC candidates. In the following, we provide a brief overview of the individual galaxies:

- **IRAS F17138−1017** is an almost edge-on spiral galaxy with IR luminosity $\log(L_{\rm IR}/L_\odot) = 11.42$ at a distance $D_L \sim 72$ Mpc. This LIRG with a highly extinguished central region (Alonso-Herrero et al. 2006) is part of an atlas of a representative sample of local LIRGs and ULIRGs which were observed with the integral field spectroscopy of the VLT/SINFONI (Piqueras López et al. 2012; Piqueras López et al. 2013). By drawing the 2D distribution of the ionized gas in the galaxy central regions, they have found that the nuclear regions of IRAS F17138−1017 emit strong Brγ emission. The prominence of such a hydrogen recombination line indicates the presence of recent star formation activity. Kankare et al. (2008), on the other hand, have discovered an optically hidden CCSNe in the dusty nuclear regions of the galaxy based on follow-up observations with NIR AO imaging. The extinction $A_V = 15.7$ mag of SN2008cs is believed to be the highest extinction ever measured for a SN so far. Finally, IRAS F17138−1017 along with other low-z (U)LIRGs were subject of SSC study by Miralles-Caballero et al. (2011) over their whole survey. With the detection of thousands of optically-selected star clusters, that they refer to as "knots", they were able to confirm, for instance, that there is a clear correlation between the cluster mass and radius and that the properties of the knots depend on the interaction phase of the system (e.g. more luminous knots with larger radii are hosted by post-merger galaxies).

- **IRAS 18293−3413** is a gas-rich spiral luminous IR galaxy ($\log L_{\rm IR} = 11.81\,L_\odot$) with a luminosity distance $D_L \sim 75$ Mpc. Based on NIR AO imaging and long-slit spectroscopy observations, Väisänen et al. (2008a) proposed that the galaxy

spiral arms are *leading*, i.e. the sense of orientation of the arms are in the opposite direction of the disk spin. Unlike *trailing* arms, *leading* arms are very rare and in the case of IRAS 18293−3413, a retrograde encounter with its small companion galaxy might have caused its dynamics to exhibit such an unusual phenomenon. The target is also a well-known laboratory for CCSNe hunting; it hosts SN2004ip which is the first SN ever discovered using NIR AO systems (Mattila et al. 2007; Ryder et al. 2014). Radio follow-up observations by Pérez-Torres et al. (2007) confirmed that optical surveys failed to detect SN2004ip, simply because it is located in the dust-obscured circumnuclear regions of the galaxy. Furthermore, IRAS 18293−3413 is one of our first NIR SSC pilot studies as the galaxy hosts hundreds of K-selected SSC candidates. In Section 3.4.5, the cluster luminosity function of IRAS 18293−3413 was used to test the validity of two different distributions (power-law vs. Schechter function) and their respective implications. However, the analysis remained inconclusive. By constructing the cluster mass function in the present work, we will confirm whether or not a bend/truncation of the LF is an imprint of any physical processes.

- **IC 883** or UGC 8387 is a remnant of two interacting galaxies with two tidal tails and a highly-inclined disk at a distance $D_L \sim 101$ Mpc. The high IR luminosity ($\log L_{\rm IR} = 11.67\, L_\odot$) of the galaxy merger is not surprising as it is classified as a composite starburst−AGN (Yuan et al. 2010). Such a nature has further been suppported by Modica et al. (2012) and Romero-Cañizales et al. (2012) where they suggested that the AGN activity is relatively weak compared to the intense star formation factory of massive stars and star clusters. IC 883 is also known for the AO-assisted discoveries of two consecutive optically hidden supernovae, 2010cu and 2011hi, within a 12-month period (Kankare et al. 2012). Finally, Vavilkin (2011) and Modica et al. (2012) have identified more than a hundred star clusters in the nuclear and circumnuclear regions of the late merger. Such a spatial distribution is believed to be the result of a collision in the past between two galaxies.

- **ESO 550−IG025** is a luminous IR galaxy pair ($\log L_{\rm IR} = 11.45\, L_\odot$) at a distance $D_L \sim 135$ Mpc. In an early merging stage, the system is composed of two distinct components. While the morphology of the northern galaxy displays some spiral patterns, the shape of the southern component, however, is less disturbed with an inclined disk. Based on radio continuum spectral index maps, Vardoulaki et al. (2014) classified ESO 550−IG025-S as a radio-AGN and ESO 550−IG025-N as a mixture of nuclear starburst and radio-AGN. The formation of the massive star clusters preferentially occur in the northern component where $\sim$20 percent of the SSC population are believed to be younger than 7.6 Myr (Vavilkin 2011).

- **IRAS 19115−2124**, dubbed the Bird galaxy because of its morphology, is the result of three mutual merging galaxies. The head, the wings, the heart, the body, and an extended tail of the Bird are clearly resolved using AO NIR observations (Väisänen et al. 2008b). This is the most distant target and the most luminous

LIRG of the SUNBIRD survey, i.e $D_L \sim 206$ Mpc and $\log(L_{\rm IR}/L_\odot) = 11.87$. Detailed study of the system by Väisänen et al. (2008b) reported that most of the energy that fuels such a high IR emission comes from the ongoing intense star formation in the head of the Bird. They also performed preliminary analysis of the SSC candidates in IRAS 19115−2124. Most of the objects of interest are concentrated along the west and the north-west wings of the interacting LIRG. Note, however, that blending effects should be taken into account because of the distance of this target.

These targets are more distant compared to the sample of non-LIRG starburst systems from previous SSC studies (e.g Bik et al. 2003; Haas et al. 2008; Sollima et al. 2014). Except for IRAS 19115−2124, the distance should not be an issue since results from the MC simulations and analyses in Section 3.5.1 showed that blending effects should not be significant especially if $D_L \lesssim 100$ Mpc. There are a number of papers in preparation based on the results and discussion of this work

5.3.1 Data, source extraction, and HST photometry

The already-processed HST optical data of the targets were also retrieved from the Hubble Legacy Archive. The broad-band filters F435W(B) and F814W(I) of the ACS/WFC camera were used to image each galaxy. More details of the HST observations are provided in Section 2.3.2. BI-images were resampled to match with the pixel sizes of the NIR images taken with Gemini/NIRI or VLT/NaCo. BIK-color images of the five LIRGs are shown in Figure 5.13, Figure 5.14, Figure 5.15, Figure 5.16, and Figure 5.17.

The same method described in Section 5.2.1 was adopted for object detection. The noise level in B-band data is too high in the case of IRAS F17138-1017, hence there is no need to get a BI-combined image. Instead, the unsharp-masked version of the I-band image was used to run `SExtractor`. Aperture photometry were derived by using fixed aperture radii of 2, 3 or 5 pixels depending on the pixel scale of the NIR images: 0.054, 0.027 or 0.022 arcsec/pixel, respectively. The corresponding sky annuli are respectively, 3 to 4.5, 5 to 7, and 7 to 10 pixels. Growth curves of bright and isolated sources were used to measure the aperture correction and the VEGAMAG photometric zeropoints were obtained from the HST/ACS data manuals. Table 5.3 summarizes the photometric calibrations applied to the data to derive the apparent magnitudes of the extracted sources. Note that systematic errors of $\sim 0.1-0.2$ mag were also considered due to resampling of the optical data.

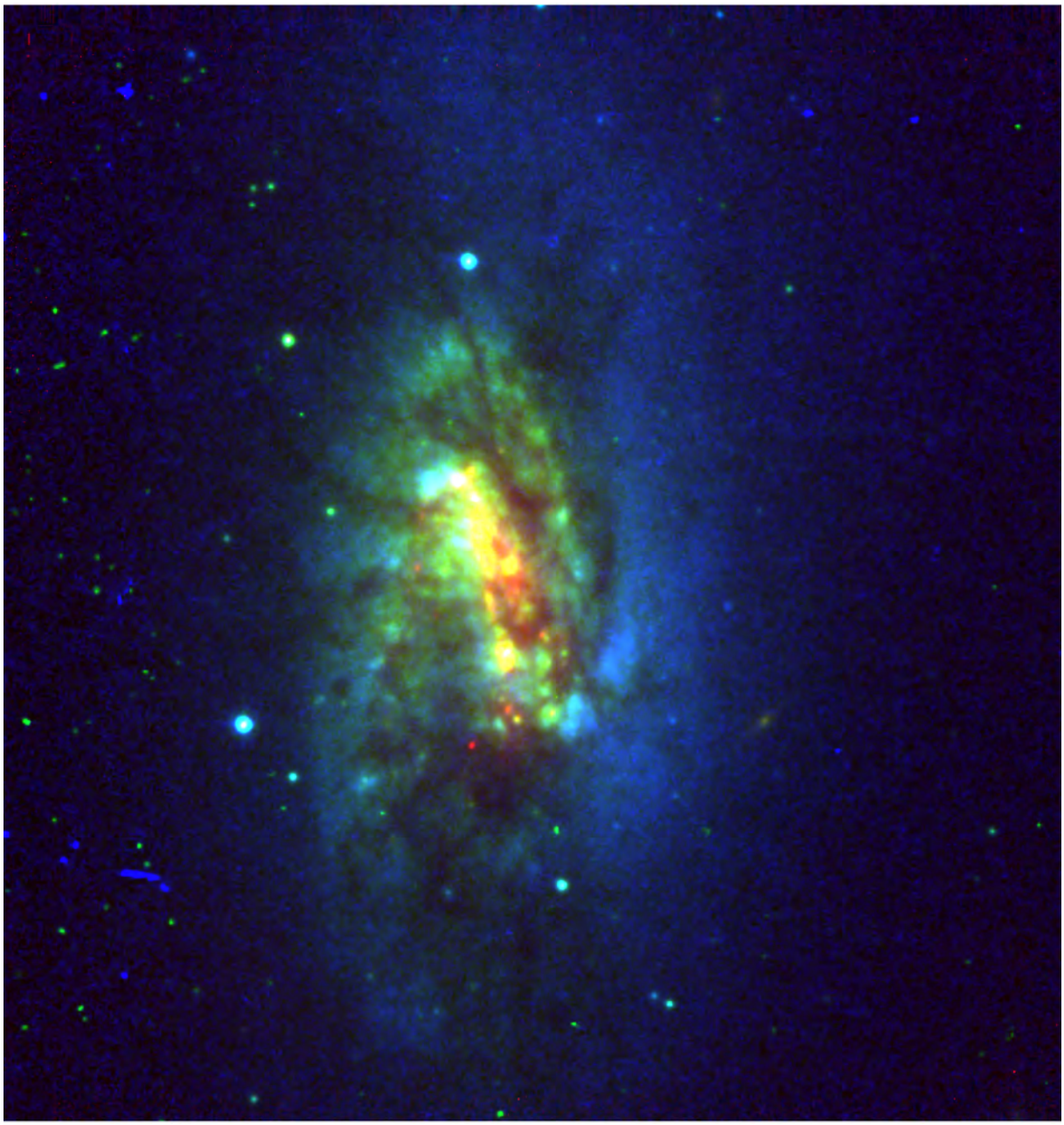

Figure 5.13: *BIK* three-color image of **IRAS F17138−1017** in a $22'' \times 22''$ field. *B*-band (blue) and *I*-band (green) data were observed with the HST/ACS and *K*-band data (red) were imaged with Gemini/NIRI. Red color in RGB-image does not always mean old, it could also be due to the effect of RSGs or high dust-obscuration areas.

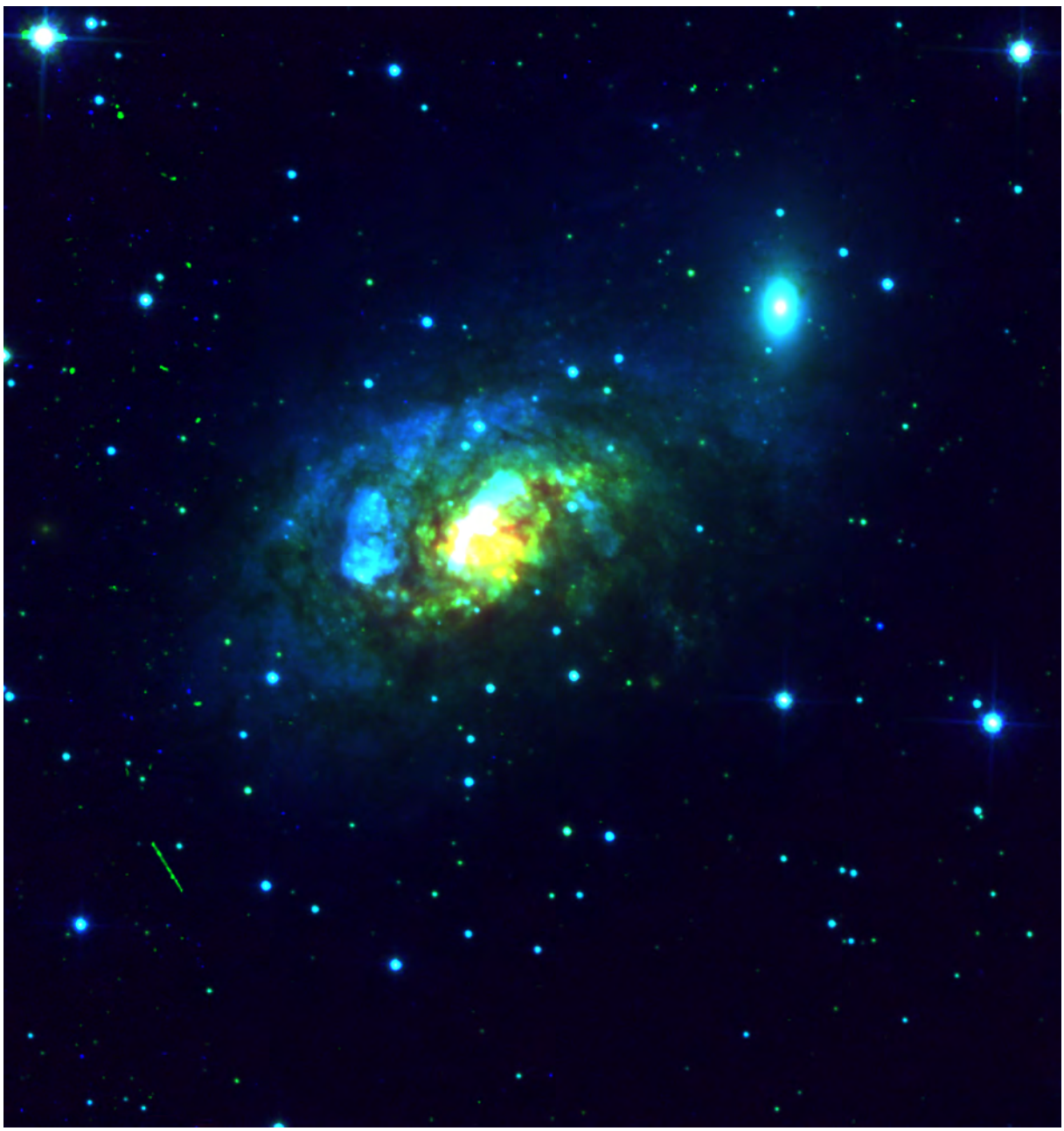

Figure 5.14: As of Figure 5.13 but for **IRAS 18293−3413** except that the NIR data were imaged with VLT/NaCo. The image has a FoV of $27'' \times 27''$.

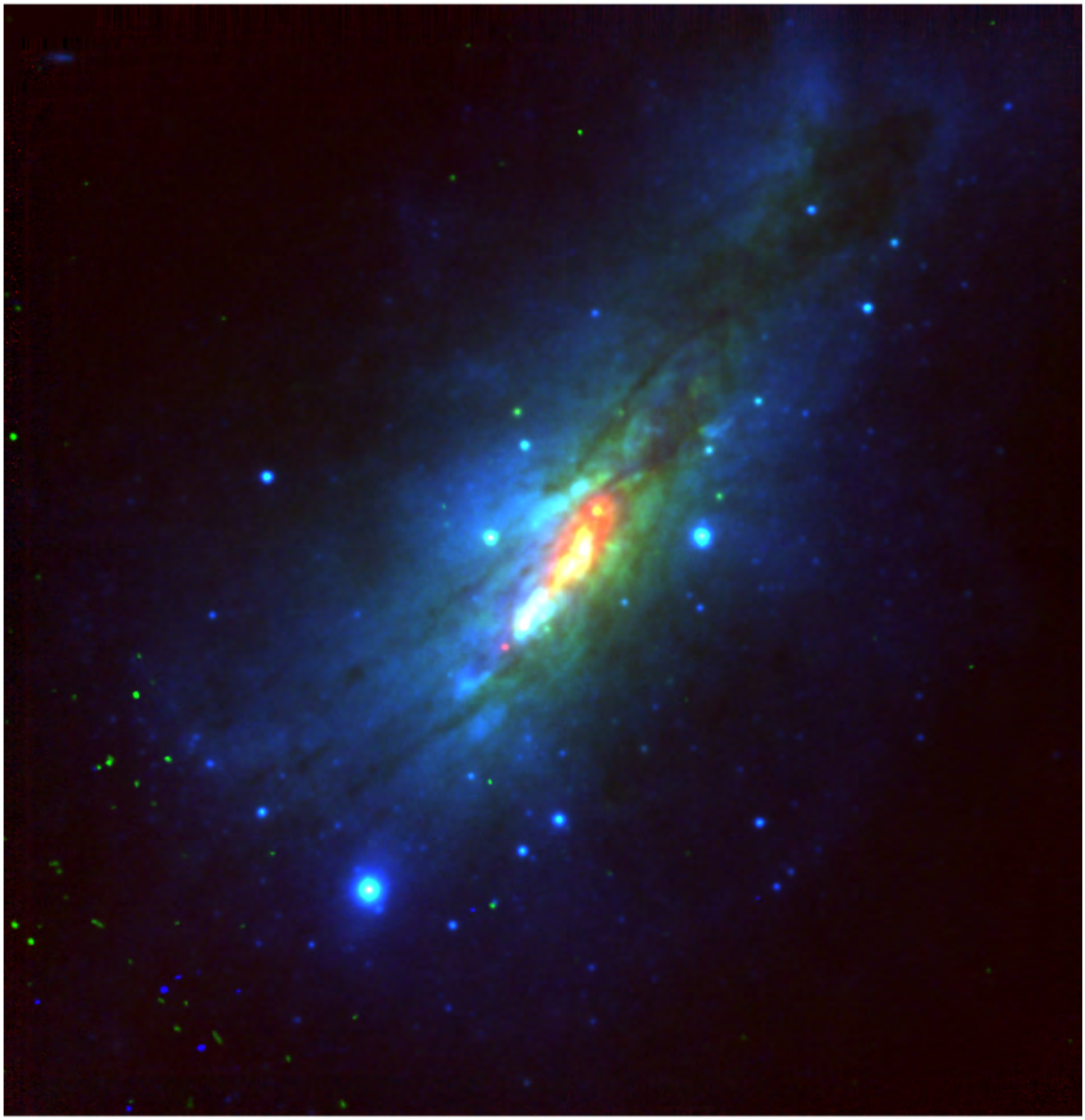

Figure 5.15: As of Figure 5.13 but for **IC 883**. The image has a FoV of $22'' \times 22''$.

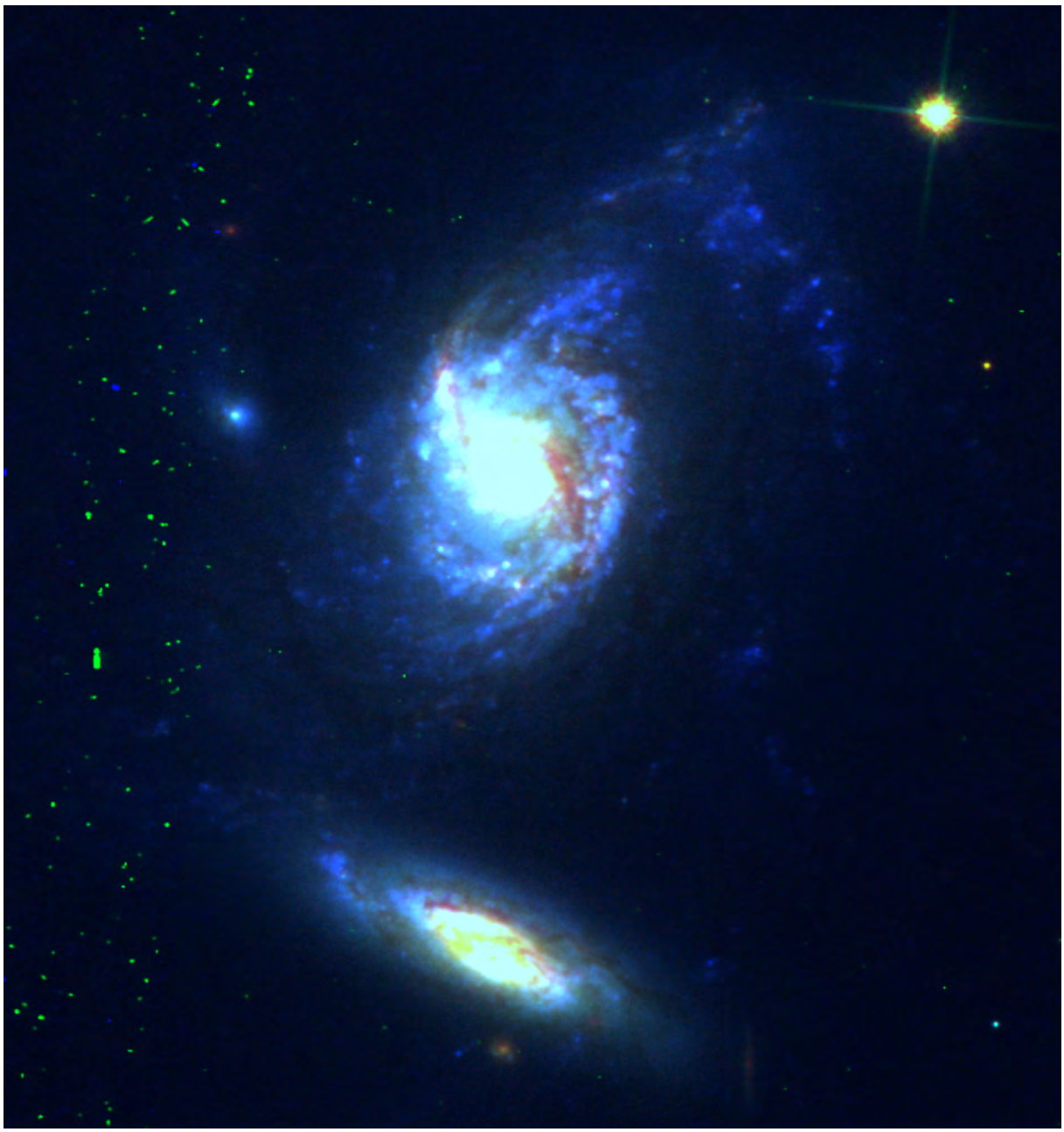

Figure 5.16: As of Figure 5.13 but for **ESO 550−IG025** except that the NIR data were imaged with VLT/NaCo. The image has a FoV of $54'' \times 54''$.

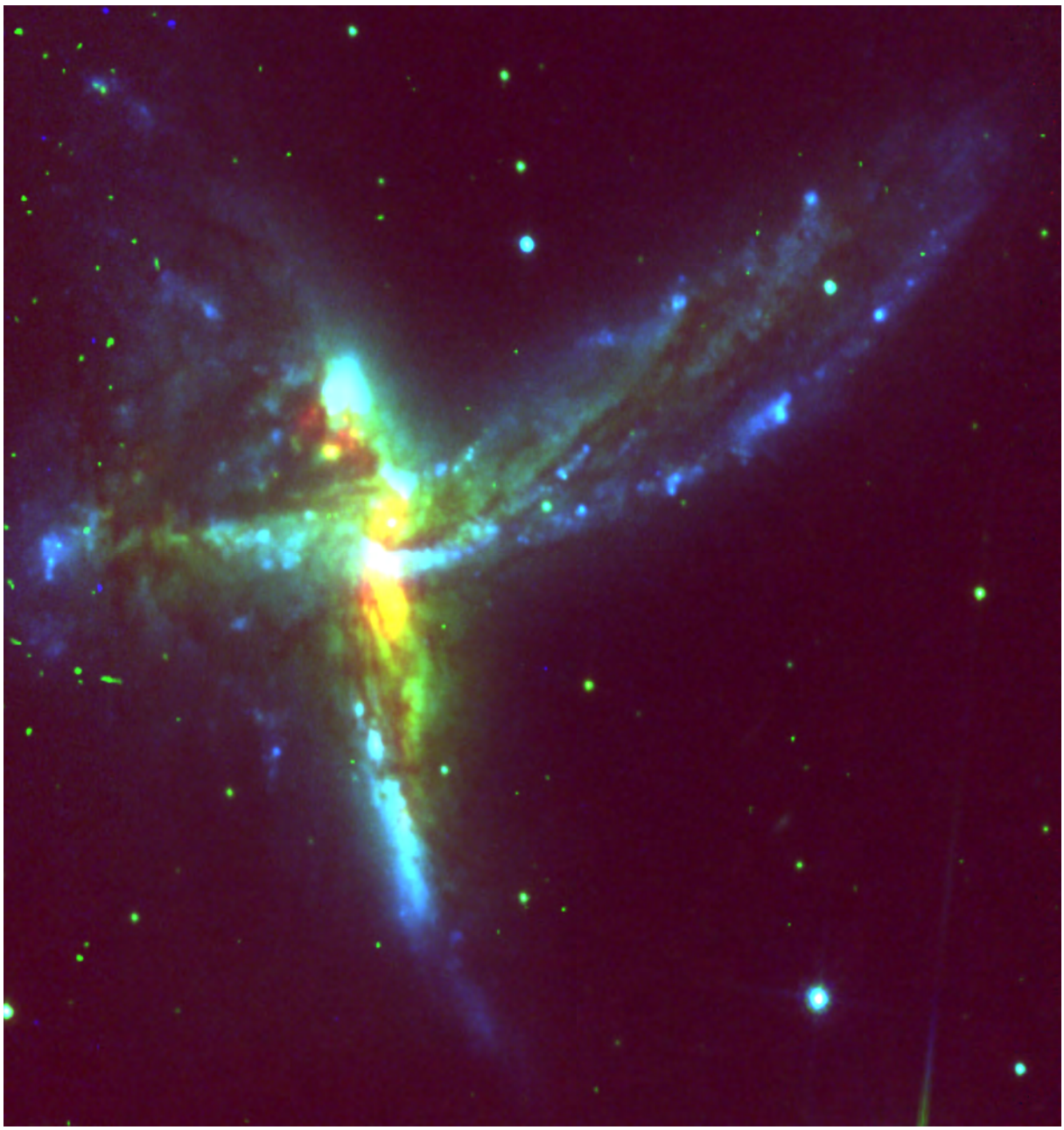

Figure 5.17: As of Figure 5.13 but for **IRAS 19115−2124** or the Bird, except that the NIR data were imaged with VLT/NaCo. The image has a FoV of $27'' \times 27''$.

5.3.2 Optically-selected clusters and photometric diagrams

We adopted similar steps as reported in Section 5.2.2 to draw the final catalogues of the optically-selected star clusters of each galaxy. The only difference in this case is that the selection was based on the cross-identification of the BI-catalogues. The number of the detected SSCs (with magnitude errors $\sigma \leq 0.35$) per filter as well as the Vega-based magnitude limits are listed in Table 5.3. If `SExtractor` failed to detect an optically-selected SSC in the Gemini/NIRI or the VLT/NaCo field, the corresponding K-band magnitude limit was considered to represent the Vega-magnitude of the star cluster. The final number of the BIK SSC catalogues are reported in Table 5.4 where the results from Arp 299 are also included to increase the statistics of any further analysis. Again, a large population of super star clusters are distributed within the galactic fields of the subsample of LIRGs. In the case of ESO 550−IG025, the tabulated value in the first column of Table 5.3 represents the total number of the SSCs from both northern and southern components.

For the less distant targets ($D_L < 150$ Mpc), the color-magnitude diagrams (left panels) and the BIK color-color diagrams (right panels) of the star cluster candidates are shown in Figure 5.18. The `Yggdrasil` models are represented by the blue lines. System-

Table 5.3: Photometric measurements of the subsample of LIRGs

Galaxy name	A_λ (mag)	PSF/FWHM (arcsec)	$m_0; a_c$ (mag)	$N(\sigma \leq \sigma_m)$	Mag-limit (Vega-mag)
(1)	(2)	(3)	(4)	(5)	(6)
		F435W (B-band)			
IRAS F17138−1017	2.49	0.11	25.78, −0.39	239	26.5
IRAS 18293−3413	0.51	0.12	25.78, −0.57	589	28.4
IC 883	0.05	0.12	25.78, −0.37	333	28.7
ESO 550−IG025	0.15	0.11	25.76, −0.33	514	28.1
IRAS 19115−2124	0.46	0.11	25.78, −0.74	382	27.8
		F4814W (I-band)			
IRAS F17138−1017	1.03	0.11	25.53, −0.54	416	25.7
IRAS 18293−3413	0.21	0.10	25.53, −0.77	602	26.7
IC 883	0.02	0.11	25.53, −0.51	343	27.3
ESO 550−IG025	0.06	0.10	25.51, −0.45	457	26.8
IRAS 19115−2124	0.19	0.10	25.53, −0.84	411	25.7
		K_S-band			
IRAS F17138−1017	0.21	0.11	26.53, −1.12	202	21.4
IRAS 18293−3413	0.04	0.12	26.95, −1.34	354	21.6
IC 883	0.02	0.13	26.80, −1.22	94	21.9
ESO 550−IG025	0.01	0.13	27.57, −1.20	259	22.2
IRAS 19115−2124	0.04	0.12	19.41, −0.92	253	23.8

Notes. Column 1: Galaxy name; Column 2: foreground galactic reddening from NED Database; Column 3: PSF/FWHM of bright isolated stars in the original image; Column 4: zeropoint magnitude and aperture correction; Column 5: number of SSCs with $\sigma_m \leq 0.35$; Column 6: the corresponding Vega-based magnitude limits.

Table 5.4: Characteristics of the optically-selected clusters

Galaxy name	Nb. SSC			Av-range	Mass-range
	$\sigma_{BI} \leq 0.35$	$\sigma_{BIK} \leq 0.35$	$\tau \leq 30$ Myr	(mag)	($\log M_{cl}$)
(1)	(2)	(3)	(4)	(5)	(6)
IC 694	995	343	66 %	0.00 – 4.50	3.1 – 8.4
NGC 3690	1229	443	77 %	0.00 – 4.41	2.8 – 8.0
IRAS F17138−1017	229	104	26 %	0.00 – 5.83	3.5 – 8.6
IRAS 18293−3413	536	309	34 %	1.00 – 5.94	3.6 – 8.8
IC 883	315	79	25 %	0.03 – 3.57	3.4 – 8.6
ESO 550−IG025	415	182	58 %	0.01 – 3.16	3.9 – 8.5
IRAS 19115−2124	326	234	-	-	-
The Subsample	4045	1694	47 %	0.00 – 5.94	2.8 – 8.8

Notes. Column 1: Galaxy name; Columns 2 & 3: number of SSCs of the BI- and UBI/BIK- catalogues; Column 4: the percentage of SSCs with age younger than 30 Myr; Columns 5 & 6: range of the derived extinction and mass of the optically-selected clusters. Note that the star cluster properties of Arp 299 are also listed for comparison. The bottom row indicates the total numbers of SSCs along with the percentage of young clusters, extinction and mass ranges in the LIRG subsample.

atic offsets of $\sim 0.2-0.4$ mag due to uncertainties of the AO data absolute calibration had to be applied to the K-band magnitude so that the data will match with the model. This final absolute magnitude offset was derived by comparing the colors of the field stars or those of the very bright SSCs if there were no enough point sources with the colors of a range of all stellar spectral types (Johnson 1966) or the `Yggdrasil` models, respectively. The CMDs suggest that the star clusters have masses between $\approx 10^4 - 10^7\,M_\odot$, where IRAS F17138−1017 and IRAS 18293−3413 appear to host the most massive clusters. These will be confirmed in Section 5.3.5. Unlike the UBI CCDs of Figure 5.3, it is not trivial to get a first approximation of the cluster ages with the present color-color diagrams due to the loop of the SSP evolutionary track between $10 - 500$ Myr. We, therefore, expect higher uncertainties of the derived ages from the BIK-fits.

Figure 5.19 shows the "SSC" CMD and CCD of IRAS 19115−2124, the most distant target. In this case, the derived magnitudes are no longer reliable as they are expected to be heavily contaminated by blending effects (refer to Section 3.5.1). In fact, most of the detected objects are likely blends of SSCs or complexes of SSCs which could then possibly result in a biased distribution of the data points in the diagrams. Because we have not performed simulations of filter-dependent blending effects, we will not attempt to fit the ages, masses and extinctions of the star clusters hosted by the Bird galaxy. Note, however, that the majority of the selected objects are located in the head and the wings of the merging galaxies.

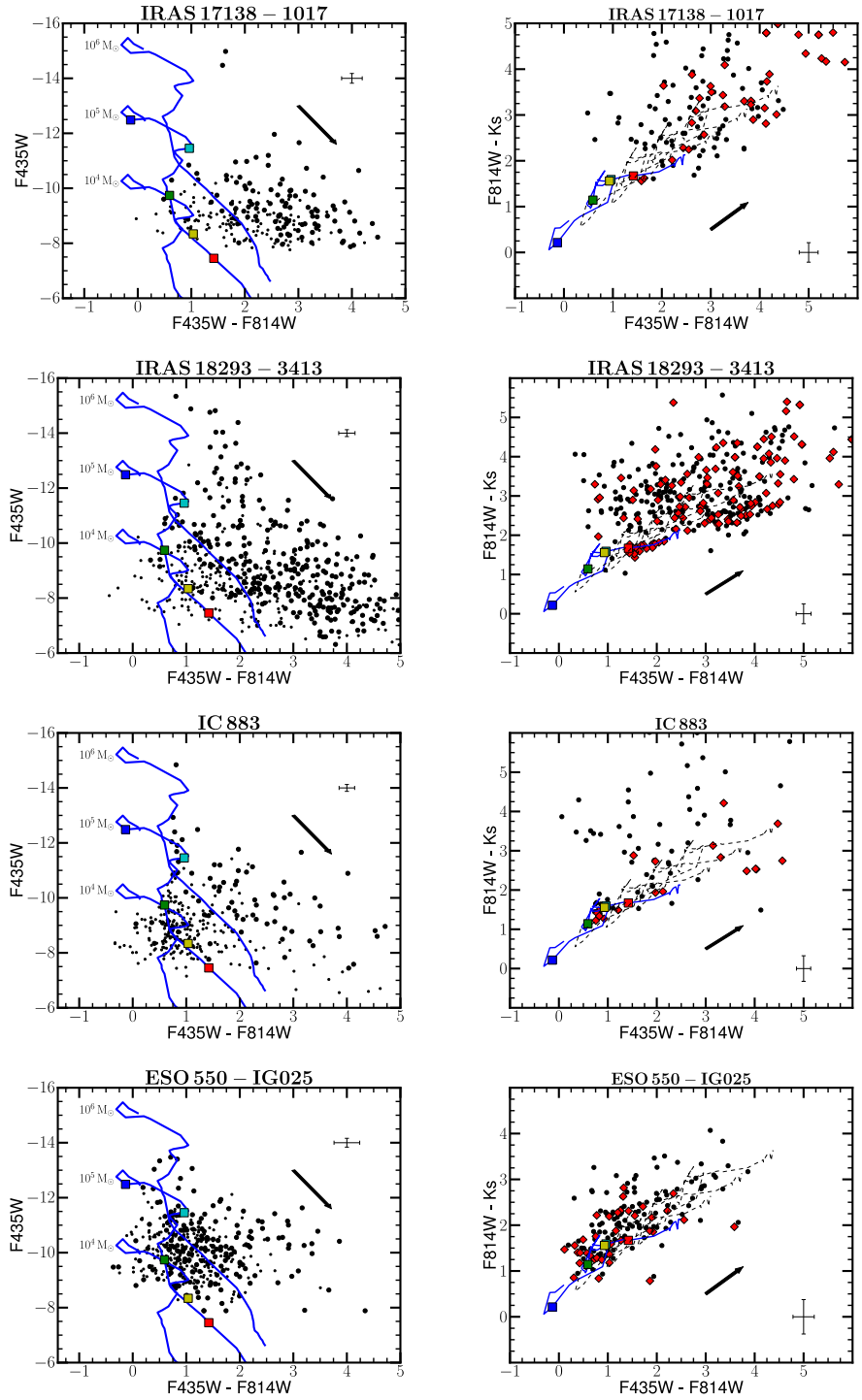

Figure 5.18: SSC color magnitude (left) and color-color (right) diagrams of the four less distant LIRGs overplotted with `Yggdrasil` SSP models (solid and dashed lines). Only star clusters with photometric uncertainties $\sigma_m \leq 0.35$ in all images are included in the CCDs and the red diamonds indicate the K-selected cluster candidates. Blue, cyan, green, yellow and red squares mark 5, 10, 100, 500 and 1000 Myr in the evolutionary track, respectively. The arrows indicate a reddening of $E(B-V) = 0.25$. The model is plotted with 10^4, 10^5, and $10^6 M_\odot$.

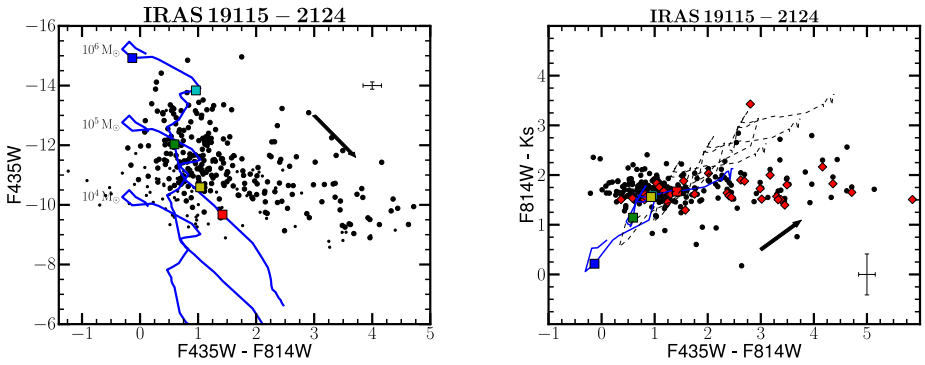

Figure 5.19: SSC CMD (left) and CCD (right) of IRAS 19115−2124 overplotted with `Yggdrasil` SSP models (solid lines). Only star clusters with photometric uncertainties $\sigma_m \leq 0.35$ in all images are included in the plot. Labels the same as in Figure 5.18.

5.3.3 Extinction maps

To constrain the range of the extinction prior to SED fitting, we followed the same steps as in Section 5.2.4 to produce the reddening maps of each galaxy. Since there are no U-band images, we used the following expression to get a broad-band $B-I$ color map:

$$B - I = -2.5\ log\ \frac{f_{B,\,\mathrm{Vega}}}{f_{I,\,\mathrm{Vega}}} \tag{5.7}$$

An intrinsic $(B-I)$ color of ≈ 0.90 was then retrieved from the synthetic spectrum fitting to a starburst galaxy template by Kinney et al. (1996) to produce the extinction maps under the Calzetti dust reddening law.

Figure 5.20 shows the color maps (left) and the resulting extinction maps (right) of the targets. As already mentioned in Section 5.2.4, the values of the extinction ranges throughout the galactic fields are lower compared to those derived from NIR color maps that can reproduce the reddening beyond the optical dust screen. For instance, the nuclear starburst regions of IRAS F17138−1017 have an extinction $A_V \sim 6.8$ mag based on our extinction map. However, Depoy et al. (1988) have found a reddening of $A_V \sim 8$ mag while Piqueras López et al. (2013) derived an extinction $A_V = 15.2$ mag using VLT/SINFONI data in the NIR. Such high values are not surprising since LIRGs, usually with high SFR, host more dusty nuclear regions than galaxies with lower SFR (e.g. Piqueras López et al. 2013). Nevertheless, we will use the maps based on the optical colors to estimate A_V^0 in order to constrain the extinction range of each selected object.

5.3.4 The model and χ^2 fitting

The SSC pilot study of Arp 299 demonstrated that `Yggdrasil` models with solar-metallicity produce results with the best fits of the star cluster ages and masses. There-

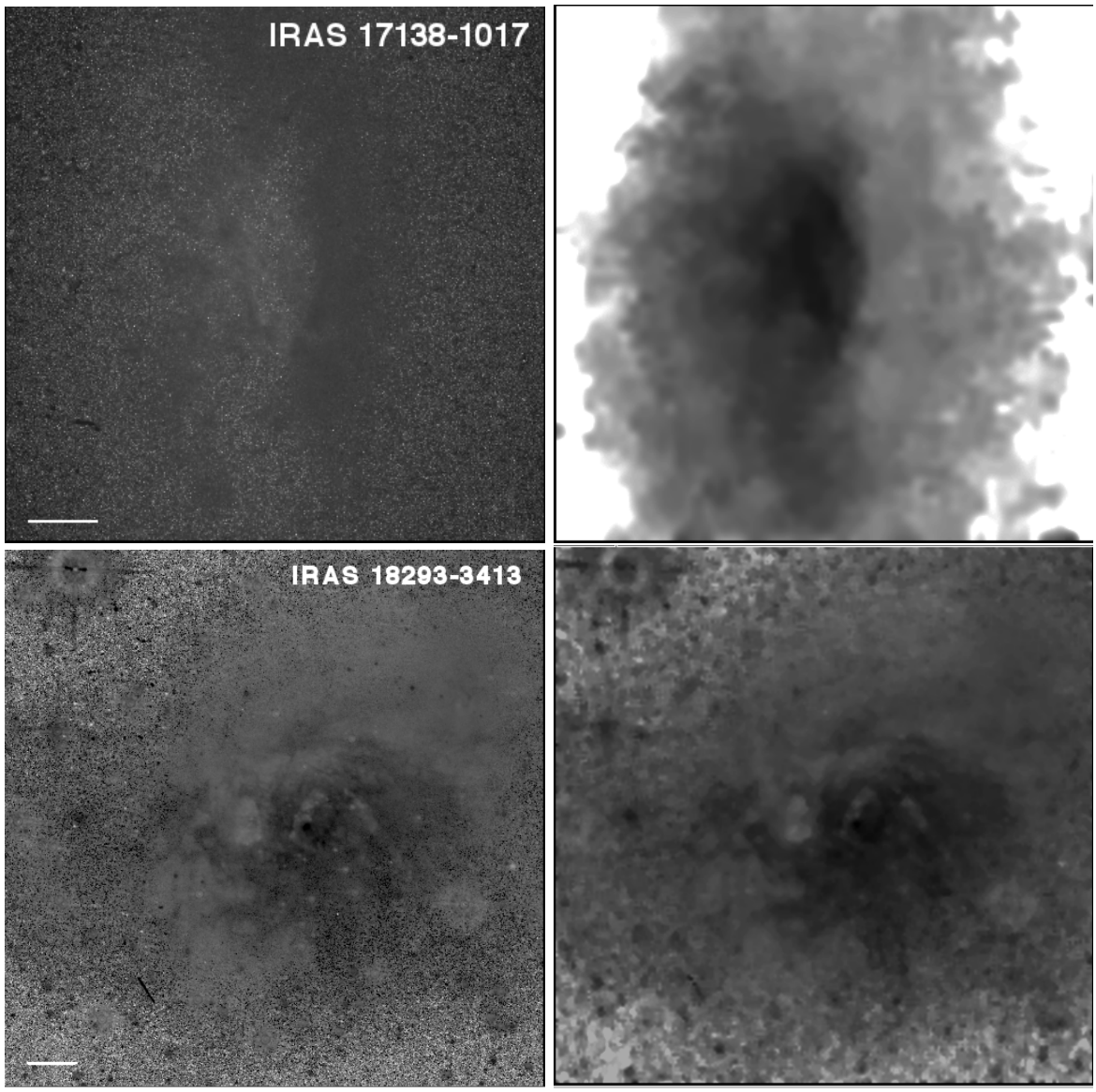

Figure 5.20: *Left:* $B-I$ color-maps of the five LIRGs. *Right:* Extinction maps produced from a convolved version of the color maps and assuming an uniform intrinsic color of $B-I \sim 0.90$ to the galaxies. Darker shades are associated with higher colors/extinctions in the maps, except for IC 883.

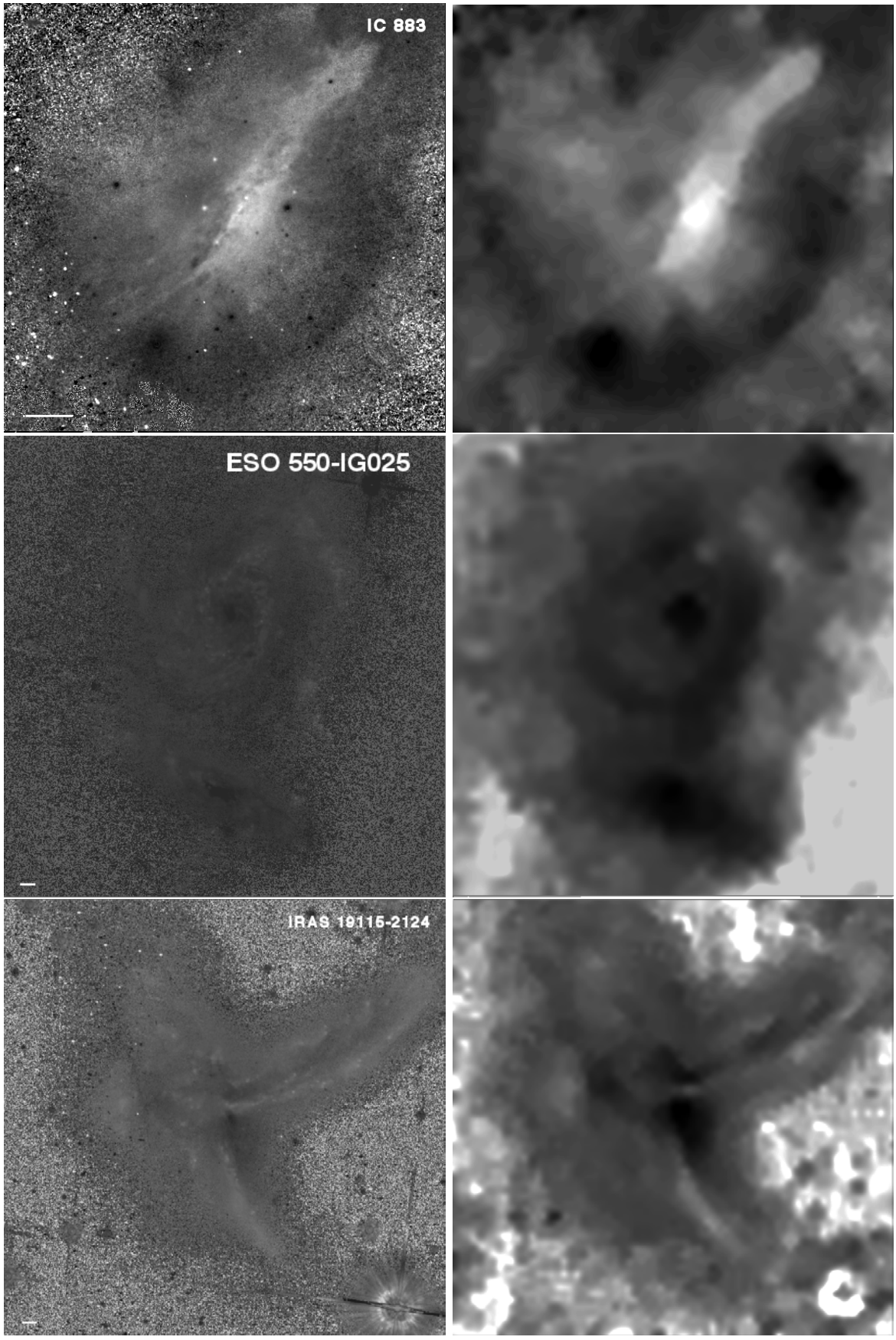

Figure 5.20: −Continued

fore, we will no longer fit the data with `Starburst99` in the present analysis. Calzetti reddening law is still adopted since the subsample is composed of strongly star-forming galaxies. A brief description of the SSP model is already highlighted in Section 5.2.3.

We used the same algorithm as in Section 5.2.5 to estimate the physical parameters of the star clusters. Note, however, that only three filters are available, i.e. $\lambda = \{B, I, K\}$ in Equation 5.4, and that the K-band magnitudes should not be used to estimate the cluster mass in Equation 5.5. We also used the expressions in Equation 5.6 to define the extinction range necessary to run the χ^2 fitting of each individual source with an initial estimate A_V^0.

Finally, we also examined the robustness of the fits before deriving the final results of the overall sample. The star clusters with low photometric uncertainties ($\sigma \leq 0.25$ mag) of ESO 550−IG025 were used for this purpose. Age, mass, and extinction distributions from the analyses are displayed in Figure B.5 and Figure B.6 of Appendix B. Star clusters predicted to have low and high extinction values were selected for the test. The estimates from the χ^2 minimization are indeed in agreement with the distribution of the data points in the CMDs/CCDs, though the cluster ages of those which fall in the red loop of the evolutionary track are likely to have higher uncertainties because of the age-extinction degeneracy.

5.3.5 Mass, age, and extinction of the clusters

After comparing the BIK- spectral energy distribution of the observed data with that of the SSP `Yggdrasil` model, we have derived the age, mass, and extinction of each optically-selected cluster candidate hosted by the subsample of LIRGs. Figure 5.21 shows the cluster mass-age plane (left) of each target and the distribution of the resulting extinction (middle). The ranges of physical parameters are listed in Table 5.4. Based on these results, IRAS F17138−1017 and IRAS 18293−3413 host the most massive and the most extinguished star clusters. In fact, the values of the cluster lower mass limits for $\tau < 30$ Myr are above $10^6\,M_\odot$ in these cases and for the extinction values, some of the clusters have $A_V > 5.5$ mag. Note, however, that we will exclude data points with masses above $10^{8.5} M_\odot$ in further analysis; we may be looking at some star cluster complexes in such cases or the use of BIK-filters for SED fitting has possibly led to an overestimate of the cluster mass.

In all four targets, more than ≈ 25 percent of the ages of the star clusters are younger than ~ 30 Myr (Table 5.4). Clusters with intermediate-ages (between 100 Myr to 1 Gyr) and a non-negligible population of old cluster candidates with ages above 1 Gyr are preferentially hosted by IRAS 18293−3413 and IC 883. As already mentioned in Section 5.2.6, chimneys are observed in the age distribution of the star clusters probably due to the appearance of AGB stars at around $\log \tau \sim 8.2$.

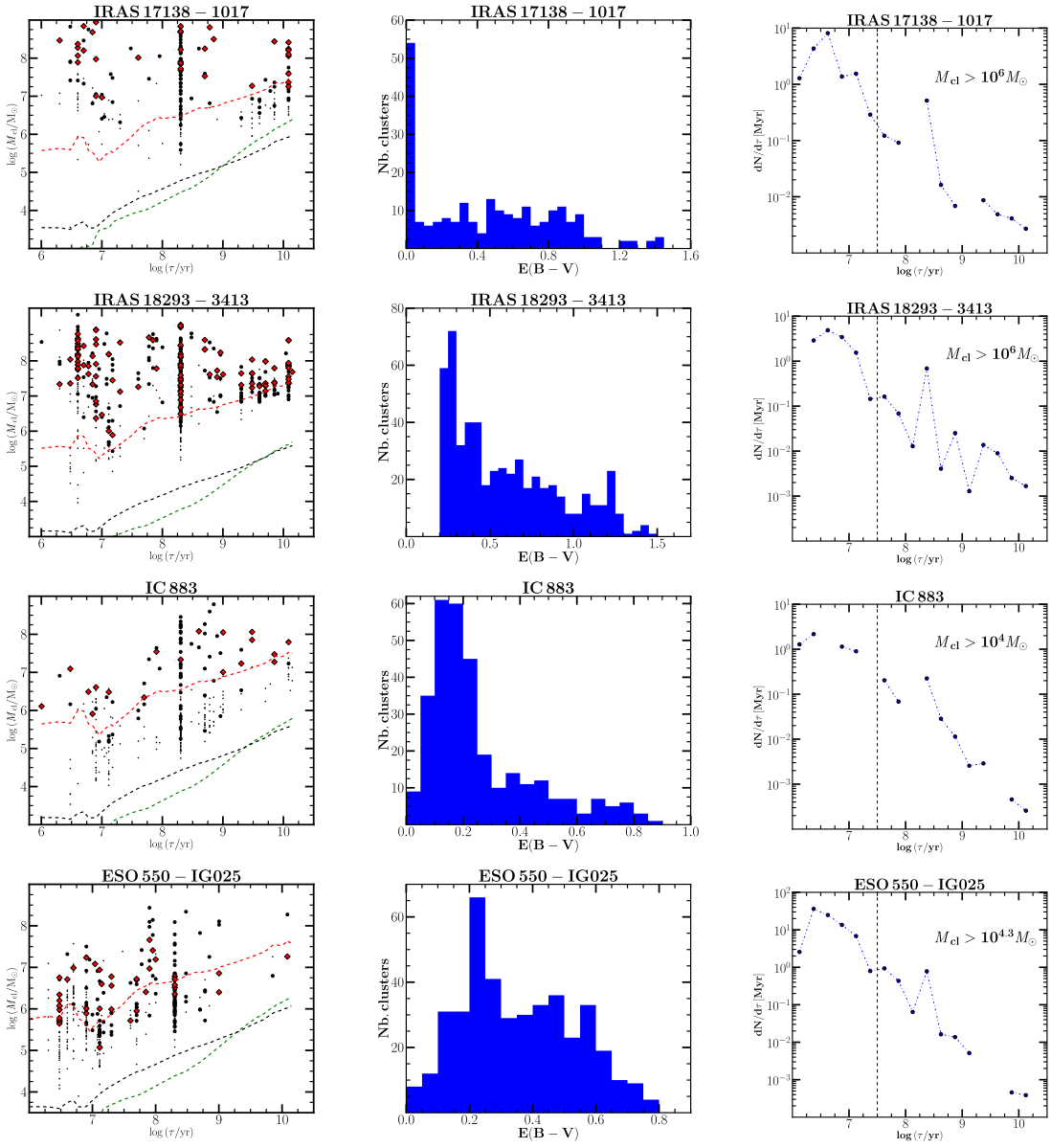

Figure 5.21: *Left*: Cluster mass plotted against the age. The K-selected candidates are labelled as red diamonds. The dashed lines represent the evolutionary fading lines of considering B- (green), I- (black) and K-band synthetic colors from the `Yggdrasil` model. A chimney is seen at around $\log \tau \sim 8.2$. *Middle*: Distribution of the resulting extinction. The SSC candidates of IRAS 17138-1017 and IRAS 18293−3413 have a high range of dust reddening. *Right*: The cluster frequency including only star clusters above a certain cutoff mass limit. The bump seen at $\log\ \tau \sim 8.2$ is due to the presence of the chimney in the age distribution because of the appearance of AGB stars at that age.

While most of the K-selected SSC candidates, labelled as red diamonds, practically follow the predicted colors of the SSP model in the CCDs (Figure 5.18), some of these objects also suffer from NIR excess, especially in the case of IRAS F17138−1017 and IRAS 18293−3413. Hence, an overestimate of the corresponding cluster masses is observed in the age-mass planes of Figure 5.21. Nevertheless, one should be careful in interpreting the results because of the age-extinction degeneracy.

We should also note that Bastian et al. (2014) have reported that the derived ages and masses from NIR data suffer more from the effects of spatial resolution compared to those estimated using optical data. We expect our datasets to be less contaminated by such effects, except in the case of ESO 550−IG025 ($D_L = 135$ Mpc), since we already adopted the smallest aperture radii possible.

5.3.6 Cluster spatial distributions

The left panels of Figure 5.22 show the age spatial distributions of the star clusters in the galactic field of each target. Except in the case of ESO 550−IGC025, the following age bins were used to plot the SSCs with different labels: $\tau \leq 30$ Myr (blue stars), 30 Myr $< \tau \leq 1$ Gyr (crosses), and $\tau > 1$ Gyr (filled circles). These age ranges are $\tau \leq 30$ Myr, 30 Myr $< \tau \leq 150$ Myr, and $\tau > 150$ Myr in the field of ESO 550−IGC025. Such limits were chosen based on the 1-D distribution of the cluster ages.

The majority of the old clusters of IRAS F17138-1017 are located in the inner regions of the galaxy while the opposite distribution is happening in the case of ESO 550−IG025: young star clusters converge in the galaxy center and the old ones lie in the outer fields. This would support the cruel cradle effect scenario. IRAS 18293−3413, on the other hand, has its own peculiar distribution: young and intermediate-age clusters mostly occupy the North-East regions of the galaxy while the old candidates are clustered in the opposite direction. This could be a reflection of the interaction scenario being played out in the galaxy or perhaps an imprint of a a bimodal starburst activity. The old clusters could have formed in the nuclear regions but later being moved to their current positions due to another extreme episode of SF occuring at a later stage. More arguments of this scenario are reported in Section 5.3.8. Finally, the SSC candidates of IC 883 do not follow a clear distribution. Clusters with intermediate ages are scattered all over the galactic field and the inner regions are composed of a mixed population of different cluster ages.

The extinction spatial distributions are displayed in the right panels of Figure 5.22. Clusters were grouped as a function of their extinction values and the different ranges were chosen based on the 1-D distribution of $E(B-V)$ (see the middle panels of Figure 5.21). Least extinguished clusters are labelled as blue stars, those with a medium extinction value as crosses and the most extinguished ones as filled circles. While the clusters are randomly distributed in the case of IRAS F17138−1017 and IRAS 18293−3413, there is however a clear pattern in the case of IC 883 and ESO 550−IG025. In the latter

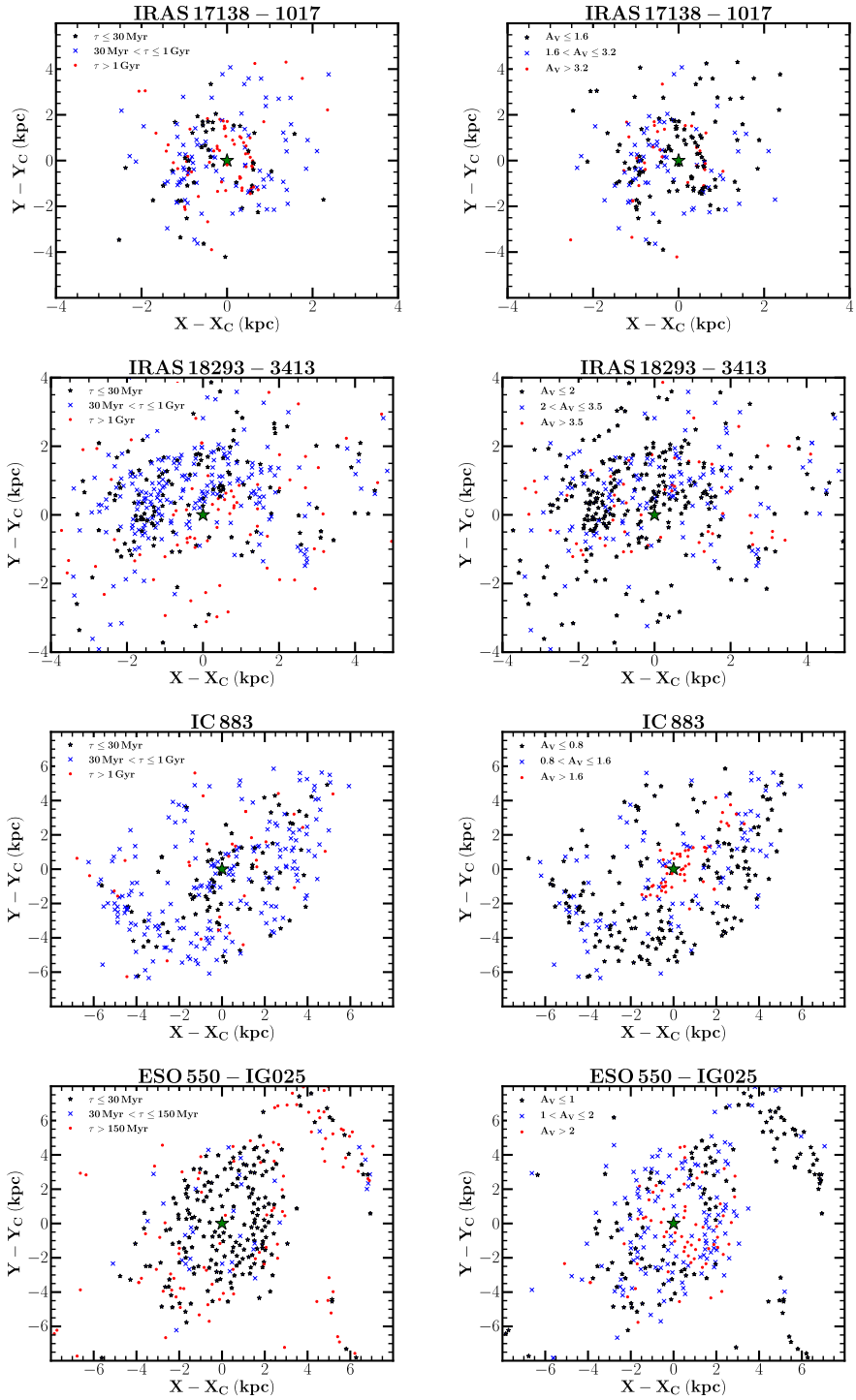

Figure 5.22: Age (*left*) and extinction (*right*) spatial distributions in the field of the LIRGs. The green star represents the position of the galaxy center. The blue stars, the crosses and the filled circles represent respectively the positions of young, intermediate and old ages in the case of the left panels. They correspond to the positions of the least extinguished clusters, those with a medium A_V value and the most extinguished ones in the right panels.

cases, the most extinguished clusters converge in the nuclear starburst regions and as we move away from the galaxy center, we start to observe candidates with less extinction values. In particular, less extinguished star clusters populate the spiral arms of ESO 550−IG025. In addition, with a correlation coefficient of $r = -0.34 \pm 0.02$, there seems to be a weak statistical trend between the cluster age and extinction spatial distributions in the same galaxy. The highly-extinguished Av clusters have ages less than 10 Myr, whereas some with medium extinction values have ages less than 30 Myr. The former groups are still embedded in their dust cocoons, hence a high value of A_V, while the former have already recently entered the secular evolution after surviving the infant mortality due to the gas expulsion phase. Finally, the older clusters are the least extinguished, these could be good candidates to evolve as proto-globular clusters.

5.3.7 The cluster mass functions

The CMFs of the subsample of LIRGs are shown in Figure 5.23. Two different age bins were considered to draw the distribution: $\tau \leq 30$ Myr (left panels) and $30\,\mathrm{Myr} < \tau \leq 1$ Gyr (right panels), and a power-law fit was applied to the high-mass end of the data. The values of the slope β are less than 2, except in the case of ESO 550−IG025. However, we should be careful in interpreting the results of this target because of possible blending effects due to its distance ($D_L = 135$ Mpc).

Younger clusters have CMFs with steeper slopes than the distribution associated with older candidates in all cases. This possibly indicates a mass-dependent disruption mechanism. In the opposite case, the value of the slope β is expected to remain constant, from one to another MF with different age bins. However, the smaller values of $\beta < 2$ compared to the ones derived in Section 5.2.9 are still in the range of 1.8−2.2 within their uncertainties as suggested by de Grijs et al. (2003a) and McCrady & Graham (2007). We may also be dealing with a cluster disruption depending on the galactic environments, though it is too early to draw a firm conclusion based on the nature and the number of the filters used.

There is no evidence of high-mass truncation in the case of IRAS F17318−1017. The power-law function is a good representation of the MF. However, in the case of ESO 550−IG025, the CMF of the younger ages could partially be truncated and a Schechter distribution may also fit the data. As already mentioned in Section 5.2.9, the bend of such a fit is located at a higher mass range of order $\approx 10^6\,M_\odot$. Such an approximation may have been slightly above the true value since results from BIK-fit tend to overestimate the cluster masses. For IRAS 18293−3413 and IC 883, the shapes of the CMFs are somewhat ambiguious. For the former target, the presence of a chimney around $\log\tau \sim 6.5$ in the age-mass plane could contribute to such a trend (see Figure 5.21). The artificial distribution is in fact composed of a significant number of massive clusters ($10^{5.5}\,M_\odot \lesssim M_{cl} \lesssim 10^{8.5}\,M_\odot$). The bright NIR luminosities (affecting the fit) at this critical age are due to the appearance of RSGs and subsequently bias

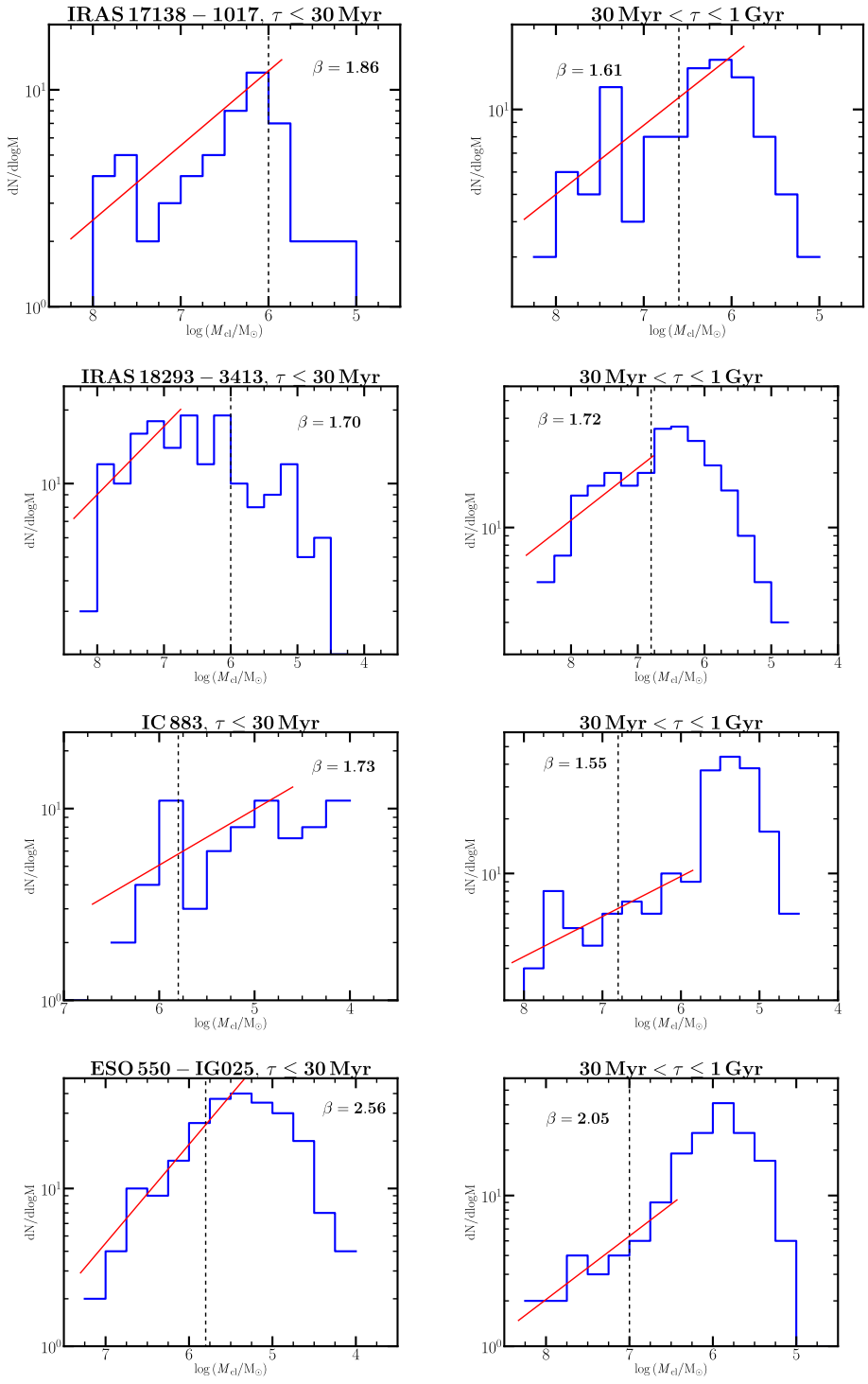

Figure 5.23: The cluster mass functions using two different age bins. The solid lines represent the resulting power-law fit of the high-mass end. The dashed lines show approximate cluster mass limits estimated using the age-mass plane. The left panels correspond to the distribution of clusters younger than 30 Myr ($\log \tau \lesssim 7.5$) and the right panels for sources with ages between 30 Myr and 1 Gyr. There is no clear sign of high-mass truncation in the CMFs associated with younger ages, except in the case of ESO 550−IG025 which could already be affected by blending. On the other hand, the mass distribution of IRAS 18293−3413 indicates a high disruption rate of low-mass SSCs.

the mass estimates. In summary, the high-mass end MF shapes which could indicate high-mass truncation of SSCs thus remain somewhat inconclusive.

The low-mass end of the MF, on the other hand, may contain information of mass-dependent disruption of SSCs. This can obviously be verified only above mass completeness limits of the relevant age bin. In the case of IRAS 18293−3413, there appears to be a clear flattening, or turnover, of young cluster MF at around $10^7\,M_\odot$ which is still comfortably an order of magnitude above the completeness limit. Assuming the clusters are born with a power-law MF, this indicates very rapid cluster dissolution in this galaxy. Similar effects were also observed in the starburst ring of NGC 5253 (de Grijs et al. 2013) and NGC 2328 (Väisänen et al. 2014). Such results are unusual and thus are definitely worth warranting further investigations.

5.3.8 The cluster formation histories

Before deriving the values of the cluster formation efficiency Γ, we first plotted the star cluster frequencies as a function of time as shown in the right panels of Figure 5.21. Lower mass limits of $10^6\,M_\odot$ were used in the case of IRAS F17138−1017 and IRAS 18293−3413so that the sample is complete at ages below 30 Myr. For IC 883 and ESO 550−IG025, the limits are $\sim\ 10^4\,M_\odot$. Beyond 10 Myr, the cluster formation rates have decreased with increasing ages because of evolutionary fading. There is however a peak around $\log\tau \sim 8.2$ in all cases. One should not associate such a behaviour with an instantaneous burst, but rather the chimney caused by the presence of AGBs at that age (see left panels of Figure 5.21). Another chimney around $\log\tau \sim 6.8$ also results in an artificial peak in the case of IC 883. This is due to the appearance of RSGs. For IRAS 18293−3413, at least two intense starburst activities have occured in the past ($\log\tau \sim 9$ and 9.5). Star clusters, with ages older than 1 Gyr, that populate the western part of the galactic field may have formed during the burst around $\log\tau \sim 9.5$. We should not, perhaps, however draw firm conclusions yet because of the limited number of filters being used in estimating the cluster ages.

The same age range of $10 - 100$ Myr was used to estimate the CFR followed by the CFE of each target using Equation 1.8 and Equation 1.7, respectively. While the CFE of IRAS F17138−1017 (17 %), IRAS 18293−3413 (19 %), and ESO 550−IG025 (23 %) agree with the derived values of Γ for starburst galaxies, we found a very low percentage (Γ = 1 %) for IC 883. The values of Γ together with the SFR of the LIRGs are summarized in Table 5.5. The low CFE of IC 883 is similar to that of a gas-poor spiral galaxy. This suggests that the merger remnant IC 883 has exhausted most of its gas necessary to form a large population of star clusters. It could also be that SFR being assumed for IC 883 is contaminated by AGN contribution. Such a statement should however be checked by studying in more details the physical characteristics of gas and stars in the LIRG galaxy. Finally, a weak correlation has been found between the values of Γ and the host galaxy SFR despite the inclusion of two more data points from Arp 299.

Table 5.5: The values of the cluster formation efficiency

Galaxy name	SFR ($M_\odot\,\mathrm{yr}^{-1}$)	Γ (percent)
(1)	(2)	(3)
IC 694	77 ±27	10
NGC 3690	52 ±18	16
IRAS F17138−1017	45 ±13	17
IRAS 18293−3413	110 ±33	19
IC 883	79 ±24	1
ESO 550−IG025	48 ±15	23

Notes. Column 1: Galaxy name; Column 2: SFR estimated from the IR luminosity; Column 3: the values of the CFE assuming an age range of $10 - 100$ Myr.

5.3.9 Summary

Section 5.3 focused on probing the characteristics of optically-visible super star clusters of five other luminous infrared galaxies: IRAS F17138−1017, IRAS 18293−3413, IC 883, ESO 550−IG025 and IRAS 19115−2124 (also known as the Bird galaxy). They all have high SFRs and a luminosity distance $D_L \sim 72 - 135$ Mpc and $D_L \approx 200$ Mpc in the case of IRAS 19115−2124. Only three filters were used to estimate the cluster parameters: BI-band images taken with HST/ACS camera and K-band data from NIR AO imaging. Optical star cluster catalogues were matched and a cutoff magnitude error of $\sigma_m = 0.35$ mag was performed to output the final list of the SSC candidates. After deriving the extinction maps based on $B - I$ colors and constraining the extinction range of each individual cluster, we have used `Yggdrasil` SSP models to fit the age, mass and extinction of a given cluster. Note, however, that age-extinction degeneracy could not be broken with BIK-data only. This should be kept in mind when interpreting the results.

We did not attempt to estimate the cluster parameters of IRAS 19115−2124. At a distance $D_L \approx 200$ Mpc, blending effects are likely to contaminate the photometric magnitudes of the detected objects. Nevertheless, we have found that the head and the wings of the interacting system are the regions which host most of the "SSC" candidates or more probably complexes of SSCs in this case. For the other less distant targets, they generally host young star clusters. At least 50 % of the cluster populations have ages below 30 Myr. We also noticed that the cluster mass-age planes presented a chimney around $\log\tau \sim 8.2$ due to the presence of AGBs at that age. Such a concentration manifests as an artificial peak in the cluster frequency of each target. The cluster MFs we derived did not show evidence for clear mass-dependent cluster disruption, except in the case of IRAS 18293−3413 where a turnover is detected an order of magnitude away from the mass-completeness limit. The CMF power-law slopes β, however, decrease as a function of the age range which indicate the effects from evolutionary fading. In addition, the CMFs of younger ages have slopes shallower than 2 and vary between 1.70 and 1.86,

except for ESO 550−IG025 with $\beta = 2.56$. As for the K-selected cluster candidates, they do not show NIR excess with the exception of a non-negligible number of sources hosted by IRAS 18293−3413. The values of the cluster formation efficiency $\Gamma = 17 - 23\,\%$ fall within the range of those associated with starburst galaxies, except in the case of IC 883. Finally, the main results of each target are summarized as follows:

1. IRAS F17138−1017: after applying the selection criteria, only 104 clusters were included in the final BIK-band catalogue. The target hosts massive star clusters in the range of $\sim 10^4 - 10^{8.5}\,M_\odot$. The inclusion of some star cluster complexes in the SSC catalogues might explain the high value of the upper mass limit. Alternatively, an overestimate of the cluster mass is a possibility since a NIR filter was part of the SED fitting. Some of the most extinguished cluster candidates of the LIRG subsample are also located in the nuclear starburst regions of IRAS F17138−1017 ($A_V > 5.2$ mag). As for the age spatial distribution, older star clusters tend to converge in the inner regions whereas the younger ones preferentially lie in the outer field.

2. IRAS 18293−3413: spectral energy distribution of 309 optically-selected SSCs were compared with the SSP model to estimate the cluster parameters. Mass and extinction ranges similar to those of IRAS F17138−1017 were derived for the star cluster population. The age spatial distribution is one of the interesting results for this target: most of the clusters below the age of 1 Gyr are located in the North-East regions of the galactic field, whereas the older ones reside in the opposite field. IRAS 18293−3413 could have probably undergone at least two intense starburst activities over its lifetime. This could also explain the other peaks (apart from the artificial one) seen in the cluster frequency. Furthermore, a peculiar distribution of the CMF at younger ages suggest that low-mass star clusters of IRAS 18293−3413 underwent rapid disruption mechanism.

3. IC 883: we have recovered 79 star cluster candidates that follow a clear pattern in their extinction spatial distribution: the value of A_V decreases as we move away from the galaxy center. In addition, IC 883 has less massive SSCs compared to those of the two closest LIRGs: a lower mass limit of $10^4\,M_\odot$ at which the sample should be complete below 30 Myr of age. We also noticed another artificial peak around $\log\tau \sim 6.8$ in the cluster frequency. This is due to the appearance of RSG stars. As for the value of $\Gamma = 1\,\%$, this is a very small value for a starburst galaxy. Either IC 883 has exhausted most of its gas or statistical and physical biases are at play and affecting the parameter. Another possible reason could be that the galaxy SFR is overestimated due to e.g. AGN contribution, though the galaxy spectral properties (from NED database) along with the radio observations (Herrero-Illana, private communication) do not support this scenario. We should therefore carry out further analyses.

4. ESO 550−IG025: the final cluster catalogue is composed of 182 clusters. We should note that blending effects may become an issue because of the distance

D_L = 135 Mpc of the target. ESO 550−IG025 has a narrower extinction range compared to the other targets, i.e. $0 < E(B-V) < 0.8$. Its mass and age ranges are however similar to those of IC 883, except that there are few clusters older than 1 Gyr. The spatial distribution of the clusters as a function of age indicates that older clusters may have been thrown out from the inner field due to the external effect of global interaction of host galaxies which is known as the cruel cradle effect. We also noticed that the age and extinction spatial distributions are weakly related: the least extinguished clusters tend to be older, while the ones with high extinction values are younger ages. We should however not forget that age-extinction degeneracy could not be broken.

5.4 Conclusions

In this Chapter, we have performed photometric studies of optically-visible super star clusters in Arp 299 and five other luminous infrared galaxies. The physical characteristics of the clusters were used to test the universality of the CIMF and to constrain cluster formation histories in starburst galaxies. Based on the summary in Section 5.2.12 and Section 5.3.9, intensely star-forming galaxies such as LIRGs host indeed a significant number of young clusters and produce more massive star clusters than quiescent dwarf and normal spirals. SSC analyses of Arp 299 have also confirmed the possibility of a mass-dependent disruption mechanism. Apart from statistical effects, such a physical process could explain the observed high-mass truncation in the CIMF for clusters younger than 10 Myr. Finally, this work supports the idea that the cluster formation efficiency is not a constant parameter, but is rather an environmentally-dependent quantity. High-pressure environments of interacting systems favor star formation to happen in bound stellar clusters.

Future works will be driven by answering the following questions: *How does the cluster disruption affect smaller scales of the galactic fields in the case of the SUNBIRD sample (e.g. disk vs. circumnuclear regions)? How accurate is the CFE - SFR density relation?* Therefore, we will compare the values of Γ in different regions of the same galaxy. We also plan to expand our targets of interest to deepen our current understanding of the cluster formation and evolution. And even from the limited sample here we see that some CMF shapes suggest strong and rapid cluster destruction (IRAS 18293−3413) and evidence of SSCs surviving together in specific regions (e.g. nuclear areas in case of IRAS F17138−1017 but on the other hand outer regions in case of ESO 550−IG025). It will be intriguing to study in more detail how the galaxy interactions affect the survival of SSC, *do they e.g. throw out SSCs from inner regions to safer areas to survive to become old GGs (Kruijssen et al. 2011; Väisänen et al. 2014)?*

References

Adamo, A., & Bastian, N. 2015, The lifecycle of clusters in galaxies, to appear in *T*he Birth of Star Clusters, editor S.W. Stahler, Springer edition, submitted

Adamo, A., Östlin, G., Zackrisson, E., et al. 2010, MNRAS, 407, 870

Alonso-Herrero, A., Rieke, G. H., Rieke, M. J., et al. 2006, ApJ, 650, 835

Alonso-Herrero, A., Rieke, G. H., Colina, L., et al. 2009, ApJ, 697, 660

Alonso-Herrero, A., Roche, P. F., Esquej, P., et al. 2013, ApJL, 779, LL14

Alonso-Herrero, A., Rieke, G. H., Rieke, M. J., & Scoville, N. Z. 2000, ApJ, 532, 845

Alonso-Herrero, A., Rieke, G. H., Rieke, M. J., & Scoville, N. Z. 2002, AJ, 124, 166

Anders, P., Bissantz, N., Fritze-v. Alvensleben, et. al. 2004, MNRAS, 347, 196

Anders, P., Kotulla, R., de Grijs, R., & Wicker, J. 2013, ApJ, 778, 138

Anderson, J. P., Habergham, S. M., & James, P. A. 2011, MNRAS, 416, 567

Andrews, J. E., Calzetti, D., Chandar, R., et al. 2014, ApJ, 793, 4

Ballo, L., Braito, V., Della Ceca, R., et al. 2004, ApJ, 600, 634

Bastian, N., Adamo, A., Gieles, M., et al. 2012, MNRAS, 419, 2606

Bastian, N., Adamo, A., Schirmer, M., et al. 2014, MNRAS, 444, 3829

Bastian et al. 2005, A&A, 431, 905

Bastian, N. 2008, MNRAS, 390, 759

Bastian, N., Adamo, A., Gieles, M., et al. 2011, MNRAS, 417, L6

Bastian, N., Hempel, M., Kissler-Patig, M., Homeier, N. L., & Trancho, G. 2005, A&A, 435, 65

Bastian, N., Trancho, G., Konstantopoulos, I. S., & Miller, B. W. 2009, ApJ, 701, 607

Baumgardt, H., Parmentier, G., Anders, P., & Grebel, E. K. 2013, MNRAS, 430, 676

Bessell, M. S., Castelli, F., & Plez, B. 1998, A&A, 333, 231

Bik, A., Lamers, H. J. G. L. M., Bastian, N., Panagia, N., & Romaniello, M. 2003, A&A, 397, 473

Bondi, M., Pérez-Torres, M. A., Herrero-Illana, R., & Alberdi, A. 2012, A&A, 539, AA134

Calzetti, D., Armus, L., Bohlin, R. C., et al. 2000, ApJ, 533, 682

Chandar, R., Whitmore, B. C., Kim, H., et al. 2010, ApJ, 719, 966

Cresci, G., Vanzi, L., & Sauvage, M. 2005, A&A, 433, 447

de Grijs, R., Anders, P., Bastian, N., et al. 2003a, MNRAS, 343, 1285

de Grijs, R., Anders, P., Zackrisson, E., & Östlin, G. 2013, MNRAS, 431, 2917

de Grijs, R., Fritze-v. Alvensleben, U., Anders, P., et al. 2003b, MNRAS, 342, 259

de Grijs, R., & Goodwin, S. P. 2008, MNRAS, 383, 1000

Depoy, D. L., Wynn-Williams, C. G., Hill, G. J., & Becklin, E. E. 1988, AJ, 95, 398

Gallais, P., Charmandaris, V., Le Floc'h, E., et al. 2004, A&A, 414, 845

Gieles, M., Lamers, H. J. G. L. M., & Portegies Zwart, S. F. 2007, ApJ, 668, 268

Gieles, M. 2009, MNRAS, 394, 2113

Gieles, M. 2010, Galaxy Wars: Stellar Populations and Star Formation in Interacting Galaxies, 423, 123

Goddard, Q. E., Bastian, N., & Kennicutt, R. C. 2010, MNRAS, 405, 857

Haas, M. R., Gieles, M., Scheepmaker, R. A., Larsen, S. S., & Lamers, H. J. G. L. M. 2008, A&A, 487, 937

Johnson, H. L. 1966, ARA&A, 4, 193

Johnson, L. C., Seth, A. C., Dalcanton, J. J., et al. 2012, ApJ, 752, 95

Kankare, E., Mattila, S., Ryder, S., et al. 2008, ApJL, 689, L97

Kankare, E., Mattila, S., Ryder, S., et al. 2012, ApJL, 744, LL19

Kankare, E., Mattila, S., Ryder, S., et al. 2014, MNRAS, 440, 1052

Keel, W. C., & Wu, W. 1995, AJ, 110, 129

Kinney, A. L., Calzetti, D., Bohlin, R. C., et al. 1996, ApJ, 467, 38

Kruijssen, J. M. D. 2012, MNRAS, 426, 3008

Kruijssen, J. M. D., Pelupessy, F. I., Lamers, H. J. G. L. M., et al. 2012, MNRAS, 421, 1927

Kruijssen, J. M. D., Pelupessy, F. I., Lamers, H. J. G. L. M., Portegies Zwart, S. F., & Icke, V. 2011, MNRAS, 414, 1339

Lai, O., Rouan, D., Rigaut, F., Doyon, R., & Lacombe, F. 1999, A&A, 351, 834

Lamers, H. J. G. L. M. 2009, Ap&SS, 324, 183

Larsen, S. S. 2000, MNRAS, 319, 893

Larsen, S. S. 2009, A&A, 494, 539

Leitherer, C., Schaerer, D., Goldader, J. D., et al. 1999, ApJS, 123, 3

McCrady, N., & Graham, J. R. 2007, ApJ, 663, 844

Mattila, S., Dahlen, T., Efstathiou, A., et al. 2012, ApJ, 756, 111

Mattila, S., & Kankare, E. 2010, Central Bureau Electronic Telegrams, 2145, 1

Mattila, S., Väisänen, P., Farrah, D., et al. 2007, ApJL, 659, L9

Miralles-Caballero, D., Colina, L., Arribas, S., & Duc, P.-A. 2011, AJ, 142, 79

Modica, F., Vavilkin, T., Evans, A. S., et al. 2012, AJ, 143, 16

Neff, S. G., Ulvestad, J. S., & Teng, S. H. 2004, ApJ, 611, 186

Newton, J., Puckett, T., & Orff, T. 2010, Central Bureau Electronic Telegrams, 2144, 2

Pérez-Torres, M. A., Alberdi, A., Romero-Cañizales, C., & Bondi, M. 2010, A&A, 519, LL5

Pérez-Torres, M. A., Mattila, S., Alberdi, A., et al. 2007, ApJL, 671, L21

Pérez-Torres, M. A., et. al. 2009, A&A, 507, L17

Piqueras López, J., et. al. 2012, A&A, 546, AA64

Piqueras López, J., et. al. 2013, A&A, 553A, 85

Portegies Zwart, S. F., et al. 2010, ARA&A, 48, 431

Romero-Cañizales, C., et. al. 2012, A&A, 543, AA72

Romero-Cañizales, C., et. al. 2014, MNRAS, 440, 1067

Ryder, S. D., Mattila, S., Kankare, E., & Vaisanen, P. 2014, arXiv:1408.0593

Ryder, S. D., Mattila, S., Kankare, E., Väisänen, P. 2014, Proc. SPIE, 9148, 91480D

Ryon, J. E., Adamo, A., Bastian, N., et al. 2014, AJ, 148, 33

Sadler, E. M., Oosterloo, T. A., Morganti, R., & Karakas, A. 2000, AJ, 119, 1180

Sanders, D. B., et al. 2003, AJ, 126, 1607

Silva-Villa, E., Adamo, A., Bastian, N., Fouesneau, M., & Zackrisson, E. 2014, MNRAS, 440, L116

Sollima, A., Cignoni, M., Gratton, R. G., et al. 2014, MNRAS, 437, 1918

Väisänen, P., Ryder, S., Mattila, S., & Kotilainen, J. 2008a, ApJL, 689, L37

Väisänen, P., et al. 2008b, MNRAS, 384, 886

Väisänen, P., Barway, S., & Randriamanakoto, Z. 2014, ApJL, 797, LL16

Vardoulaki, E., Charmandaris, V., Murphy, E. J., et al. 2014, arXiv:1408.4177

Vavilkin, T. 2011, Ph.D. Thesis

Whitmore, B. C., Schweizer, F., Leitherer, C., Borne, K., & Robert, C. 1993, AJ, 106, 1354

Whitmore, B. C., Zhang, Q., Leitherer, C., et al. 1999, AJ, 118, 1551

Whitmore, B. C., Chandar, R., Bowers, A. S., et al. 2014, AJ, 147, 78

Zackrisson, E., Rydberg, C.-E., Schaerer, D., Östlin, G., & Tuli, M. 2011, ApJ, 740, 13

Zhang, Q., & Fall, S. M. 1999, ApJL, 527, L81

Yuan, T.-T., Kewley, L. J., & Sanders, D. B. 2010, ApJ, 709, 884

Chapter 6

Closing remarks

Overview

This Chapter provides a general overview of the thesis. The most relevant results from this work as well as the concluding remarks are outlined. We also include new perspectives that can be done in the near future.

Our current understanding of star formation activity in extragalactic sources has greatly increased since the commissioning of the Infrared Astronomical Satellite (IRAS). With a strong infrared emission ranging in between $10^{11} - 10^{12}\,L_{\odot}$, luminous infrared galaxies (LIRGs) have been the subject of various studies. It has been found that the majority of these galaxies are interacting systems that harbor intense starburst activities in their nuclear regions. Therefore, it is not surprising that LIRGs provide adequate/suitable environments for the birth of the most massive star clusters in the local Universe. Also referred to as super star clusters, these extreme form of star clusters are believed to contain vital information regarding the physical conditions under which strong and massive star formation occurs. However, the early stages of evolution as well as the role of the environment in shaping the cluster initial mass functions are not yet fully understood and has thus far generated diverging arguments in this research field.

This thesis was designed to provide more insight into the universality of the cluster initial mass function (CIMF) and to pursue investigations on whether external factors play an important role during cluster formation and disruption mechanisms. To this end, we analyzed the characteristics of super star cluster candidates obtained from a high-resolution multi-wavelength study of a selected sample of nearby star-forming galaxies. Near-infrared (NIR) observations together with optical HST data were used to achieve three different but complementary immediate objectives of the thesis: *i)* to check the effects of blending in the NIR cluster luminosity functions; *ii)* to establish for the first time the brightest cluster - SFR relation using NIR data; *iii)* and to estimate the age, mass and extinction of optically-selected clusters. The analysis of these results can then be used to study the CIMF and formation and disruption mechanisms.

The main datasets of the thesis were imaged using K-band NIR adaptive optics systems (VLT/NaCo or Gemini-North/NIRI) under the ongoing SUperNovae and starBursts in the InfraReD (SUNBIRD) survey. NIR AO observations are invaluable as they are able to reduce effects of visual extinction by a factor of 10 and hence allow the detection of clusters that are optically hidden in the dust-obscured regions of the galaxies. A representative sample of 42 starbursts and LIRGs was selected to form the survey. To the best of our knowledge, the SUNBIRD project is one of its kind because of the high number of both host galaxies and clusters in the NIR AO sample. With luminosity distances between $25 - 150$ Mpc and $D_L \approx 200$ Mpc for a handful of the most distant cases, the targets were chosen because of their high SFRs and their cool IRAS colors. In addition, they span a wide variety of morphologies and merging stages. They also uniformly represent starburst-dominated galaxies with IR luminosities in the range of $\log(L_\odot/L_{IR}) = 10.6 - 11.9$. To perform the multi-wavelength study, we retrieved from the Hubble Legacy Archive, whenever available, the corresponding F336W (U), F435W (B) and F814W (I) images of the targets taken with WFC/ACS or WFC3/UVIS camera.

We described K-band data reduction, source extraction and the cluster selection process in Chapter 2. Aperture photometry was performed on the detected objects using the smallest possible radii: 2 and 3 for S54 and S27 cameras of the VLT/NaCo and 5 pixels for the Gemini/NIRI data. To avoid photometric bias, only objects with a magnitude error $\sigma \leq 0.35$ mag were short listed as potential SSC candidates. A variable aperture correction dependent on the distance to the AO-star was applied to the data. Vega-based magnitude zeropoints were used to output the cluster absolute fluxes in the same photometric system. Next, we selected the SSC candidates of each target using NIR data only. The concentration index together with the fuzziness of the objects were used to draw the cluster catalogues after excluding the galaxy nuclei, foreground stars and any spurious sources. The number of selected clusters ranged between $\sim 10 - 400$, with the galactic field of ESO 221−IG008 hosting the most cluster candidates.

Chapter 3 investigated the luminosity functions of clusters and the effects of blending. Both constant and variable binning result in similar values of the power-law slopes $\alpha = 1.5-2.4$. The median and average of the indices are 1.86 ± 0.24 and 1.92, respectively. Out of the 34 constructed CLFs, 65 % have flatter distributions with $\alpha < 2$. The most important result of this work revealed that starburst galaxies have shallower slopes than normal spirals where $\alpha \approx 2.4$. It is suggested that strongly star-forming galaxies such as LIRGs host SSCs that are disrupted in a way depending on their mass or environment. This would then result in a smaller value of the power-law index α of the CLF. In fact, a weak correlation has been found between α and the SFR. Note, however, that star clusters with different ages were binned together while drawing the LFs. In Chapter 3, analyses based on Monte-Carlo simulations and star cluster population in a redshifted Antennae showed that shallower slopes cannot be the result of blending for a target less distant than ≈ 100 Mpc, unless the cluster surface densities are close to confusion limit. Such a limit is quickly reached in case of more distant targets and/or with data taken

with poorer resolution. An interesting avenue would be to investigate whether or not the values of α vary with the different merging stages of our targets. In this case, a varying α would support the argument that CLFs evolve with the merging stages of the system. For reasons of statistical significance, such a study would require a larger sample than the one presented in this study.

Chapter 4 also used the NIR AO observations of the SUNBIRD survey to check whether one could reproduce a well-known empirical relation that has been established in the optical regime. Indeed, we found a positive correlation between the brightest cluster magnitude and the galaxy SFR. It is expressed as $M_K^{brightest} = -2.56 \times \log \mathrm{SFR} - 13.39$, considering a distance cutoff $D_L = 150\,\mathrm{Mpc}$. Note that the galaxy IR luminosity was the tracer being used to estimate the corresponding SFR for each target. The conversion eventually assumes that the IR energy is starburst-dominated. The brightest cluster - SFR relation, which is also one of the most relevant results from the thesis, is the first ever being drawn in the NIR regime. We have provided statistical interpretations of the relation: a size-of-sample effect. This simply means that it is more likely for more luminous clusters to form in an environment with extreme star formation activity. However, we also suggested physical interpretations to explain the small scatter seen in the relation. The effects of the galactic environments on cluster formation efficiency or/and possibly other internal cluster effects such as the mass-luminosity relation are likely to play an important role as well. Apart from an estimate of the star cluster physical properties, determining the exact roles of the environments and the galaxy reddening would be the next steps required to fully understand the NIR relation.

The last part of the thesis focused on characterizing the physical properties of optically-selected star cluster candidates. NIR AO observations of seven LIRGs were therefore combined with HST optical images in Chapter 5. New star cluster catalogues were first derived based on optical detection. The selection criteria resulted in hundreds of SSCs for each target. A fixed aperture radius was used to perform aperture photometry in all $UBIK$-band or BIK-band images. We compared `Yggdrasil` SSP models with the observed SEDs to fit the cluster age, mass, and extinction of starburst-dominated galaxies. Photoionized gas from nebular emission and continuum are particularly considered by this new SSP model. Note that extinction ranges were first set on an individual basis depending on the cluster positions in a derived extinction map before χ^2 fitting . A large fraction of the star cluster populations have ages younger than 30 Myr. In the case of Arp 299, age-extinction degeneracy could very reliably be broken due to inclusion of a UV-filter. The cluster masses of the interacting systems are generally between $10^4 - 10^8\,M_\odot$. Such values are quite massive compared to the mass ranges associated with star clusters hosted in more quiescent environments. Nevertheless, more analyses should be performed to quantify the overestimate of the cluster mass in case of a BIK-fit. The spatial distributions of ages of some cases supported the cruel cradle effect scenario while others indicated the possibility of a mixed population. At least one of the LIRGs (NGC 3690) has its star cluster population disrupted in a mass-dependent manner. The turnover in the LFs, a truncation of the CMFs at high-mass end, and the

distribution of the cluster frequency serve as a basis for such an argument. Moreover, the cluster formation histories of the LIRG subsample revealed that more formation of the star clusters are foreseen since the galaxy environments are rich of giant molecular clouds necessary for the birth of massive clusters. Finally, we also found that cluster formation efficiency $\Gamma = 10 - 23\,\%$ of the interacting starburst-dominated galaxies are relatively high compared to those of dwarfs and normal spirals. The next steps of this work would be *i)* to correct the cluster masses from observational incompleteness. This would strengthen conclusions drawn from the CIMFs; *ii)* to adopt a more accurate way in considering both extinction to the stars and to the gas; *iii)* to run MC simulations to predict the age distribution of a given synthetic population with the same observed magnitudes; *iv)* and to study the variation of the cluster formation efficiency on local scales.

Overall, we have shown the capability of NIR AO systems in opening a new window into the understanding of SSC formation, evolution, and disruption mechanisms. It has also been found that interacting systems such as LIRGs offer a totally different environment which can bias the long-term survival chance of its star cluster population. The SUNBIRD survey, which was an integral part of this thesis, offers useful data, with the potential of answering some of the most important questions in the field of star cluster research. However, there are still limitations in studying these most massive clusters. New instruments such as the multi-conjugate AO systems mounted in Gemini-South (GEMS) will push down the detection limit and therefore allow the analyses of faint and low-mass star clusters. On the other hand, extending the sample of the survey into a lower SFR baseline would also offer more insights into the star formation process in general. Finally, it will also be interesting to study the kinematics, underlying stellar populations, and the gas of the host galaxies to correlate SSC properties with physical characteristics of the host as a whole in the SUNBIRD sample using the available data from SALT/RSS spectroscopic observations.

Appendix A

List of publications

Overview

This Appendix lists the publications (peer-reviewed and in preparation) based on the thesis and related work I collaborated to. Selected non-refereed papers that were presented during international conferences are also included.

A.1 Published peer-reviewed papers

- Väisänen P., Barway S. & **Randriamanakoto Z.**
  Star clusters in a nuclear star-forming ring: The disappearing string of pearls
  2014, ApJ Letters, 797, 16

- **Randriamanakoto Z.**, Escala A., Väisänen P., et al.
  Near-infrared Adaptive Optics Imaging of Infrared Luminous Galaxies: The Brightest Cluster Magnitude-Star Formation Rate Relation
  2013, ApJ Letters, 775, 38

- **Randriamanakoto Z.**, Väisänen P., Ryder S., et al.
  The K-band luminosity functions of super star clusters in luminous infrared galaxies, their slopes and the effects of blending
  2013, MNRAS, 431, 554

A.2 Peer-reviewed papers in preparation

- **Randriamanakoto Z.**, Väisänen P., Ryder S., et al.
WFC3/UVIS imaging of young massive clusters in the interacting system Arp 299
MNRAS, in prep

- Väisänen P., **Randriamanakoto Z.**, Ryder S., et al.
Photometric properties of the IRAS 18293−3413 super star clusters
MNRAS, in prep

- **Randriamanakoto Z.**, Escala A., Väisänen P., et al.
Characterizing the star clusters in star-forming galaxies: the SUNBIRD survey
MNRAS, in prep

- Herrero-Illana R., **Randriamanakoto Z.**, et al.
Combined analysis of luminous infrared galaxies in the radio and NIR wavelengths
MNRAS, in prep

A.3 Selected non-refereed papers

- Väisänen P., **Randriamanakoto Z.**, Escala A., et al.
Super Star Clusters in Luminous Infrared Galaxies: the SUNBIRD Survey
2014, Massive Young Star Clusters Near and Far: From the Milky Way to Reionization, 185; arXiv: 1402.2357

- Väisänen P., Escala A., Kankare E., ..., **Randriamanakoto Z.**, et al.
Central regions of LIRGs: rings, hidden starbursts, Supernovae and star clusters
2012, Journal of Physics Conference Series, 372, 012045; arXiv: 1202.6236

- **Randriamanakoto Z.** & Väisänen P.
Super Star Cluster Luminosity Functions in Interacting Luminous Infrared Galaxies
2011, IAU Symposium, 277, 37

- Väisänen P., **Randriamanakoto Z.**, Kankare E., et al.
Super star clusters and Supernovae in interacting LIRGs unmasked by NIR AO
2010, Galaxies and their Masks, 147; arXiv: 1009.5039

Appendix B

Testing the accuracy of the fits

Overview

This Appendix is composed of a list of figures that was used to assess the robustness of the results from the mass and age modelling and to investigate sources with NIR excess. Only star clusters with low photometric uncertainties ($\sigma \leq 0.25$ mag) in the field of NGC 3690 and ESO 550−IG025 were considered in the analyses.

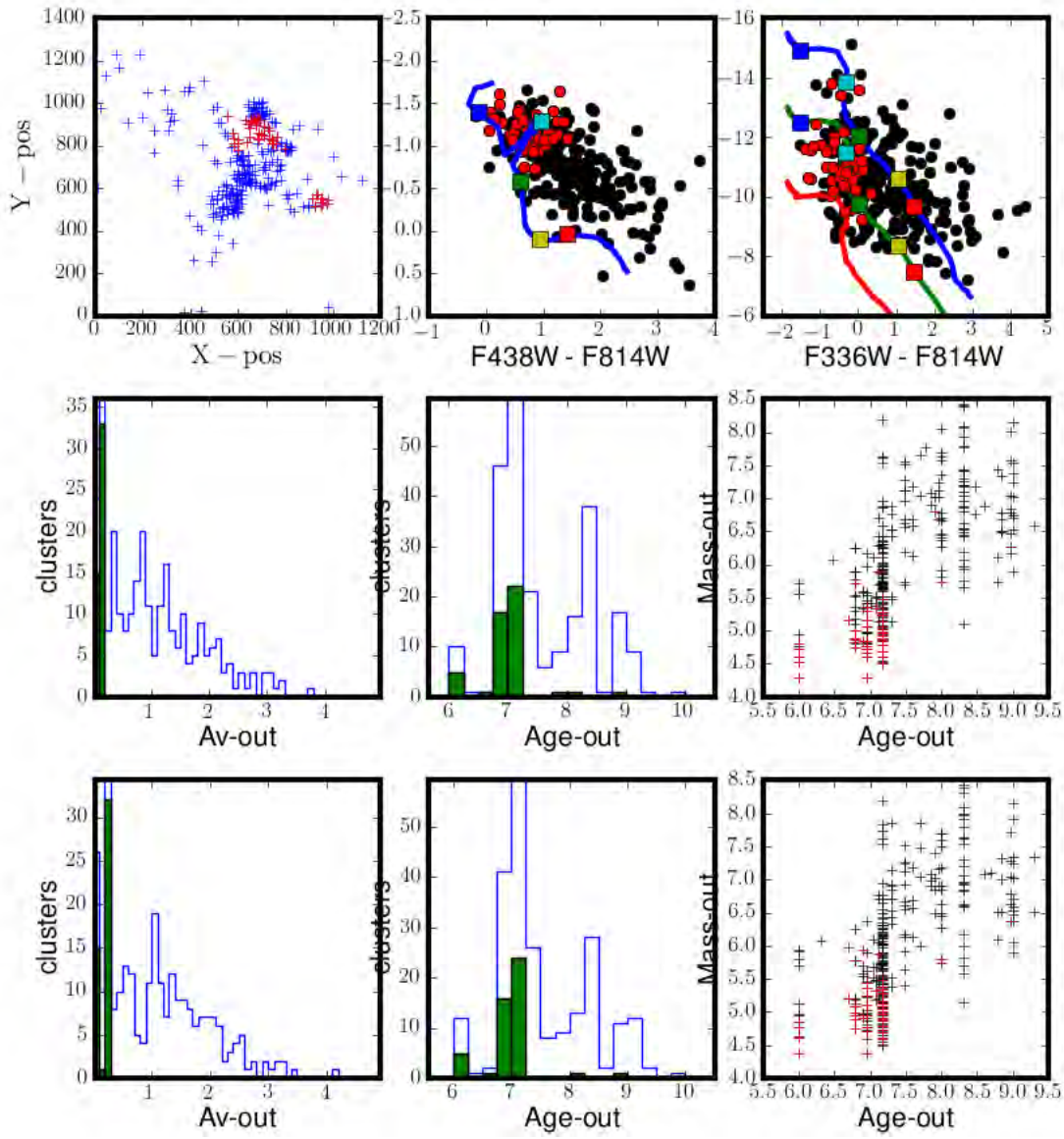

Figure B.1: Deriving physical parameters of clusters with less patchy dust distributions ($A_V^0 < 0.25$) in the field of NGC 3690. The top panels show their distribution (red points) in a 1-D plot of the extinction map, in a color-color and color-magnitude diagrams, respectively. Two sets of extinction ranges were used to fit the age, mass, and extinction: $A_V = 0 - 0.15$ (middle panels) and $A_V = 0 - 0.25$ (bottom panels). Results from the SED fitting show that both extinction ranges output similar age and extinction distributions of the clusters (in green) as well as age-mass planes (red crosses).

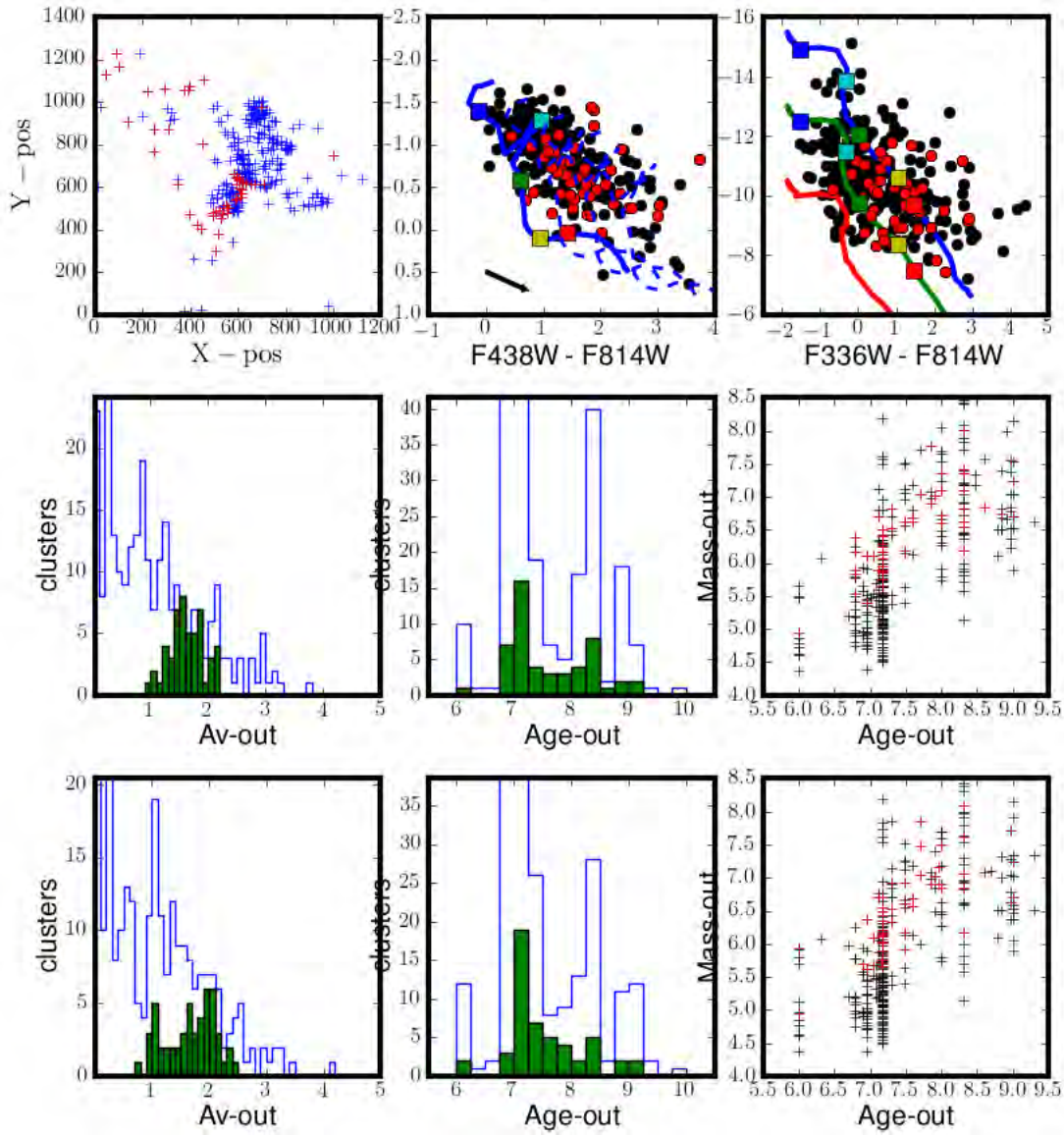

Figure B.2: Deriving physical parameters of clusters with high dust distributions ($1.2 < A_V^0 < 2$) in the field of NGC 3690. The top panels show their distribution (red points) in a 1-D plot of the extinction map, in a color-color and color-magnitude diagrams, respectively. Two sets of extinction ranges were used to fit the age, mass, and extinction: $A_V^0 \pm 0.25$ (middle panels) and $A_V^0 \pm 0.5$ (bottom panels). The results are consistent with the distribution of the data points in the CCD regardless of the extinction ranges.

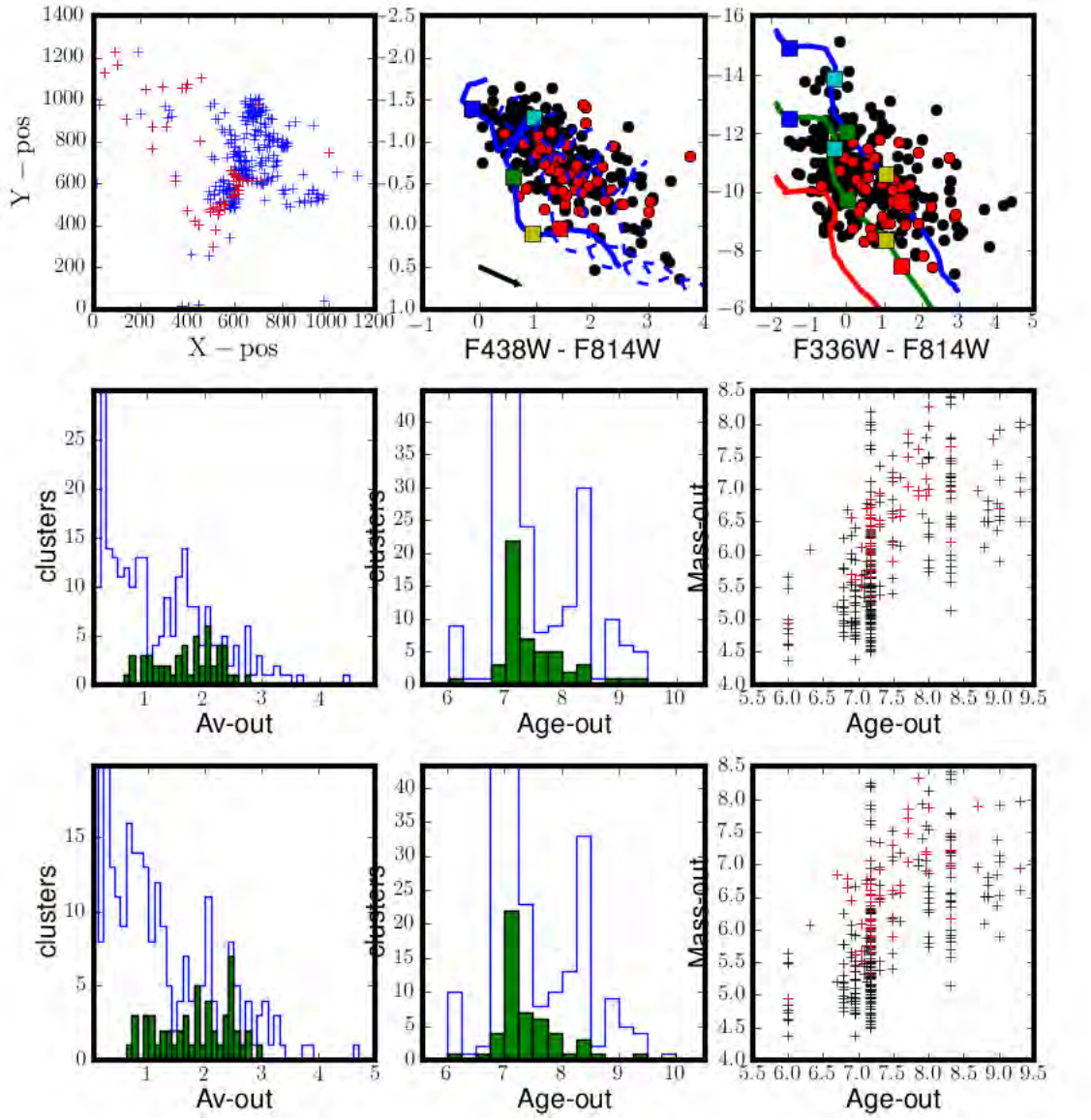

Figure B.3: The same as in Figure B.2 but for $A_V^0 \pm 0.75$ (middle panels) and $A_V^0 \pm 1$. Again, the results are consistent with the distribution of the data points in the CCD regardless of the extinction ranges.

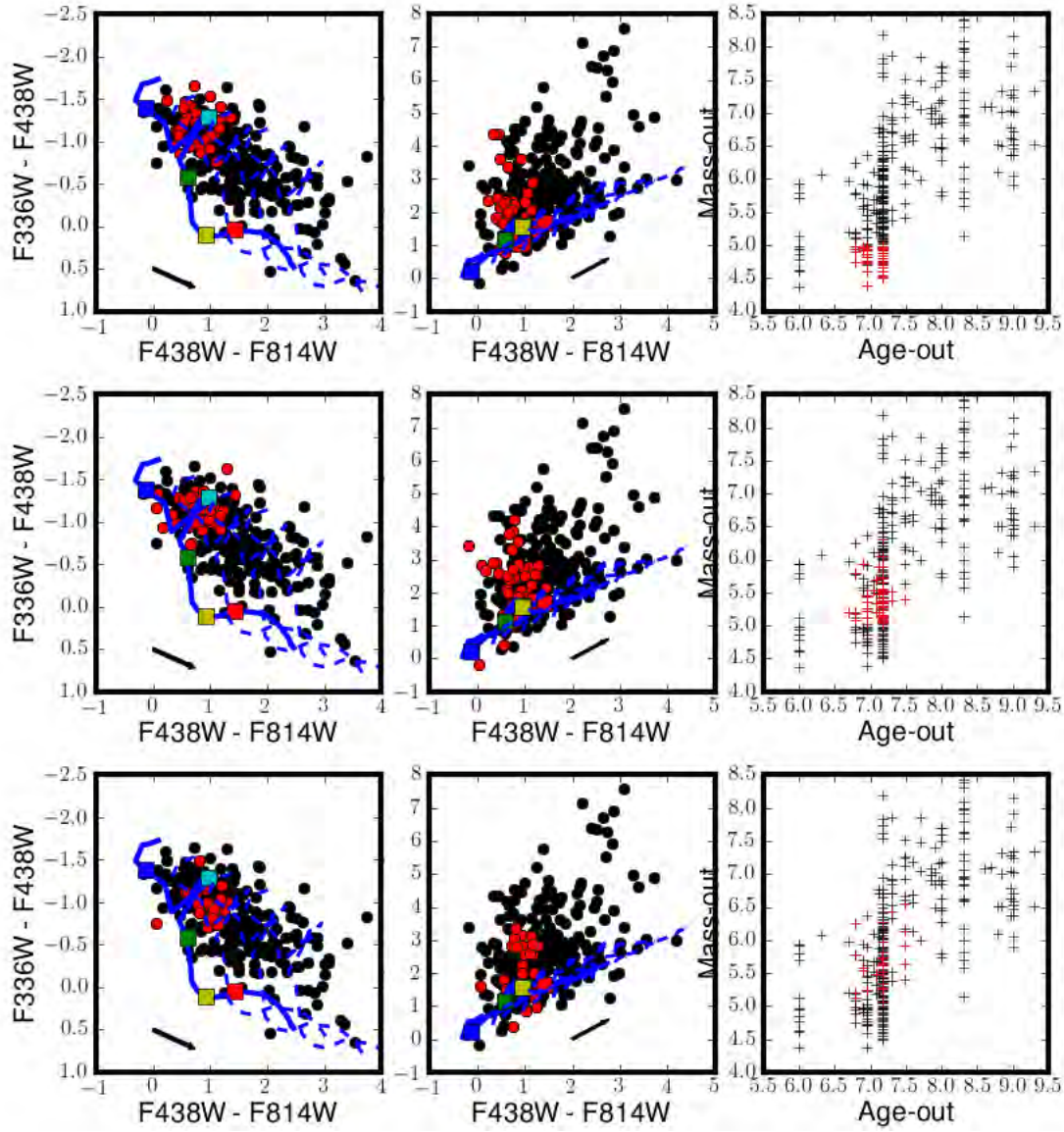

Figure B.4: Test to check whether NIR excess is due to stochasticity. Clusters of NGC 3690 with different masses but within the same age bins ($6.5 < \log \tau < 7.5$) are considered. The values of the predicted extinction ranges, A_V^0, are less than 0.5 mag. The distribution of low-mass clusters ($M_{cl} \leq 10^5\,M_\odot$, top panels) in $I-K$ versus $B-I$ colors (middle panels) were compared to that of the massive star clusters ($M_{cl} > 10^5\,M_\odot$, middle and top panels). The distribution of the SSCs in the CCD does not seem to depend on their cluster mass.

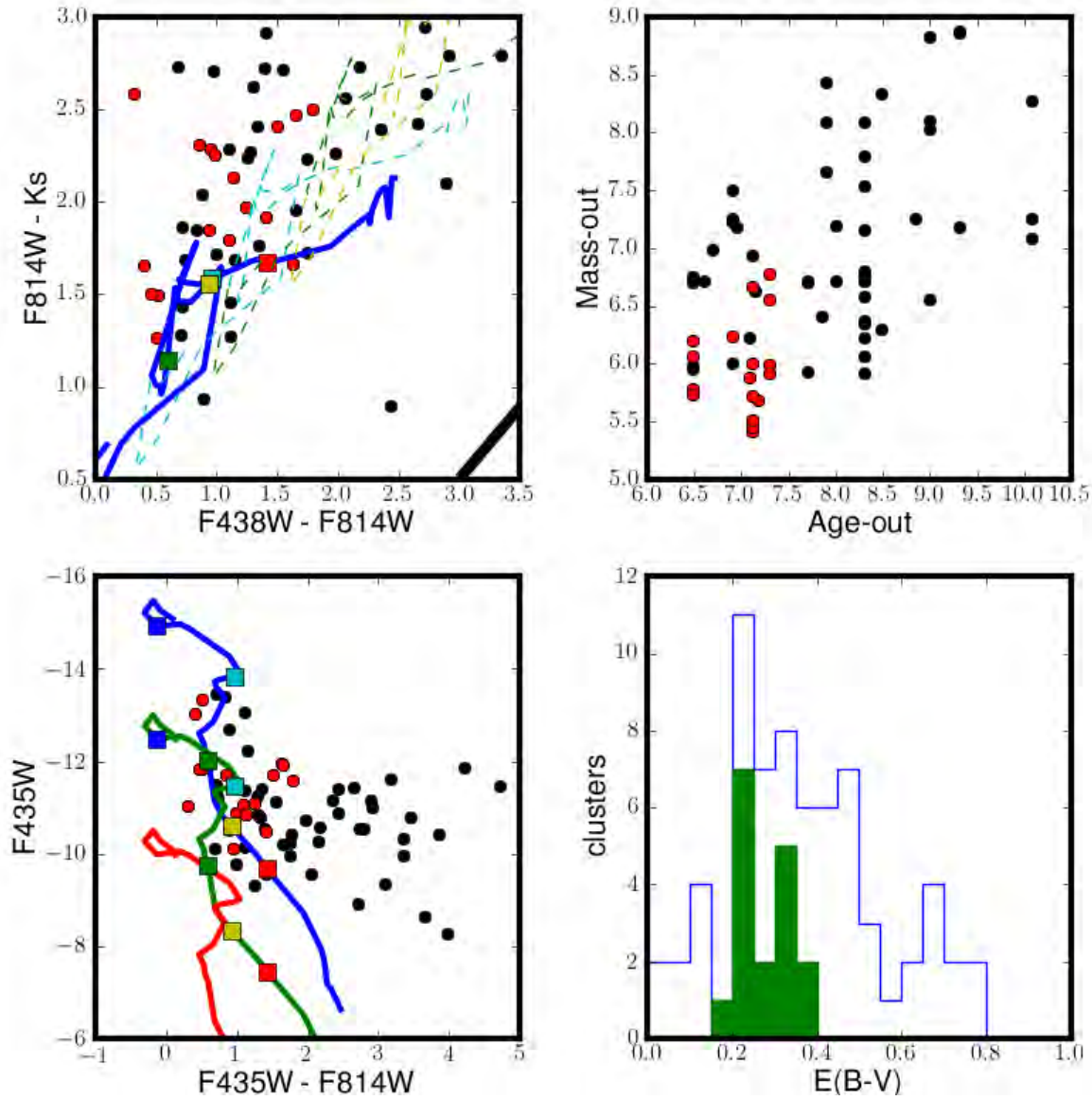

Figure B.5: Test to check whether the derived cluster mass, age, and extinction are consistent with the distribution of the data points in the CMD/CCD (left panels). Young clusters ($log\,\tau < 7.5$) with low extinction values ($A_V \leq 1.62$, green histogram in the bottom right panel) in the field of ESO 550−IG025 were considered. They are labelled as red points in the CMD/CCD and the age-mass plane (upper right). The plots indicate that the estimates from the χ^2 minimization are generally consistent with the distribution of the data points in the CMD/CCD.

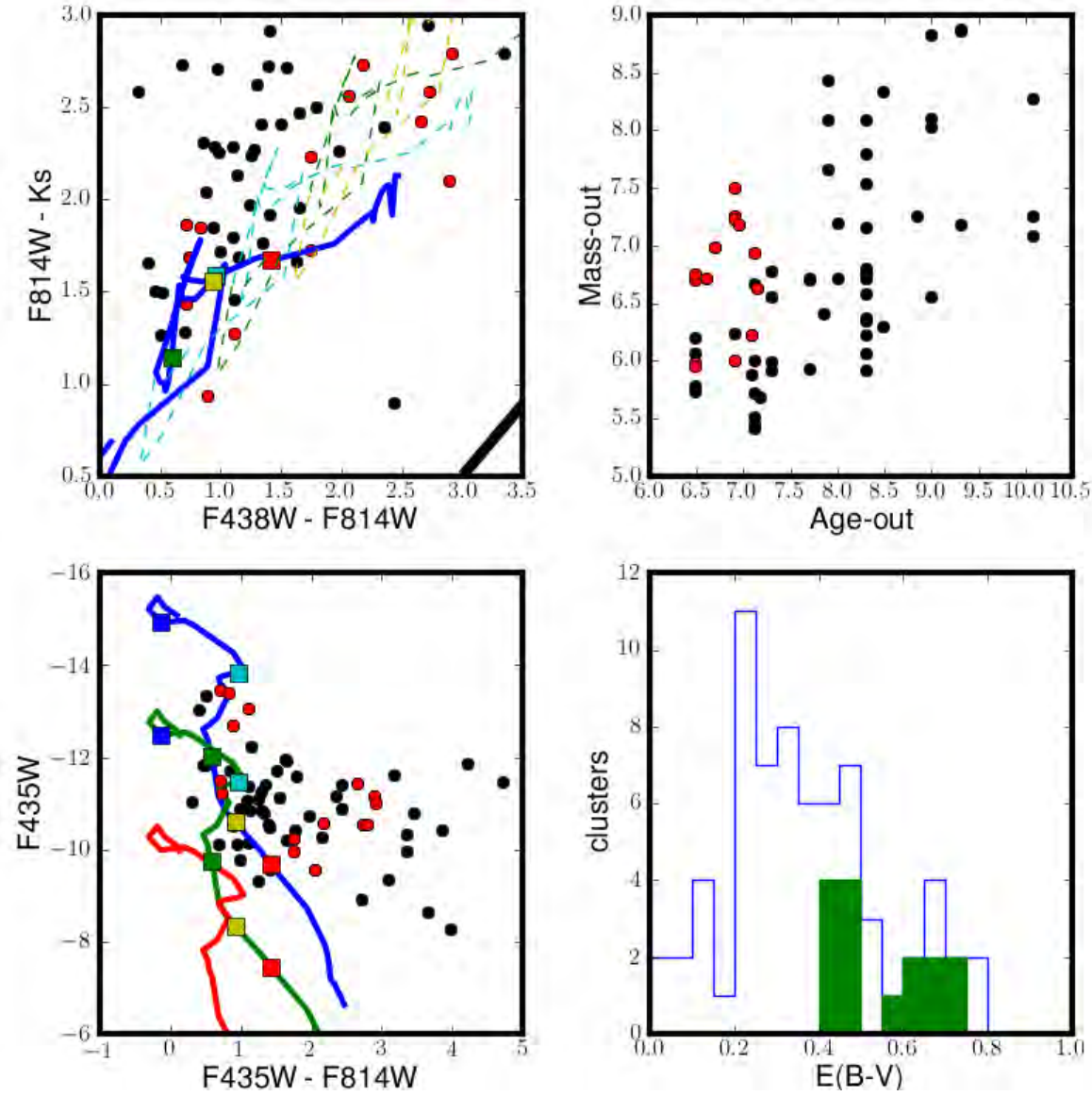

Figure B.6: The same as in Figure B.5 but for young clusters ($log\,\tau < 7.5$) with high extinction values ($A_V > 1.62$, green histogram in the bottom right panel). Again, the estimates from the χ^2 minimization correlate with the distribution of the data points in the CMD/CCD.

Appendix C

Results using Starburst99

Overview

This Appendix shows the colors of the SSC candidates overplotted with `Starburst99` model. It also presents the resulting mass and age distribution of the star cluster population.

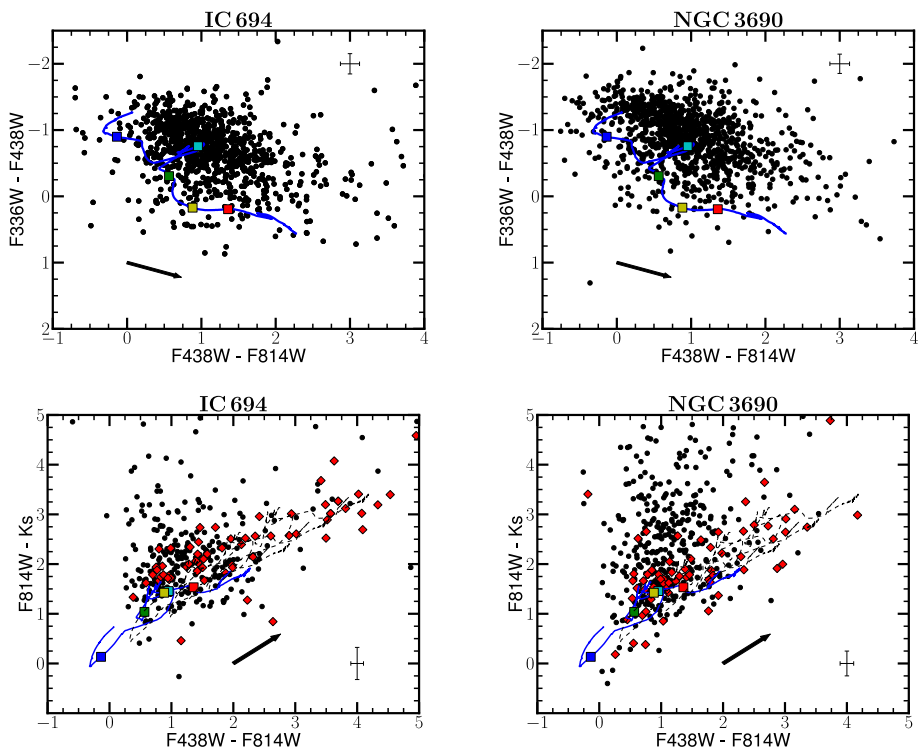

Figure C.1: SSC color-color diagrams of Arp 299 overplotted with `Starburst99` model (solid lines). Labels the same as in Figure 5.3. *Top:* $U-B$ versus $B-I$ colors. *Bottom:* $I-K$ versus $B-I$ colors.

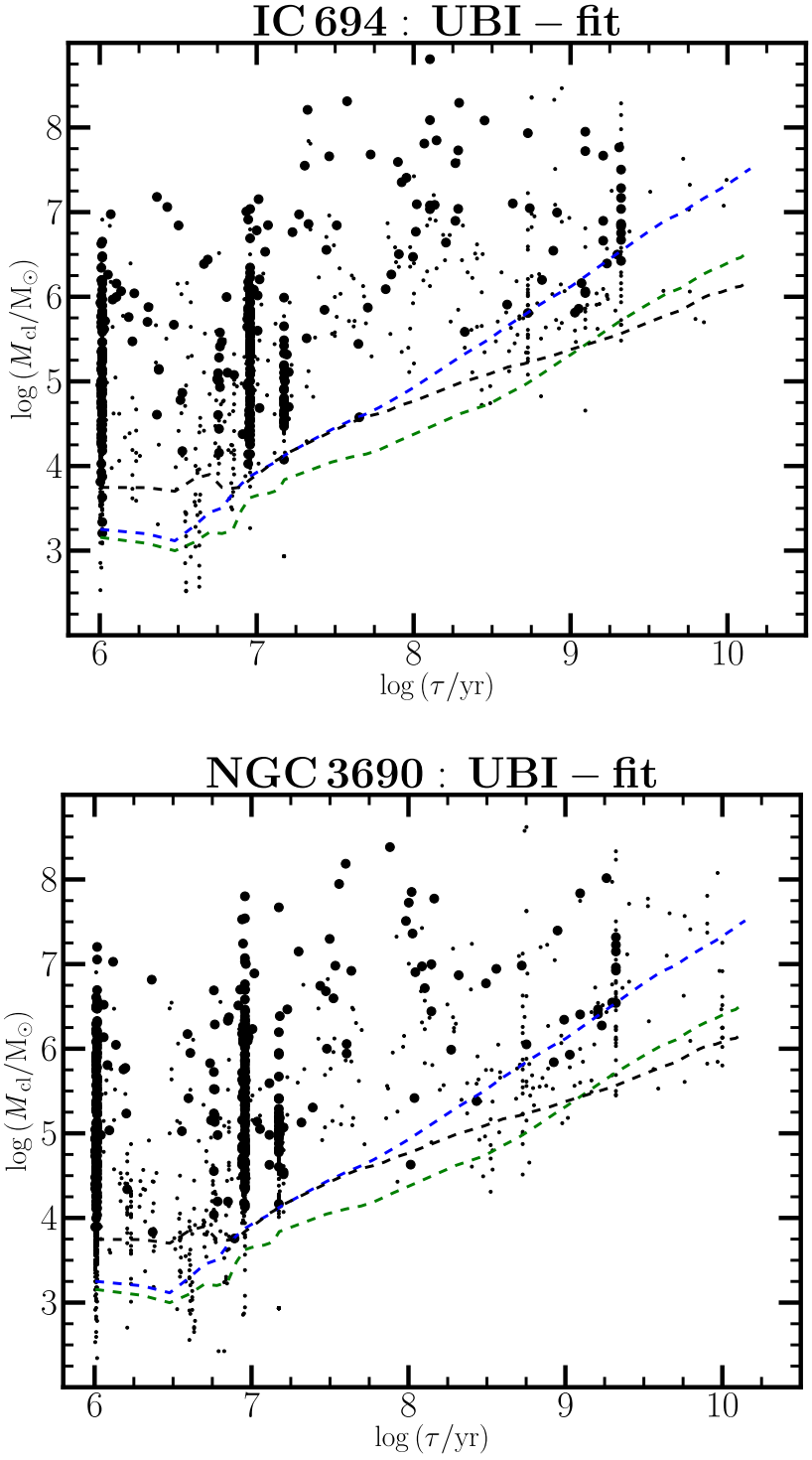

Figure C.2: The cluster age-mass planes of IC 694 (top) and NGC 3690 (bottom) from the χ^2-fit considering UBI-filters and `Starburst99` SSP model. More pronounced chimneys are seen at around ≈ 1 Myr and ≈ 10 Myr compared to those observed in Figure 5.5.